

Synthesis and Application of Transition Metal Oxides as Oxygen Evolution Catalysts

Thèse N° 7355

Présentée le 20 août 2019

à la Faculté des sciences de base

Laboratoire de synthèse et de catalyse inorganique

Programme doctoral en chimie et génie chimique

pour l'obtention du grade de Docteur ès Sciences

par

Laurent LIARDET

Acceptée sur proposition du jury

Prof. K. Sivula, président du jury

Prof. X. Hu, directeur de thèse

Prof. C. Tard, rapporteur

Prof. D. Zhang, rapporteur

Prof. A. Hagfeldt, rapporteur

2019



ÉCOLE POLYTECHNIQUE
FÉDÉRALE DE LAUSANNE

"L'eau est le charbon de l'avenir"

Jules Verne, L'Île mystérieuse

Acknowledgements

At first, I would like to thank Professor Xile Hu, director of the Laboratory of Inorganic Synthesis and Catalysis (LSCI), for having offered me the opportunity to accomplish my doctoral thesis in his group. I am grateful for the projects he offered me and for his guidance, help and trust. His advice were extremely precious to me in order to complete my scientific formation.

I thank also the jury members, Prof. Cédric Tard, Prof. Anders Hagfeldt, Prof. Di Zhang and Prof Kevin Sivula who reviewed and evaluated this work.

Then, I want to acknowledge all the present and previous members of the LSCI with whom I have worked and spent time. I would like to especially thank Prof. Carlos Morales for having led me during the early stages of my thesis and Prof. Jordan Katz for all the help and fruitful discussions and collaborations in photoelectrochemistry. I also thanks Dr. Heron Vrubel for the guidance and technical aspect advice he gave me throughout my different projects. I also would like to thank Dr. Fang Song, Dr. Lucas Stern, Aliko Moysiadou, Lichen Bai, Weiyan Ni and Dr. Elitsa Petkucheva for all the discussions and collaborations we had together in electrochemistry. I also express gratitude to Dr. Pablo Perez, Dr. Thomas Di Franco, Guido Barzanò, Marten Ploeger, Xiangli Yi, Albert Daubry, Céline Prange and Murat Alkan for all the lunches, coffee breaks and time spent together with a special emphasis for Céline and Guido for the translation of the abstract.

I also thank Prof. Michael Grätzel, Prof. Jingshan Luo and Dr. Matthew Mayer from the LPI laboratory for the collaboration and advice they gave me on the hematite project.

I would like to also express gratitude to all the staff of the chemical store of our building and of the mechanical and electronic workshop of ISIC. I also thank the personnel of the CIME for the training and help on the electronic microscopes and Pierre Mettraux for the XPS analyses.

I also thank Anne-Sophie Chauvin for having mentoring me during these 4 years and for all her generosity and advice that helped me to successfully accomplish my doctoral studies.

Last but not least, I would like to thank my family and friends as well as Amélie for their love, support and constant motivation during my doctoral years. This thesis would not have been possible without them.

Abstract

Nowadays, mankind is facing an important energy challenge. Depletion in fossil fuels reserves and increasing energy demand, coupled with the problematic greenhouse effect induced by massive anthropogenic release of carbon dioxide into the atmosphere, are driving forces for the development of renewable and carbon-free energy technologies. Hydrogen gas is considered as the energy carrier of the future and is expected to replace fossil fuels in order to create a Hydrogen Economy. Hydrogen is viable for decarbonization of our society only if it is produced from sustainable and renewable energies. Water splitting, the redox reaction producing hydrogen and oxygen gas by reducing and oxidizing water, respectively, is a promising technique to produce clean hydrogen. However, the kinetics of the oxidative half-reaction, namely the oxygen evolution reaction (OER), are slow and catalysts are required in order to increase the global efficiency of water splitting. Moreover, in order to perform water splitting at large scale, catalysts based on Earth-abundant elements should be developed. This thesis focuses on the development of transition metal oxides catalysts, by different synthesis techniques, for electrochemical and photoelectrochemical oxygen evolution.

Chapter 2 focuses on the atomic layer deposition (ALD) of different cobalt-based metal oxides and the development of procedures to fabricate bi- and trimetallic oxides catalysts. Cobalt vanadium oxide (CoVO_x), cobalt iron oxide (CoFeO_x) as well as cobalt vanadium iron oxide (CoVFeO_x) are deposited by ALD and evaluated for OER. The ALD deposition method allowed us to apply these material on high-surface area nickel foam substrates. Among them, CoFeO_x shows the highest catalytic activity for water oxidation and can compete with state-of-the art electrocatalysts for OER in alkaline solution.

In Chapter 3, we focused on developing a photoelectrodeposition method to deposit CoFeO_x on nanocauliflower hematite photoanodes. This photoelectrodeposition method allowed the deposition of an ultrathin, amorphous and optically transparent CoFeO_x layer that induced a large cathodic shift of the photocurrent onset potential of hematite and a high enhancement of the photocurrent at 1.0 V vs RHE. Additionally, the reason of the improvement of the onset potential was explored in detail in order to differentiate between possible activity enhancement effects such as an increase of charge transfer kinetics, a reduction of surface recombination, a modification of the flat band potential or an increase of the photovoltage. We concluded that CoFeO_x improved

the OER efficiency of nanocauliflower hematite photoanodes by purely enhancing the kinetics of water oxidation.

Chapter 4 details the development of a hydrothermal route to fabricate CoVO_x . On the basis of a volcano plot that correlates the OER activity to the M-OH bond strength of metal oxides, CoVO_x was predicted to be a highly active electrocatalyst that could compete with the most active OER electrocatalysts in alkaline solution. After characterization, this hydrothermally synthesized cobalt vanadium oxide was seen to be amorphous and provided high catalytic activity towards OER. This chapter, in addition to increasing the library of OER electrocatalysts, demonstrates the usefulness of M-OH bond strength as a simple descriptor for experimental development of OER catalysts.

Keywords: Oxygen evolution, water splitting, hematite photoanode, transition metal oxides, atomic layer deposition, photoelectrodeposition, hydrothermal synthesis.

Résumé

Aujourd'hui, l'humanité se trouve face à un important défi énergétique. L'épuisement des énergies fossiles, la croissance de la demande énergétique ainsi que la problématique du réchauffement climatique induit par l'émission anthropogène de dioxyde de carbone sont des arguments en faveur du développement d'énergies et de technologies renouvelables sans émission de CO₂. L'hydrogène gazeux est considéré comme le vecteur énergétique de l'avenir et pourrait remplacer les combustibles fossiles afin de créer une "Economie de l'hydrogène". L'hydrogène est utile pour la decarbonization de notre société seulement s'il est produit par des énergies durables et renouvelables. L'électrolyse de l'eau, la réaction d'oxydo-réduction produisant de l'hydrogène et de l'oxygène gazeux par réduction et oxydation de l'eau, est une technique prometteuse pour produire de l'hydrogène durable. Cependant, la cinétique de la demi-réaction d'oxydation, appelée "évolution d'oxygène (OER)", est lente et des catalyseurs sont requis pour augmenter le rendement de production d'hydrogène. De plus, afin de déployer l'hydrolyse de l'eau à grande échelle, des catalyseurs faits d'éléments abondants dans l'écorce terrestre doivent être développés. Cette thèse se concentre sur le développement, par différentes techniques de synthèse, de catalyseurs basés sur des oxydes de métaux de transition pour l'évolution d'oxygène électrochimique et photoélectrochimique.

Le chapitre 2 se concentre sur l'Atomic Layer Deposition (ALD) de différents oxydes basés sur le cobalt et sur le développement de procédures pour la fabrication d'oxydes bi- et trimétalliques. L'oxyde de cobalt-vanadium (CoVO_x), l'oxyde de cobalt-fer (CoFeO_x) ainsi que l'oxyde de cobalt-vanadium-fer (CoVFeO_x) sont déposés par ALD et leur activité catalytique pour l'évolution d'oxygène est évaluée. La déposition par ALD nous permet aussi d'appliquer ces matériaux sur des substrats poreux de mousse de nickel. Parmi ces matériaux, CoFeO_x est le plus actif pour catalyser l'oxydation de l'eau et rivalise avec les meilleurs catalyseurs pour l'évolution d'oxygène en milieu alcalin.

Dans le chapitre 3, nous nous concentrons sur le développement d'une méthode de photoélectrodéposition pour appliquer du CoFeO_x sur des photoanodes d'hématite en nanostructure de nano chou-fleur. Cette méthode de photoélectrodéposition nous permet de déposer une couche ultrafine de CoFeO_x amorphe et optiquement transparente qui induit un large déplacement cathodique du potentiel de commencement du photocourant ainsi qu'un accroissement du

photocourant à 1.0 V vs RHE. De plus, la raison de cette amélioration du potentiel de commencement est investiguée afin de différencier entre de possibles effets d'augmentation d'activité tels que l'accélération de la cinétique de transfert de charges, la réduction de recombinaison à la surface, la modification de la bande plate ou l'augmentation du photovoltage. Nous concluons que le CoFeO_x améliore l'évolution d'oxygène de ces photoanodes d'hématite par un effet purement d'accélération de la cinétique.

Le chapitre 4 détaille le développement d'une synthèse hydrothermal pour fabriquer CoVO_x . Sur la base d'un graphique en volcan corrélant l'activité OER à la force de liaison M-OH des oxydes de métaux, nous prédisons que CoVO_x pourrait être un électrocatalyseur hautement actif qui pourrait rivaliser avec les catalyseurs les plus actifs pour l'évolution d'oxygène en milieu alcalin. Après analyse, ce CoVO_x produit par synthèse hydrothermale a une cristallinité amorphe et est hautement actif pour l'évolution d'hydrogène. Ce chapitre, en plus de compléter la librairie des électrocatalyseurs disponibles, démontre l'utilité de la force de liaison M-OH comme descripteur simple pour le développement expérimental de catalyseurs pour OER.

Mots-clés: Evolution d'oxygène, photoanode d'hématite, oxydes de métaux de transition, atomic layer deposition, photoelectrodeposition, synthèse hydrothermale.

Riassunto

Oggi, l'umanità deve affrontare un'imponente sfida energetica. La scarsità di combustibili fossili e l'incremento della domanda per essi, accompagnata dall'emissione da parte dell'uomo di importanti quantità di gas serra come l'anidride carbonica, porta a concentrarsi sullo sviluppo di tecnologie rinnovabili e senza emissioni. L'idrogeno gassoso è considerato il vettore energetico del futuro e ci si aspetta che sostituisca i combustibili fossili per formare un'economia basata su di esso. È possibile pensare all'idrogeno come sostituto per la "decarbonizzazione" della nostra società solo se viene prodotto con metodi sostenibili e rinnovabili. Il "water splitting", la reazione redox che produce idrogeno e ossigeno gassosi riducendo e ossidando rispettivamente l'acqua, è una tecnica promettente per la produzione di idrogeno. Purtroppo, le cinetiche della semi-reazione riguardante l'ossidazione dell'acqua, soprannominata reazione di evoluzione di ossigeno (OER), sono lente e, per rendere il procedimento efficiente, è necessario usare dei catalizzatori. In oltre, per poter portare questo processo ad una produzione in larga scala è necessario utilizzare catalizzatori economici e abbondanti sulla terra. Questa tesi si concentra sulla catalisi degli ossidi metallici di transizione, sintetizzati con differenti metodi, per l'evoluzione di ossigeno elettrochimicamente e fotoelettrochimicamente.

Il secondo capitolo si concentra sulla "atomic layer deposition" (ALD) di vari ossidi di cobalto e lo sviluppo di procedure per fabbricare catalizzatori di ossidi bi e trimetallici. Ossidi di cobalto/vanadio, cobalto/ferro e cobalto/vanadio/ferro sono depositati mediante ALD e valutati per OER. Utilizzando il metodo ALD è possibile applicare questi materiali su una grande superficie di spugna di nichel. Tra questi, gli ossidi di cobalto/ferro hanno la più alta attività catalitica per l'ossidazione dell'acqua, e può competere con gli elettrocatalizzatori OER in soluzione alcalina già noti in letteratura.

Il capitolo 3 si concentra sullo sviluppo di un metodo di fotoelettrodeposizione di CoFeO_x su fotoanodi di ematite "nanocavolfiore". Questo metodo di fotoelettrodeposizione permette la formazione di uno strato ultrafine, amorfo e otticamente trasparente di CoFeO_x che induce un grande spostamento catodico del potenziale dell'ematite e un grande innalzamento della corrente a 1.0 V vs RHE. In più, la causa dell'innalzamento di potenziale è stata studiata più in dettaglio per poter differenziare tra possibili effetti di innalzamento come l'incremento del trasferimento cinetico di carica, riducendo la ricombinazione di superficie, modificando la banda piatta di

potenziale o innalzando il fotovoltaggio. La conclusione è stata che CoFeO_x innalzava l'efficienza OER dei fotoanodi di ematite "nanocavolfiore" innalzando la cinetica dell'ossidazione dell'acqua.

Il capitolo 4 esplora lo sviluppo di una strada idrotermica per produrre CoVO_x . Sulla base di un "vulcano plot" che correla l'attività OER e la forza del legame M-OH, è stato possibile prevedere che CoVO_x sarebbe stato molto attivo come elettrocatalizzatore, in grado di competere con i più attivi catalizzatori alcalini per OER. Questo capitolo, non solo allarga la libreria di elettrocatalizzatori per OER, ma dimostra anche l'utilità dell'uso della forza del legame M-OH come semplice parametro per lo sviluppo sperimentale di catalizzatori per OER.

Parole chiave: evoluzione di ossigeno, divisione dell'acqua, fotoanodo di ematite, ossidi dei metalli di transizione, deposizione di strato atomico, fotoelettrodeposizione, sintesi idrotermica.

Zusammenfassung

Die Menschheit von heute steht vor wichtigen Herausforderungen in der Energieversorgung. Das Aufbrauchen der fossilen Energiereserven und die steigende Nachfrage nach Strom und fossilen Brennstoffen, zusammen mit dem von Menschen verursachten Ausstoss des problematischen Treibhausgases Kohlenstoffdioxid in die Atmosphäre, motivieren die Entwicklung von erneuerbaren und kohlenstoffdioxidfreien Technologien. Wasserstoffgas wird als Energieträger der Zukunft betrachtet und es wird erwartet, dass Wasserstoff fossile Brennstoffe ersetzen und eine Wasserstoffwirtschaft entstehen wird. Die Dekarbonisierung unserer Gesellschaft ist nur realisierbar, wenn Wasserstoff von nachhaltigen und erneuerbaren Energien produziert wird. Die elektrolytische Spaltung von Wasser, eine Redoxreaktion, die Wasserstoff- und Sauerstoffgas durch das Reduzieren respective Oxidieren des Wassers produziert, ist eine vielversprechende Technik sauberen Wasserstoff herzustellen. Die Kinetik der Oxidation als Teilprozess, auch Sauerstoffentwicklungsreaktion (OER) genannt, ist langsam, und Katalysatoren sind nötig um die Gesamteffizienz der Wasserspaltung zu erhöhen. Um diese in grossem Massstab zu betreiben, sollten darüber hinaus Katalysatoren entwickelt werden, die aus in der Erde reichlich vorkommenden Elementen bestehen. Diese Arbeit ist fokussiert auf das Entwickeln von Übergangsmetalloxidkatalysatoren für die elektrochemische und photochemische Sauerstoffentwicklung durch verschiedene Synthesetechniken.

Das zweite Kapitel behandelt die Atomlagenabscheidung (ALD) von verschiedenen kobalt-basierten Metalloxiden und die Entwicklung von Verfahren zur Herstellung von zwei- oder dreimetallinen Oxidkatalysatoren. Kobaltvanadiumoxid (CoVO_x), Kobalteisenoxid (CoFeO_x) und Cobaltvadiumeisenoxid (CoVFeO_x) wurden durch ALD abgeschieden und mithilfe von OER ausgewertet. Die ALD-Methode erlaubte uns diese Materialien auf grosse Oberflächen von Nickelschaums substraten anzuwenden. Unter anderem zeigte CoFeO_x die höchste katalytische Aktivität in der Oxidation von Wasser und es konkuriert mit den modernsten Elektrokatalysatoren für OER in basischer Lösung.

Im dritten Kapitel wird die Entwicklung der Photoelektroabscheidungsmethode zur Abscheidung von CoFeO_x auf Photoanoden aus Nanocauliflowerhematit behandelt. Diese Photoelektroabscheidungsmethode erlaubte die Abscheidung einer ultradünnen, amorphen und optisch transparenten Lage, welche eine grosse Verschiebung in der Kathode beim anfänglichen

Photostrompotential des Hematits und eine hohe Steigerung des Photostroms bei 1.0 V vs RHE herbeiführt. Zusätzlich wurde der Grund für die Verbesserung der Anfangspotentialsverschiebung detailliert untersucht um zwischen möglichen aktivitätssteigernden Effekten wie erhöhte Ladungstransportkinetik, verkleinerter Oberflächenrekombination, verändertem Flachbandpotential oder erhöhter Photospannung zu unterscheiden. Wir kamen zum Schluss, dass CoFeO_x die OER-Effizienz von Photoanoden aus Nanocauliflowerhematit erhöht, indem es rein die Kinetik der Wasseroxidation steigert.

Das vierte Kapitel berichtet über die Entwicklung der Hydrothermalroute für die Herstellung von CoVO_x . Auf Basis eines Volcano Plots, der die OER-Aktivität mit der M-OH Bindungsstärke der Metalloxide korreliert, wurde vorausgesagt, dass CoVO_x ein hochaktiver Elektrokatalysator sei, der mit den aktivsten OER Elektrokatalysatoren in basischer Lösung konkurrenzieren könne. Nach der Charakterisierung wurde beobachtet, dass das hydrothermal hergestellte Kobaltvanadiumoxid amorph war und hohe katalytische Aktivität in OER lieferte. Dieses Kapitel, zusätzlich zu der steigenden Zahl an OER Elektrokatalysatoren, zeigt auf, dass die M-OH Bindungsstärke ein einfacher Kennwert für das experimentelle Entwickeln von OER Katalysatoren ist.

Schlüsselbegriffe: Sauerstoffentwicklung, Wasserspaltung, Hematitphotoanode, Übergangsmetalloxide, Atomlagenabscheidung, Photoelektrodenabscheidung, Hydrothermalsynthese.

Symbols and Abbreviations

α	charge transfer coefficient
AC	alternative current
AFC	alkaline fuel cell
ALD	atomic layer deposition
ALE	atomic layer epitaxy
AM	air mass
APCVD	atmospheric pressure chemical vapor deposition
BE	binding energy
ca.	circa
CB	conduction band
CCS	carbon capture and storage
C_{sc}	capacitance of the space-charge
CSP	concentrated solar thermal power
C_{ss}	capacitance of the surface states
CVD	chemical vapor deposition
Δ	differential (finite)
DC	direct current
DFT	density Functional Theory
DH	double hydroxide
DMAMFc	N,N-Dimethylaminomethylferrocene
DMFC	direct methanol fuel cell
e	exponential
e^-	electron

EDX	energy-dispersive X-ray spectroscopy
E_F	Fermi level
$E^*_{F,n}$	quasi Fermi level of electrons
$E^*_{F,p}$	quasi Fermi level of holes
e.g.	example given
E_g	band gap energy
EIS	electrochemical impedance spectroscopy
Eq.	equation
<i>et al.</i>	<i>et alii</i>
F	Faraday constant
FTO	fluorine-doped tin oxide
GPC	growth rate per cycle
η	overpotential
η_a	activation overpotential
η_c	concentration overpotential
η_{inj}	charge injection efficiency
η_{sep}	charge separation efficiency
h^+	hole
HAADF	high-angle annular dark-field
HER	hydrogen evolution reaction
HR	high resolution
i	current
i_0	exchange current
j	current density
j_0	exchange current density

JCPDS	Joint Committee on Powder Diffraction Standards
k_{ct}	charge-transfer rate constant
λ	wavelength
LDH	layered double hydroxides
LSV	linear sweep voltammetry
MCFC	molten carbonate fuel cell
MPC	mass flow controller
NF	nickel foam
NHE	normal hydrogen electrode
OER	oxygen evolution reaction
PAFC	phosphoric acid fuel cell
PEC	photoelectrochemical
PEMFC	polymer electrolyte membrane fuel cell
PID	proportional-integral-derivative
PL	photoluminescence
PV	photovoltaics
QCM	quartz crystal microbalance
R	universal gas constant
R_{ct}	charge transfer resistance
RDS	rate-determining step
RHE	reversible hydrogen electrode
ROM	rule of mixture
rpm	revolutions per minute
R_{rec}	recombination resistance
R_s	solution resistance

R_{tot}	total resistance
SAED	selected area electron diffraction
SEM	scanning electron microscope
SOFC	solid oxide fuel cell
STEM	scanning transmission electron microscope
STH	solar-to-hydrogen
τ	time constant
T	temperature (K)
TEM	transmission electron microscope
TDMASn	tetrakis(dimethylamino)tin
TDMAT	tetrakis(dimethylamino)titanium
TMA	trimethylaluminium
VB	valence band
vs	versus
wt%	weight percent
XPS	X-ray photoelectron spectroscopy
XRD	X-ray diffraction
z	number of electrons

Units and Prefixes

G	giga- (10^9)	Å	ångström
T	tera- (10^{12})	W	watt
k	kilo- (10^3)	min	minute
c	centi- (10^{-2})	s	second
m	milli- (10^{-3})	h	hour
μ	micro (10^{-6})	M	molar
n	nano- (10^{-9})	a.u.	arbitrary units
ppm	part per million	Hz	hertz
m	meter		
J	joule		
L	liter		
g	gram		
K	kelvin		
C	coulomb		
°C	degree Celsius		
V	volt		
A	ampere		
eV	electronvolt		
dec	decade		

List of Figures

Figure 1.1	Source of hydrogen production and consuming sectors.....	6
Figure 1.2	Overview of the different hydrogen storage methods.....	7
Figure 1.3	Overview of the different types of fuel cells.....	8
Figure 1.4	Alkaline and PEM electrolyzers.....	11
Figure 1.5	Hydrogen evolution mechanism in acidic solution on a surface of an electrode...	13
Figure 1.6	Volcano plot of the exchange current density of several HER catalysts vs the Gibbs free energy of hydrogen adsorption.....	14
Figure 1.7	Oxygen evolution reaction sequence.....	15
Figure 1.8	Volcano plot of OER activity vs different descriptors (M-OH bond strength, ΔG_{O^*} - ΔG_{OH^*} and e_g electrons).....	16
Figure 1.9	Simplified scheme of natural photosynthesis.....	21
Figure 1.10	Band structure diagram for an insulator, semiconductor and metal.....	23
Figure 1.11	Interfacial band edge energetics for a p-type and n-type semiconductor/electrolyte interface before and after equilibrium in the dark.....	24
Figure 1.12	Band diagram for an n-type semiconductor in equilibrium in the dark and under illumination.....	25
Figure 1.13	Scheme of PV-electrolysis (PV cell connected to a PEM electrolyzer).....	26
Figure 1.14	AM 1.5G solar spectrum with fractions of spectrum absorbed by some selected semiconductors and band structure of different semiconductors).....	27
Figure 1.15	Dual-absorber PEC cell with photoanode and photocathode in tandem).....	28
Figure 2.1	ALD sequence of Al_2O_3 deposition.....	39
Figure 2.2	Initial ALD setup.....	42
Figure 2.3	Second ALD setup.....	43
Figure 2.4	Ozone generator and bubbler system.....	44
Figure 2.5	GPC rate of different metal oxides.....	45
Figure 2.6	Polarization curves in 1 M KOH of $CoFeO_x$ and $CoVO_x$ deposited with different ALD supercycles on FTO.....	48
Figure 2.7	Comparison between XPS Co content and Co content from ROM.....	49
Figure 2.8	XPS depth profiles of $CoFeO_x$ on FTO.....	51

Figure 2.9	GPC, overpotentials at different thicknesses and Tafel slopes of CoVO _x and CoFeO _x	52
Figure 2.10	XPS analysis of CoVO _x	54
Figure 2.11	XPS analysis of CoFeO _x	54
Figure 2.12	XRD patterns of CoFeO _x , CoVO _x , CoO _x , FeO _x and VO _x on Si (100) substrates.....	55
Figure 2.13	Polarization curves and Tafel slopes in 1 M KOH and 1 M Fe free KOH of CoFeO _x , CoVO _x and CoO _x on nickel foam. Stability and Faradaic efficiency of CoFeO _x and CoVO _x	57
Figure 2.14	SEM images of CoFeO _x on nickel foam before and after polarization in 1 M Fe free KOH.....	58
Figure 2.15	Polarization curves of CoVFeO _x deposited with different supercycles and overpotentials at different thicknesses.....	59
Figure 2.16	XRD spectra of CoVFeO _x on Si (100) substrate.....	60
Figure 2.17	XPS spectra of CoVFeO _x	61
Figure 2.18	Polarization curves, Tafel slopes, stability and faradaic efficiency of CoVFeO _x on nickel foam.....	62
Figure 2.19	SEM images of CoVFeO _x on nickel foam before and after polarization in 1 M Fe free KOH.....	63
Figure 3.1	Cross-section SEM images of APCVD hematite.....	78
Figure 3.2	Polarization curves in 1 M KOH of Fe ₂ O ₃ and Fe ₂ O ₃ coated with Al ₂ O ₃ and different OER catalysts under simulated AM 1.5G illumination and Fe ₂ O ₃ coated with CoFeO _x photoelectrodeposited and electrodeposited by different conditions.....	80
Figure 3.3	Polarization curves and stability in 1 M KOH under simulated AM 1.5G illumination at 1.0 V vs RHE of hematite photoanodes coated with CoFeO _x with different number of linear sweeps.....	81
Figure 3.4	Transmittance of hematite photoanodes, uncoated and coated with CoFeO _x deposited with different number of LSV sweeps. Stability at 1.0 and 1.23 V vs RHE under AM 1.5G illumination in 1 M KOH of CoFeO _x -coated hematite and faradaic efficiency of CoFeO _x -coated hematite at 1.23 V vs RHE.....	82
Figure 3.5	XPS spectra of CoFeO _x -coated hematite.....	83
Figure 3.6	XPS spectra of catalyst-free CoFeO _x hematite.....	83
Figure 3.7	SEM images of catalyst-free and CoFeO _x -coated hematite.....	84

Figure 3.8	TEM images of catalyst-free and CoFeO _x -coated hematite and STEM-EDX mapping of CoFeO _x -coated hematite.....	85
Figure 3.9	High-resolution STEM mapping of CoFeO _x -coated hematite.....	86
Figure 3.10	Steady-state photocurrents between 0.6 and 1.5 V vs RHE of catalyst-free and CoFeO _x -coated hematite in 1 M KOH and 1 M KOH + 0.5 M H ₂ O ₂	88
Figure 3.11	Charge injection and separation efficiencies of catalyst-free and CoFeO _x -coated hematite.....	89
Figure 3.12	Photoluminescence emission spectra of catalyst-free and CoFeO _x -coated hematite with and without Al ₂ O ₃	90
Figure 3.13	Polarization curves under simulated AM 1.5G illumination CoFeO _x -coated hematite with and without Al ₂ O ₃	91
Figure 3.14	Photovoltage of catalyst-free and CoFeO _x -coated hematite.....	92
Figure 3.15	Impedance analysis of catalyst-free and CoFeO _x -coated hematite.....	93
Figure 3.16	Nyquist plot of catalyst-free and CoFeO _x -coated hematite.....	94
Figure 4.1	Volcano plot of OER activity vs M-OH bond strength.....	108
Figure 4.2	Evolution of the mass of CoVO _x film during electrodeposition and polarization curves in 1 M KOH of CoVO _x and CoFeO _x	109
Figure 4.3	XPS analysis of electrodeposited CoVO _x before and after anodic polarization in 1 M KOH.....	110
Figure 4.4	Polarization curves, overpotentials and Tafel slopes of hydrothermally synthesized <i>m</i> -CoVO _x , CoO _x and VO _x	112
Figure 4.5	XRD patterns and extracted diffraction peaks of <i>m</i> -CoVO _x , CoO _x and VO _x	113
Figure 4.6	SEM images of <i>m</i> -CoVO _x and CoO _x and TEM and STEM-EDX images of <i>m</i> -CoVO _x	114
Figure 4.7	SEM images of <i>m</i> -CoVO _x on nickel foam.....	115
Figure 4.8	Polarization curves in 1 M KOH and 1 M Fe free KOH and stability of <i>m</i> -CoVO _x on nickel foam.....	115
Figure 4.9	Polarization curves and overpotentials in 1 M KOH and 1 M Fe free KOH of CoVO _x with different Co:V ratios.....	116
Figure 4.10	SEM, TEM and STEM-EDX of <i>a</i> -CoVO _x and SEM images of <i>a</i> -CoVO _x on nickel foam.....	117
Figure 4.11	XRD pattern of <i>a</i> -CoVO _x	118

Figure 4.12	XPS analysis of α -CoVO _x	119
Figure 4.13	XPS spectrum of Na 1s region of α -CoVO _x and polarization curves of α -CoVO _x in 1 M Fe free KOH and 1 M Fe free NaOH.....	120
Figure 4.14	Polarization curves and in 1 M KOH and 1 M Fe free KOH of α -CoVO _x on glassy carbon and on nickel foam. Stability and faradaic efficiency of α -CoVO _x in 1 M Fe free KOH...	121
Figure 4.15	SEM images of α -CoVO _x on nickel foam before and after anodic polarization, STEM-EDX mapping of α -CoVO _x after polarization.....	122
Figure 4.16	Mass activity and volcano plot of the mass activity vs M-OH bond strength of Co _y V _{1-y} O _x with different Co:V ratios.....	124

List of Tables

Table 2.1	Conditions used for the deposition and growth per cycle rate of TiO ₂ , Al ₂ O ₃ , ZnO, SnO ₂ , CoO _x , NiO _x , FeO _x and VO _x	46
Table 2.2	XPS composition of Fe, Co and V in CoVFeO _x deposited by different supercycles on FTO.....	59
Table 2.3	Summary of overpotentials at 10 mA cm ⁻² and Tafel slopes of CoO _x , CoVO _x , CoFeO _x and CoVFeO _x on FTO and nickel foam in 1 M KOH and in 1 M Fe free KOH.....	63
Table 4.1	Comparison between the Co:V concentration ratios in the deposition solution and the Co:V ratios determined by XPS in the catalysts.....	120
Table 4.2	Bond strength of Co _y V _{1-y} O _x with different Co:V ratios.....	123
Table 4.3	Summary of mass activities of different Co _y V _{1-y} O _x physical mixtures.....	123

Table of Content

Acknowledgements.....	I
Abstract.....	II
Résumé.....	IV
Riassunto.....	VI
Zusammenfassung.....	VIII
Symbols and Abbreviations.....	X
Units and Prefixes.....	XIV
List of Figures.....	XV
List of tables.....	XIX
Table of Content.....	XX
Chapter 1 Introduction.....	1
1.1 The energy crisis: a major challenge for the 21 st century.....	3
1.2 The Hydrogen Economy.....	5
1.3 Production of hydrogen by water splitting.....	9
1.3.1 The Hydrogen evolution reaction.....	13
1.3.2 The Oxygen evolution reaction.....	15
1.4 Electrocatalysts for OER.....	17
1.4.1 OER catalysts.....	17
1.4.2 Synthesis of OER catalysts.....	18
1.5 Sunlight-driven water splitting.....	21
1.5.1 PV-electrolysis.....	26
1.5.2 Photoelectrochemical water splitting.....	27
1.6 Outline of the following chapters.....	29
1.7 References.....	30

Chapter 2 Atomic Layer Deposition of Transition Metal Oxides as Electrocatalysts for Oxygen Evolution.....	37
2.1 Introduction.....	39
2.2 Atomic layer deposition system.....	41
2.2.1 Initial ALD setup	41
2.2.2 Second ALD setup	43
2.3 ALD-deposited CoVO_x and CoFeO_x as OER catalysts	46
2.3.1 Approach to deposit mixed metal oxides.....	46
2.3.2 CoVO_x and CoFeO_x	48
2.4 Trimetallic oxides as OER catalysts	58
2.5 Conclusions.....	63
2.6 Experimental section.....	65
2.7 References.....	70
Chapter 3 Ultrathin Cobalt Iron Oxide Catalyst for Water Oxidation on Nanostructured Hematite Photoanodes	75
3.1 Introduction.....	77
3.2 Activity of CoFeO_x -coated hematite photoanode	79
3.3 Characterization of CoFeO_x overlayer.....	82
3.4 Role of CoFeO_x	86
3.5 Conclusions.....	95
3.6 Experimental section.....	96
3.7 Contributions.....	100
3.8 References.....	101
Chapter 4 Amorphous Cobalt Vanadium Oxide as Electrocatalyst for Oxygen Evolution	105

4.1 Introduction.....	107
4.2 Electrodeposited cobalt vanadium oxide catalyst.....	109
4.3 Hydrothermally deposited cobalt vanadium oxide catalysts	111
4.3.1 Mixed-phase cobalt vanadium oxide	111
4.3.2 Pure-phase amorphous cobalt vanadium oxide.....	116
4.4 Conclusions.....	124
4.5 Experimental section.....	125
4.6 Contributions.....	128
4.7 References.....	129
Conclusions and Outlook	133
Curriculum Vitae	139

Chapter 1

Introduction

1.1 The energy crisis: a major challenge for the 21st century

One of the greatest challenge of the 21st century for mankind will be to face and solve the predicted energy crisis. In 2015, the world energy consumption rate was evaluated to be close to 17.5 TW and is expected to rise by 28 % to reach 24.5 TW in 2040. In 2015, 14.5 TW (83 %) of the total energy consumption rate were produced by the consumption of fossil fuels. 5.8 TW (33 % of total energy consumption rate) were produced by burning oil and other petroleum-based liquids, 4.7 TW (27 %) were produced by coal and 4.0 TW (23 %) by natural gas. The remaining of energy was supplied by renewable energies (2.2 TW, 13 %) and nuclear power (0.8 TW, 4 %).^[1] The combustion of fossil fuels engenders huge amounts of carbon dioxide that are released into the atmosphere. The atmospheric CO₂ concentration has been fluctuating between 170 and 300 ppm for the last 400'000 years until the 18th century and was strongly correlated to temperature changes.^[2] Since the beginning of the Industrial Revolution, the CO₂ level has been constantly increasing by anthropogenic emissions and is currently surpassing 400 ppm.^[3,4] This gas actively plays a key role in global climate warming and acidification of oceans, inducing problems such as disturbances of the terrestrial and marine ecosystems, extinctions of species, and rise of sea level.^[5,6] In opposite to fossil fuels, nuclear power is a carbon-free energy source and does not directly release carbon dioxide into the atmosphere. But this source of energy is not renewable nor sustainable. Uranium is not a renewable resource and nuclear power plants hold a small, but yet significant environmental hazards in case of nuclear accident. Moreover the wastes produced need thousands of year to for their radioactivity to decay and no secure disposal or storage systems exist yet.

The reduction of CO₂ emissions is essential if mankind wants to avoid global warming and all disastrous effects related to it. Carbon capture and storage (CCS) could provide a solution towards decarbonization of the society. CCS aims to collect, purify and concentrate CO₂ emissions from large and concentrated sources such as industries, power plants as well as cement factories and transport it to storage sites where this gas will be sequestered at several hundredth of meters below the surface of the Earth. The CO₂ can then undergo mineral carbonation and be fixed permanently in the ground as carbonate, preventing it to reach back the surface and the atmosphere.^[7,8] Alternatively, the collected carbon dioxide could be used as feedstock to produce

valuable chemicals.^[9] Carbon capture and storage could be a solution to rapidly reduce the anthropogenic CO₂ emissions but fossil fuels reserves are not unlimited and will become scarce in the future.^[10]

Based on all the reasons previously described, it is of great importance to develop at large scale CO₂-free power sources that do not rely on non-renewable feedstocks such as fossil fuels and uranium but that are based on renewable resources. Among all the renewable energy sources available on Earth, which include sunlight, wind, tidal energy, biomass, geothermal heat and hydroelectricity, solar power is the most abundant.^[11,12] Even though a combination of those aforementioned renewables will probably be developed based on their geographical availabilities, sunlight has the highest potential for fulfilling the increasing energy needs of our society. The theoretical amount of energy arriving from the sun and that reaches the surface of the Earth is estimated to be 3×10^{24} joules per year.^[13] This corresponds to a power of approximately 95'000 TW, that is approximately 4000 times more than the projected 24.5 TW that humanity will need in 2040. In other words, covering 0.26 % of the Earth's surface with 10 % efficient solar cells would be sufficient to provide 24.5 TW of power.

Sunlight energy can be harvested by different ways directly into either heat or electricity. Solar thermal applications rely on collectors that convert solar energy into heat which is then transferred to a working fluid (air, water or oil). The heat carried by the working fluid can then be used for diverse applications such as production of hot water, heating, desalinization of water or production steam for industrial processes.^[14] Sunlight can also be directly converted to electricity by using concentrated solar thermal power (CSP) and photovoltaics (PV). CSP is based on arrays of mirrors or parabolic troughs which concentrate sunlight towards a tower filled with molten salts. The heat recovered is then used to drive a steam turbine connected to an electrical power generator. In 2017, the total power generated by CSP facilities was 4.9 GW. Photovoltaic cells are based on semiconductor materials that can convert photons to electricity by the photovoltaic effect. In 2017, the total power capacity of PV was 402 GW.^[15]

However, solar irradiation is not constant and its intermittency, due to atmospheric conditions and to the natural cycle of day and night, prevents having a stable solar electricity production. Therefore, efficient storage systems are required and need to be developed to buffer the mismatch between periods of energy production and consumption. Batteries could be used but their cost is not yet low enough to be economically viable at large scale. A second method is to

use solar electricity to drive turbines and pump water to higher ground levels in artificial lakes and when energy demand is higher than production, the water is let to flow down through turbines to generate electricity. Although this storage method is relatively inexpensive, it is not compatible to be implemented at large scale due to the limited available places to build dams and artificial lakes.^[16] Another alternative is the conversion of sunlight into chemical bonds to form chemical fuels. Fuels have the advantage to achieve high energy densities. Hydrogen gas (H₂) has been suggested as the energy carrier of the future.^[17] H₂ is considered as a clean energy carrier as it only emits water when burnt with oxygen and is sustainable when produced from renewable energies. A shift of our fossil fuels based economy towards a "Hydrogen Economy" has been envisaged as a long-term solution to global warming.^[18] This change of paradigm will be one of the greatest challenge of the 21st century.

1.2 The Hydrogen Economy

Already in 1874, Jules Verne, recognizing that coal reserves were not inexhaustible and foreseeing the possibilities of hydrogen derived from water electrolysis, said "water will be the coal of the future".^[19] Among fuels (hydrocarbon and nitrogen-based fuels), hydrogen gas has the largest energy density by mass (143 MJ kg⁻¹).^[20] Moreover hydrogen gas is a clean energy carrier that can release its energy either in heat engines by combustion or provide efficiently heat and electricity in fuel cells (efficiency up to 60 % compared to 45 % for the most efficient diesel engines), producing only water as exhaust gas.^[21,22] Hydrogen is thus a suitable energy vector to transport and store energy from renewable sources. The total replacement of fossil fuels by hydrogen was named "Hydrogen Economy" by Neal Triner in 1970 and John Bockris later described that concept in several publications.^[18] Several technological aspects of the Hydrogen Economy are to be considered in order for hydrogen to drive the global energy system: production, storage, distribution, and conversion of hydrogen to electricity with fuel cells.^[23]

Nowadays, hydrogen is obtained at 96 % from steam reforming of methane or partial oxidation of hydrocarbons and is mainly employed for oil refining as well as ammonia and methanol production (Figure 1.1). As a fuel, nowadays, hydrogen is used in applications such as spaceship propulsion, individual and public transport vehicles. Additionally, commercialization of fuel cells for heating and energy supply of households is expected in the next few years ^[21,24] Hydrogen produced from reforming is not CO₂-free and thus not sustainable. But hydrogen produced from

reforming could be transitorily used in order to develop at large scale hydrogen-related infrastructures necessary for the Hydrogen Economy. In a second step, decarbonization of the Hydrogen Economy would be necessary. For this, water splitting is of great importance. Obviously, the energy used for water splitting must come from carbon-free sources such as sunlight, hydropower and wind.

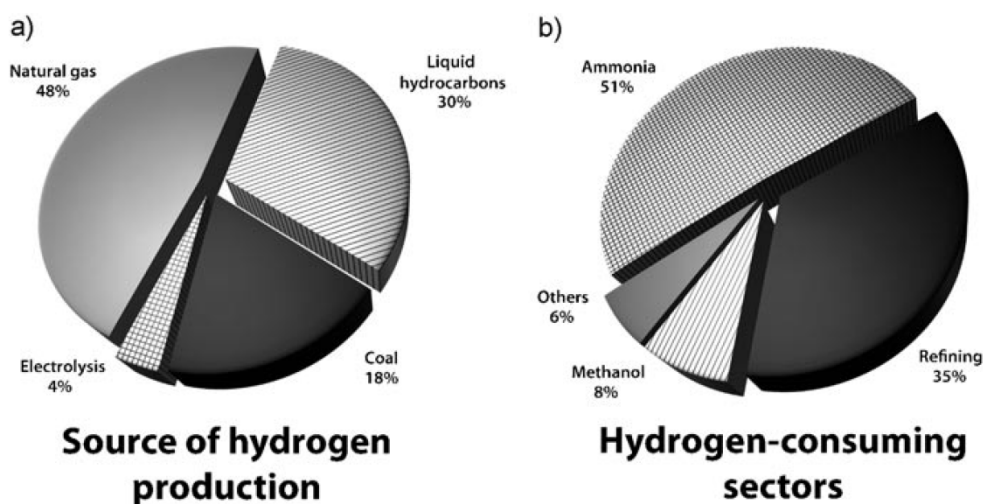


Figure 1.1 Source of hydrogen production and consuming sectors. Reproduced with permission of John Wiley and Sons from reference [25].

The delivery of hydrogen is an important aspect for a viable Hydrogen Economy. This requires an infrastructure to carry hydrogen from where it is produced to where it will be used, for example at refueling stations or power facilities. Three delivery pathways are possible: Compressed hydrogen carried by conventional transport vehicles and ships (trucks, tankers and trains), compressed hydrogen pipelines and cryogenic transport ship and vehicles. Among them, pipelines are the most cost-effective and energy efficient to transport hydrogen over long distances. Transporting hydrogen in compressed or liquid state by trucks, ships or train is favored in the initial phase of the Hydrogen Economy. Due to the very low gravimetric density of hydrogen (8.5 MJ L^{-1}),^[25] liquid hydrogen is more efficient for transportation (4000 kg of liquid H_2 compared to only 300 kg of compressed H_2 (180 bars) can be carried on a tanker truck) but higher energy use is needed for liquefaction than compression.^[26]

The storage of hydrogen gas is a key aspect that needs to be considered. To date, utilization of hydrogen as a fuel has been hindered by the lack of efficient storage methods. Hydrogen storage can be classified into two categories: physical storage and material-based storage. An illustration of the different methods is shown in Figure 1.2. Physical storage includes compressed and liquid hydrogen. Typically, a light-duty vehicle needs 6 kg of hydrogen to run 500 km.^[27] At 700 bars, this amount requires a 150 L storage tank. Liquid hydrogen has a larger volumetric density of 71 g L⁻¹ at 20 K. But boil-off issues due to heat input from the surrounding environment is still yet an

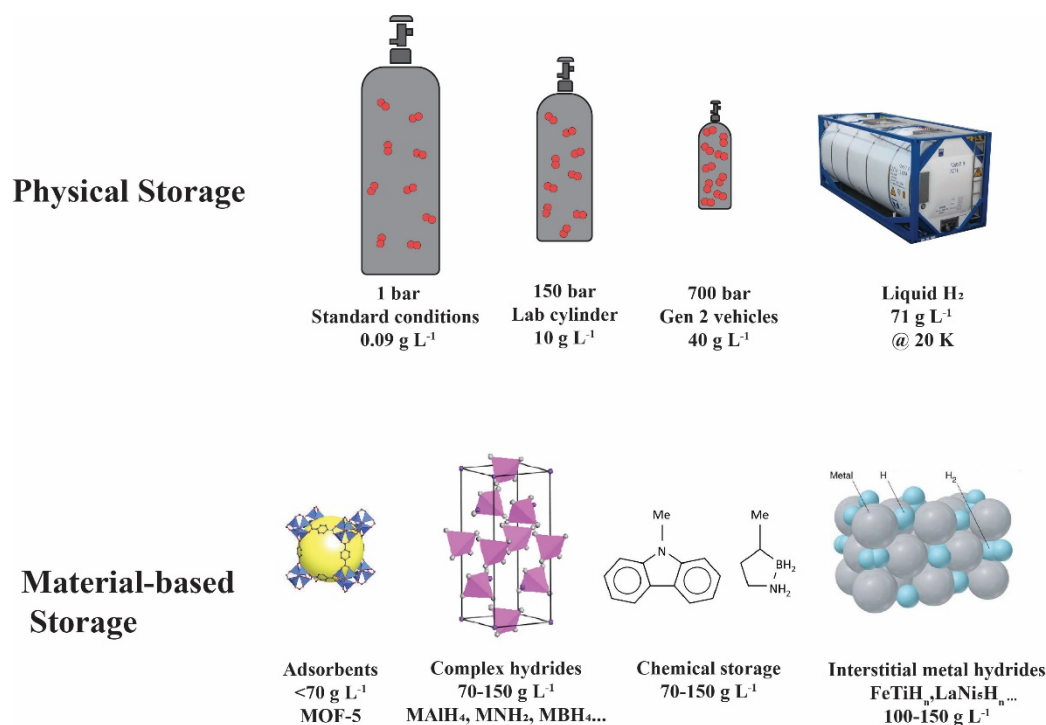


Figure 1.2 Overview of the different hydrogen storage methods.

issue that prevents liquid hydrogen storage to be used. The second category of storage is based on materials. Hydrogen can be stored by chemisorption (hydrogen molecules dissociate first on the surface and then hydrogen atoms diffuse into the metal host lattice) as in the case of interstitial and complex hydrides (e.g. MH_n, AB_xH_n, Alanates...) as well as chemical hydrides (e.g. organic heterocycles). Storage relying on physisorption (the hydrogen molecules are bound via weak interactions on the surface of porous materials) is also used with materials such as zeolites, metal-organic frameworks (MOF) and nanostructured carbon materials (e.g. carbon nanotubes and nanofibers).^[28,29] Currently, liquid hydrogen would be favored for large volume storage but for

lower volume, such as for transportation vehicles, car manufacturers focus their efforts on compressed hydrogen.^[30]

In order to release its energy, for heat or mechanical energy production, hydrogen can either be burnt in combustion engines or used in a fuel cell in order to produce electricity and heat. The principle of fuel cells was conceptualized in the early 1800s by Sir William Grove that discovered that the reverse process of electrolysis (combining hydrogen and oxygen gas) could be used to generate electricity. Grove initially named his device a "gas battery". Today, different types of fuel cells have been designed and are used in diverse applications, from the W- to MW-level, such as portable and stationary power generators (consumer electronic devices that normally run on batteries, power supplies for off-the-grid residential and industrial sectors), emergency back-up power supplies, transportation, auxiliary power units... Six different types of fuel cells exist and are depicted in Figure 1.3: alkaline fuel cells (AFC), direct methanol fuel cells (DMFC), molten carbonate fuel cells (MCFC), phosphoric acid fuel cells (PAFC), solid oxide fuel cells (SOFC) and polymer electrolyte membrane (or proton exchange membrane) fuel cells (PEMFC).^[31] All of them

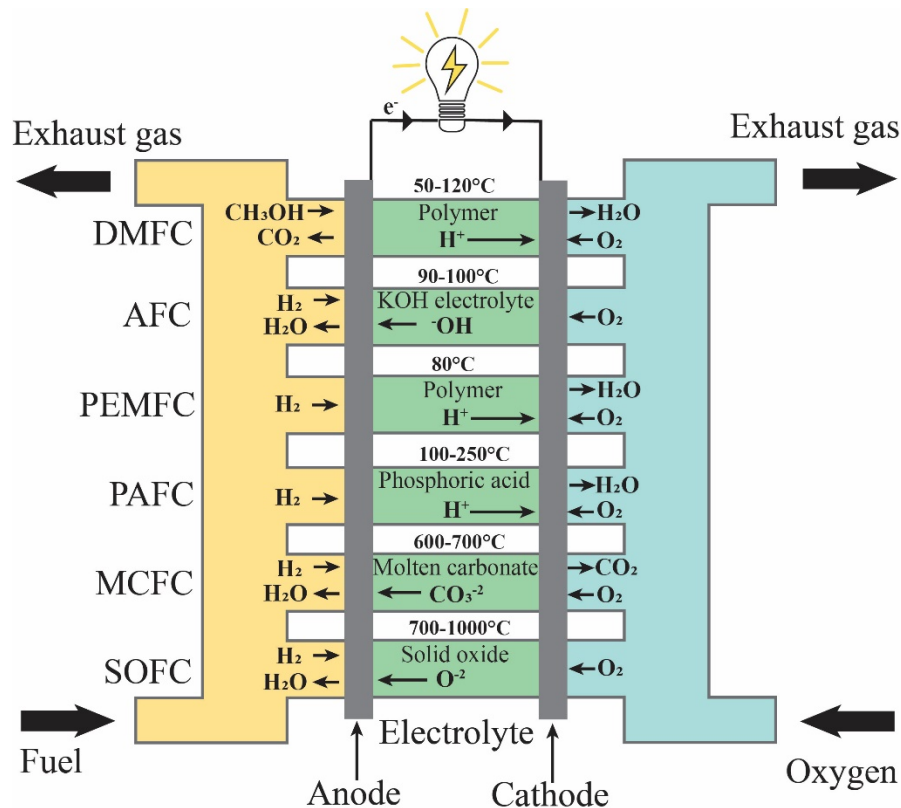


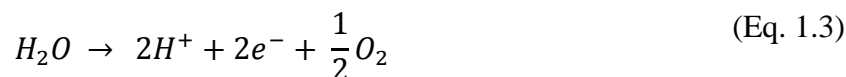
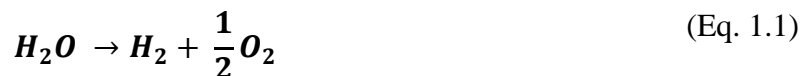
Figure 1.3 Overview of the different types of fuel cells.

consist of two electrodes, an anode and a cathode, covered with a layer of catalyst and separated by an electrolyte. The fuel (hydrogen gas or alcohols) are fed to the anode and the fuel molecules are oxidized on the electrode surface to yield electrons that are forced through an external circuit to drive an electrical load. At the cathode, electrons reduce the supplied oxygen. As long as fuel is supply, fuel cells continuously produce power.

1.3 Production of hydrogen by water splitting

Water splitting is a chemical reaction in which water is decomposed into hydrogen and oxygen gas. This reaction can be performed by water electrolysis, a reaction that reduces and oxidizes water on the cathode and anode of an electrolysis cell, respectively. This redox reaction was first mentioned in 1789 by Deiman and van Troostwijk who described to have decomposed water into "combustible air" and "life-giving air" but the limited electrochemical knowledge of that time prevented the rational explanation of this decomposition reaction. The relation between electricity and water electrolysis was later discovered by Nicholson and Carlisle in 1800.^[32]

As previously mentioned, the water splitting reaction (Eq. 1.1) can be divided into two half-reactions: the hydrogen evolution reaction (HER, Eq. 1.2) and the oxygen evolution reaction (OER, Eq. 1.3).



The standard Gibbs energy (ΔG^0 , standard conditions of 1 bar and 25 °C) for a reaction can be expressed by Eq. 1.4 where ΔH_r^0 is the standard enthalpy of reaction, T is the temperature and ΔS^0 is the change of entropy. The standard potential E^0_{cell} of a redox cell is related to ΔG^0 by Eq.

1.5 were z is the number of electrons involved in the process and F the Faraday constant ($F= 96485$ C mol⁻¹).

$$\Delta G^0 = \Delta H_r^0 - T \cdot \Delta S^0 \quad (\text{Eq. 1.4})$$

$$E_{cell}^0 = -\frac{\Delta G^0}{z \cdot F} \quad (\text{Eq. 1.5})$$

Knowing that for water splitting $z = 2$, $\Delta H_r^0 = 285.8$ kJ mol⁻¹, and $\Delta S^0 = 0.163$ kJ mol⁻¹ K⁻¹ ($S^0(H_2) = 130.6$, $S^0(O_2) = 205.1$ and $S^0(H_2O) = 70$ J mol⁻¹ K⁻¹), the cell potential E_{cell}^0 can be calculated and is equal to -1.23 V. This value is the minimum potential necessary to split water under standard conditions and by considering that the heat corresponding to $T \cdot \Delta S^0$ can be supplied by the external environment of the cell. In a closed cell system (which operates adiabatically without any heat transfer with the external environment), this heat cannot be supplied anymore and the minimum potential E_{th}^0 (thermoneutral potential) required to split water is given by Eq. 1.6.

$$E_{th}^0 = -\frac{\Delta H_r^0}{z \cdot F} = -1.48 \text{ V} \quad (\text{Eq. 1.6})$$

A water splitting cell, such as an electrolyzer, will thus absorb heat if operated between 1.23 V and 1.48 V and will dissipate heat if operated above 1.48 V. In an electrolyzer, the HER happens at the cathode and the OER at the anode. In a real system, an overpotential (defined as the difference between the thermodynamic and the applied potential) has to be applied in addition to the thermodynamic value (-1.23 V or -1.48 V in the case of an adiabatic system) in order to split water. To reduce to a minimum this overpotential, anodes and cathodes are covered with materials that are able to efficiently catalyze water reduction and oxidation. Two types of electrolyzers exist: alkaline electrolyzers and polymer electrolyte membrane (PEM) electrolyzers (Figure 1.4). Alkaline electrolysis is a mature technology that has already been implemented worldwide at a commercial level for more than 100 years.^[33] These systems are reliable, safe and have extended lifetime (up to 15 years). They are composed of two electrodes immersed in a harsh alkaline electrolyte (20-30 % KOH). A diaphragm separating the two electrodes prevents forming an explosive gas mixture by H₂ and O₂ mixing. Both cathodes and anodes are generally composed of non-noble metal alloys of nickel, iron and/or cobalt.^[34] PEM electrolyzers are a more recent technology developed in the 1960s. Those device are characterized by a solid polymer electrolyte.

PEM electrolyzers, compared to alkaline ones, have the advantages to be more compact systems and being able to operate at higher pressures and current densities, thus reducing the operational costs. Cathodes are generally coated with platinum-based catalysts and anodes by oxides of ruthenium and iridium. However, high cost and low durability of components, as well as catalysts based on precious metals are drawbacks that are yet to solve for large scale implementation of PEM electrolyzers.^[35]

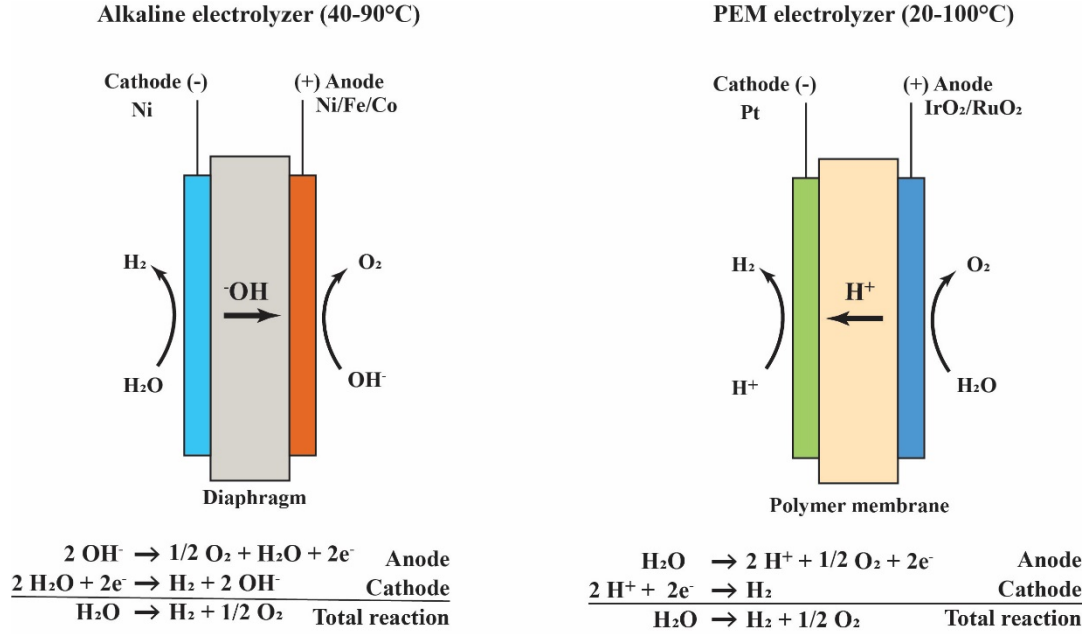


Figure 1.4 Alkaline and PEM electrolyzers.

In opposite of a chemical reaction, in which the kinetics strongly depends on temperature (through the Arrhenius equation), the kinetics of an electrochemical reaction directly depends on the applied potential at the electrodes and can be described by the Butler-Volmer equation (Eq.1.7). This relation, describing the dependence of the electrical current on an electrode in function of the potential for redox reactions occurring on the same electrode, was derived from Nernst and Arrhenius relations:^[36]

$$j = j_0 \left(e^{\frac{-\alpha z F (E - E_{eq})}{RT}} - e^{\frac{(1-\alpha) z F (E - E_{eq})}{RT}} \right) \quad (\text{Eq. 1.7})$$

$$\eta = E - E_{eq} \quad (\text{Eq. 1.8})$$

where j is the current density, j_0 the exchange current density, z is the number of electrons involved in the process, α is the charge transfer coefficient, E is the electrode potential, E_{eq} is the equilibrium potential, R is the universal gas constant, F the Faraday constant and T the temperature.

The overpotential η , defined here as the difference between the electrode potential and the equilibrium potential (Eq. 1.8), is the key criterion that governs the kinetics of an electrochemical reaction. At large negative overpotentials, the second term in the brackets of Eq.1.8 becomes negligible and the Butler-Volmer equation can be simplified and rearranged to yield the Tafel relation (Eq. 1.9):

$$\eta = a + b \log i \quad (\text{Eq. 1.9})$$

where i is the current, a and b are constants that correspond to:

$$a = \frac{2.3 RT}{\alpha z F} \log i_0 \quad b = \frac{-2.3 RT}{\alpha z F}$$

The term b represents the Tafel slope when plotting $\log i$ in function of the overpotential η . The Tafel slope is a useful tool to evaluate the kinetic parameters of electrochemical reactions. In Eq. 1.7, the overpotential represents the activation energy required to drive the reaction and is also referred as activation overpotential (η_a). At high activation overpotentials, the concentration of species can drastically decrease at the electrode interface and mass-transfer effects start to manifest. Under those circumstances, an additional activation energy (required to drive mass transfer at the rate needed to support the current) called concentration overpotential (η_c) will also contribute to the total overpotential.^[36] A last overpotential contribution is related to the ohmic drop (iR_s) in all electrochemical systems. The ohmic drop, which can be seen as the difference between the applied potential (by the potentiostat) and the real potential at the electrode, arises from highly resistive electrolytes and electrodes. The total overpotential is expressed in Eq.1.10 as:

$$\eta = \eta_a + \eta_c + iR_s \quad \text{Eq. 1.10}$$

In practical systems, η_c and iR_s are often much smaller than η_a . Finding materials that can efficiently catalyze water splitting (HER and OER) is thus of crucial importance in order to reduce

to a minimum the activation overpotential. In the next sections, the mechanism of HER and OER will be reviewed and examples of different state-of-the-art electrocatalysts will be presented.

1.3.1 The Hydrogen evolution reaction

The HER is a multi-step reaction that takes place on the surface of an electrode. For the case of hydrogen evolution in acidic electrolytes, three reactions are assumed to dominate and are represented in Figure 1.5.^[37] The proton source is, in acidic solutions, hydronium cations (H_3O^+). In neutral or alkaline solutions, the proton source is water molecules.

The initial step of HER is the Volmer step or discharge reaction. In this step, a proton captures an electron from the electrode and binds with the electrode surface to form an adsorbed hydrogen atom (H_{ads}). Release of H_2 can occur via two different mechanisms depending on the second reaction step. One possibility is that two adsorbed hydrogen atoms combine together. This step is named combination reaction or Tafel step. The second possibility is the ion + atom reaction or Heyrovsky step in which a proton and an electron both react with the adsorbed hydrogen to

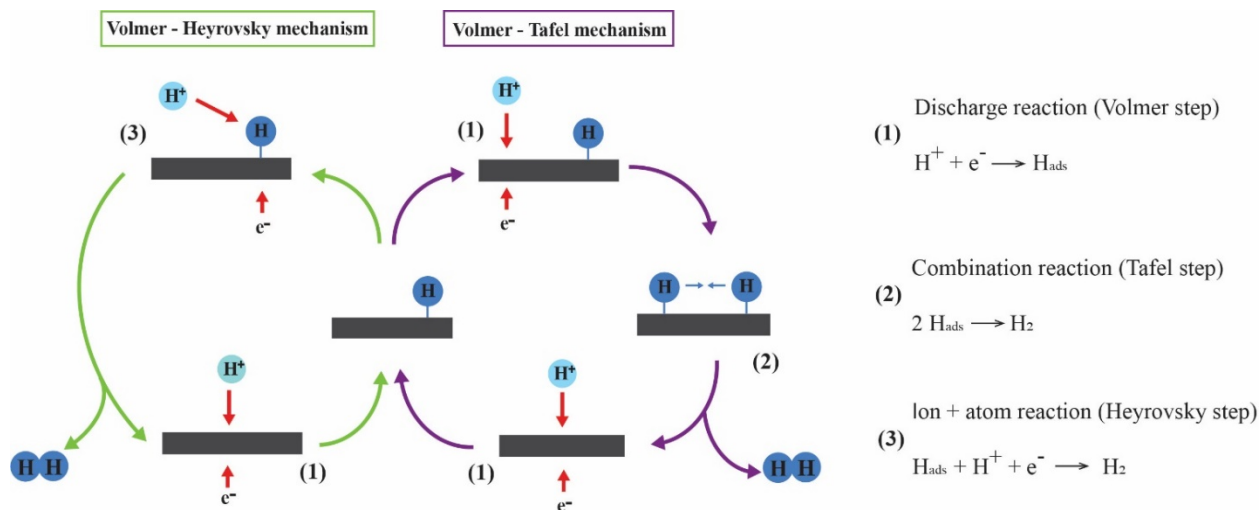


Figure 1.5 Hydrogen evolution mechanism in acidic solution on a surface of an electrode.

directly yield H_2 . The first reaction cycle (represented by violet arrows) is named Volmer-Tafel mechanism and the second (represented by green arrows) is the Volmer-Heyrovsky mechanism. Three limiting cases can be derived from Eq. 1.9 that yield different Tafel slope values depending on which reactions is the rate limiting step.^[38] Tafel slopes are commonly used to discern the predominant HER mechanism and indicate the potential difference that needs to be applied to

produce a 10-fold increase in current density. If the discharged reaction is the limiting step and H_2 is evolved regardless either by the combination or the ion + atom reaction, the Tafel slope can be expressed as $4.6RT/F$ (116 mV dec^{-1}). If the discharged reaction is fast and H_2 is evolved by the rate-determining recombination reaction, a Tafel slope of $2.3RT/2F$ (29 mV dec^{-1}) is obtained. In the last case where the discharged reaction is fast and H_2 is evolved by the limiting ion + atom step, a Tafel slope equals to $4.6RT/3F$ (38 mV dec^{-1}) is obtained.

The exchange current density is another important parameter that is correlated with the rate of electron transfer under reversible conditions ($\eta = 0$). The magnitude of the exchange current density is correlated with the reaction rate at other potentials. Ideal catalysts have high exchange current densities as well as low Tafel slopes.

Figure 1.5 shows that an adsorbed hydrogen intermediate plays a key role in the hydrogen evolution reaction. The Gibbs free energy of hydrogen adsorption on a metal surface (ΔG_{H^*}) has been proposed as a descriptor of the intrinsic activity of metal catalysts for HER.^[39] A volcano plot reflecting the Sabatier principle is obtained. The most efficient electrocatalysts, which are Pt, Pd, Rh etc, reach the top of the volcano. The adsorption energy of hydrogen on those precious metal

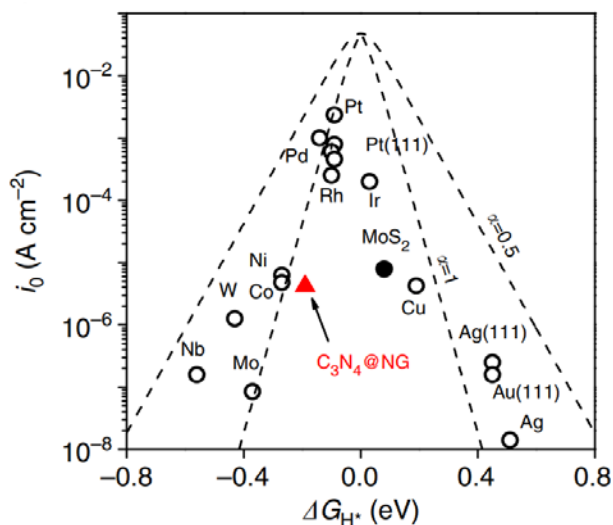


Figure 1.6 Volcano plot of the exchange current density of several HER catalysts vs the Gibbs free energy of hydrogen adsorption. Reproduced with permission of Springer Nature from reference [39].

is close to zero, which is neither too strong nor too weak.^[39,40] If ΔG_{H^*} is too positive (strong interaction), the hydrogen atom cannot unbind the surface and if ΔG_{H^*} is too negative (weak

interaction) the hydrogen can be detached easily from the surface and has not time to perform the Tafel or Heyrovsky step to yield H_2 .

As previously mentioned, the best HER electrocatalysts are composed of precious metals from the platinum group. These metals are not suitable for large scale applications due to their high cost and scarcity in the Earth's crust.^[41] Earth-abundant materials have been developed as alternatives to noble metal catalysts and are composed of a wide variety of crystalline or amorphous materials made of different transition metals sulfides, phosphides or carbides of Mo, Fe, Co, Ni or W as well as Ni-Mo alloys.^[42-44]

1.3.2 The Oxygen evolution reaction

The oxygen evolution reaction is a reaction that involves the transfer of 4 electrons per oxygen molecule (Eq. 1.3). Due to this, the OER is kinetically sluggish and is considered as the bottleneck of the water splitting reaction.^[45] The mechanism of OER is represented in Figure 1.7. Due to the oxidative potential required to drive the OER, this reaction will never occur on a bare metal surface but will happen on a surface oxide layer. Similarly to HER, the Tafel slope can be used to rapidly identify the rate-determining step (RDS) of OER. However, same Tafel values can originate from different reaction pathways. For this reason, a full kinetic analysis, in addition to

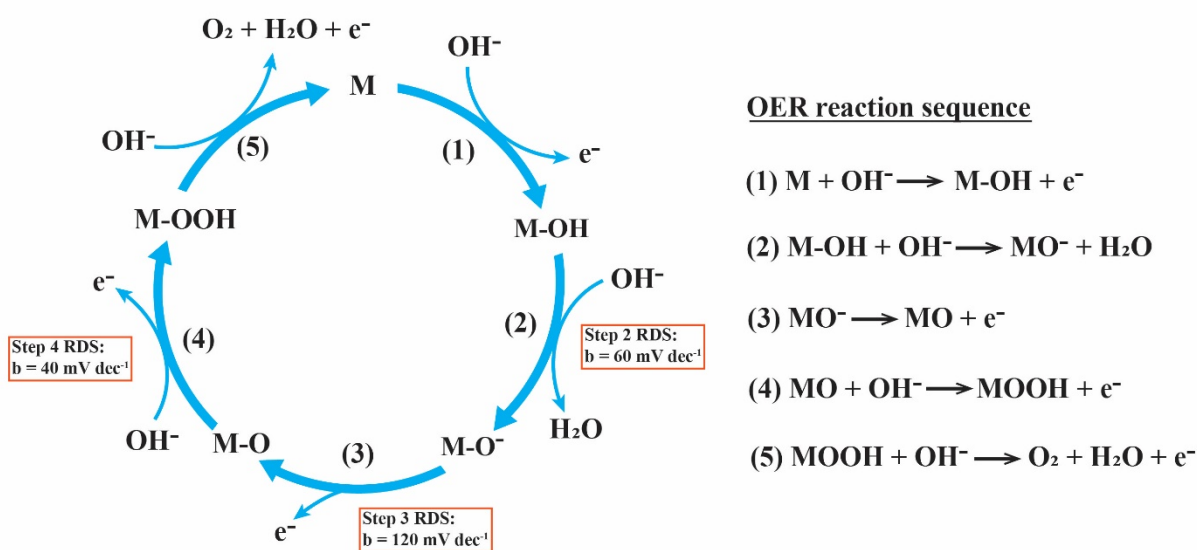


Figure 1.7 Oxygen evolution reaction sequence.

Tafel slope analysis, is necessary to probe the detailed reaction mechanism depending on the electrode material used as catalyst.^[46]

The full kinetic description of OER on metal oxides is not an easy task. For this reason, single measurable or calculable parameters, or descriptors, can be correlated to OER activity in order to quickly search and investigate potential catalytic materials. For example, Bockris and Ottogawa demonstrated that the metal-OH bond strength was correlated to the activity of different perovskite oxides, therefore highlighting the importance of the bonding strength of surface-oxygenated intermediates on the OER activity (Figure 1.8a).^[47] Another example of descriptor is $\Delta G_{O^*} - \Delta G_{OH^*}$, the difference of free energy between the two subsequent intermediates O^* and OH^* in the OER reaction sequence. This descriptor correlates with the overpotential of several metal oxides (Figure 1.8b).^[48] Another descriptor is the e_g orbitals occupancy of metal cations. Shao-Horn and co-workers showed that the intrinsic OER activity of different perovskite oxides

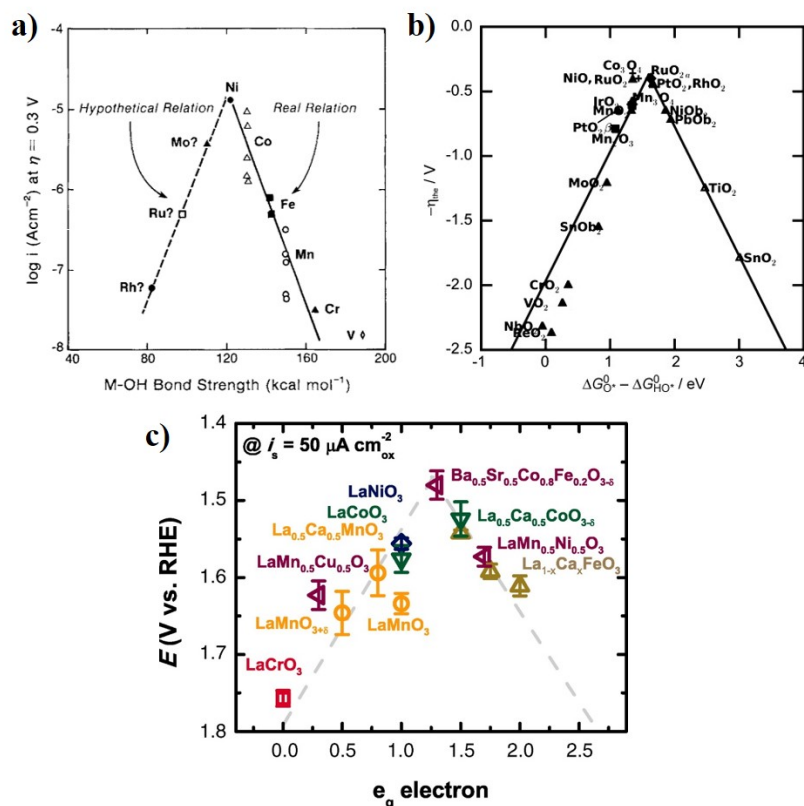


Figure 1.8 a) Volcano plot of OER activity vs the metal-OH bond strength of LaMO₃ perovskites (M = Rh, Ru, Mo, Ni, Co, Fe, Mn, Cr and V), reproduced with permission of The Electrochemical Society from reference [47]. b) Volcano plot of the overpotential vs $\Delta G_{O^*} - \Delta G_{OH^*}$ free energy difference of different metal oxides, reproduced with permission of John Wiley and Sons from reference [48]. c) Volcano plot of the overpotential vs number of e_g electrons for different perovskite oxides, reproduced with permission of the American Association for the Advancement of Science from reference [49].

correlated, in a volcano plot, with the occupancy of the metal cation 3d orbitals having an e_g symmetry.^[49]

1.4 Electrocatalysts for OER

1.4.1 OER catalysts

As seen previously, the oxygen evolution reaction is kinetically difficult due to the transfer of 4 electrons. This leads to a high overpotential associated to this half-reaction compared to HER. Among the best heterogeneous catalysts used to decrease this overpotential are RuO_2 and IrO_2 . RuO_2 can oxidize water in alkaline and acidic solutions with overpotentials close to 200 mV at a current density of 10 mA cm^{-2} .^[20] This current density of 10 mA cm^{-2} (that takes into account the geometric surface area) is standardly used to compare overpotentials of catalysts as it is the current density expected at the anode in a 10 % efficient solar water splitting device.^[50]

First row transition metal oxides composed of Fe, Co, Ni, Mn and V are extensively studied as they have shown promising OER activity and stability in alkaline solutions. Moreover, those metals, compared to Ir and Ru, are much more abundant in the Earth's crust.^[41] Norskøv and coworkers demonstrated, through DFT calculations, that metal oxides composed of Ni, Mn and Co can have theoretical overpotentials close to the ones of precious metal oxides.^[48] However, good theoretical electrocatalytic materials suffer from poor electrical conductivity due to the insulating nature of transition metal oxides. Reducing the distance required for the charges to travel through the oxide and reach the electrolyte is thus of crucial importance. Preparing thin films of catalysts is a potential solution. However, in the case of a thin film, the surface area in contact with the electrolyte is not large and the overall current density will be low. In order to keep the good conductivity of a thin film but having a large surface area, nanostructuring of electrocatalytic materials can be performed.^[51]

In the late 1980', Corrigan showed that Fe impurities in KOH electrolytes could increase the OER activity of nickel oxide (NiO_x) and could prepare a cathodically electrodeposited nickel iron oxide (NiFeO_x) material containing 50 % of Fe. This material exhibited an overpotential of 233 mV at 8 mA cm^{-2} and a Tafel slope of 21 mV dec^{-1} in 25 wt% KOH.^[52] NiFeO_x has attracted a lot of attention and is widely studied. For example layered double hydroxide (LDH) catalysts based on Ni and Fe have been synthesized. Those LDH can be exfoliated to yield two dimensional

(2D) LDH nanosheets. 2D materials have close to maximum surface to bulk ratio, leading to more abundant active sites and have a higher conductivity than their bulk counterpart. NiFe LDH can reach 10 mA cm^{-2} at an overpotential of 300 mV and has a Tafel slope of 40 mV dec^{-1} in 1 M KOH.^[53] Other LDH catalysts, such as NiV, CoMn, CoNi and CoFe were also reported.^[46]

Maximizing the surface area, and thus the number of surface active sites is of utmost importance to enhance the OER activity of a material. Obtaining high surface area metal oxides has been achieved via anodic electrodeposition. A variety of amorphous secondary and tertiary metal oxides such as NiO_x , MnO_x , CoO_x , FeO_x , NiCoO_x , NiFeO_x and CoFeO_x were shown to have high OER activities. Among them, the best activity (240 mV at 10 mA cm^{-2} in 1 M KOH) was reached with CoFeO_x electrodeposited on a high-surface area Ni foam substrate.^[54]

Fixating OER catalysts on high-surface carbon supports (carbon nanotubes, graphene etc) is an efficient strategy to enhance their OER activity. These hybrid materials have a high specific surface area and the carbon substrates facilitate electron transfer kinetics. As an example, NiFe-LDH immobilized on carbon nanotubes can be cited. This material can provide 5 mA cm^{-2} at an overpotential of 290 mV in 1 M KOH and was shown to be more active than NiFe-LDH alone.^[55]

The OER activity being related to the specific surface area of a material, downsizing the size of conventional nanoparticle catalysts to nanocluster or single atom level has recently emerged as a research focus.^[56] An example is single atoms embedded in nitrogen-doped holey graphene frameworks (M-NHGFs with $M = \text{Ni, Fe, Co}$). The best activity among them was reached by Ni-NHGFs that has an overpotential of 330 mV at 10 mA cm^{-2} with a Tafel slope of 63 mV dec^{-1} in 1 M KOH.^[57]

1.4.2 Synthesis of OER catalysts

Different methods for the synthesis and deposition of electrocatalysts exist. Among them, electrodeposition, hydrothermal synthesis, co-precipitation, solution-casting, atomic layer deposition and photochemical deposition are widely used to produce materials having catalytic properties towards OER, such as oxides, nitrides, phosphides, selenides and sulfides.^[58-65]

Hydrothermal method is a common and effective strategy to fabricate inorganic nanomaterials with a wide variety of morphologies and compositions. In this method, a solution containing dissolved reactants is placed into a sealed autoclave and the reaction takes place under high pressure and temperature conditions. Hydrothermal synthesis refers to reactions taking place

in aqueous media above 1 bar and 100°C. When non-aqueous solvent are used, this method is referred as solvothermal synthesis. Teflon-lined stainless steel autoclaves are generally used as they can withstand high temperatures and pressures as well as strongly acidic or alkaline conditions. The properties, size, morphology and structure of nanomaterials produced by hydrothermal synthesis can be tailored by changing the different reaction parameters, such as temperature, reaction time, concentration of the reactants, pH and reaction medium.^[66] LDH materials are an example of highly active OER catalysts produced by hydrothermal synthesis.^[63] Moreover, another advantage of hydrothermal method is that catalysts can be grown directly on 3-dimensional substrates.^[67-69] A hydrothermal method is used in this thesis to fabricate a cobalt vanadium oxide electrocatalysts that can be grown directly on nickel foam (see Chapter 4).^[70]

Another solution-based method for synthesizing OER catalyst is co-precipitation. In this method, a solution containing reactants, usually metal salts, is stirred under inert atmosphere and precipitation is obtained by slowly modifying the pH by dropwise addition of base or acid. The precipitate can be collected and undergo additional post-treatments such as annealing in order to obtain the desired crystalline phase. Co-precipitation methods have the advantages to be simple and cheap to realize as only standard synthesis equipment is required. LDH materials, perovskites hydroxides, are examples of OER catalyst produced by co-precipitation methods.^[63,71]

Solution casting is another method used for preparing OER catalysts. This method rely on the preparation of a solution containing dissolved metal salts as reactants. The solution can then be cast on substrates by different procedures such as drop-casting or spin coating for example. Post-treatment of the deposited solution film by annealing is required in order to produce the active OER material. Solution casting, when combined with spin coating, allows the creation of thin films with thicknesses of a few nanometers.^[59] A drawback with solution casting methods is that producing nanostructured catalysts or coating high-aspect ratio nanostructures with conformal thin films remains difficult.

Smith *et al.* developed a method relying on photodecomposition of organometallic precursors to synthesis amorphous metal oxides. This method, based on the solution casting one, uses spin-coating to deposit conformal layers of organometallic compounds dissolved in organic solvents. The active catalysts are then produced by decomposition under UV illumination followed by annealing. This photochemical route has the advantage to be able to produce mixed-metal oxides with precise control on their composition.^[58]

Electrodeposition is another widely used technique to produce OER catalyst films. This method exploits the redox properties of metal salts dissolved in aqueous electrolytes. The metal ions in solution can be reduced or oxidized and precipitate in different forms, such as oxides, nitrides, selenides, sulfides or phosphides, on the surface on an electrode.^[54,65,72] The underlying substrate indeed needs to be conductive. Moreover, by controlling the applied potential or the current flowing through the electrode, a wide variety of morphologies and nanostructures can be obtained.^[73]

Another deposition method, strongly related to electrodeposition, is photoelectrodeposition. This method is used to deposit directly thin films of catalysts on photoelectrodes by using, in addition to an applied bias, the photovoltage arising from the photoabsorber under illumination. Compared to electrodeposition, photo-assisted electrodeposition allows the deposition of more uniform and active layers of catalysts by depositing only onto areas producing photogenerated holes.^[74,75] Chapter 3 focuses on the photoelectrodeposition of CoFeO_x on a nanostructured hematite photoanode.

Atomic layer deposition (ALD) can also be used to produce highly conformal layers of OER catalysts. This deposition technique, which belongs to the chemical vapor deposition family, is explained more in detail in Chapter 2. ALD has been used to produce several transition metal catalysts as well as catalytic coatings for photoanodes for OER.^[61,76-78] ALD has the advantage of precise control over the composition of the synthesized material and multiple procedures for ALD deposition of mono- and bimetallic oxides, nitrides and sulfides as well as trimetallic oxide materials have been reported.^[79] Moreover, conformal coatings of high aspect-ratio nanostructured substrates and particles are possible with ALD.^[80] This makes ALD highly valuable for synthesis of catalysts despite having a few drawbacks, such as a high cost and complexity of the ALD setup as well as a slow deposition rate.^[81]

1.5 Sunlight-driven water splitting

Life on Earth would not be possible without autotrophic organisms (such as plants and algae) that can harvest sunlight to convert CO_2 into organic molecules essential for life.^[82] This conversion is made possible by the natural photosynthesis process (Figure 1.9). Photosynthesis uses low energy electrons from the Oxygen Evolving Complex (a water-oxidizing enzyme) and promotes them to higher energy states through the photosystem II (PSII) and then through the photosystem I (PSI) protein complex by using solar energy. Electrons in high energy states are then used to drive the reduction of CO_2 , which is a thermodynamically uphill process, into carbohydrates. Photosynthesis can be decomposed into three steps:

- 1) **Light harvesting and charge generation:** Both photosystems (PSII and PSI) can absorb photons in the visible electromagnetic spectrum with their chromophore unit (P680 of PSII can absorb photons with wavelength of 680 nm and P700 of PSI can absorb photons of 700 nm).
- 2) **Charge separation and transport:** The excited pigments (P680* and P700*) reduce molecules in their surroundings. This triggers a cascade of reductive reactions which transport electrons away from the yet oxidized pigments (P680⁺ and P700⁺). These

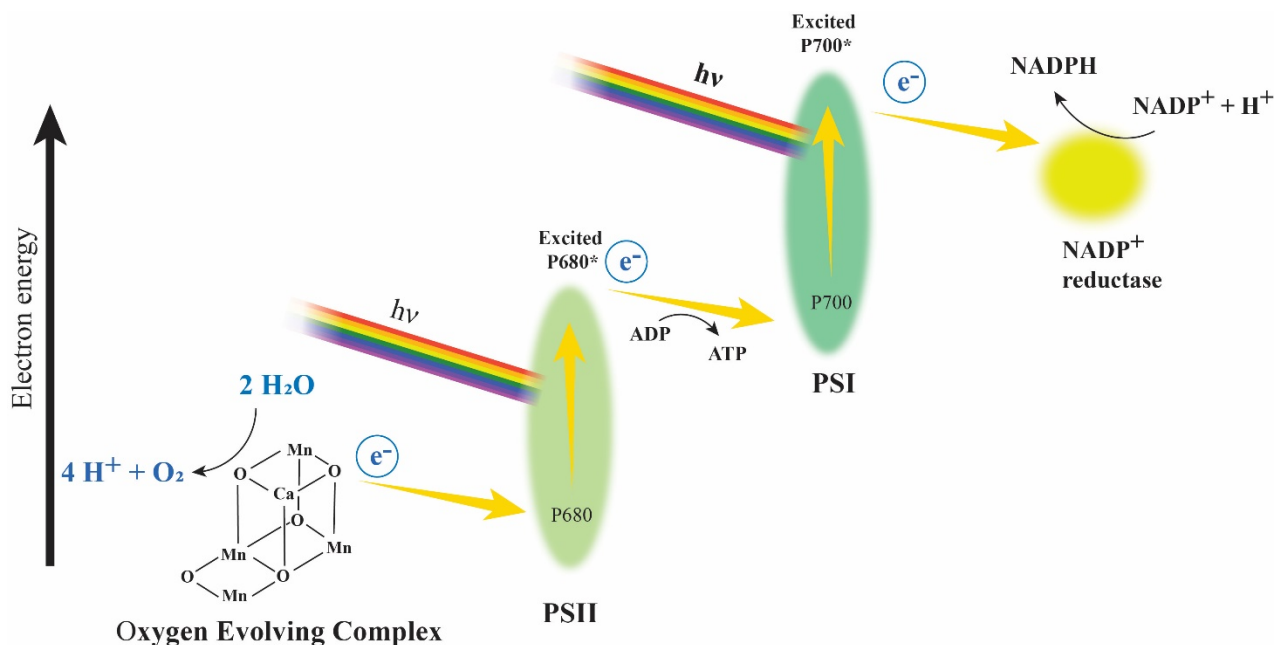


Figure 1.9 Simplified scheme of natural photosynthesis.

oxidized pigments will then drive the oxidation of other molecules in their surroundings, starting a chain of oxidation reactions in the opposite directions of the electrons movement. This processes allows physical separation of photogenerated electrons from the oxidized pigments in order to reduce the probability of recombination and increase the lifetime of charges. At the same time, the oxidized pigments are regenerated to their resting states before the next photons arrive.

- 3) Charge transfer by catalyst:** The pumped electrons by the PSII and PSI are transferred to the NADP^+ reductase enzyme that drives the reduction of NADP^+ into NADPH. NADPH can then enter the Calvin cycle to reduce CO_2 into carbohydrates through light-independent reactions. In the other side, the chain of oxidation reactions finishes at the Oxygen Evolving Complex that catalyzes oxidation of water to produce oxygen, protons and electrons.

The overall photosynthesis efficiency does not exceed 2-4 % depending on the type of photosynthesis used by plants.^[83] On the other hand, artificial photosynthesis, defined as the use of sunlight to yield fuels, can be engineered by using a wide variety of materials and techniques in order to reach high efficiencies in solar-to-chemical energy conversion. Artificial photosynthesis is based on the same three main steps as its natural counterpart (light absorption, charge separation and transport and charge transfer by catalyst). Two main approaches of artificial photosynthesis can be used in order to produce sustainable clean fuels: photoelectrochemical (PEC) water splitting or photovoltaic (PV) cells connected to electrolyzers. These concepts are described more in detail in sections 1.5.1 and 1.5.2 of this chapter.

Both technologies rely on semiconductors to harvest light and produce excited electrons and holes. Absorption of light depends on the bandgap of semiconductors. The band theory of solids describes the range of energies that an electron can have in a solid material. When atoms are together in a solid, their orbitals overlap to form bonding and antibonding combinations that form two continuums of energy levels, the valence (VB) and conduction band (CB). This is in opposition of free atoms or molecules that have discrete energy levels. The energy gap between the valence and conduction band (where no energy levels are found) is called band gap (E_g). Materials can be classified according to their band gap (Figure 1.10). Insulators have a large band gap and a valence band filled with electrons. The conduction band energy is so high that electrons cannot be thermally promoted from the valence to the conduction band and therefore, there is no conductivity

at ordinary temperatures. Semiconductors have a well-defined band gap which is much smaller than insulators. At ordinary temperatures, a small proportion of electrons have enough energy, according to the Fermi-Dirac distribution, to jump into the conduction band energy states. Semiconductors are, for this reason, considered as weak conductors. In both insulators and semiconductors, the Fermi level lies in the middle of the valence and conduction band. The Fermi level (E_F) is defined as the energy level that has a 50 % probability to be filled with electrons.

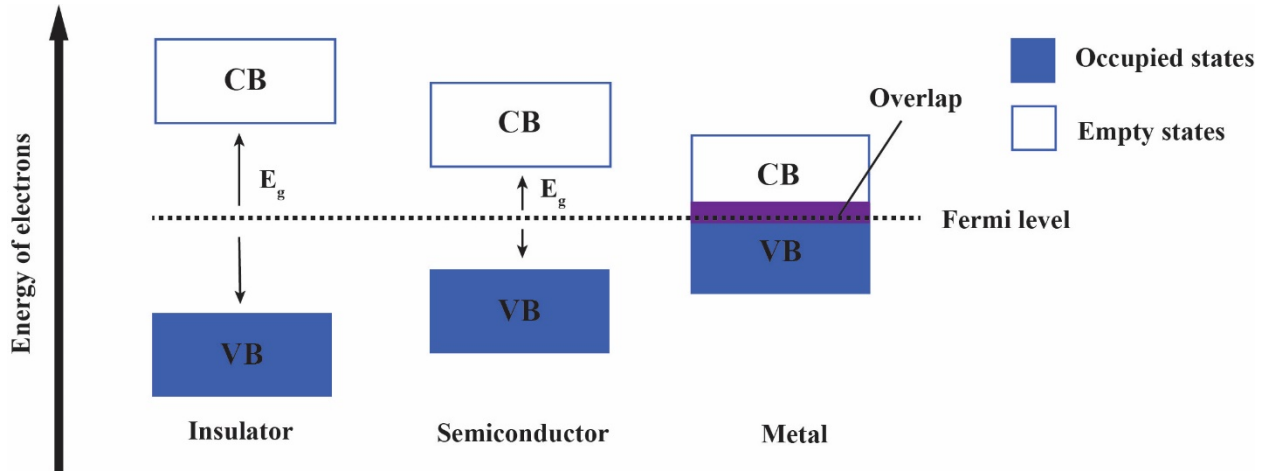


Figure 1.10 Band structure diagram for an insulator, semiconductor and metal.

However, in semiconductors, electrons cannot be found inside the band gap as this is a forbidden energy zone. In metals, the valence and conduction band overlap and the filled and empty energy states mix up to form a continuum of electronic levels. Valence electrons are essentially free to move to empty states of the conduction bands with little amount of energy, leading to a good electrical conductivity of metals.

In intrinsic (undoped) semiconductors, the number of electrons in the conduction band is the same as the number of holes (h^+) in the valence band. Semiconductors can be doped by intentionally introducing impurities in their structure to influence their electronic properties. Replacing some atoms of the semiconductor by foreign atoms having one more or one less valence electron will change the number of electrons and holes in the conduction and valence band, thus shifting the initial equilibrium of electrons and holes of the intrinsic semiconductor. By adding an element that has one additional valence electron than the atoms composing the semiconductor, this additional electron can be thermally promoted to the conduction band. In this case the material

will become an n-type semiconductor. Similarly, in a p-type material, an element having a lower number of valence electrons is added and can accept an electron from the valence band of the semiconductor. In p-type materials, the Fermi level is located just above the valence band and in n-type materials the Fermi level lies just below the conduction band. When a doped semiconductor is immersed in an electrolyte solution, for example in a PEC water splitting device, the type of doping will influence the band structure at the interface between the semiconductor and the electrolyte. In order for the two phases to be in equilibrium, their electrochemical potential should be the same. The redox potential of the semiconductor is determined by the Fermi level. The electrochemical potential of the solution is determined by the redox potential of the electrolyte. If both potential are not the same, a movement of charge will happen between the solution and the semiconductor in order to equilibrate the two phases. In p-type materials, electrons generally flow from the electrolyte to the semiconductor, thus producing an accumulation of charges that extends for a significant distance into the material. This region is called the space charge layer and has an associated electrical field. Accumulation of electrons in the space charge region causes a downward bending in the band edges. This region is also referred as depletion layer because the holes in the space charge are removed by the excess of electrons. In the case of an n-type material, the Fermi level is typically higher than the redox potential of the solution and therefore, electrons are transferred into the solution. An upward bending of the band edges is observed due to the positive charge associating to the depletion region of the space charge.^[84] The interfacial band edges energetics of p- and n-type semiconductors in the dark are represented Figure 1.11.

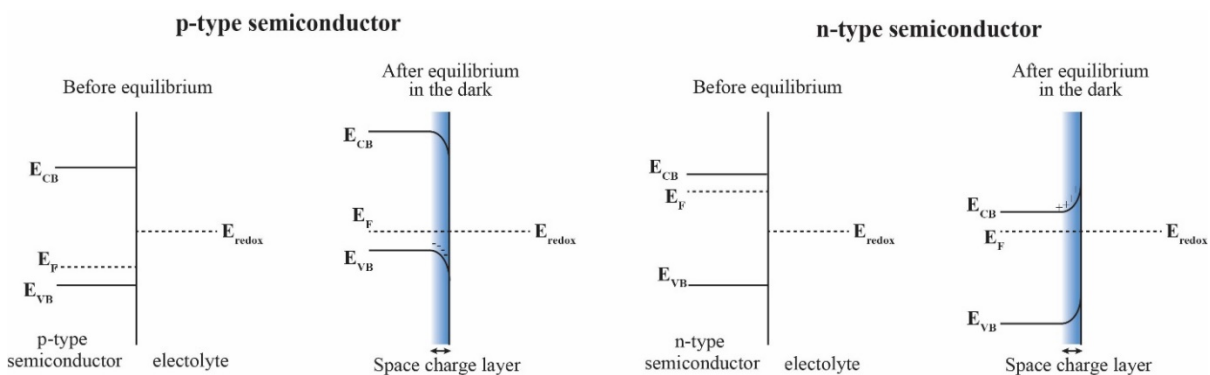


Figure 1.11 Interfacial band edge energetics for a p-type and n-type semiconductor/electrolyte interface before and after equilibrium in the dark.

When a semiconductor is illuminated, absorption of photons with energy greater than its band gap will occur. Upon absorption of a photon, an electron in the valence band will be excited and promoted to the conduction band and a hole will be created in the valence band. Depending in which region of the semiconductor photons are absorbed (bulk or space charge region), different processes can happen. If absorption occurs in the bulk of the material, electron-hole pairs will recombine as no electric field is present to separate them. In the other case, when a photon is absorbed in the space charge region, the build-in electric field will separate the photoexcited electron from the hole. In the case of an n-type material, as represented in Figure 1.12, the electron will be driven to the back contact and the hole to the semiconductor/electrolyte interface where it will oxidize species in solution. Moreover, upon illumination, the Fermi level will increase with the internal photovoltage and band bending will decrease. Since the system is no longer in equilibrium due to the generation of electron-hole pairs, particularly in the space charge region, the use of a single Fermi level is no longer appropriate. For this reason, the Fermi level splits into two quasi-Fermi levels ($E_{F,n}^*$ for electrons $E_{F,p}^*$ for holes).^[85]

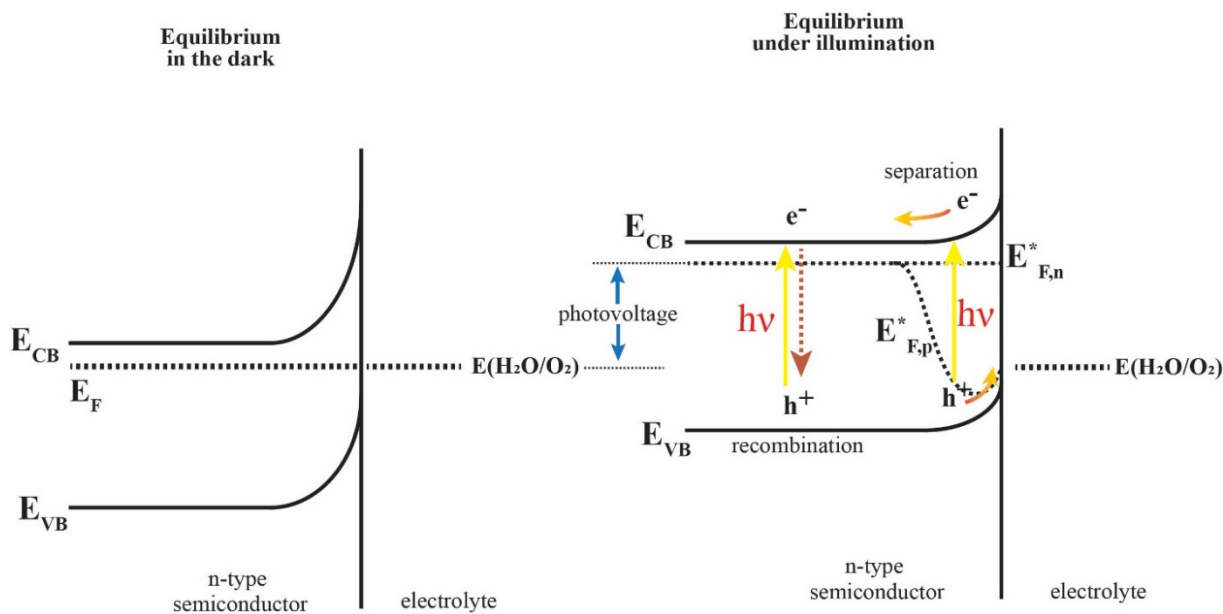


Figure 1.12 Band diagram for an n-type semiconductor in equilibrium in the dark and under illumination.

1.5.1 PV-electrolysis

Both electrolyzers and photovoltaic cells are mature technologies that are already in the commercialization stage. Solar cells and electrolyzers can be either connected together directly, forming a PV-electrolyzer device (Figure 1.13), or can be connected through the electrical grid. If connected through the grid, the electrical transmission efficiency in the power lines is typically in the order of 93 %. Additionally an inverter is required in order to produce AC current (that can be injected into the grid) from the DC current generated in PV cells. Electrolyzers are commonly operated above 1.8 V in order to reach high current densities and lower their operational costs. By taking into consideration a solar cell with an efficiency of 20 %, a solar-to-hydrogen (STH) efficiency of 12.7 % ($0.93 \times 0.20 \times 1.23/1.8$) would be obtained. These systems are thus able to reach high enough STH efficiencies to be of technological relevance for hydrogen production. However the cost of hydrogen produced by PV-electrolysis remains higher compared to hydrogen produced by steam reforming due to the inverter needed and the high cost of precious metal catalysts used. Connecting solar cells directly to electrolyzers would remove the cost of inverters and the loss of efficiency arising from the power line transport, making the cost of hydrogen closer to economic competitiveness. A drawback would be that the PV cell would not provide a constant power to the electrolyzer due to weather conditions, leading to a less optimal use of the electrolyzer.^[86]

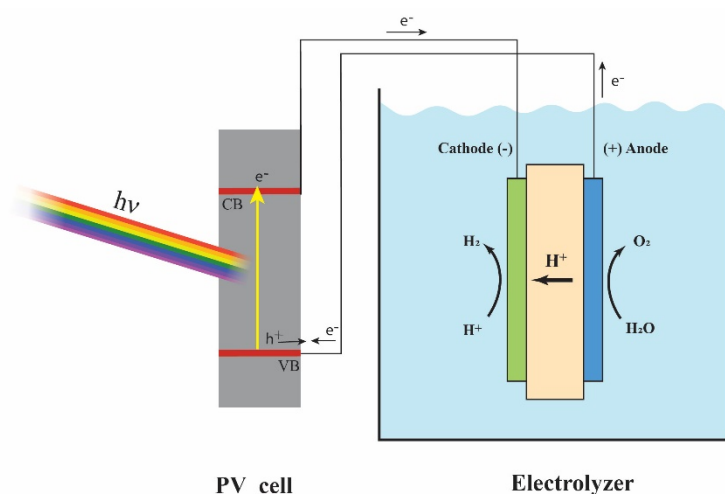


Figure 1.13 Scheme of PV-electrolysis (PV cell connected to a PEM electrolyzer).

1.5.2 Photoelectrochemical water splitting

In 1972, Fujishima and Honda demonstrated for the first time photo-driven water splitting by using TiO_2 . This oxide has a large bandgap, depending on its crystalline phase, between 3.0 and 3.2 eV which allows photo-oxidation and photo-reduction of water into oxygen and hydrogen gas by absorption of UV light without any applied electrical bias.^[87] UV light ($\lambda < 400$ nm) represents only a small portion of the AM 1.5G solar spectra (Figure 1.14 a). AM 1.5G represents the solar irradiation that reaches the surface of the Earth after attenuation by the atmosphere and when the solar zenith has an angle of 48.2° . In order to develop highly efficient and cheap photoelectrodes for PEC water splitting, multiple constraints need to be taken into account. First, for a given semiconductor, the edge of its valence band should be located more positive than the OER redox potential and its conduction band more negative than the HER potential in order to provide a thermodynamic driving force. Second, its bandgap needs to be large enough to provide sufficient overpotential but still low enough (smaller than ca. 3 eV) in order for the material to be able to absorb a large part of the solar spectrum. Third, the material should be preferably non-toxic, based on inexpensive and abundant elements and be stable in aqueous media under illumination. No material respecting all these criteria has been discovered so far (Figure 1.14 b).

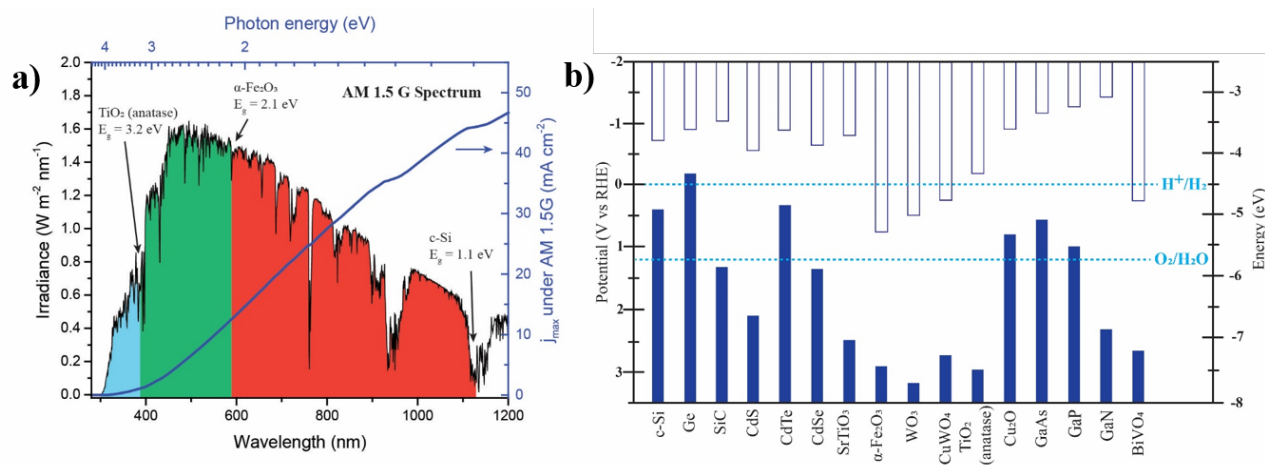


Figure 1.14 a) AM 1.5G solar spectrum and theoretical maximum photocurrent densities reachable depending on the absorbed portion of the solar spectrum (blue curve, integral of solar spectrum). The fractions of the solar spectrum absorbed by some selected semiconductors (TiO_2 , $\alpha\text{-Fe}_2\text{O}_3$ and c-Si) are also represented. **b)** Band structure of different semiconductors compared to the thermodynamic water oxidation and reduction potentials (pH=0).

In order to perform unassisted water splitting by using sunlight, coupling two photoabsorbers to build a PEC device is an attractive solution. In such devices, the portion of the light that is not absorbed by the first photoelectrode can be absorbed by an underneath photoabsorber having a smaller band gap than the front one. The principle of dual-absorber PEC devices is represented in Figure 1.15. Different configurations of PEC tandem cells are possible. A photoanode that evolves oxygen can be coupled directly to a photocathode that evolves hydrogen. Another configuration is to couple a photoanode performing OER to a PV cell to reach the required photovoltage for unassisted water splitting. In order to perform the second half reaction (HER in that case) a dark cathode is connected in series to the photoanode-PV cell. Both of these designs allows for the development, manufacturing and investigations of the different electrodes separately. Dual absorbers tandem PEC cells have been predicted to reach over 25 % STH efficiency.^[88] Various systems for artificial photosynthesis have been proposed to date with experimental STH efficiencies of up to 18 %.^[89-91] However these high efficiencies systems are based on expensive semiconductors and precious metal electrocatalysts, thus preventing the use of these devices at large scale. PEC tandem cells made with Earth-abundant materials have been developed but efficiencies remain low with STH conversions of a few percent, hence the large scale commercialization of these devices remains elusive nowadays.^[92]

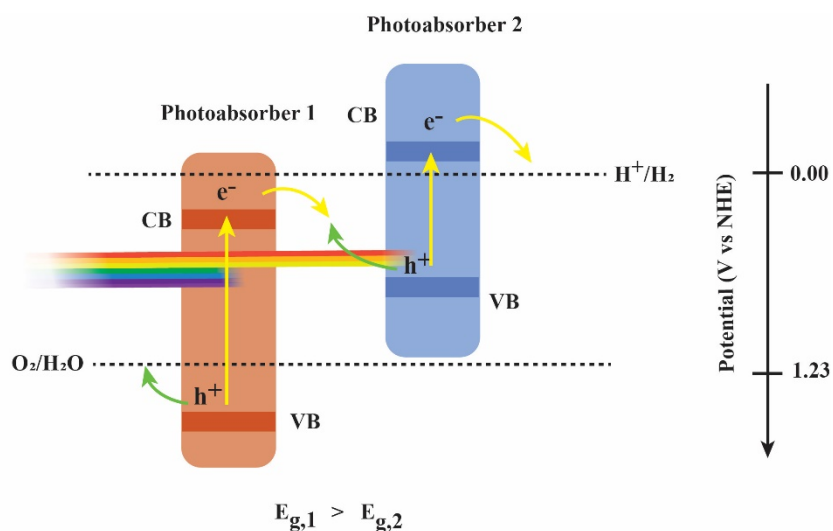


Figure 1.15 Dual-absorber PEC cell with photoanode and photocathode in tandem.

1.6 Outline of the following chapters

Sustainable production of hydrogen as energy carrier is of crucial importance to reduce the emissions of CO₂ and to avoid a global environmental crisis. For this, research and development of new materials, which are cheap and Earth-abundant, for catalyzing the water splitting reaction and more precisely the oxygen evolution reaction is of tremendous importance. The following chapters of this thesis are based on the development and synthesis of new catalysts for electrochemical and photoelectrochemical OER by different methods. Chapter 2 describes the fabrication of different mixed transition metal oxides composed of cobalt, iron and vanadium by atomic layer deposition (ALD) and their application on high surface nickel foam as a 3-dimensional substrate for the production of highly active anodes for OER. Chapter 3 is based on the development of a photoelectrodeposition method that yields an ultrathin layer of CoFeO_x on cauliflower nanostructured hematite photoanodes. Characterization of this CoFeO_x-coated hematite photoanode was performed to investigate the causes of the enhancement of the OER activity by the CoFeO_x layer. Finally, Chapter 4 describes an amorphous CoVO_x OER catalyst fabricated by hydrothermal synthesis. All materials synthesized were shown to be remarkably active and could compete with state-of-the-art OER electrocatalysts.

1.7 References

- [1] U.S. Energy Information Administration. International energy outlook 2017. (Washington DC, 2017).
- [2] Hansen, J., Sato, M., Kharecha, P., Beerling, D., Berner, R., Masson-Delmotte, V., Pagani, M., Raymo, M., Royer, D. L. & Zachos, J. C. Target atmospheric CO₂: Where should humanity aim? *Open Atmos. Sci. J.* **2**, 217-231,(2008).
- [3] Ekwurzel, B., Boneham, J., Dalton, M. W., Heede, R., Mera, R. J., Allen, M. R. & Frumhoff, P. C. The rise in global atmospheric CO₂, surface temperature, and sea level from emissions traced to major carbon producers. *Climatic Change* **144**, 579-590,(2017).
- [4] *Trends in Atmospheric Carbon Dioxide*, <https://www.esrl.noaa.gov/gmd/ccgg/trends/weekly.html> (Accessed 09 January 2019).
- [5] Meinshausen, M., Meinshausen, N., Hare, W., Raper, S. C. B., Frieler, K., Knutti, R., Frame, D. J. & Allen, M. R. Greenhouse-gas emission targets for limiting global warming to 2°C. *Nature* **458**, 1158-1162,(2009).
- [6] Doney, S. C., Fabry, V. J., Feely, R. A. & Kleypas, J. A. Ocean Acidification: The Other CO₂ Problem. *Annual Review of Marine Science* **1**, 169-192,(2009).
- [7] Haszeldine, R. S. Carbon Capture and Storage: How Green Can Black Be? *Science* **325**, 1647-1652,(2009).
- [8] Matter, J. M., Stute, M., Snæbjörnsdóttir, S. Ó., Oelkers, E. H., Gislason, S. R., Aradóttir, E. S., Sigfusson, B., Gunnarsson, I., Sigurdardóttir, H., Gunnlaugsson, E., Axelsson, G., Alfredsson, H. A., Wolff-Boenisch, D., Mesfin, K., Taya, D. F. d. l. R., Hall, J., Dideriksen, K. & Broecker, W. S. Rapid carbon mineralization for permanent disposal of anthropogenic carbon dioxide emissions. *Science* **352**, 1312-1314,(2016).
- [9] Aresta, M. *Carbon Dioxide as Chemical Feedstock*. 1-13 (WILEY-VCH, 2010).
- [10] Höök, M. & Tang, X. Depletion of fossil fuels and anthropogenic climate change—A review. *Energy Policy* **52**, 797-809,(2013).
- [11] MacKay, D. J. C. *Sustainable Energy- Without the Hot air*. (UIT, Cambridge, UK, 2009).
- [12] Quirin Schiermeier, J. T., Tony Scully, Alexandra Witze & Oliver Morton. Energy alternatives: Electricity without carbon. *Nature*, 816-823,(2008).
- [13] Gratzel, M. Photoelectrochemical cells. *Nature* **414**, 338-344,(2001).
- [14] Tian, Y. & Zhao, C. Y. A review of solar collectors and thermal energy storage in solar thermal applications. *Applied Energy* **104**, 538-553,(2013).
- [15] REN21. *Renewables 2018 Global Status Report*. (2018).
- [16] Lewis, N. S. & Nocera, D. G. Powering the planet: Chemical challenges in solar energy utilization. *Proceedings of the National Academy of Sciences* **103**, 15729-15735,(2006).
- [17] Carl-Jochen Winter, J. N. *Hydrogen as an Energy Carrier*. (Springer-Verlag, 1988).
- [18] Bockris, J. O. M. The origin of ideas on a Hydrogen Economy and its solution to the decay of the environment. *International Journal of Hydrogen Energy* **27**, 731-740,(2002).
- [19] Verne, J. *The Mysterious Island*. (1874).
- [20] Cook, T. R., Dogutan, D. K., Reece, S. Y., Surendranath, Y., Teets, T. S. & Nocera, D. G. Solar Energy Supply and Storage for the Legacy and Nonlegacy Worlds. *Chemical Reviews* **110**, 6474-6502,(2010).
- [21] Marban, G. & Valdes-Solis, T. Towards the hydrogen economy? *International Journal of Hydrogen Energy* **32**, 1625-1637,(2007).

-
- [22] Crabtree, G. W., Dresselhaus, M. S. & Buchanan, M. V. The hydrogen economy. *Physics Today*, 39-44,(2004).
- [23] Barreto, L., Makihira, A. & Riahi, K. The hydrogen economy in the 21st century: a sustainable development scenario. *International Journal of Hydrogen Energy* **28**, 267-284,(2003).
- [24] Töpler, J. L., J. *Hydrogen and Fuel Cell, Technologies and Market Perspectives*. (Springer, 2014).
- [25] Armaroli, N. & Balzani, V. The Hydrogen Issue. *ChemSusChem* **4**, 21-36,(2011).
- [26] Balat, M. Potential importance of hydrogen as a future solution to environmental and transportation problems. *International Journal of Hydrogen Energy* **33**, 4013-4029,(2008).
- [27] von Helmolt, R. & Eberle, U. Fuel cell vehicles: Status 2007. *Journal of Power Sources* **165**, 833-843,(2007).
- [28] Ren, J., Musyoka, N. M., Langmi, H. W., Mathe, M. & Liao, S. Current research trends and perspectives on materials-based hydrogen storage solutions: A critical review. *International Journal of Hydrogen Energy* **42**, 289-311,(2017).
- [29] Züttel, A. Materials for hydrogen storage. *Materials Today* **6**, 24-33,(2003).
- [30] Eberle, U., Felderhoff, M. & Schüth, F. Chemical and Physical Solutions for Hydrogen Storage. *Angewandte Chemie International Edition* **48**, 6608-6630,(2009).
- [31] Sharaf, O. Z. & Orhan, M. F. An overview of fuel cell technology: Fundamentals and applications. *Renewable and Sustainable Energy Reviews* **32**, 810-853,(2014).
- [32] Trasatti, S. *Erratum to "Water electrolysis: who first?"*. Vol. 481 (2000).
- [33] Ursua, A., Gandia, L. M. & Sanchis, P. Hydrogen Production From Water Electrolysis: Current Status and Future Trends. *Proceedings of the IEEE* **100**, 410-426,(2012).
- [34] Hall, D. E. Electrodes for Alkaline Water Electrolysis. *Journal of The Electrochemical Society* **128**, 740-746,(1981).
- [35] Carmo, M., Fritz, D. L., Mergel, J. & Stolten, D. A comprehensive review on PEM water electrolysis. *International Journal of Hydrogen Energy* **38**, 4901-4934,(2013).
- [36] Bard, A. J., Faulkner, L. R. *Electrochemical methods: Fundamentals and Applications*. 87-137 (John Wiley & Sons, 2001).
- [37] Bockris, J. O. M., Potter, E. C. The Mechanism of the Cathodic Hydrogen Evolution Reaction. *J. Electrochem. Soc.* **99**, 169-186,(1952).
- [38] Thomas, J. G. N. Kinetics of electrolytic hydrogen evolution and the adsorption of hydrogen by metals. *Transactions of the Faraday Society* **57**, 1603-1611,(1961).
- [39] Nørskov, J. K., Bligaard, T., Logadottir, A., Kitchin, J. R., Chen, J. G., Pandalov, S. & Stimming, U. Trends in the Exchange Current for Hydrogen Evolution. *Journal of The Electrochemical Society* **152**, J23-J26,(2005).
- [40] Zheng, Y., Jiao, Y., Zhu, Y., Li, L. H., Han, Y., Chen, Y., Du, A., Jaroniec, M. & Qiao, S. Z. Hydrogen evolution by a metal-free electrocatalyst. *Nature Communications* **5**, 3783,(2014).
- [41] Hans Wedepohl, K. The composition of the continental crust. *Geochimica et Cosmochimica Acta* **59**, 1217-1232,(1995).
- [42] Zou, X. & Zhang, Y. Noble metal-free hydrogen evolution catalysts for water splitting. *Chemical Society Reviews* **44**, 5148-5180,(2015).
- [43] McKone, J. R., Sadtler, B. F., Werlang, C. A., Lewis, N. S. & Gray, H. B. Ni–Mo Nanopowders for Efficient Electrochemical Hydrogen Evolution. *ACS Catalysis* **3**, 166-169,(2013).
-

-
- [44] Vrubel, H. & Hu, X. Molybdenum Boride and Carbide Catalyze Hydrogen Evolution in both Acidic and Basic Solutions. *Angewandte Chemie International Edition* **51**, 12703-12706,(2012).
- [45] Tahir, M., Pan, L., Idrees, F., Zhang, X., Wang, L., Zou, J.-J. & Wang, Z. L. Electrocatalytic oxygen evolution reaction for energy conversion and storage: A comprehensive review. *Nano Energy* **37**, 136-157,(2017).
- [46] Song, F., Bai, L., Moysiadou, A., Lee, S., Hu, C., Liardet, L. & Hu, X. Transition Metal Oxides as Electrocatalysts for the Oxygen Evolution Reaction in Alkaline Solutions: An Application-Inspired Renaissance. *Journal of the American Chemical Society* **140**, 7748-7759,(2018).
- [47] Bockris, J. O. M. & Otagawa, T. The Electrocatalysis of Oxygen Evolution on Perovskites. *Journal of The Electrochemical Society* **131**, 290-302,(1984).
- [48] Man, I. C., Su, H.-Y., Calle-Vallejo, F., Hansen, H. A., Martínez, J. I., Inoglu, N. G., Kitchin, J., Jaramillo, T. F., Nørskov, J. K. & Rossmeisl, J. Universality in Oxygen Evolution Electrocatalysis on Oxide Surfaces. *ChemCatChem* **3**, 1159-1165,(2011).
- [49] Suntivich, J., May, K. J., Gasteiger, H. A., Goodenough, J. B. & Shao-Horn, Y. A Perovskite Oxide Optimized for Oxygen Evolution Catalysis from Molecular Orbital Principles. *Science* **334**, 1383-1385,(2011).
- [50] McCrory, C. C. L., Jung, S., Peters, J. C. & Jaramillo, T. F. Benchmarking Heterogeneous Electrocatalysts for the Oxygen Evolution Reaction. *Journal of the American Chemical Society* **135**, 16977-16987,(2013).
- [51] Viswanathan, V., Pickrahn, K. L., Luntz, A. C., Bent, S. F. & Nørskov, J. K. Nanoscale Limitations in Metal Oxide Electrocatalysts for Oxygen Evolution. *Nano Letters* **14**, 5853-5857,(2014).
- [52] Corrigan, D. The Catalysis of the Oxygen Evolution Reaction by Iron Impurities in Thin Film Nickel Oxide Electrodes. *J. of The Electrochemical Society* **134**, 377-384,(1986).
- [53] Song, F. & Hu, X. Exfoliation of layered double hydroxides for enhanced oxygen evolution catalysis. *Nat Commun* **5**,(2014).
- [54] Morales-Guio, C. G., Liardet, L. & Hu, X. Oxidatively Electrodeposited Thin-Film Transition Metal (Oxy)hydroxides as Oxygen Evolution Catalysts. *Journal of the American Chemical Society* **138**, 8946-8957,(2016).
- [55] Gong, M., Li, Y., Wang, H., Liang, Y., Wu, J. Z., Zhou, J., Wang, J., Regier, T., Wei, F. & Dai, H. An Advanced Ni-Fe Layered Double Hydroxide Electrocatalyst for Water Oxidation. *Journal of the American Chemical Society* **135**, 8452-8455,(2013).
- [56] Zhu, C., Shi, Q., Feng, S., Du, D. & Lin, Y. Single-Atom Catalysts for Electrochemical Water Splitting. *ACS Energy Letters* **3**, 1713-1721,(2018).
- [57] Fei, H., Dong, J., Feng, Y., Allen, C. S., Wan, C., Voloskiy, B., Li, M., Zhao, Z., Wang, Y., Sun, H., An, P., Chen, W., Guo, Z., Lee, C., Chen, D., Shakir, I., Liu, M., Hu, T., Li, Y., Kirkland, A. I., Duan, X. & Huang, Y. General synthesis and definitive structural identification of MN₄C₄ single-atom catalysts with tunable electrocatalytic activities. *Nature Catalysis* **1**, 63-72,(2018).
- [58] Smith, R. D. L., Prévot, M. S., Fagan, R. D., Zhang, Z., Sedach, P. A., Siu, M. K. J., Trudel, S. & Berlinguette, C. P. Photochemical Route for Accessing Amorphous Metal Oxide Materials for Water Oxidation Catalysis. *Science* **340**, 60-63,(2013).
-

-
- [59] Trotochaud, L., Ranney, J. K., Williams, K. N. & Boettcher, S. W. Solution-Cast Metal Oxide Thin Film Electrocatalysts for Oxygen Evolution. *Journal of the American Chemical Society* **134**, 17253-17261,(2012).
- [60] Yan, Y., Xia, B. Y., Zhao, B. & Wang, X. A review on noble-metal-free bifunctional heterogeneous catalysts for overall electrochemical water splitting. *Journal of Materials Chemistry A* **4**, 17587-17603,(2016).
- [61] Pickrahn, K. L., Park, S. W., Gorlin, Y., Lee, H.-B.-R., Jaramillo, T. F. & Bent, S. F. Active MnOx Electrocatalysts Prepared by Atomic Layer Deposition for Oxygen Evolution and Oxygen Reduction Reactions. *Advanced Energy Materials* **2**, 1269-1277,(2012).
- [62] Pickrahn, K. L., Garg, A. & Bent, S. F. ALD of Ultrathin Ternary Oxide Electrocatalysts for Water Splitting. *ACS Catalysis* **5**, 1609-1616,(2015).
- [63] Anantharaj, S., Karthick, K. & Kundu, S. Evolution of layered double hydroxides (LDH) as high performance water oxidation electrocatalysts: A review with insights on structure, activity and mechanism. *Materials Today Energy* **6**, 1-26,(2017).
- [64] Xie, J. & Xie, Y. Transition Metal Nitrides for Electrocatalytic Energy Conversion: Opportunities and Challenges. *Chemistry – A European Journal* **22**, 3588-3598,(2016).
- [65] Anantharaj, S., Ede, S. R., Sakthikumar, K., Karthick, K., Mishra, S. & Kundu, S. Recent Trends and Perspectives in Electrochemical Water Splitting with an Emphasis on Sulfide, Selenide, and Phosphide Catalysts of Fe, Co, and Ni: A Review. *ACS Catalysis* **6**, 8069-8097,(2016).
- [66] Rao, B. G., Mukherjee, D. & Reddy, B. M. in *Nanostructures for Novel Therapy Chapter 1 - Novel approaches for preparation of nanoparticles* 1-36 (Elsevier, 2017).
- [67] Wang, P., Song, F., Amal, R., Hau Ng, Y. & Hu, X. Efficient Water Splitting Catalyzed by Cobalt PhosphideBased Nanoneedle Arrays Supported on Carbon Cloth. *ChemSusChem*, 472-477,(2016).
- [68] Li, W., Gao, X., Xiong, D., Wei, F., Song, W.-G., Xu, J. & Liu, L. Hydrothermal Synthesis of Monolithic Co₃Se₄ Nanowire Electrodes for Oxygen Evolution and Overall Water Splitting with High Efficiency and Extraordinary Catalytic Stability. *Advanced Energy Materials* **7**, 1602579,(2017).
- [69] Luo, J., Im, J.-H., Mayer, M. T., Schreier, M., Nazeeruddin, M. K., Park, N.-G., Tilley, S. D., Fan, H. J. & Grätzel, M. Water photolysis at 12.3% efficiency via perovskite photovoltaics and Earth-abundant catalysts. *Science* **345**, 1593-1596,(2014).
- [70] Liardet, L. & Hu, X. Amorphous Cobalt Vanadium Oxide as a Highly Active Electrocatalyst for Oxygen Evolution. *ACS Catalysis* **8**, 644-650,(2018).
- [71] Zhu, Y., Zhou, W. & Shao, Z. Perovskite/Carbon Composites: Applications in Oxygen Electrocatalysis. *Small* **13**, 1603793,(2017).
- [72] Kanan, M. W., Surendranath, Y. & Nocera, D. G. Cobalt–phosphate oxygen-evolving compound. *Chemical Society Reviews* **38**, 109-114,(2009).
- [73] Gurrappa, I. & Binder, L. Electrodeposition of nanostructured coatings and their characterization—A review. *Science and Technology of Advanced Materials* **9**, 043001,(2008).
- [74] Zhong, D. K., Cornuz, M., Sivula, K., Gratzel, M. & Gamelin, D. R. Photo-assisted electrodeposition of cobalt-phosphate (Co-Pi) catalyst on hematite photoanodes for solar water oxidation. *Energy & Environmental Science* **4**, 1759-1764,(2011).
-

-
- [75] Liardet, L., Katz, J. E., Luo, J., Grätzel, M. & Hu, X. An ultrathin cobalt–iron oxide catalyst for water oxidation on nanostructured hematite photoanodes. *Journal of Materials Chemistry A* **7**, 6012-6020,(2019).
- [76] Riha, S. C., Klahr, B. M., Tyo, E. C., Seifert, S., Vajda, S., Pellin, M. J., Hamann, T. W. & Martinson, A. B. F. Atomic Layer Deposition of a Submonolayer Catalyst for the Enhanced Photoelectrochemical Performance of Water Oxidation with Hematite. *ACS Nano* **7**, 2396-2405,(2013).
- [77] Nardi, K. L., Yang, N., Dickens, C. F., Strickler, A. L. & Bent, S. F. Creating Highly Active Atomic Layer Deposited NiO Electrocatalysts for the Oxygen Evolution Reaction. *Advanced Energy Materials* **5**, n/a-n/a,(2015).
- [78] Singh, J. A., Yang, N. & Bent, S. F. Nanoengineering Heterogeneous Catalysts by Atomic Layer Deposition. *Annual Review of Chemical and Biomolecular Engineering* **8**, 41-62,(2017).
- [79] Mackus, A. J. M., Schneider, J. R., MacIsaac, C., Baker, J. G. & Bent, S. F. Synthesis of Doped, Ternary, and Quaternary Materials by Atomic Layer Deposition: A Review. *Chemistry of Materials* **31**, 1142-1183,(2019).
- [80] Marichy, C., Bechelany, M. & Pinna, N. Atomic Layer Deposition of Nanostructured Materials for Energy and Environmental Applications. *Advanced Materials* **24**, 1017-1032,(2012).
- [81] Lubitz, M., Medina, P. A., Antic, A., Rosin, J. T. & Fahlman, B. D. Cost-Effective Systems for Atomic Layer Deposition. *Journal of Chemical Education* **91**, 1022-1027,(2014).
- [82] Lambers, H., Chapin, F. S. & Pons, T. L. in *Plant Physiological Ecology* Photosynthesis 11-99 (Springer New York, 2008).
- [83] Zhu, X.-G., Long, S. P. & Ort, D. R. What is the maximum efficiency with which photosynthesis can convert solar energy into biomass? *Current Opinion in Biotechnology* **19**, 153-159,(2008).
- [84] Bott, A. W. Electrochemistry of semiconductors. *Current Separation* **17**,(1998).
- [85] van de Krol, R. & Graetzel, M. *Photoelectrochemical Hydrogen Production*. 47-49 (Springer 2012).
- [86] Jacobsson, T. J., Fjällström, V., Edoff, M. & Edvinsson, T. Sustainable solar hydrogen production: from photoelectrochemical cells to PV-electrolyzers and back again. *Energy & Environmental Science* **7**, 2056-2070,(2014).
- [87] Fujishima, A. & Honda, K. Electrochemical Photolysis of Water at a Semiconductor Electrode. *Nature* **238**, 37-38,(1972).
- [88] Hu, S., Xiang, C., Haussener, S., Berger, A. D. & Lewis, N. S. An analysis of the optimal band gaps of light absorbers in integrated tandem photoelectrochemical water-splitting systems. *Energy & Environmental Science* **6**, 2984-2993,(2013).
- [89] Licht, S., Wang, B., Mukerji, S., Soga, T., Umeno, M. & Tributsch, H. Efficient Solar Water Splitting, Exemplified by RuO₂-Catalyzed AlGaAs/Si Photoelectrolysis. *The Journal of Physical Chemistry B* **104**, 8920-8924,(2000).
- [90] Khaselev, O. & Turner, J. A. A Monolithic Photovoltaic-Photoelectrochemical Device for Hydrogen Production via Water Splitting. *Science* **280**, 425-427,(1998).
- [91] Rongé, J., Bosserez, T., Martel, D., Nervi, C., Boarino, L., Taulelle, F., Decher, G., Bordiga, S. & Martens, J. A. Monolithic cells for solar fuels. *Chemical Society Reviews* **43**, 7963-7981,(2014).
-

- [92] Prévot, M. S. & Sivula, K. Photoelectrochemical Tandem Cells for Solar Water Splitting. *The Journal of Physical Chemistry C* **117**, 17879-17893,(2013).

Chapter 2

*Atomic Layer Deposition of Transition
Metal Oxides as Electrocatalysts for
Oxygen Evolution*

2.1 Introduction

The Atomic layer deposition (ALD) designation dates back to the year 2000. Before that, this technique was referred as atomic layer epitaxy (ALE). The history of ALD and ALE started in the 1970s in Finland with the pioneer work of Suntola who demonstrated some of the first ALE processes in 1974. The first literature report on ALE was published in 1980.^[1,2] ALD belongs to a subtype of chemical vapor deposition (CVD). In opposite to CVD reactions, ALD exposes the substrate to reagents separately in two sequential, self-limited surface reactions.^[3] A thin film can be grown by pulsing a sequence of two precursors. Figure 2.1 shows the mechanism of ALD based on the deposition of Al_2O_3 with trimethylaluminum and water as reactants. The first step consists of saturating the surface of the substrate with the first precursor, which is generally composed of an organometallic compound. The organometallic molecules will chemisorb on reactive sites, generally hydroxyl groups, present on the surface of the substrate. In an ideal case, all active sites on the surface of the substrate are saturated with the precursor molecules, therefore self-limiting the growth to a maximum of one monolayer. In reality, steric hindrance of organometallic precursors prevents the formation of a complete monolayer as not all active sites are available. In a second step, excess of precursors and formed products are purged out with an inert gas, leaving

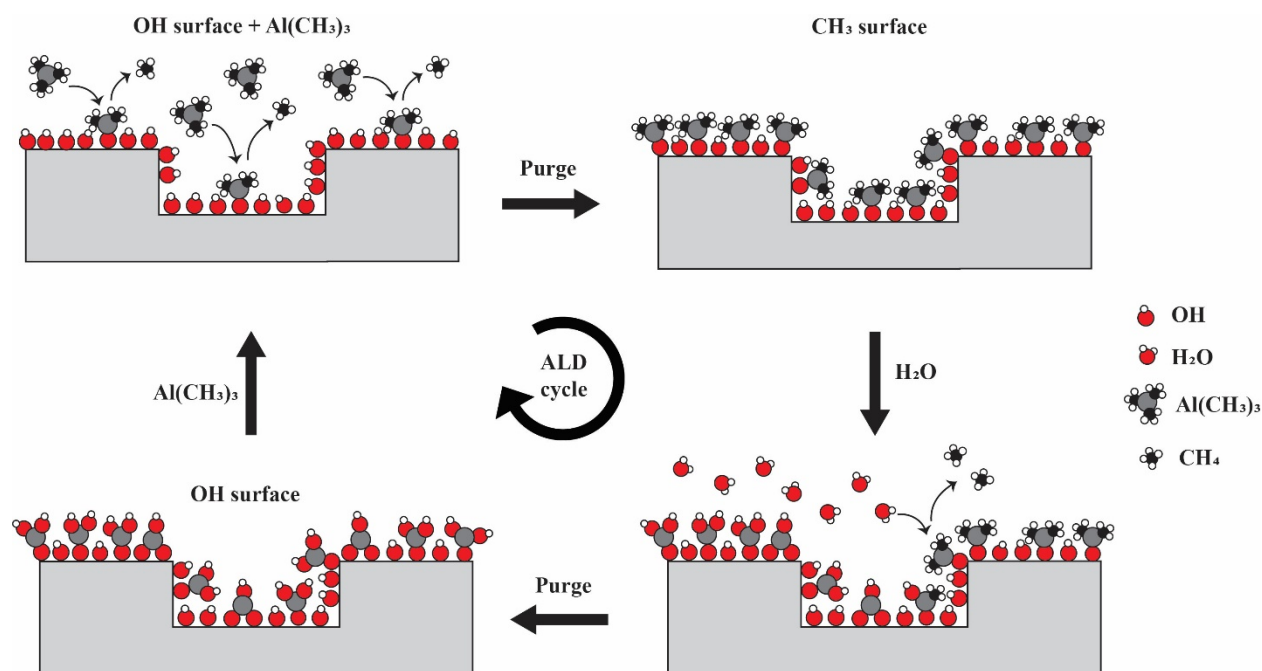


Figure 2.1 ALD sequence of Al_2O_3 deposition.

the surface coated with one layer of the organometallic precursor. After this, a second reactant is injected to react with the first one, forming the desired product layer. A last purging step is necessary to remove all byproducts and unreacted molecules. Those four steps combined, referred as an ALD cycle, can be repeated to grow a material layer by layer. With a proper adjustment of the experimental conditions, the ALD process occurs via saturated coverage steps and the growth is stable and the film thickness increase is constant in each deposition cycle. Moreover, ALD processes are generally performed in a rough vacuum of approximately 1 mbar. At this pressure, the inert carrier gas is in the viscous flow regime and can efficiently carry reactants and remove stagnant product gases in the reactor in a reasonable time.^[3] In this flow regime, molecules have a short mean free path and can diffuse into all pores of a structure and does not need line-of-sight to the substrate (compared to physical vapor deposition techniques). This allows conformal coating of high-aspect ratio nanostructures.

Nowadays, ALD is widely used in the microelectronics industry in the process fabrication of DRAM memories and transistors as it can deposit highly uniform and pinhole-free films with well-controlled thicknesses and high dielectric constants.^[4] ALD is also commonly used in the field of photovoltaic devices with numerous applications reported to date. For example, ALD is used to produce materials for back contact passivation, to tune the work function in organic solar cells, to deposit blocking layers to prevent recombination in dye-sensitized solar cells as well as creating light absorbing layers and to engineer electrical junction of solar cells.^[4,5] ALD was also explored to fabricate protective layers for photoabsorbers for photoelectrochemical water splitting in harsh conditions. For example, amorphous TiO₂ coatings are used to improve stability of various photocathodes and photoanodes, such as Cu₂O photocathodes and Si, GaAs or GaP photoanodes in acidic and alkaline electrolytes.^[6,7] Another application of ALD in the field of photoelectrochemical water splitting is the deposition of a subnanometric layer of Al₂O₃ as passivation layer against electron-hole recombination in surface trap-states on hematite photoanodes.^[8]

ALD has been used to deposit a wide range of mono- and bimetallic oxides, nitrides, sulfides, tellurides, carbides and arsenide materials. A few trimetallic oxides and nitrides were also reported.^[9] Despite a large amount of materials produced by ALD, only a few examples were studied as OER catalysts. Bent and coworkers studied in detail NiO_x, MnO_x as well as MnTiO_x bimetallic oxides fabricated by ALD for water oxidation.^[10-12] Li *et al.* reported a bifunctional

Co₉S₈ electrocatalyst deposited on carbon nanotubes for ORR and OER^[13] Moreover, ultrathin layers of CoO_x were deposited by ALD on the surface of hematite and bismuth vanadate photoanodes in order to increase their photoactivity. A submonolayer of CoO_x acting as OER catalyst was proposed by Riha *et al.* to enhance the photoelectrochemical performance of hematite and Lichterman *et al.* demonstrated the improvement of OER activity of bismuth vanadate when a thin layer of CoO_x (ca. 1 nm) was deposited on it.^[14,15]

In this chapter, we focus on synthesizing different transition metal oxides, such as CoO_x, VO_x, and FeO_x and combined them to yield mixed metal oxide catalysts such as CoVO_x, CoFeO_x and CoVFeO_x to evaluate their activity towards OER.

2.2 Atomic layer deposition system

2.2.1 Initial ALD setup

The atomic layer deposition system used in this chapter is a custom built ALD. Initially, the setup (represented in Figure 2.2) was made as a cold wall type ALD. Different precursors can be loaded in sampling cylinders that can be attached to the block manifold. This manifold is pierced with two separate distribution lines that go to the vacuum chamber. On this block manifold are mounted different pneumatic actuators (valves). These valves can be actuated for precise amounts of time in order to inject vapors of precursors into the distribution lines. Both the block and the precursor cylinders can be heated at desired temperatures. Nitrogen flows, regulated by mass-flow controllers (MFC), can be passed through the distribution lines in order to carry the precursor vapors to the vacuum chamber. Both lines are ended with showerhead tubes that deliver the vapors directly on top of substrates. A hot plate is mounted inside the vacuum chamber and allows to warm substrates. Moreover, a pressure sensor is connected to the vacuum chamber and the vacuum is obtained with a dry scroll pump. All component and parameters, such as heating elements, pump speed, actuation of valves and nitrogen flows can be controlled with a custom design software created with Labview software.

The vacuum chamber is made of a stainless steel cylinder with dimensions of 30 x 19 cm (diameter x height, volume of ca. 14 liters). The hot plate has a diameter of 13 cm and its temperature is regulated by a PID controller taking values from two k-type thermocouples. The block manifold contains 8 valves that can accommodate up to 8 precursor cylinders.

This initial configuration never fully worked and imperfections as well as malfunctions were noticed. For example, a major problem was a short circuit occurring randomly during deposition procedures. A small amount of current was leaking from one of the component, which had the consequence to switch off a residual current circuit breaker, thus stopping electricity supply. This

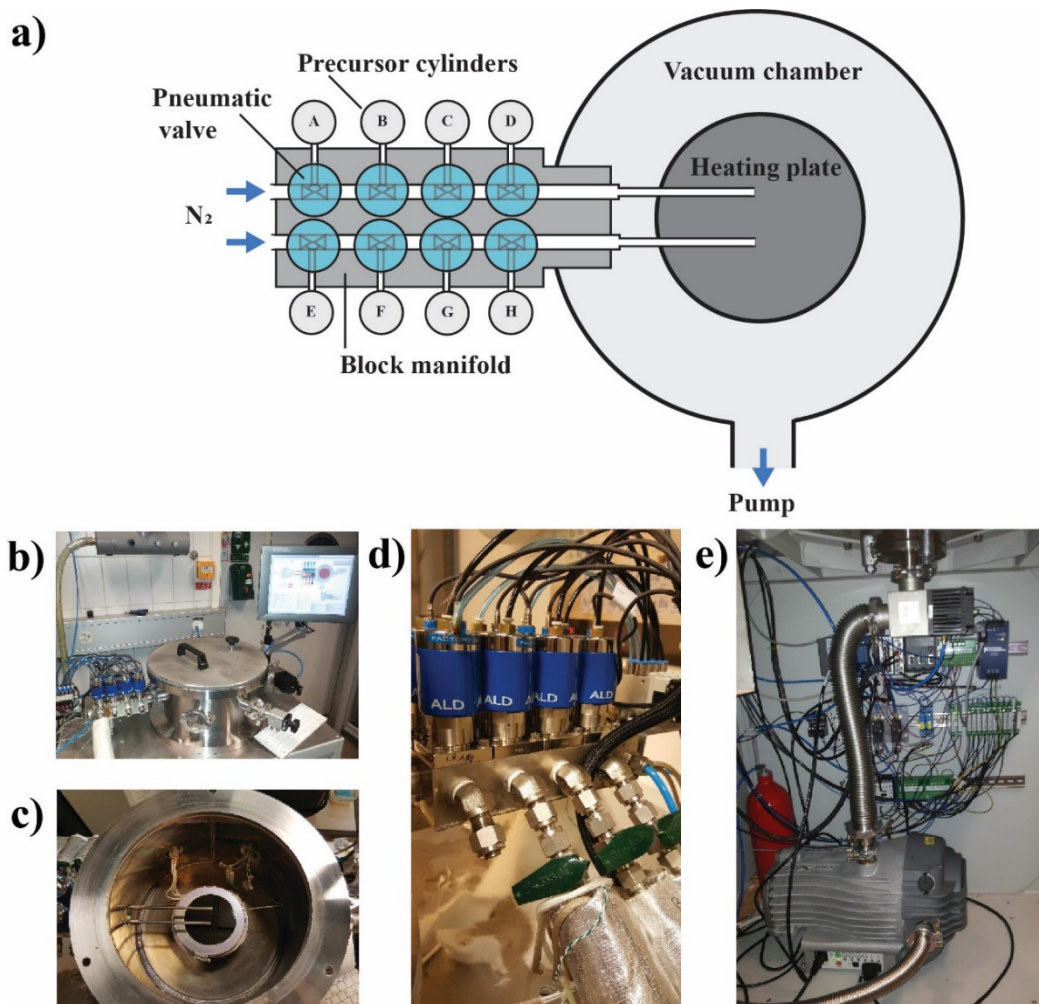


Figure 2.2 a) Top-down view of schematic of the custom-built cold wall ALD setup, b) Overall system, c) Vacuum chamber with heating plate, d) block manifold with pneumatic valves and precursor cylinders attached and e) electronic part and pump.

issue arose from a short circuit in the hot plate. During depositions, thin layers of oxides were seen to deposit on the ceramic insulation of the electrical resistance of the heating plate. These thin layers of oxides were making the ceramic slightly conductive and induced a small current leak from the electrical resistance to the metal vacuum chamber. Another issue with this ALD configuration was that the vacuum chamber was too large for the size of the headspace of the

precursor cylinders. This led to difficulty to efficiently saturate the chamber with precursor vapors. Only highly volatile metal organic compounds, such as trimethylaluminium, diethylzinc or titanium tetraisopropoxide could be used. However, the deposited films were not homogenous in thickness, depending on where the substrate was placed on the heated plate, due to the greater concentration of precursor vapors near the showerhead tubes. Precursors with lower vapor pressures, such as tetrakis(dimethylamino)titanium, needed to be heated to have usable vapors. However, thermal decomposition at a high temperature was noticed in those precursors, therefore making them unusable for our ALD configuration. Due to these limitations, a new ALD system configuration was built in this work.

2.2.2 Second ALD setup

In order to efficiently saturate the atmosphere of the vacuum chamber and also to reduce the purging step duration, the vacuum chamber size was decreased. It was replaced by a smaller tubular structure heated by an electrical resistance band wrapping (Figure 2.3). In addition, the software was modified to allow fast closing and opening of a valve that isolates the chamber from the pump during pulses, therefore increasing the exposure time of the substrates to the precursors. With this new configuration, films homogeneous in thickness, of TiO_2 , Al_2O_3 , ZnO and SnO_2

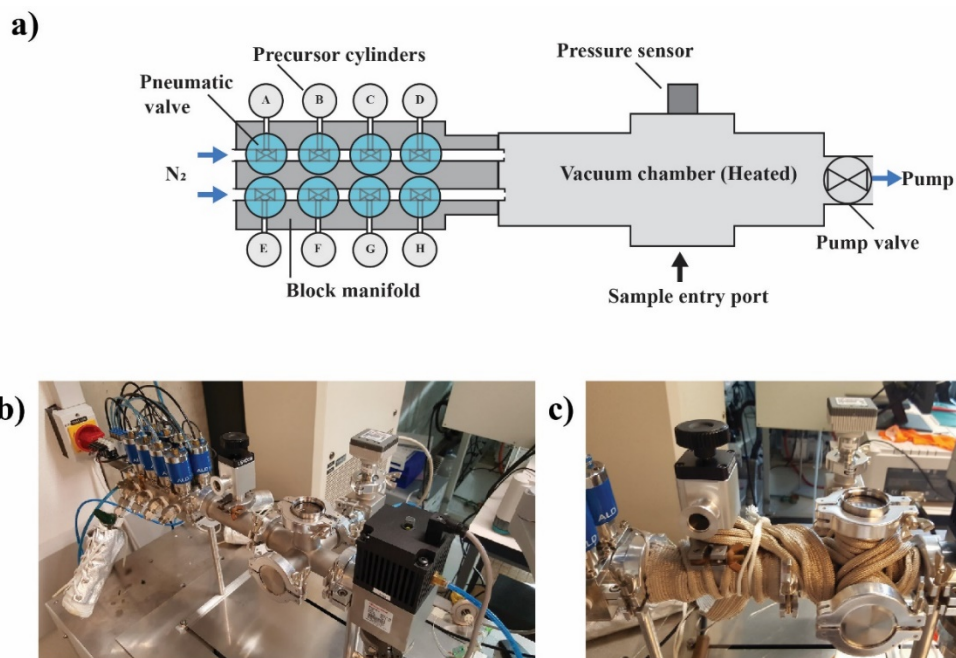


Figure 2.3 a) Top-down view of schematic of the hot wall ALD setup, b) overall system and c) vacuum chamber with heating element.

could be obtained. These oxides were deposited by using hydrogen peroxide (H_2O_2) as oxidant. For other oxide materials, such as cobalt, iron and nickel oxides, a stronger oxidant is required to oxidize their respective metal organic precursors. Thus, an ozone generator was interfaced to the ALD system (Figure 2.4 a). In order to produce an outlet gas stream with constant concentration of ozone, the ozone generator required an additional mass flow regulator as well as a storage cylinder to buffer the mismatch between sequential pulses of ALD depositions and continuous production of ozone from the generator. An ozone destruct element was added for safety considerations, in order to catalytically remove unused ozone. At last, to increase the amount of vapors from low-volatility precursors, a bubbler system was design and interfaced to the ALD setup (Figure 2.4 b,c).^[16] This device is composed of a pneumatic actuator, similar as the ones mounted on the block manifold, which can be opened for a precise amount of time in order to bubble a desired amount of nitrogen in metal organic precursors. The software was modified to allow simultaneous opening of the bubbler and manifold valves. The growth per cycle (GPC) rate of different monometallic oxides that can be deposited with our ALD system are shown in Figure

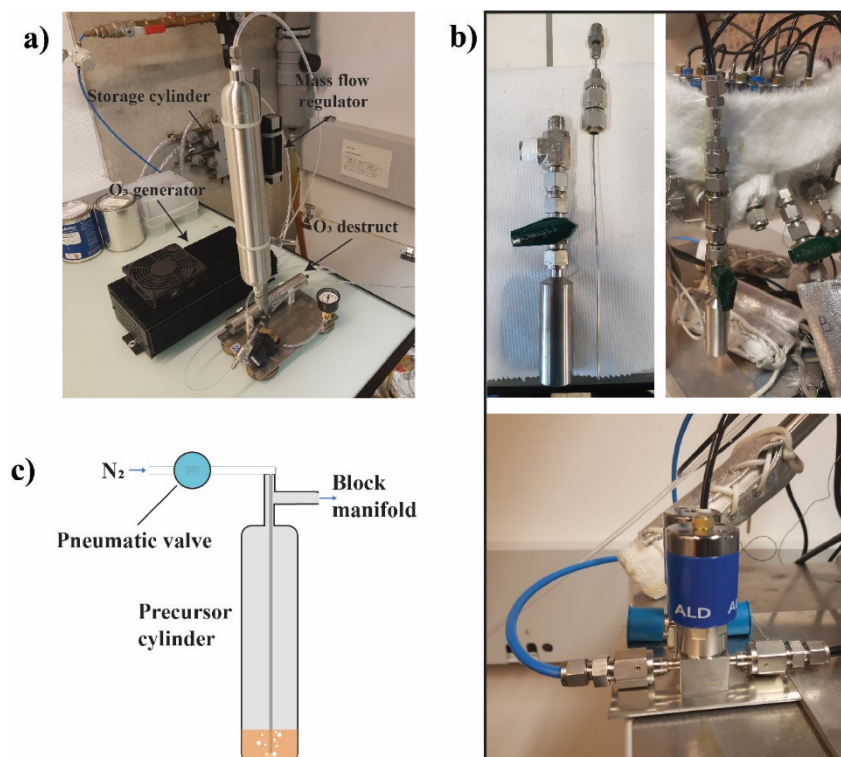


Figure 2.4 a) Ozone generator system with storage cylinder, mass flow regulator and ozone destruct element. b) Pictures of the bubbler system. c) Schematic of the bubbler system.

2.5 a-h. The precursors and conditions used for depositing the different oxides are summarized in Table 2.1. GPC values are in accordance with values reported in the literature for similar oxides deposited with the same precursors, except for VO_x which grows faster (GPC $0.058 \text{ nm cycle}^{-1}$) compared to a reported GPC of about $0.03 \text{ nm cycle}^{-1}$.^[17-23]

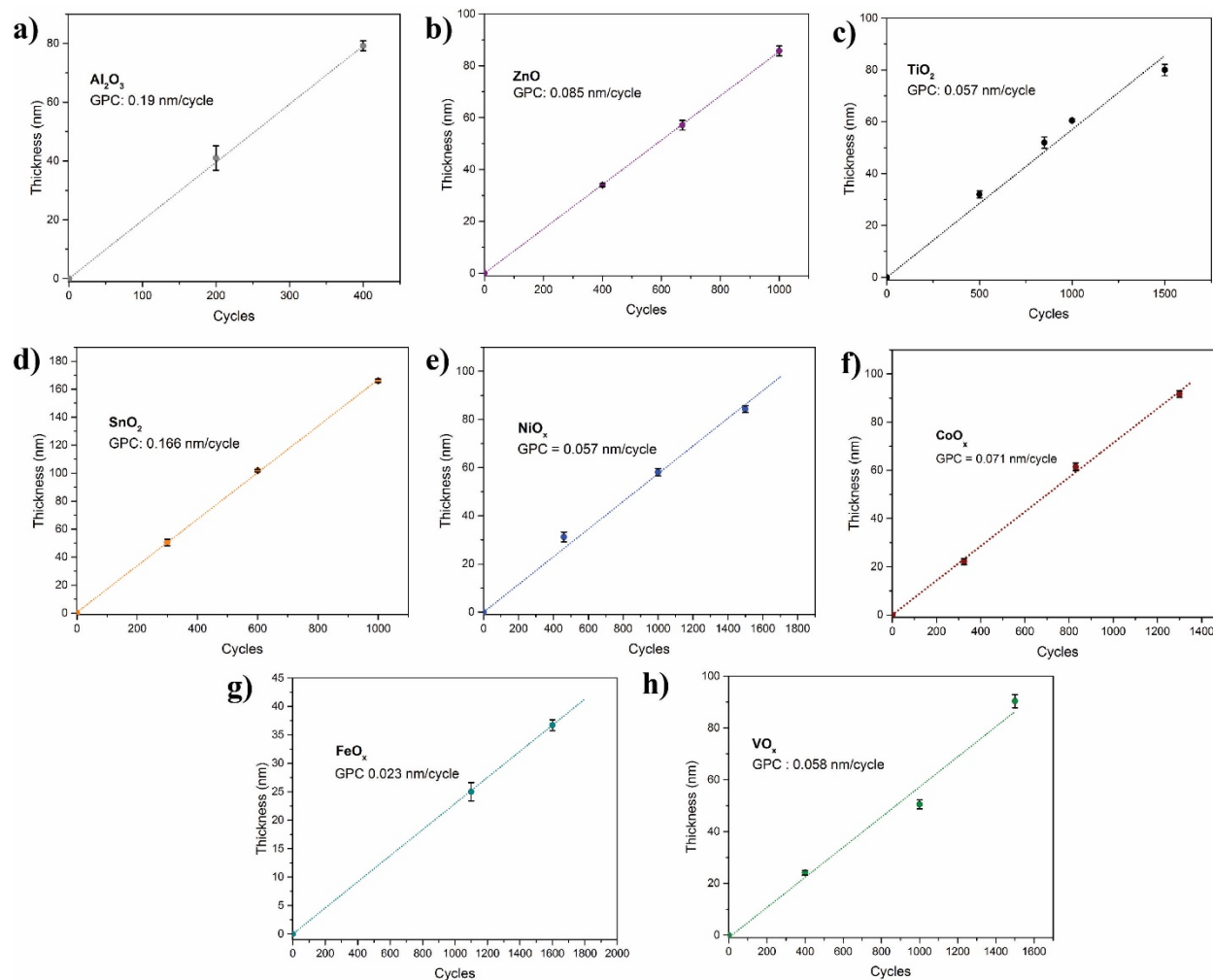


Figure 2.5 Growth per cycle rate (GPC) of **a)** Al_2O_3 , **b)** ZnO, **c)** TiO_2 , **d)** SnO_2 , **e)** NiO_x , **f)** CoO_x , **g)** FeO_x and **h)** VO_x deposited by ALD on Si (100) wafer substrates.

Table 2.1 Conditions used for the deposition and growth per cycle rate of TiO₂, Al₂O₃, ZnO, SnO₂, CoO_x, NiO_x, FeO_x and VO_x.

Material	Metal precursor	Bubbler needed	Oxidant	Chamber temperature [°C]	GPC [nm cycle ⁻¹]
TiO ₂	Tetrakis(dimethylamino)titanium	No	H ₂ O ₂	150	0.057
Al ₂ O ₃	Trimethylaluminium	No	H ₂ O ₂	130	0.190
ZnO	Diethylzinc	No	H ₂ O ₂	120	0.085
SnO ₂	Tetrakis(dimethylamino)tin	No	H ₂ O ₂	150	0.166
CoO _x	Dicarbonylcyclopentadienyl cobalt	No	O ₃	150	0.071
NiO _x	Bis(ethylcyclopentadienyl)nickel	Yes	O ₃	150	0.057
FeO _x	N,N-Dimethylaminomethylferrocene	Yes	O ₃	150	0.023
VO _x	Vandium oxytriisopropoxide	Yes	H ₂ O	150	0.058

2.3 ALD-deposited CoVO_x and CoFeO_x as OER catalysts

2.3.1 Approach to deposit mixed metal oxides

ALD deposition of ternary and quaternary materials has been widely studied in the past decade. Different strategies have been employed to produce multicomponent materials. The most common one is to use a "supercycle" approach that combines two or more binary ALD cycles of sequential precursor and co-reactant pulses (which produce monometallic materials) into a "cycle of cycles". An ALD supercycle can be defined as the minimum sequence of binary cycles that results in the deposition of a sublayer of the desired material within the total film. Because one ALD cycle deposits a submonolayer of material with a thickness generally smaller than 2 Å, supercycles with regular switching of binary cycles can produce compositionally uniform films. The properties and composition of the deposited film can be tailored by changing the cycle ratio (defined as the number of cycles of one binary process in the supercycle divided by the total amount of cycles in the supercycle) of one of the binary ALD cycle compared to the other inside the supercycle. Another parameter that can be used to control the composition is the bilayer period

(the number of ALD cycles in a supercycle). Short bilayer periods are often desired in order to deposit a well-mixed films and large bilayer periods can be used to produce multilayered materials. A second strategy to deposit mixed metal materials consists of pulsing all metal precursors at the same time. However, this co-dosing approach suffers from competitive adsorption of the two precursors when they have different reactivity on the substrate, thus making the control of composition difficult. Sequential dosing of multiple precursors one after the other without performing a co-reactant step in between, in an ABC-type cycle, is also used. Competitive adsorption is avoided in this approach but how much of the second precursor reacts with the surface depends on the interaction between the two precursors and the surface coverage of the first precursor. A last approach is to use precursors that contain multiple metal centers. A major drawback with this method is that the composition of the film is fixed by the structure of the precursor molecule.^[9]

Deposition of mixed metal materials is of tremendous importance in the field of OER catalysis as the most active OER catalysts are generally composed of mixed metal oxides.^[24] Several example of unary oxides, such as CoO_x , NiO_x and MnO_x , synthesized by ALD have been reported for OER so far. ^[10,12,14,25,26] However, despite a large library of bi- and tri-metallic oxides fabricated by ALD, mixed metal oxides applied as water oxidation catalysts remain rare.^[9] To our knowledge, only one example of binary Ti-Mn oxide system has been used as electrocatalyst for OER.^[11] Therefore, in the present work, we focused in synthesizing different mixed metal oxides by ALD and evaluated their OER activity. We used the supercycle approach in order to deposit CoFeO_x and CoVO_x , two highly active OER electrocatalysts as well as a trimetallic CoVFeO_x .^[24,27,28]

2.3.2 CoVO_x and CoFeO_x

CoVO_x and CoFeO_x were synthesized by using different ALD supercycles in order to modify the Co:V and Co:Fe ratio of the materials. The OER activity of oxide layers with a thickness of approximately 50 nm is shown in Figure 2.6. For CoFeO_x, the best activity, that is, an overpotential of 410 mV for 10 mA cm⁻², was reached when the ALD supercycle was composed of 1 cycle of CoO_x and 5 cycles of FeO_x (Figure 2.6 a). Other deposition supercycles yielded to films with slightly higher overpotentials. FeO_x was deposited as a control sample (supercycle: 0 cycle CoO_x + 1 cycle FeO_x in Figure 2.6 a). A lower OER activity was observed for this oxide than for CoFeO_x.

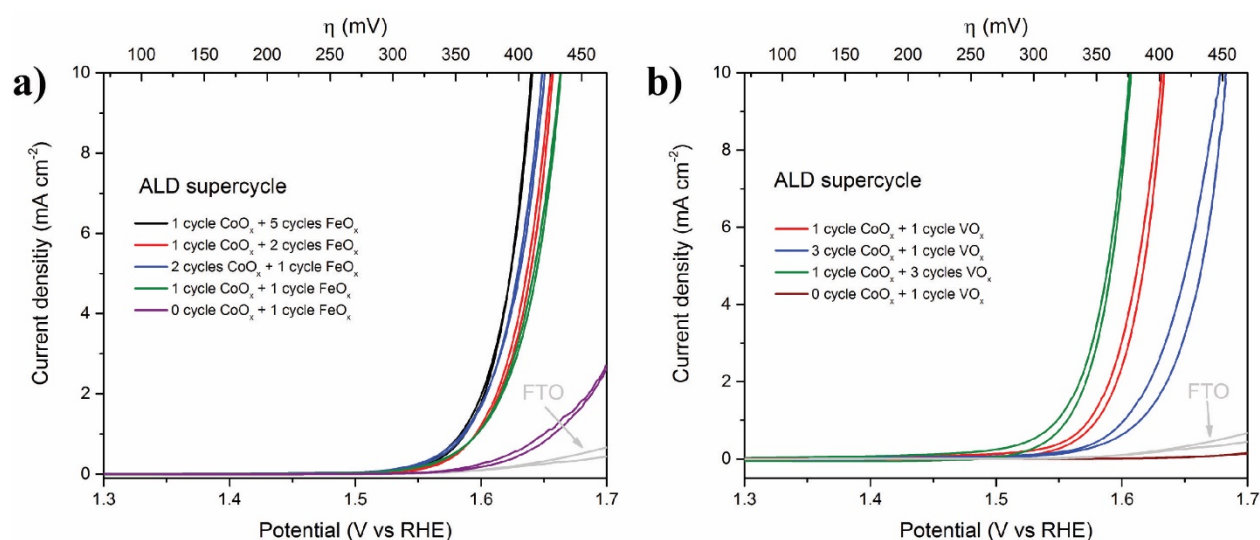


Figure 2.6 Polarization curves in 1 M KOH of **a)** CoFeO_x and **b)** CoVO_x (thickness 50 nm) deposited with different ALD supercycles on FTO. Scan rate: 10 mV s⁻¹, iR drop corrected.

For CoVO_x, different supercycle depositions yielded films with larger differences in activity compared to CoFeO_x films (Figure 2.6 b). The optimized deposition (supercycle: 1 cycle CoO_x + 3 cycles VO_x in Figure 2.6 b) gave a film with an overpotential of 375 mV at 10 mA cm⁻². A control sample of VO_x was also deposited (supercycle: 0 cycle CoO_x + 1 cycle VO_x in Figure 2.6 b). The observed OER activity of this material is lower than the FTO substrate. Therefore, VO_x is not active towards OER.

The influence of different supercycles on the composition of the deposited mixed metal oxides was probed. As CoO_x, VO_x and FeO_x have different GPC rates (Table 2.1), we do not expect the composition of CoFeO_x and CoVO_x to be proportional to the cycle ratios of the two unary oxides used in the supercycles. Instead, the concentration of each metal ion can be estimated by

the rule of mixture (ROM) represented in Eq. 2.1,^[11] where α_{Co} and α_X are the GPC rate of CoO_x and the second metal oxide (VO_x or FeO_x) and β_{Co} and β_X are the fraction of cycles of CoO_x and the second metal oxide (VO_x or FeO_x) in the supercycle, respectively. Figure 2.7 shows the comparison between the estimated Co content (by the ROM) and the Co content determined by XPS of $CoFeO_x$ and $CoVO_x$ deposited with different supercycles.

$$\%Co_{ROM} = \frac{\alpha_{Co} \beta_{Co}}{\alpha_{Co} \beta_{Co} + \alpha_X \beta_X} \times 100 \quad (\text{Eq. 2.1})$$

For $CoFeO_x$ (Figure 2.7 a), the Co concentration determined by XPS largely deviated from the values estimated from the ROM. Moreover, different cycle ratios of CoO_x/CoO_x+FeO_x yielded a similar content of Co (50 to 60 %). For $CoVO_x$ (Figure 2.7 b), although the Co concentrations increased with an increase in the cycle ratios of CoO_x over $CoO_x + VO_x$, the Co concentrations determined by XPS were greater than the values estimated from the ROM. According to depth profiles (vide infra), the surface and bulk concentrations of metals are similar for both $CoFeO_x$ and $CoVO_x$. The origins of the deviation from compositions estimated by ROM remain unclear. It is likely that the growth rates of a unary metal oxide vary substantially depending on the nature of the underlying layers. These results indicate that the development and precise control of the compositions of mixed metal oxides are challenging. Previous reports also showed that the

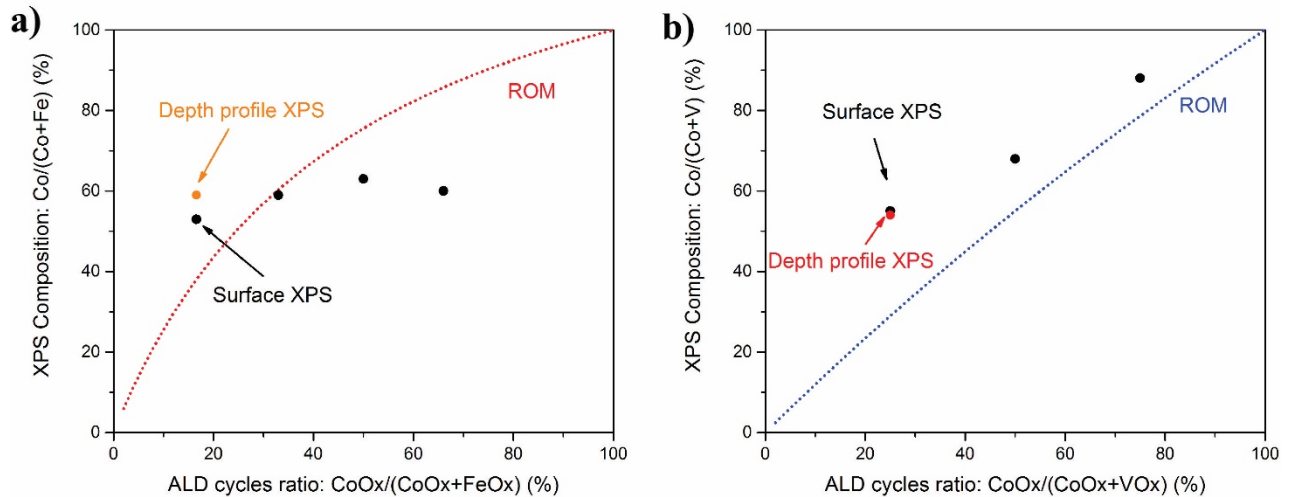


Figure 2.7 Comparison between the XPS Co content (dots) and the theoretical one obtained from the rule of mixture (Eq. 2.1) for **a)** $CoFeO_x$ and **b)** $CoVO_x$ deposited with different ALD supercycles. Depth profile data points are an average of the Co concentrations from Figure 2.8 e,f between etching depths from 6.5 and 120 nm for $CoFeO_x$ and from 6.5 and 50 nm for $CoVO_x$.

composition of bimetallic materials fabricated by ALD deviated from the targets due to a variety of factors such as precursor ligand interactions and nucleation effects.^[9]

XPS compositions were obtained from surface XPS analysis. In order to verify if the composition was the same in the bulk and at the surface of these oxides, XPS depth profiling was performed. Depth profile of the Co 2p, Fe 2p and V 2p regions of CoFeO_x and CoVO_x are represented in Figure 2.8 a-d. No increase in intensity is observed among the spectra acquired at different moments during the Ar ion etching, indicating no major changes in the compositions throughout the depth of the materials. Thus both CoFeO_x and CoVO_x can be considered as a single phase material. For CoFeO_x, the Co:Fe ratio is constant in the bulk up to a sputter depth of approximately 120 nm (Figure 2.8 e). Below a sputter depth of approximately 10 nm, carbon was observed, indicating adventitious carbon contamination at the surface of CoFeO_x.^[29] At sputter depths higher than 120 nm, Sn from the underlying FTO substrate appeared. For CoVO_x, constant Co and V concentrations were observed up to a sputter depth of 50 nm (Figure 2.8 f). Adventitious carbon was also observed at the surface and residual carbon contamination of a few atomic percent (<5 nm) was even visible in the bulk of CoVO_x. At a sputter depth higher than 60 nm, Sn from the FTO substrate appeared. We note that the sputter depth is estimated by the etching rate of the XPS instrument calibrated with SiO₂, so this depth is not an accurate measure of the thickness of the ALD deposited oxides, since every material has a different etching speed.^[30] The GPC rates of CoVO_x and CoFeO_x are shown in Figure 2.9 a,b. For CoVO_x, the growth rate (per supercycle composed of 1 cycle CoO_x + 3 cycles VO_x) is 0.263 nm supercycle⁻¹. This growth rate should be equal to a linear combination of the GPC of the unary constituents of this material (1 x GPC (CoO_x) + 3 x GPC (VO_x)). By taking GPC values of 0.071 and 0.058 nm cycle⁻¹ for CoO_x and VO_x, respectively, we estimated a theoretical growth rate of CoVO_x of 0.245 nm supercycle⁻¹. The estimated value is slightly lower than the experimental one. For CoFeO_x, the experimental growth rate per supercycle is 0.257 nm supercycle⁻¹ (Figure 2.9 b), which is significantly higher than the 0.186 nm supercycle⁻¹ predicted by adding the growth rates of CoO_x and FeO_x alone. The differences between experimental and predicted growth rates again suggest that the growth rates of these unary oxides depend on the nature of the underlayers (FTO vs. another oxide).

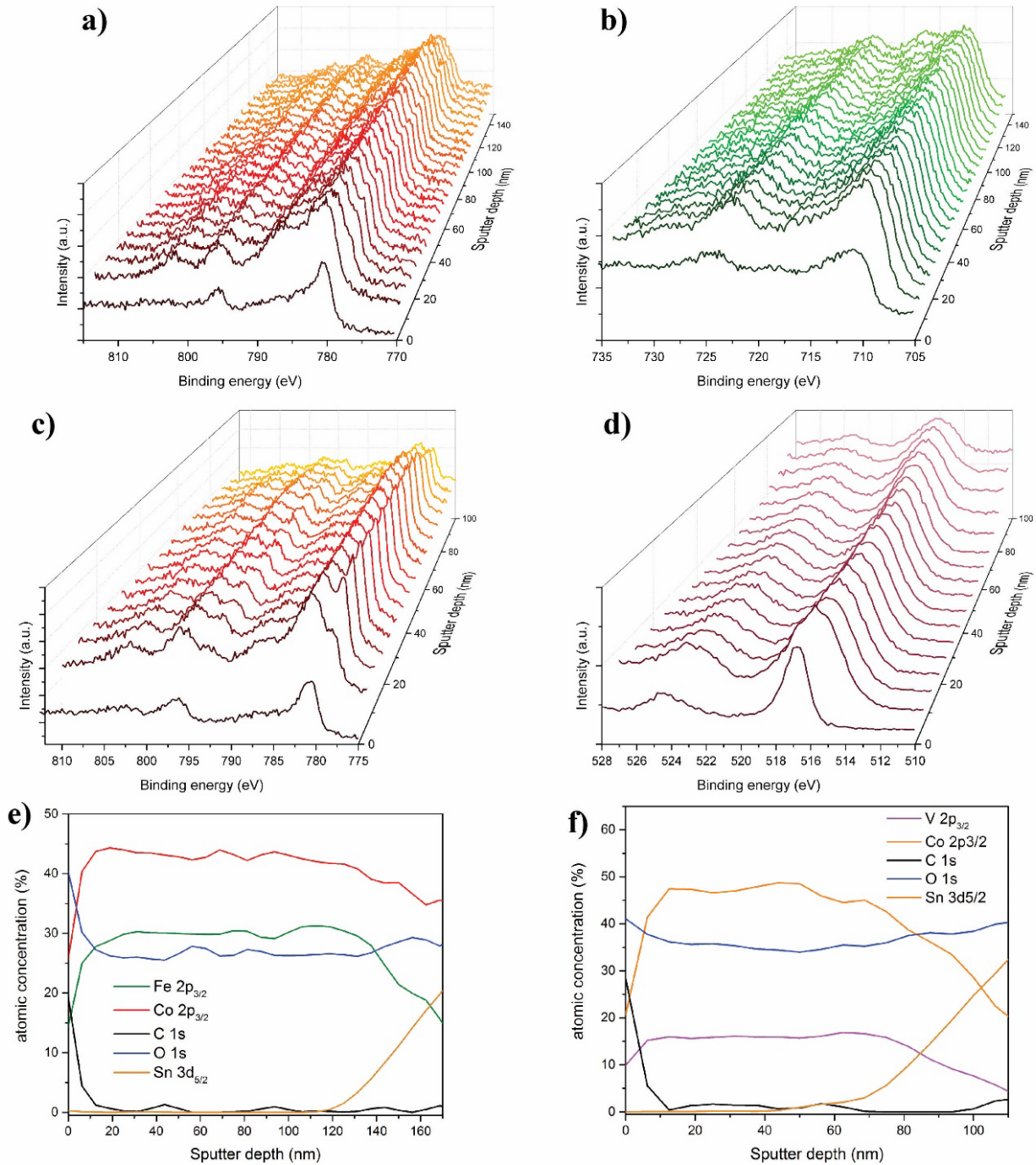


Figure 2.8 Ar sputter XPS depth profiles of **a)** Co 2p region and **b)** Fe 2p region of CoFeO_x. Ar sputter XPS depth profile of **c)** Co 2p region and **d)** V 2p region of CoVO_x. **e)** Atomic concentrations of Fe, Co, C, O and Sn in CoFeO_x layer deposited on FTO. **f)** Atomic concentrations of V, Co, C, O and Sn in CoVO_x layer deposited on FTO.

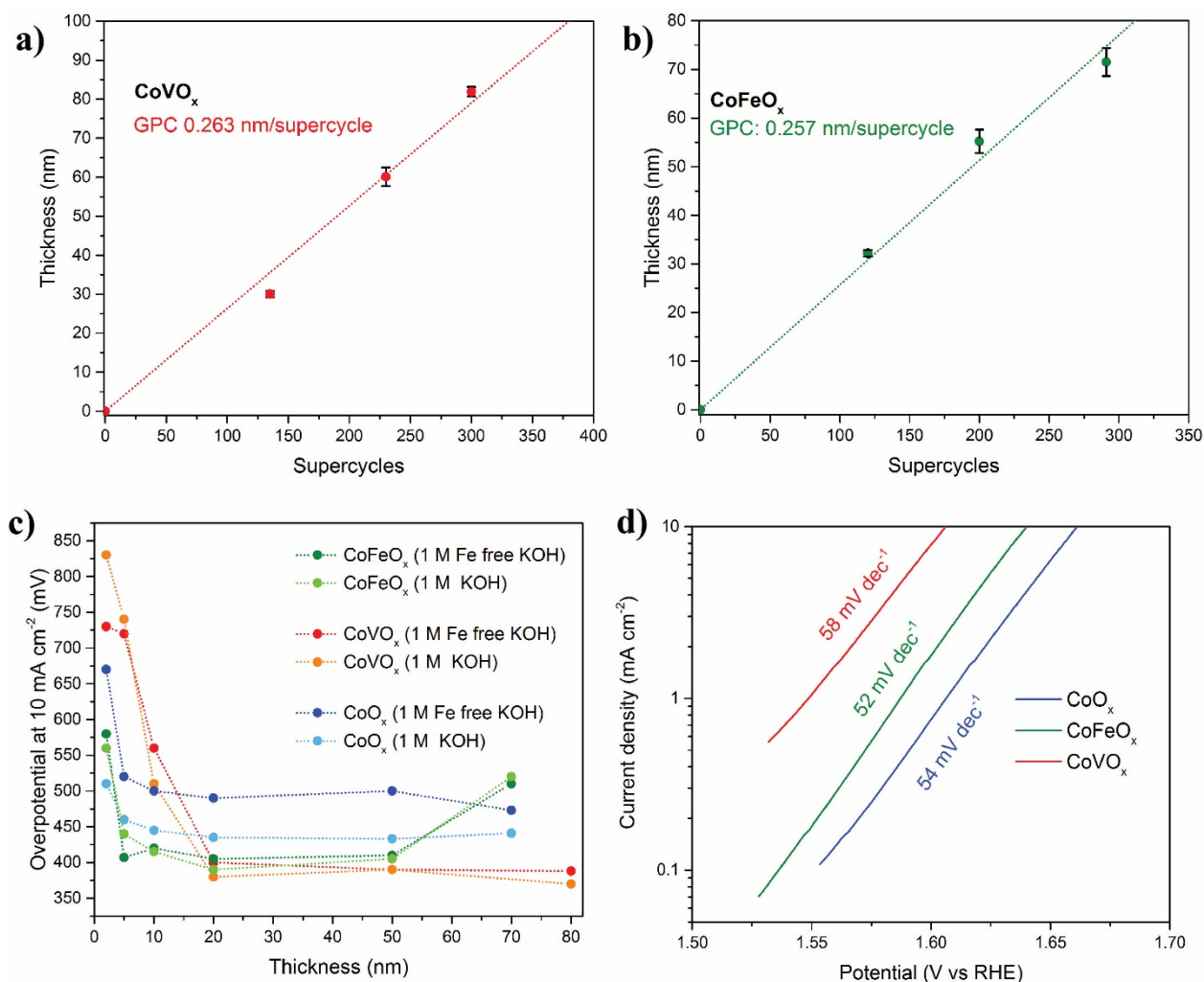


Figure 2.9 Growth rate per cycle of **a)** CoVO_x and **b)** CoFeO_x. **c)** Overpotentials at 10 mA cm⁻² in 1 M KOH and 1 M Fe free KOH of CoO_x, CoFeO_x and CoVO_x with different thicknesses. **d)** Tafel slopes of CoO_x, CoFeO_x and CoVO_x with a thickness of 50 nm on FTO in 1 M KOH.

The OER activity of ALD-deposited CoFeO_x and CoVO_x films on FTO with various thicknesses was determined in 1 M KOH and 1 M Fe free KOH (Figure 2.9 c). Control samples of unary CoO_x were also investigated. A minimum thickness of approximately 10 nm is found for CoO_x and CoFeO_x to reach their optimal OER catalytic activity, while a minimum thickness of about 20 nm is found for CoVO_x. The activity of all three materials plateaus at larger thickness. This saturation can be explained by the fact that ALD films are compact and only the surface layers are in contact with the electrolyte. After a minimum thickness, increasing the thickness and loading of catalysts has no effect for the overall OER activity. At thicknesses higher than 50 nm, the activity of CoFeO_x starts to decrease due to an increased resistance of the material layer.^[28] This increase in resistance is not observed for CoO_x and CoVO_x with a thicknesses of up to 70 and 80

nm. The CoO_x control samples with a thickness of 20 nm have overpotentials of 490 and 435 mV in 1 M Fe free KOH and 1 M KOH, respectively. The higher activity in normal KOH electrolyte is due to incorporation of Fe ions which exist as a trace impurity in commercial KOH electrolyte.^[31] For both CoVO_x and CoFeO_x , the OER activity is not strongly influenced by the presence of Fe ions in the KOH electrolyte. For a film of 20 nm, CoFeO_x provides 10 mA cm^{-2} at 400 and 380 mV overpotential in 1 M Fe free KOH and 1 M KOH, respectively. An analogous CoVO_x film has overpotentials of 400 and 390 mV in 1 M Fe free KOH and 1 M KOH, respectively. Tafel slopes (Figure 2.9 d) are 54, 52 and 58 mV dec^{-1} in 1 M KOH for CoO_x , CoFeO_x and CoVO_x , respectively.

XPS was used to characterize CoVO_x and CoFeO_x (Figures 2.10 and 2.11). Co is present in CoVO_x as Co^{2+} , as suggested by the binding energy (BE) of 780.5 eV (Figure 2.10 a). Moreover, outer-shell excitation satellite peaks are present at higher BE, indicating high spin Co^{2+} .^[32] Two signals at BE of 530.0 and 531.3 eV are representative of O^{2-} in oxide and hydroxide (Figure 2.10 b). Vanadium exists as V^{5+} and V^{4+} species as indicated by the two peaks at 517.2 and 516.5 eV, respectively (Figure 2.10 c).^[33,34] Additionally, a difference between surface and bulk spectra at the Co 2p region is observed (Figures 2.8 a and c). After deconvolution of the Co 2p region, a peak at 790.0 eV appears for the material etched by Ar ions. This signal, characteristic of metallic Co atoms, probably arises from reduction of Co^{2+} by Ar ions which are known to induce chemical transformations and reduction of metal oxides during the etching process.^[35,36] For this reason, in order to avoid parasitic chemical changes by Ar sputtering, qualitative characterization was done by surface XPS for both CoFeO_x and CoVO_x . XPS spectra of CoFeO_x are shown in Figure 2.11. Co is present in this oxide as Co^{2+} , as indicated by the peak at BE of 780.1 eV. A Fe Auger LMM signal is visible in the Co 2p region at BE of 784.4 eV. In the Fe 2p region, a signal at 710.5 eV indicates Fe^{3+} . In the O 1s region, signals at 529.5 and 531.3 eV are representative of O^{2-} in metal oxide and hydroxide, respectively.^[33]

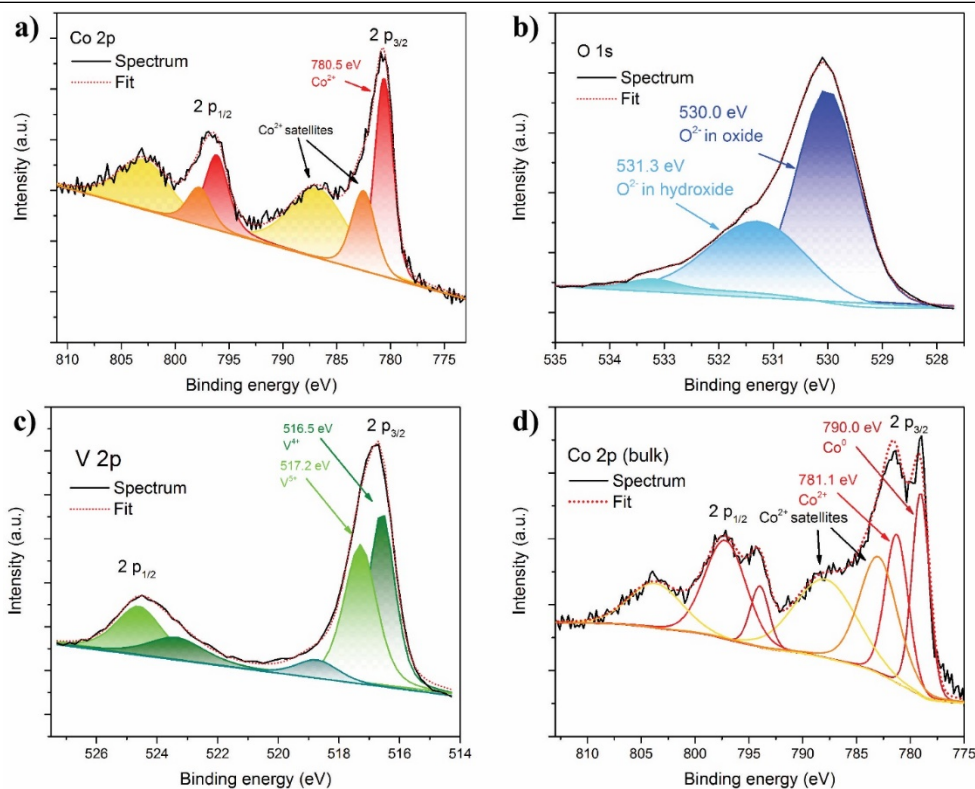


Figure 2.11 Surface XPS spectra of CoVO_x deposited on FTO of **a)** Co 2p region, **b)** O 1s region and **c)** V 2p region. **d)** High resolution spectrum of Co 2p region in the bulk of CoVO_x acquired at a sputter depth of 20 nm.

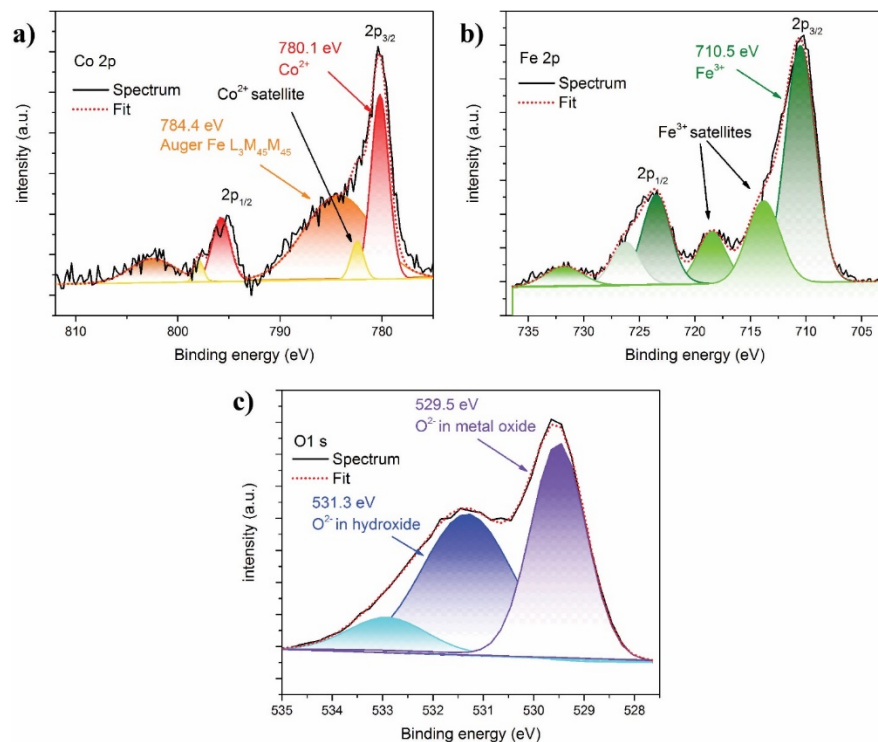


Figure 2.10 Surface XPS spectra of CoFeO_x deposited on FTO with high resolution spectra of **a)** Co 2p region, **b)** Fe 2p region and **c)** O 1s region.

X-ray diffraction (XRD) was performed to investigate the crystalline composition of CoVO_x and CoFeO_x . Figure 2.12 shows the XRD spectra of CoFeO_x and CoVO_x as well as CoO_x , FeO_x and VO_x deposited on Si (100) wafer substrates. Si (100) substrates were used as they only show one sharp diffraction peak at 33° which is related to the Si (200) plane (Figure 2.12 f). When CoFeO_x is deposited by ALD, crystalline features are visible on its XRD spectrum (Figure 2.12 a) which can be attributed to $\text{Co}_4(\text{CO})_{12}$ (JCPDS 01-089-8209). CoVO_x is X-ray amorphous as seen with the absence of diffraction peaks in Figure 2.12 b. Among the unary metal oxides, only CoO_x has crystallinity that can be attributed to Co_3O_4 (JCPDS 00-001-1152) (Figure 2.12 c). FeO_x and VO_x are amorphous (Figure 2.12 d,e).

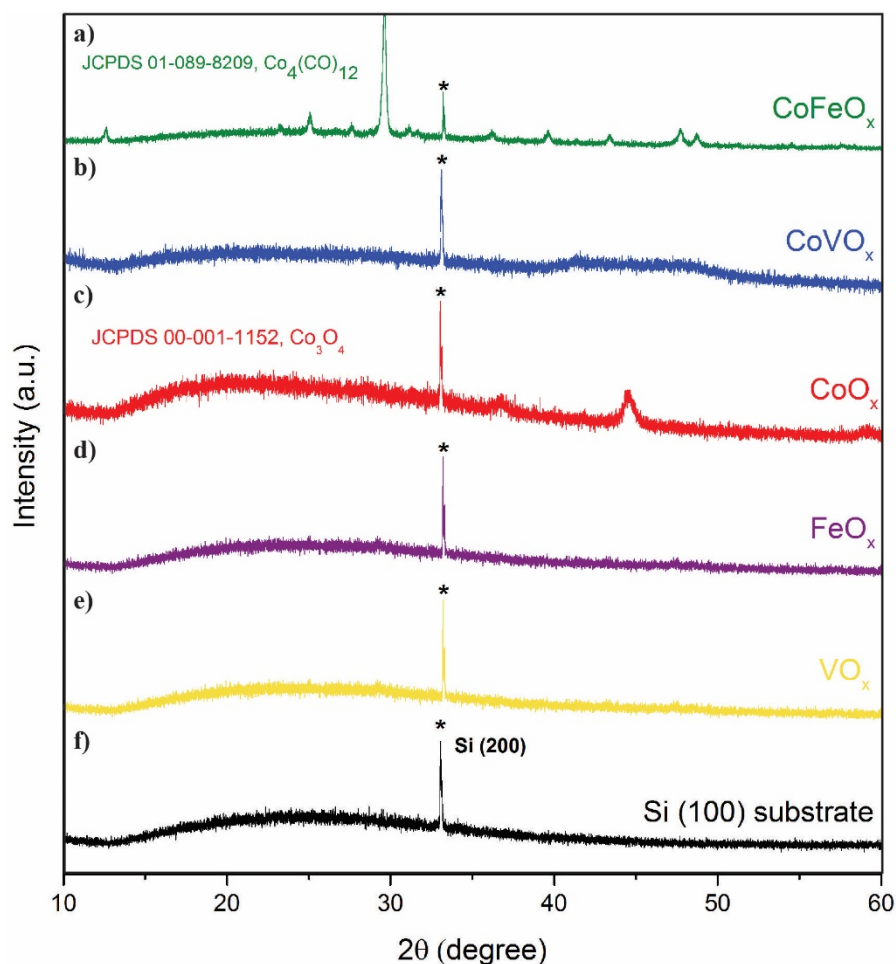


Figure 2.12 XRD patterns of a) CoFeO_x , b) CoVO_x , c) CoO_x , d) FeO_x , e) VO_x deposited on f) Si (100) wafer substrates.

CoFeO_x and CoVO_x were further deposited on nickel foam (NF) in order to increase the surface areas of these catalysts. The OER activity of both materials as well as a control CoO_x are shown in Figure 2.13 a. CoVO_x reaches 10 mA cm² at an overpotential of 310 (315) mV in 1 M KOH (1 M Fe free KOH). The CoO_x control provides the same current density at 320 (315) mV. Bare nickel foam has an overpotential of 330 (360) mV in the same electrolytes. Therefore, CoVO_x only brings a moderate 10 mV decrease in overpotential in 1 M KOH compared to the CoO_x control sample and a 20 mV decrease in overpotential compared to nickel foam. For CoFeO_x deposited on nickel foam, an overpotential of 235 (240) is required for 10 mA cm². This activity compares favorably with that of other recently reported cobalt iron oxides deposited on nickel foam.^[28,37] This result demonstrates that ALD is a suitable deposition technique to fabricate high-performance anode electrodes. Tafel slopes of catalysts supported on nickel foam are shown in Figure 2.13 b. CoO_x has Tafel slopes of 98 and 108 mV dec⁻¹ in 1 M KOH and 1 M Fe free KOH, respectively. CoVO_x has Tafel slopes of 68 and 74 mV dec⁻¹ and CoFeO_x has Tafel slopes of 52 and 54 mV dec⁻¹ in 1 M KOH and 1 M Fe free KOH, respectively. Moreover, CoVO_x and CoFeO_x are stable during 20h at a fixed current density of 10 mA cm⁻² (Figure 2.13 c) and the faradaic efficiency for both catalysts is close to 100 % (Figure 2.13 d and e).

The surface morphology of both CoFeO_x and CoVO_x deposited on nickel foam was investigated by SEM. After ALD deposition, both catalyst layers are flat and cover conformally the nickel foam substrate (Figure 2.14 a and c). After polarization at 10 mA cm⁻² for 20 h in 1 M Fe free KOH, changes in morphology are visible for both CoFeO_x and CoVO_x (Figure 2.14 b and d). The surface structure of CoFeO_x remains flat with little asperities (inset in Figure 2.14 b) but large cracks in the micrometer range are visible on the surface of the nickel foam. For CoVO_x, a rearrangement of the surface morphology occurs (inset in Figure 2.14 d) with cracks in the nanometer range and visible nanoparticles covering the surface. Larger cracks in the micrometer range are also visible on the surface of the nickel foam, which probably arise from the oxidation of nickel foam in harsh alkaline conditions during anodic polarization, thus producing a thick layer of nickel oxide that forms cracks during OER (Figure 2.14 d).

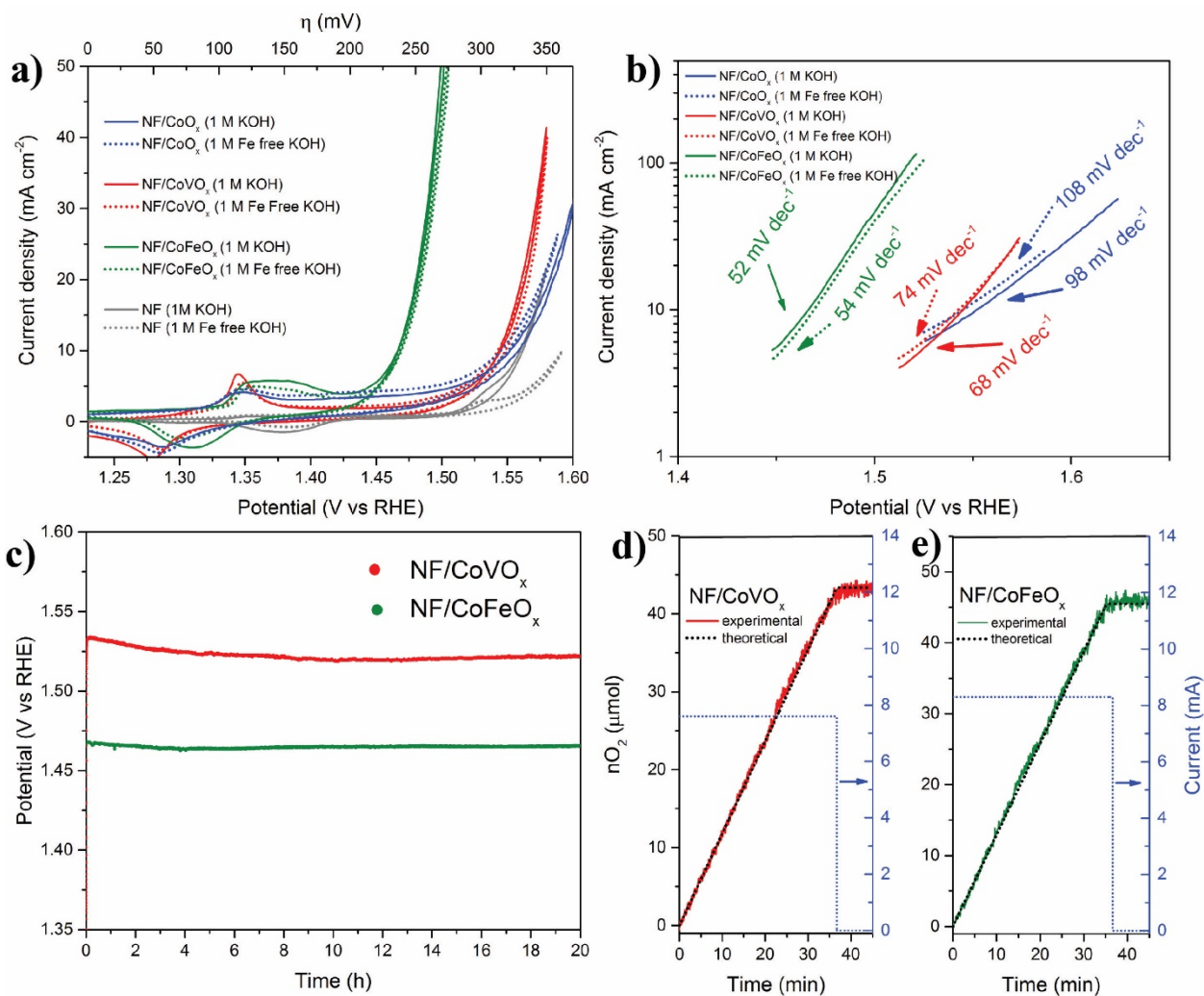


Figure 2.13 **a)** Polarization curves in 1 M KOH and 1 M Fe free of CoO_x, CoVO_x and CoFeO_x (thickness 50 nm) deposited on nickel foam (NF). Scan rate: 1 mV s^{-1} , iR drop corrected. **b)** Tafel slopes in 1 M KOH and 1 M Fe free KOH of CoO_x, CoVO_x and CoFeO_x on nickel foam. **c)** Stability of CoVO_x and CoFeO_x (thickness 50 nm) on nickel foam at 10 mA cm^{-2} in 1 M Fe free KOH, iR drop corrected. **d)** Predicted and measured number of moles of O₂ produced by NF/CoVO_x (area 0.76 cm^2) in 1 M Fe free KOH. **e)** Predicted and measured number of moles of O₂ produced by NF/CoFeO_x (area 0.83 cm^2) in 1 M Fe free KOH.

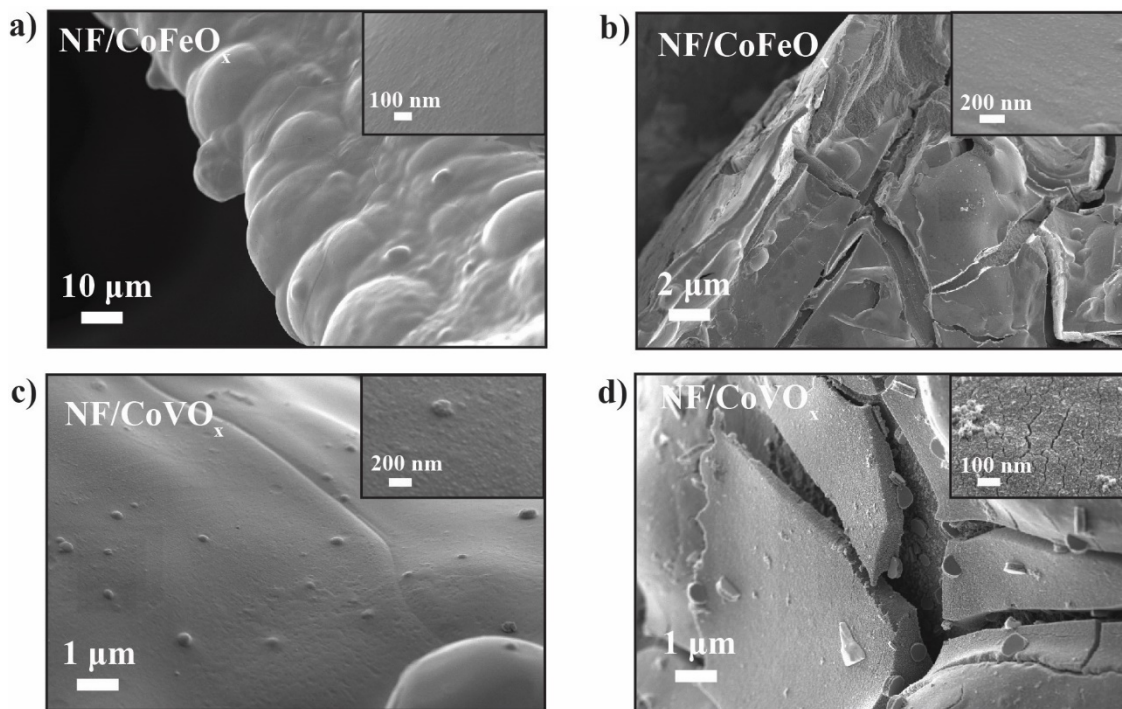


Figure 2.14 a) SEM images of CoFeO_x on nickel foam before polarization in 1 M Fe free KOH. b) SEM images of CoFeO_x on nickel foam after polarization in 1 M Fe free KOH. c) SEM images of CoVO_x on nickel foam before polarization in 1 M Fe free KOH. d) SEM images of CoVO_x on nickel foam after polarization in 1 M Fe free KOH.

2.4 Trimetallic oxides as OER catalysts

Trimetallic oxides can potentially surpass bimetallic compounds in OER activity. However, only a few examples of trimetallic OER catalysts have been developed due to the difficulty to circumvent undesirable phase segregation.^[38-40] Gao *et al.* recently proposed trimetallic V-Co-Fe oxide nanoparticles as an efficient and stable electrocatalyst for water oxidation.^[39] As we already developed procedures for depositing CoO_x, VO_x and FeO_x by ALD, we decided to deposit CoVFeO_x by ALD.

The OER activity of CoVFeO_x deposited with different supercycles procedures is represented in Figure 2.15 a. Gao *et al.* reported that mixing Fe in the lattice of CoVO_x could improve its catalytic activity.^[39] For this reason, we only varied the number of cycles of FeO_x in the deposition supercycles, while keeping the numbers of cycles of CoO_x and VO_x at 1 each in the supercycles. The composition of these oxides was analyzed by XPS and the content of Co, Fe and

V in these materials is shown in Table 2.2. In all three samples, the ratio between Co and V is close to 1:1 and the Fe content increases with the number of FeO_x cycles used in the supercycles. This result shows that ALD is indeed suitable to deposit trimetallic oxides.

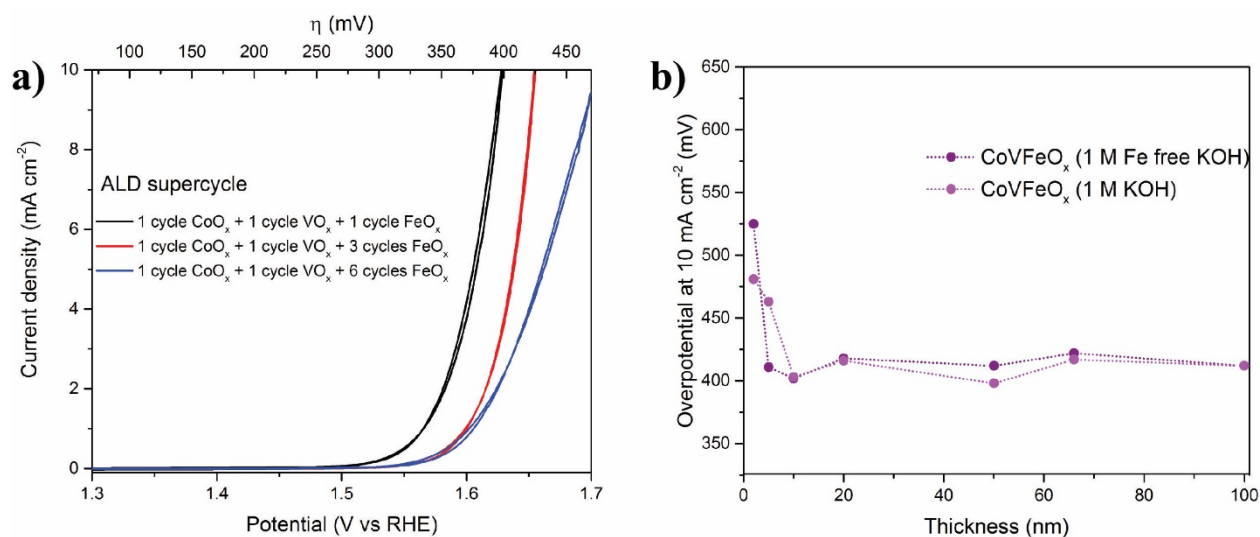


Figure 2.15 a) Polarization curves in 1 M KOH of CoVFeO_x deposited on FTO with different supercycles. **b)** Overpotentials at 10 mA cm^{-2} in 1 M KOH and 1 M Fe free KOH of CoVFeO_x with different thicknesses on FTO.

Table 2.2 XPS composition of Fe, Co and V in CoVFeO_x layers deposited by different supercycle procedures on FTO.

Deposition supercycle	Fe content (atomic %)	Co content (atomic %)	V content (atomic %)
1 cycle CoO_x + 1 cycle VO_x + 1 cycle FeO_x	6	51	43
1 cycle CoO_x + 1 cycle VO_x + 3 cycles FeO_x	35	31	34
1 cycle CoO_x + 1 cycle VO_x + 6 cycles FeO_x	41	30	29

The best OER activity was obtained with the deposition consisting of 1 cycle of CoO_x followed by 1 cycle of VO_x and 1 cycle of FeO_x . This deposition was chosen for all further experiments. Films with thicknesses between 2 and 100 nm were evaluated (Figure 2.15 b). A minimum thickness of ca. 10 nm is necessary in order to reach optimal activity. The activity of CoVFeO_x plateaus at higher film thickness, similar to that of CoFeO_x and CoVO_x . At a thickness

of 20 nm, 10 mA cm^{-2} is reached at an overpotential of 420 mV in both 1 M KOH and 1 M Fe free KOH electrolytes. The activity is inferior to that of CoFeO_x and CoVO_x on FTO.

The CoVFeO_x material was characterized by XRD (Figure 2.16). Only a sharp peak at 33° coming from the Si (200) plane of the underlying substrate is visible, therefore indicating that CoVFeO_x is X-ray amorphous.

XPS was performed to characterize CoVFeO_x , (Figures 2.17). As suggested by the binding energy (BE) of 790.8 eV, Co is present as Co^{2+} (Figure 2.17 a). Fe is present Fe^{3+} as suggested by the peak at BE of 711.5. Vanadium is presented as V^{5+} and V^{4+} species, indicated by the two signals at 518.3 and 516.8 eV, respectively (Figure 2.17 c).^[33,34] Two signals at BE of 529.8 and 530.8 eV are representative of O^{2-} in oxide and hydroxide, respectively (Figure 2.17 d).^[33]

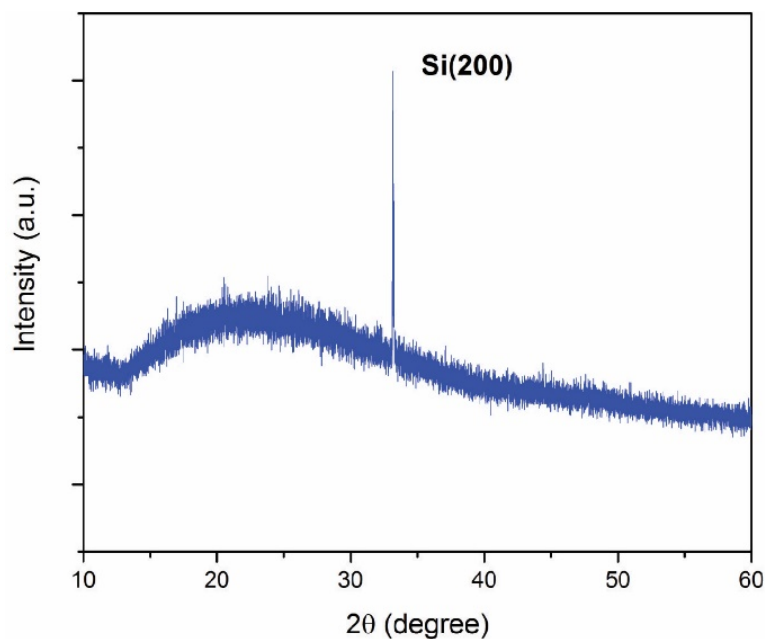


Figure 2.16 XRD pattern of CoVFeO_x on Si (100) substrate

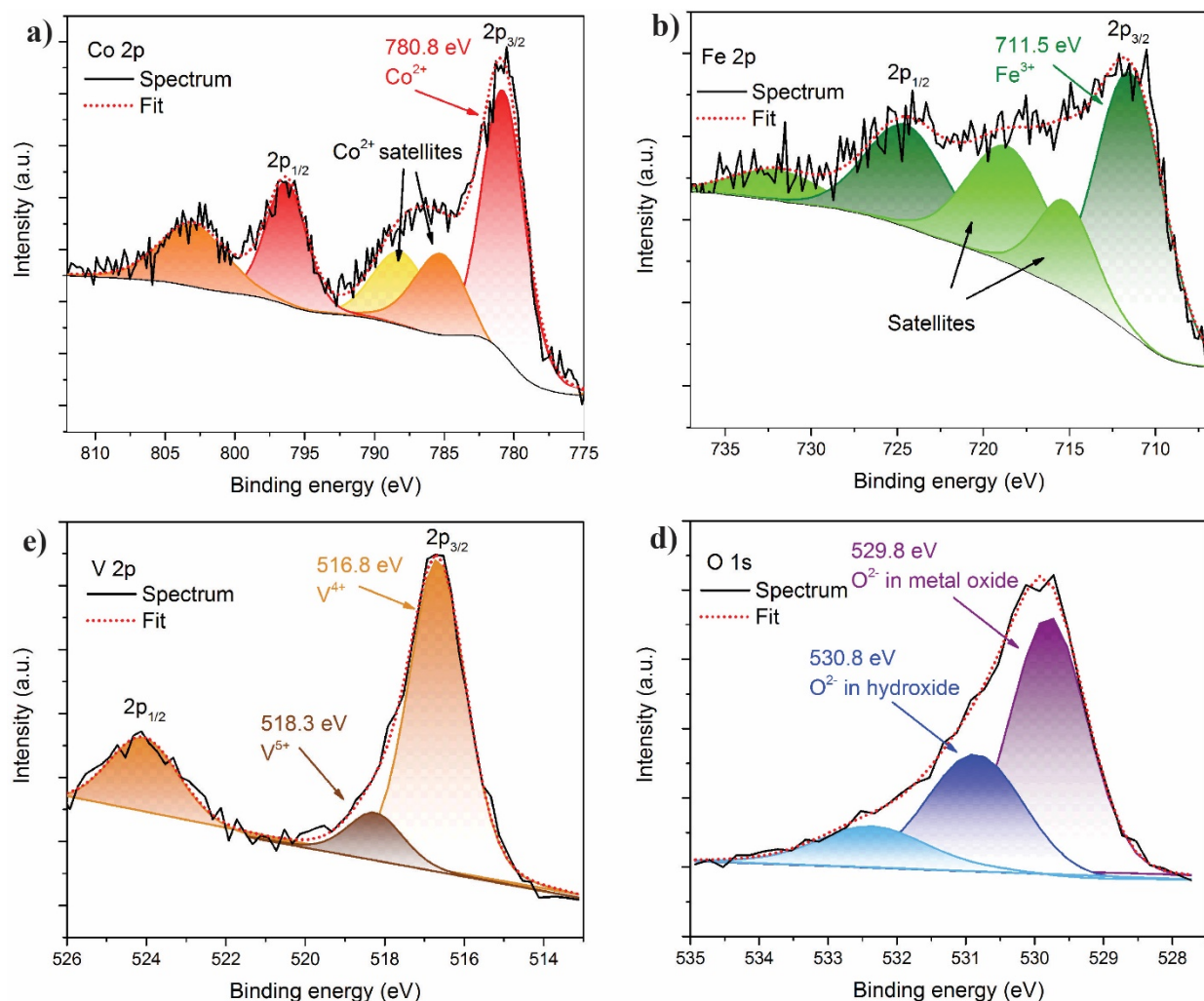


Figure 2.17 Surface XPS spectra of CoVFeO_x deposited on FTO with high resolution spectra of **a)** Co 2p region, **b)** Fe 2p region and **c)** V 2p region and **d)** O 1s region.

The CoVFeO_x was further deposited on nickel foam. The OER activity of this material is shown in Figure 2.18 a. CoVFeO_x reaches 10 mA cm² at an overpotential of 268 and 270 mV in 1 M KOH and 1 M Fe free KOH, respectively. Therefore, the CoVFeO_x material is more active than CoVO_x but less active than CoFeO_x. Additionally, the Tafel slopes are 58 and 53 mV dec⁻¹ in 1 M KOH and 1 M Fe free KOH. The values of overpotentials on FTO and nickel foam as well as the Tafel slopes of all the deposited cobalt-based oxides of this work are summarized in Table 2.3. The CoVFeO_x catalyst is stable for 20 h at 10 mA cm⁻² (Figure 2.18 b) and a faradaic efficiency close to 100 % is obtained with this oxide (Figure 2.18 c).

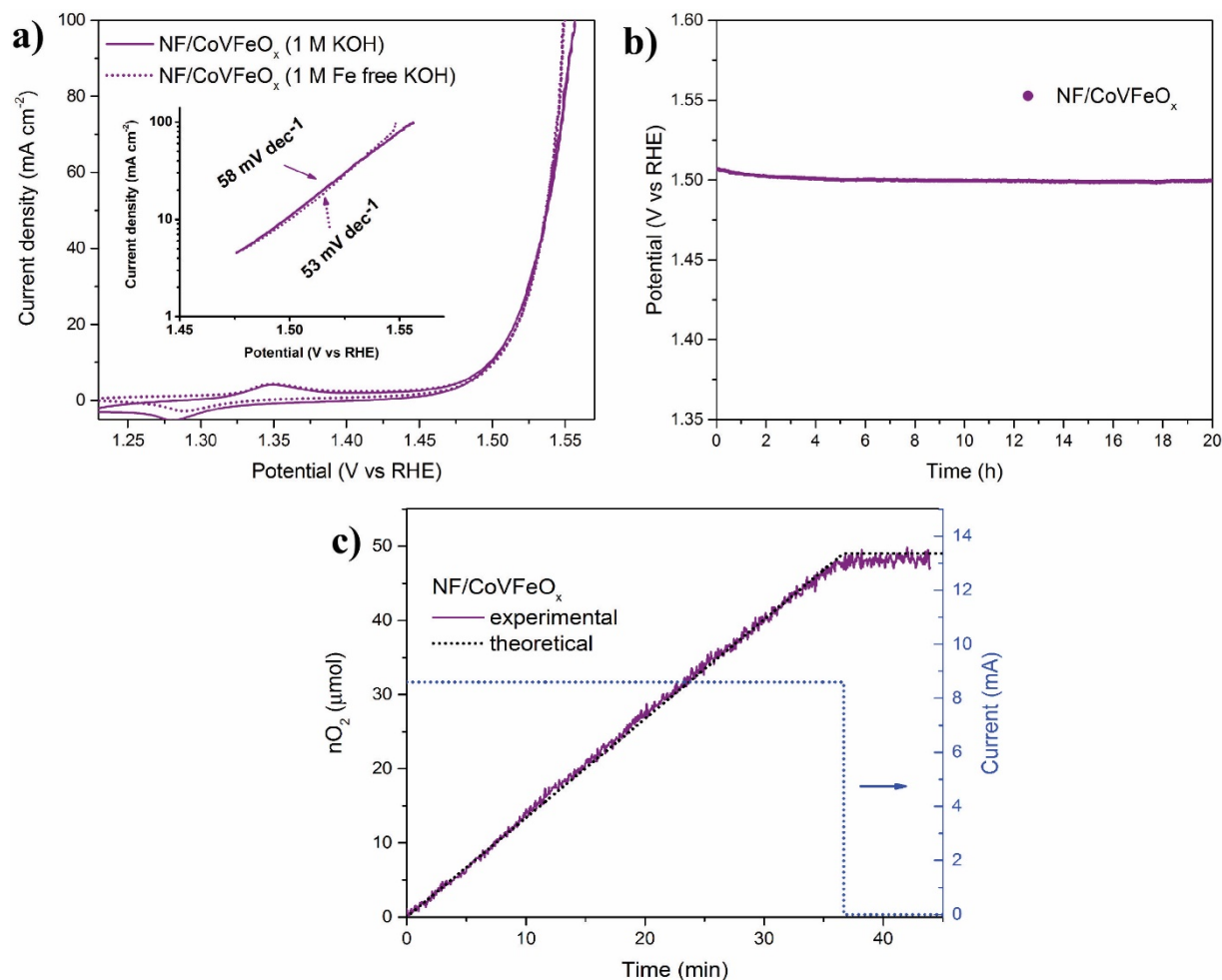


Figure 2.18 **a)** Polarization curves in 1 M KOH and 1 M Fe free of CoVFeO_x (thickness 50 nm) deposited on nickel foam (inset: Tafel slopes). Scan rate: 1 mV s, iR drop corrected. **b)** Stability of CoVFeO_x on nickel foam at 10 mA cm⁻² in 1 M Fe free KOH, iR drop corrected. **c)** Predicted and measured number of moles of O₂ produced by NF/CoVFeO_x (area 0.86 cm²) in 1 M Fe free KOH.

The morphology of CoVFeO_x as-deposited and after polarization at 10 mA cm⁻² for 20 h in 1 M Fe free KOH was investigated by SEM. After deposition, a flat and conformal coating is visible on nickel foam (Figure 2.19 a). After polarization, cracks in the CoVFeO_x layer are visible (Figure 2.19 b). However, the fine surface structure remains similar (inset in Figure 2.19 b), indicating no rearrangement of the surface.

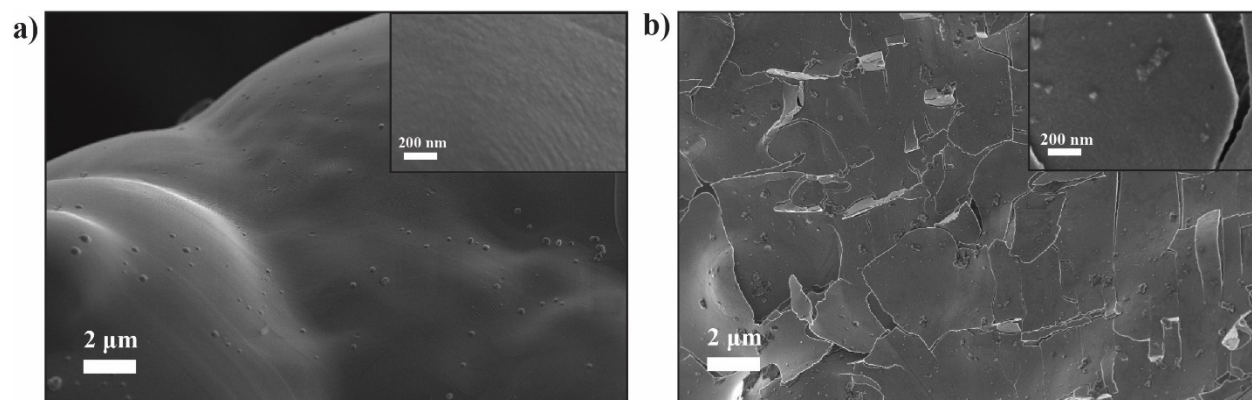


Figure 2.19 a) SEM images of CoVFeO_x on nickel foam before polarization in 1 M Fe free KOH. b) SEM images of CoVFeO_x on nickel foam after polarization in 1 M Fe free KOH.

Table 2.3 Summary of overpotentials at 10 mA cm⁻² and Tafel slopes of CoO_x, CoVO_x, CoFeO_x and CoVFeO_x on FTO and nickel foam in 1 M KOH and in 1 M Fe free KOH (values in parentheses).

Material	Overpotential (mV) on FTO (thickness 10 nm)	Overpotential (mV) on FTO (thickness 20 nm)	Overpotential (mV) on FTO (thickness 50 nm)	Overpotential (mV) on NF (thickness 50 nm)	Tafel slope on NF (mV dec ⁻¹)
CoO _x	445 (500)	435 (490)	433 (500)	322 (315)	98 (108)
CoVO _x	510 (560)	380 (400)	390(390)	315 (312)	68 (74)
CoFeO _x	415(420)	390 (405)	405 (410)	237 (239)	52 (54)
CoVFeO _x	402 (402)	416 (418)	398 (412)	268 (270)	58 (53)

2.5 Conclusions

An ALD system was custom built in the lab and different modifications were provided in order to have a fully functional setup. A library of oxides (TiO₂, Al₂O₃, ZnO, SnO₂, NiO_x, CoO_x, VO_x and FeO_x) could be deposited with our ALD setup. We focused in this chapter in developing mixed metal oxides as OER catalysts by ALD. Bimetallic oxides such as CoFeO_x and CoVO_x as well as a trimetallic CoVFeO_x compound were successfully deposited and characterized by SEM, XPS and XRD. The OER activity of these materials was optimized by changing their thickness and by tuning the ratio between their different metal constituents. The optimized thickness for CoFeO_x was between 10 and 50 nm, for CoVO_x between 20 and >80 nm and for CoVFeO_x between 10 and >100 nm. The composition of bimetallic CoFeO_x and CoVO_x differs from the theoretical

values due to possible nucleation effects, highlighting the challenge for precise control of composition of mixed metal oxides by ALD. These oxides were further deposited on high-surface nickel foam. On this substrate CoVO_x only showed moderate catalytic activity with 10 mA cm^{-2} reached at 315 mV overpotential in 1 Fe free KOH. However, CoVFeO_x and CoFeO_x could provide the same current density at 268 and 237 mV, respectively, which makes them highly competitive electrodes in alkaline conditions. This work advocates for further exploration of ALD deposition technique for oxygen evolution catalysts.

2.6 Experimental section

All reagents were obtained from commercial sources and used without further purification. Millipore deionized water 18.2 M Ω ·cm was used to prepare all solutions. All oxides were deposited on either fluorine-doped tin oxide glass (FTO, TEC 15, Sigma-Aldrich) or nickel foam (thickness 1.6 mm, porosity 95 %, Goodfellow Cambridge Limited). FTO substrates were cleaned by sonication in a detergent solution (Deconex) for 15 min followed by sonication in acetone for 15 min. Nickel foam substrates were dipped for 1 min in HCl 6 M and then thoroughly rinsed with water and dried in air before ALD deposition. After ALD deposition, the surface area of FTO electrodes were delimited with Teflon tape (area 0.196 cm²) and the active area of nickel foam substrates was delimited by applying epoxy glue (Araldite 2014-1) on the foam and carefully pressing on it with a metal rod to make it fill all the pores in order to prevent electrolyte from reaching the potentiostat clamp by capillary action. Nickel foam substrates had areas between 0.5 and 0.9 cm².

In order to calibrate the GPC of each oxides, deposition on Si (100) polished wafer substrates was done. Measurements of layer thicknesses were done by cross section SEM. For each sample, the thickness was measured at 3 different positions of the cross section and the average of these measurements was taken as the thickness of the material layer.

The ALD system used was described in detail in section 2.2

ALD deposition procedures of unary oxides

TiO₂, ZnO and Al₂O₃ were deposited according to procedures reported by Paracchino *et al.*^[17] Tetrakis(dimethylamino)titanium(IV) (TDMAT, 99.999 %, Aldrich), diethylzinc (DEZ, 95 %, Strem), Trimethylaluminium (TMA, 98 %, Strem) and hydrogen peroxide (H₂O₂, 50 wt.% in water, Sigma Aldrich) were used as the Ti, Zn, Al and O precursors, respectively. All precursors were loaded in stainless steel cylinders. TDMAT was heated to 75°C and DEZ, TMA and H₂O₂ to 30°C. The deposition sequences were as followed:

For the TiO₂ deposition, a TDMAT pulse of 0.25 s, followed by a 20 s nitrogen purge (flow of 4 ml min⁻¹), followed by a H₂O₂ pulse of 0.25 s and by a 20 s nitrogen purge (flow of 4 ml min⁻¹) were used. The vacuum chamber was held at 150°C.

For the ZnO deposition, a DEZ pulse of 0.1 s, followed by a 15 s nitrogen purge (flow of 20 ml min⁻¹), followed by a H₂O₂ pulse of 0.5 s and by a 15 s nitrogen purge (flow of 20 ml min⁻¹) were used. The vacuum chamber was held at 120°C.

For the Al₂O₃ deposition, a TMA pulse of 0.05 s, followed by a 15 s nitrogen purge (flow of 20 ml min⁻¹), followed by a H₂O₂ pulse of 0.5 s and by a 15 s nitrogen purge (flow of 20 ml min⁻¹) were used. The vacuum chamber was held at 130°C.

SnO₂ was deposited according to a procedure reported by Elam *et al.*^[19] SnO₂ was deposited by using alternating exposures of tetrakis(dimethylamino)tin(IV) (TDMASn, 99.99 %, ABCR) and hydrogen peroxide (H₂O₂, 50 wt.% in water, Sigma Aldrich). TDMASn was heated to 65°C and H₂O₂ to 30 °C. The deposition was composed of a 0.25 s TDMASn pulse, followed by a 25 s nitrogen purge step (flow of 40 ml min⁻¹), followed by a H₂O₂ pulse of 0.25 s and by a 25 s nitrogen purge step (flow of 40 ml min⁻¹). The flow of nitrogen was cut (0 ml min⁻¹) during injection of TDMASn in order to lower the base pressure of the vacuum chamber to approximately 0.1 mbar and allow more efficient vapor extraction of TDMASn from the sample cylinder.

CoO_x, NiO_x and FeO_x were deposited in exposure mode (closing of pump valve after pulsing precursors) with Cyclopentadienylcobalt(I)dicarbonyl (CoCp(CO)₂, >95 %, ABCR), Bis(ethylcyclopentadienyl)nickel(II) (Ni(EtCp)₂, >98 %, ABCR) and N,N-Dimethylaminomethylferrocene (DMAMFc, >98 %, ABCR) as Co, Ni and Fe precursors, respectively. CoCp(CO)₂, Ni(EtCp)₂ and DMAMFc were heated in stainless steel sample cylinders at 30, 90 and 95°C, respectively. Ozone with concentration of 250 g m⁻³ produced from an ozone generator (BMT 802 N, BMT Messtechnik) fed with oxygen gas (>99.9995 %, Carbagas) was used as oxidant.

The CoO_x deposition was composed of a 0.8 s pulse of CoCp(CO)₂ with a 5 s exposure (closing of the pump valve), followed by 20 s nitrogen purge step (flow of 40 ml min⁻¹), followed by a 0.5 s pulse of ozone with a 5 s exposure and by a 20 s nitrogen purge step (flow of 40 ml min⁻¹). The vacuum chamber was held at 150°C. The flow of nitrogen was cut (0 ml min⁻¹) during injection of CoCp(CO)₂ in order to lower the base pressure of the vacuum chamber to approximately 0.1 mbar and allow more efficient vapor extraction of CoCp(CO)₂ from the sample cylinder.

The NiO_x deposition used the bubbler system (described in section 2.2.2) and was composed of a 0.1 s pulse of Ni(EtCp)₂ with a simultaneous 0.1 s pulse of N₂ in the sample cylinder with 5 s

exposure time (closing of the pump valve), followed by a 1 s pulse of $\text{Ni}(\text{EtCp})_2$ (during the 5 s exposure time to empty the headspace of the sample cylinder), followed by a 20 s nitrogen purge step (flow of 40 ml min^{-1}), followed by a 0.5 s pulse of ozone with a 5 s exposure and by a 20 s nitrogen purge step (flow of 40 ml min^{-1}). The vacuum chamber was heated at 150°C . The flow of nitrogen was cut (0 ml min^{-1}) during injection of $\text{Ni}(\text{EtCp})_2$ in order to lower the base pressure of the vacuum chamber to approximately 0.1 mbar and allow more efficient vapor extraction of $\text{Ni}(\text{EtCp})_2$ from the sample cylinder.

The FeO_x deposition used the bubbler system (described in section 2.2.2) and was composed of a 0.1 s pulse of DMAMFc with a simultaneous 0.1 s pulse of N_2 in the sample cylinder with 5 s exposure time (closing of the pump valve), followed by a 1 s pulse of DMAMFc (during the 5 s exposure time to empty the headspace of the sample cylinder), followed by 20 s nitrogen purge step (flow of 40 ml min^{-1}), followed by a 0.5 s pulse of ozone with a 5 s exposure, followed by a 20 s nitrogen purge step (flow of 40 ml min^{-1}). The vacuum chamber was heated at 150°C . The flow of nitrogen was cut (0 ml min^{-1}) during injection of $\text{Ni}(\text{EtCp})_2$ in order to lower the base pressure of the vacuum chamber to approximately 0.1 mbar and allow more efficient vapor extraction of $\text{Ni}(\text{EtCp})_2$ from the sample cylinder.

The VO_x deposition used the bubbler system (described in section 2.2.2) and was composed of a 0.03 s pulse of vanadium(V) oxytriisopropoxide (VTIP, >98 %, ABCR) with a simultaneous 0.03 s pulse of N_2 in the sample cylinder, followed by a 1 s pulse of VTIP (to empty the headspace of the sample cylinder), followed by a 10 s nitrogen purge step (flow of 40 ml min^{-1}), followed by a 0.5 s pulse of H_2O and by a 10 s nitrogen purge step (flow of 40 ml min^{-1}).

ALD deposition procedures of mixed metal oxides

CoFeO_x , CoVO_x and CoVFeO_x were deposited by using linear combinations of the deposition procedures of CoO_x , VO_x and FeO_x in a supercycle approach.^[9] The deposition of CoFeO_x consisted of x cycles of CoO_x + y cycles of FeO_x in order to form a supercycle and to vary the composition of the material. The deposition of CoVO_x consisted x cycles CoO_x + y cycles VO_x and the deposition of CoVFeO_x was composed of 1 cycle of CoO_x + 1 cycle of VO_x + z cycles of FeO_x . All depositions were ended with a CoO_x deposition cycle in order to always have the same surface.

Electrochemical Characterization

The OER activity and stability were measured by cyclic voltammetry and chronopotentiometry by using an Autolab PGSTAT302N potentiostat/galvanostat (Metrohm). The third CV was taken as representative measurement for all samples on FTO and nickel foam. A three-electrode setup was used with either FTO or nickel foam substrates as working electrodes, a platinum wire as counter electrode and an Ag/AgCl (sat. KCl) reference electrode. Stirring was done only during stability measurements. Standard 1 M KOH solution (pH 13.6, Merck) was used for all experiments. 1 M Fe free KOH electrolyte was prepared from the standard 1 M KOH solution by removing trace iron using a procedure reported by the Boettcher group.^[41] Polyethylene beakers were used and cleaned with H₂SO₄ 20 wt% before each experiment in order to avoid iron contamination from conventional glassware.

In order to correct for the iR drop, the uncompensated resistance for each sample was measured by electrochemical impedance spectroscopy (EIS). The EIS data were collected at 1.2 V vs RHE and by applying 49 frequencies from 100 kHz to 0.1 Hz (10 mV amplitude). The measured resistance was close to 6-9 Ω cm² for the samples on FTO and 1.0-1.4 Ω cm² for the samples on nickel foam.

Structural and compositional Characterization

The X-ray powder diffraction (XRD) were measured on oxides deposited on Si (100) wafer substrates on a PANalytical Aeris diffractometer with a Cu K α monochromatic source and a 1 \times 1 2D detector. Data were analyzed with PANalytical X'Pert HighScore software.

SEM images were recorded with a Zeiss Merlin microscope equipped with an Inlens secondary electron detector and operated at 2 kV.

XPS was carried out by using a PHI VersaProbe II scanning XPS microprobe equipped with a 24.8 W Al K α monochromatic source with a beam size of 100 μ m. Compensation for charging effects was done by using adventitious carbon 1s peak calibrated at 284.8 eV and used as an internal standard.

Faradaic efficiency measurement

The faradaic efficiency of CoVO_x, CoFeO_x and CoVFeO_x deposited on nickel foam was measured by using an airtight glass H-cell with an optical fluorescence sensor (Ocean Optics). The

cell was purged with N₂ to have an initial O₂ content lower than 0.5 %. 10 mA cm⁻² were applied to the samples in 1 M Fe free KOH

2.7 References

- [1] Ahonen, M., Pessa, M. & Suntola, T. A study of ZnTe films grown on glass substrates using an atomic layer evaporation method. *Thin Solid Films*, 301,(1980).
- [2] Suntola, T. in *Thirty Years of ALD. An Invited Talk at AVS Topical Conderence on Atomic Layer Deposition (ALD2004), University of Helsinki, Helsinki, Finland, 2004*,
- [3] George, S. M. Atomic Layer Deposition: An Overview. *Chemical Reviews* **110**, 111-131,(2010).
- [4] Johnson, R. W., Hultqvist, A. & Bent, S. F. A brief review of atomic layer deposition: from fundamentals to applications. *Materials Today* **17**, 236-246,(2014).
- [5] Bakke, J. R., Pickrahn, K. L., Brennan, T. P. & Bent, S. F. Nanoengineering and interfacial engineering of photovoltaics by atomic layer deposition. *Nanoscale* **3**, 3482-3508,(2011).
- [6] Paracchino, A., Laporte, V., Sivula, K., Grätzel, M. & Thimsen, E. Highly active oxide photocathode for photoelectrochemical water reduction. *Nat Mater* **10**, 456-461,(2011).
- [7] Hu, S., Shaner, M. R., Beardslee, J. A., Lichterman, M., Brunschwig, B. S. & Lewis, N. S. Amorphous TiO₂ coatings stabilize Si, GaAs and GaP photoanodes for efficient water oxidation. *Science* **344**, 1005-1009,(2014).
- [8] Le Formal, F., Tetreault, N., Cornuz, M., Moehl, T., Gratzel, M. & Sivula, K. Passivating surface states on water splitting hematite photoanodes with alumina overlayers. *Chemical Science* **2**, 737-743,(2011).
- [9] Mackus, A. J. M., Schneider, J. R., MacIsaac, C., Baker, J. G. & Bent, S. F. Synthesis of Doped, Ternary, and Quaternary Materials by Atomic Layer Deposition: A Review. *Chemistry of Materials* **31**, 1142-1183,(2019).
- [10] Pickrahn, K. L., Park, S. W., Gorlin, Y., Lee, H.-B.-R., Jaramillo, T. F. & Bent, S. F. Active MnO_x Electrocatalysts Prepared by Atomic Layer Deposition for Oxygen Evolution and Oxygen Reduction Reactions. *Advanced Energy Materials* **2**, 1269-1277,(2012).
- [11] Pickrahn, K. L., Garg, A. & Bent, S. F. ALD of Ultrathin Ternary Oxide Electrocatalysts for Water Splitting. *ACS Catalysis* **5**, 1609-1616,(2015).
- [12] Nardi, K. L., Yang, N., Dickens, C. F., Strickler, A. L. & Bent, S. F. Creating Highly Active Atomic Layer Deposited NiO Electrocatalysts for the Oxygen Evolution Reaction. *Advanced Energy Materials* **5**, n/a-n/a,(2015).
- [13] Li, H., Guo, Z. & Wang, X. Atomic-layer-deposited ultrathin Co₉S₈ on carbon nanotubes: an efficient bifunctional electrocatalyst for oxygen evolution/reduction reactions and rechargeable Zn–air batteries. *Journal of Materials Chemistry A* **5**, 21353-21361,(2017).
- [14] Riha, S. C., Klahr, B. M., Tyo, E. C., Seifert, S., Vajda, S., Pellin, M. J., Hamann, T. W. & Martinson, A. B. F. Atomic Layer Deposition of a Submonolayer Catalyst for the Enhanced Photoelectrochemical Performance of Water Oxidation with Hematite. *ACS Nano* **7**, 2396-2405,(2013).
- [15] Lichterman, M. F., Shaner, M. R., Handler, S. G., Brunschwig, B. S., Gray, H. B., Lewis, N. S. & Spurgeon, J. M. Enhanced Stability and Activity for Water Oxidation in Alkaline Media with Bismuth Vanadate Photoelectrodes Modified with a Cobalt Oxide Catalytic Layer Produced by Atomic Layer Deposition. *The Journal of Physical Chemistry Letters* **4**, 4188-4191,(2013).

-
- [16] Boer, H. Mass Flow Controlled Evaporation System. *Journal de Physique IV Colloque*, 961-966,(1995).
- [17] Paracchino, A., Mathews, N., Hisatomi, T., Stefik, M., Tilley, S. D. & Gratzel, M. Ultrathin films on copper(i) oxide water splitting photocathodes: a study on performance and stability. *Energy & Environmental Science* **5**, 8673-8681,(2012).
- [18] Wang, Y., Kang, K.-M., Kim, M. & Park, H.-H. Oxygen vacancy-passivated ZnO thin film formed by atomic layer deposition using H₂O₂. *Journal of Vacuum Science & Technology A* **36**, 031504,(2018).
- [19] Elam, J. W., Baker, D., Hyrn, A., Martinson, A. B. F., Pellin, M. J. & Hupp, J. T. Atomic layer deposition of tin oxide films using tetrakis(dimethylamino) tin. *J. of Vacuum Science and Technology A*, 244,(2008).
- [20] Han, B., Choi, K. H., Park, J. M., Park, J. W., Jung, J. & Lee, W.-J. Atomic layer deposition of cobalt oxide thin films using cyclopentadienylcobalt dicarbonyl and ozone at low temperatures. *Journal of Vacuum Science & Technology A* **31**, 01A145,(2013).
- [21] Lu, H. L., Scarel, G., Wiemer, C., Perego, M., Spiga, S., Fanciulli, M. & Pavia, G. Atomic Layer Deposition of NiO Films on Si(100) Using Cyclopentadienyl-Type Compounds and Ozone as Precursors. *Journal of The Electrochemical Society* **155**, H807-H811,(2008).
- [22] Steier, L., Luo, J., Schreier, M., Mayer, M. T., Sajavaara, T. & Grätzel, M. Low-Temperature Atomic Layer Deposition of Crystalline and Photoactive Ultrathin Hematite Films for Solar Water Splitting. *ACS Nano* **9**, 11775-11783,(2015).
- [23] Singh, T., Wang, S., Aslam, N., Zhang, H., Hoffmann-Eifert, S. & Mathur, S. Atomic Layer Deposition of Transparent VO_x Thin Films for Resistive Switching Applications. *Chemical Vapor Deposition* **20**, 291-297,(2014).
- [24] Burke, M. S., Zou, S., Enman, L. J., Kellon, J. E., Gabor, C. A., Pledger, E. & Boettcher, S. W. Revised Oxygen-Evolution-Reaction Activity Trends for First-row Transition Metal (oxy)hydroxides in Alkaline Media. *The Journal of Physical Chemistry Letters*,(2015).
- [25] Yang, J., Cooper, J. K., Toma, F. M., Walczak, Karl A., Favaro, M., Beeman, Jeffrey W., Hess, Lucas H., Wang, C., Zhu, C., Gul, S., Yano, J., Kisielowski, C., Schwartzberg, A. & Sharp, Ian D. A multifunctional biphasic water splitting catalyst tailored for integration with high-performance semiconductor photoanodes. *Nature Materials* **16**, 335,(2016).
- [26] Young, K. M. H. & Hamann, T. W. Enhanced photocatalytic water oxidation efficiency with Ni(OH)₂ catalysts deposited on α -Fe₂O₃ via ALD. *Chemical Communications* **50**, 8727-8730,(2014).
- [27] Liardet, L. & Hu, X. Amorphous Cobalt Vanadium Oxide as a Highly Active Electrocatalyst for Oxygen Evolution. *ACS Catalysis* **8**, 644-650,(2018).
- [28] Morales-Guio, C. G., Liardet, L. & Hu, X. Oxidatively Electrodeposited Thin-Film Transition Metal (Oxy)hydroxides as Oxygen Evolution Catalysts. *Journal of the American Chemical Society* **138**, 8946-8957,(2016).
- [29] Barr, T. L. & Seal, S. Nature of the use of adventitious carbon as a binding energy standard. *Journal of Vacuum Science & Technology A* **13**, 1239-1246,(1995).
- [30] Gaspar, D. J., Engelhard, M. H., Henry, M. C. & Baer, D. R. Erosion rate variations during XPS sputter depth profiling of nanoporous films. *Surface and Interface Analysis* **37**, 417-423,(2005).
- [31] Burke, M. S., Kast, M. G., Trotochaud, L., Smith, A. M. & Boettcher, S. W. Cobalt–Iron (Oxy)hydroxide Oxygen Evolution Electrocatalysts: The Role of Structure and
-

- Composition on Activity, Stability, and Mechanism. *Journal of the American Chemical Society* **137**, 3638-3648,(2015).
- [32] Borod'ko, Y. G., Vetchinkin, S. I., Zimont, S. L., Ivleva, I. N. & Shul'ga, Y. M. Nature of satellites in x-ray photoelectron spectra XPS of paramagnetic cobalt (II) compounds. *Chemical Physics Letters* **42**, 264-267,(1976).
- [33] Moulder, J. F., Stickle, W.F., Sobol, P.E., Bomben, K.D. *Handbook of X-ray Photoelectron Spectroscopy*. (Physical Electronics, Inc, 1995).
- [34] Silversmit, G., Depla, D., Poelman, H., Marin, G. B. & De Gryse, R. Determination of the V2p XPS binding energies for different vanadium oxidation states (V5+ to V0+). *Journal of Electron Spectroscopy and Related Phenomena* **135**, 167-175,(2004).
- [35] Malherbe, J. B., Hofmann, S. & Sanz, J. M. Preferential sputtering of oxides: A comparison of model predictions with experimental data. *Applied Surface Science* **27**, 355-365,(1986).
- [36] González-Elipse, A. R., Alvarez, R., Holgado, J. P., Espinos, J. P., Munuera, G. & Sanz, J. M. An XPS study of the Ar+-induced reduction of Ni2+ in NiO and Ni-Si oxide systems. *Applied Surface Science* **51**, 19-26,(1991).
- [37] Bandal, H. A., Jadhav, A. R., Tamboli, A. H. & Kim, H. Bimetallic iron cobalt oxide self-supported on Ni-Foam: An efficient bifunctional electrocatalyst for oxygen and hydrogen evolution reaction. *Electrochimica Acta* **249**, 253-262,(2017).
- [38] Smith, R. D. L., Prévot, M. S., Fagan, R. D., Trudel, S. & Berlinguette, C. P. Water Oxidation Catalysis: Electrocatalytic Response to Metal Stoichiometry in Amorphous Metal Oxide Films Containing Iron, Cobalt, and Nickel. *Journal of the American Chemical Society* **135**, 11580-11586,(2013).
- [39] Gao, T., Jin, Z., Liao, M., Xiao, J., Yuan, H. & Xiao, D. A trimetallic V-Co-Fe oxide nanoparticle as an efficient and stable electrocatalyst for oxygen evolution reaction. *Journal of Materials Chemistry A* **3**, 17763-17770,(2015).
- [40] Pi, Y., Shao, Q., Wang, P., Lv, F., Guo, S., Guo, J. & Huang, X. Trimetallic Oxyhydroxide Coralloids for Efficient Oxygen Evolution Electrocatalysis. *Angewandte Chemie International Edition* **56**, 4502-4506,(2017).
- [41] Trotochaud, L., Young, S. L., Ranney, J. K. & Boettcher, S. W. Nickel–Iron Oxyhydroxide Oxygen-Evolution Electrocatalysts: The Role of Intentional and Incidental Iron Incorporation. *Journal of the American Chemical Society* **136**, 6744-6753,(2014).

Chapter 3

Ultrathin Cobalt Iron Oxide Catalyst for Water Oxidation on Nanostructured Hematite Photoanodes

The results presented in this chapter were published in:
Liardet, L., Katz E. J., Luo, J., Grätzel, M. and Hu, X., An ultrathin cobalt-iron oxide catalyst for water oxidation on nanostructured hematite photoanodes, *Journal of Material Chemistry A*, 2019, 7, 6012-6020. Reproduced by permission of the Royal Society of Chemistry.

3.1 Introduction

The maturation of photoelectrochemical devices has been hindered by the difficulty of finding materials that are earth-abundant, stable under reaction conditions, inexpensive and that lead to efficient overall solar energy conversion. Iron is a common element of the Earth's crust (6.3 wt%)^[1] and is found in the form of iron oxides everywhere around us. Iron(III) oxide, also called hematite (α -Fe₂O₃), is a red-brown solid that can be found in many geological formations such as the ones in the southwest USA. Hematite is also more commonly known as rust, a nuisance material arising from the oxidation of metallic iron when exposed to oxygen and moisture. However, due to its chromatic characteristics, hematite is able to absorb solar irradiation. Fe₂O₃, with iron atoms in the +3 oxidation state, is the fully oxidized form of iron oxide. Therefore, there are three O²⁻ anions for every two Fe³⁺. By considering this stoichiometry, there are many types of Fe₂O₃ possible including amorphous structures. The two most common crystalline structures found in nature are α -Fe₂O₃ (hematite) and γ -Fe₂O₃ (maghemite). Hematite has a trigonal crystal structure with space group $R\bar{3}c$.

Hematite, which is both non-toxic and earth-abundant, is a promising semiconducting material for oxygen evolution due to its favorable band gap and band positioning (see Figure 1.14 in Chapter 1). Despite those favorable characteristics, hematite has several intrinsic limitations that prevent it from reaching its maximum photocurrent density of 12.6 mA cm⁻² under AM 1.5G solar illumination.^[2] First, a short hole diffusion length smaller than 4 nm, in addition to a low absorption coefficient, only allows the holes created close to the semiconductor/electrolyte interface to be collected. Nanostructured architectures have been proposed to address these material limitations.^[3,4] One example is the nanocauliflower hematite photoanode that was deposited by atmospheric pressure chemical vapor deposition (referred as APCVD hematite in this chapter). This nanostructure, shown in Figure 3.1, was finely tuned to be composed of nanocrystals forming a dendritic structure with features of 10-20 nm. With this feature size and a space charge region close to 5 nm (for highly Si-doped APCVD hematite), this structure can optimally and efficiently separate photogenerated electrons and holes. Most photogenerated holes will thus reach the semiconductor/electrolyte interface.^[3,5] Second, the water splitting reaction has a kinetic bottleneck that arises from its four-electron oxidative half-reaction: the oxygen evolution reaction. The efficiency of hematite as a photoanode is limited by the sluggish OER kinetics on its surface.

Due to the limitations previously cited, the photocurrent onset potential is much more positive than the flat-band potential of hematite (0.4-0.6 V vs RHE for Si-doped APCVD-hematite)^[6] and is usually not observed below 0.8-1.0 V vs RHE.^[5,7]

The deposition of an OER catalyst on the surface of hematite can decrease the photocurrent onset potential by improving the charge transfer kinetics.^[8-11] Among OER catalysts, the cobalt phosphate catalyst "Co-Pi" has been extensively investigated.^[7,11] Electrodeposited Co-Pi produced a cathodic shift of the OER onset potential. Moreover, a photo-assisted electrodeposition route was developed and yielded Co-Pi films with superior activity due to a more uniform layer by depositing only onto areas that produce photogenerated holes, thereby avoiding the creation of catalyst nodules and islands.^[12] In the present work, we used a similar strategy to deposit a thin and uniform layer of cobalt iron oxide (CoFeO_x). This CoFeO_x material, compared to the photoelectrodeposited Co-Pi, yielded an earlier onset potential and a higher photocurrent density at 1.0 V vs RHE (vide infra).

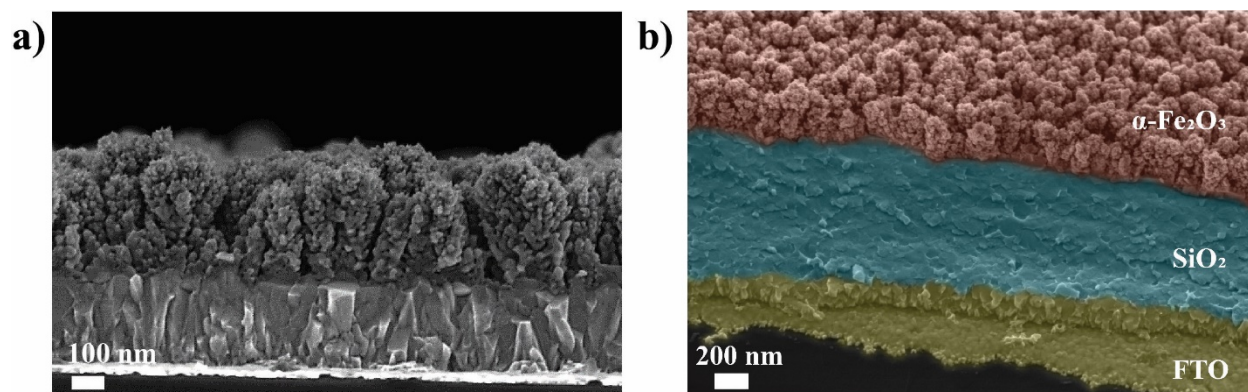


Figure 3.1 **a)** Cross-section SEM image of APCVD hematite photoanode. **b)** 45° cross-section SEM image of APCVD hematite with colorization of the different layers of the photoanode.

Recently, our group reported an oxidative electrodeposition method to produce various unary and binary transition metal oxides made of earth-abundant elements such as CoO_x , MnO_x , CoFeO_x , NiO_x and NiFeO_x . Among them, CoFeO_x had the highest turnover frequency, mass activity and lowest overpotential in alkaline solution (1 M KOH).^[13] NiFeO_x was also found to be a highly active OER catalyst when photoelectrodeposited on hematite photoanodes and was reported in a previous report by our group.^[9] For the reasons previously cited, we decided to explore anodically photoelectrodeposited CoFeO_x on hematite. Despite several studies on electrocatalytic activity of

CoFeO_x, few reports of this material on the surface of hematite anodes have been reported.^[14-17] In these reports, the role of CoFeO_x varies substantially depending on its thickness and on the type of hematite used. In the present work, we deposited CoFeO_x on nanocauliflower hematite photoanodes grown by APCVD. In order to avoid competitive light absorption by the CoFeO_x layer, we developed a photoelectrodeposition method that yielded an optically transparent, ultrathin CoFeO_x layer which enhanced the OER activity of hematite.

3.2 Activity of CoFeO_x-coated hematite photoanode

In this work, all hematite photoanodes were coated with a thin layer of Al₂O₃ by atomic layer deposition (ALD; see Chapter 2) and are referred to as Fe₂O₃/Al₂O₃. Deposition of thin oxide layers, such as Ga₂O₃, In₂O₃ and Al₂O₃, on top of hematite has been demonstrated to be an effective strategy to reduce the density of surface trap states and enhance the photoactivity.^[18,19] The beneficial effect of the Al₂O₃ layer on the hematite is shown in Figure 3.2 a, as seen by the cathodic shift of the onset potential induced by Al₂O₃. OER catalysts deposited on the surface of hematite can further increase the photoactivity. The photoactivity of hematite coated with different photoelectrodeposited OER catalysts is shown in Figure 3.2 a. The extracted onset potential (see experimental details) for the hematite coated with CoFeO_x is close to 0.8 V vs RHE, which represent a cathodic shift of approximately 200 mV compared to the uncoated hematite. These values are comparable to the ones when the hematite photoanode is coated with NiFeO_x. In comparison, here the Co-Pi catalyst has an onset potential of only ~0.9 V vs RHE. A similar value was obtained with a control hematite sample coated with CoO_x. At potentials of 1.0 and 1.23 V vs RHE, the catalyst-free hematite provides a photocurrent density of 0.2 and 1.6 mA cm², respectively. After depositing CoFeO_x, photocurrent densities of 1.6 and 2.5 mA cm² were reached at the same potentials, corresponding to a 8- and 1.5- fold increase, respectively. Additionally, when compared to NiFeO_x at potentials between 0.8 and 1.23 V vs RHE, the CoFeO_x-coated hematite has a better fill factor. When photoelectrodeposited, CoFeO_x yielded a better activity compared to when electrodeposition was used (Figure 3.2 b). This can be explained by the fact that, due to the morphology of APCVD hematite being composed of highly branched nanostructures towards the electrolyte and more compact stems near the FTO substrate,

electrodeposition will likely preferentially deposit CoFeO_x near the FTO substrate, but the photoactivity primarily arises from the fine dendritic structure in the front side.

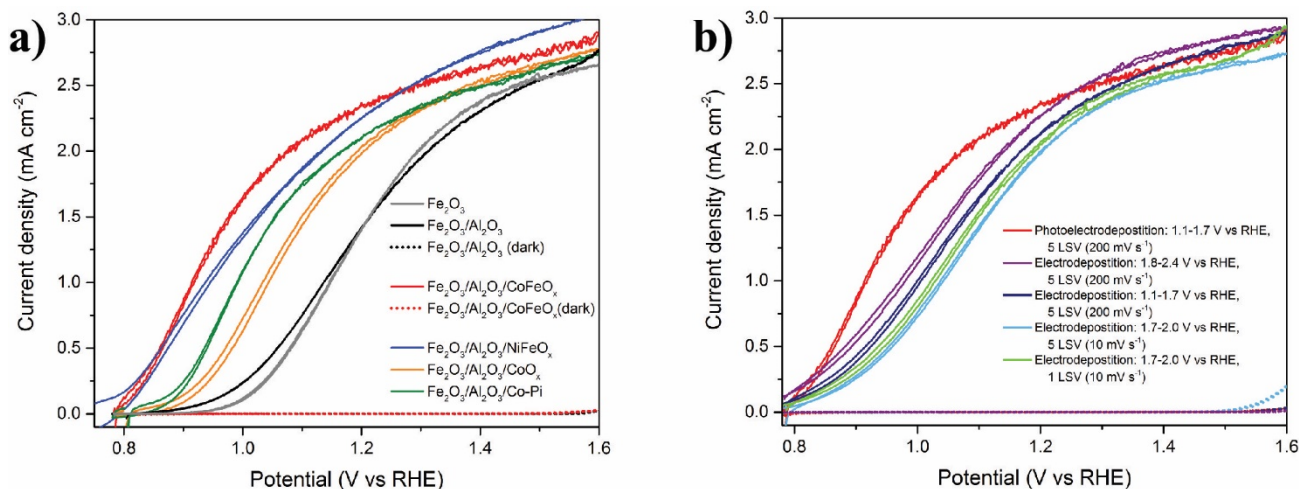


Figure 3.2 a) Polarization curves in 1 M KOH of Fe_2O_3 and Fe_2O_3 coated with Al_2O_3 and different OER catalysts under simulated AM 1.5G illumination (lines) and in the dark (dots). Scan rate: 10 mV s^{-1} . **b)** Polarization curves in 1 M KOH under illumination of Fe_2O_3 coated with CoFeO_x photoelectrodeposited and electrodeposited by different conditions.

In this work, the observed photocurrent densities (especially the plateau photocurrent density above 1.2-1.4 V vs RHE) are slightly lower than the ones reported in previous reports using the same APCVD hematite due to the methodology used to delimit the surface area which is different from the one used previously (by using epoxy glue instead of an aperture mask, a more accurate illuminated area is obtained).^[3,20]

The optimal performance was reached when 5 linear sweeps were used to photoelectrodeposit the CoFeO_x (Figure 3.3 a). Shorter or longer depositions (2, 3 and 8 LSV sweeps) yielded a more anodic onset potential. A strong dependence of the number of LSV sweeps on the CoFeO_x -coated hematite photoanodes was also observed (Figure 3.3 b). When 2 LSV sweeps were used, a loss of 27 % of the initial photocurrent occurred in the first 30 min of electrolysis at 1.0 V vs RHE under AM 1.5G illumination. With 3 LSV sweeps, approximately 12 % of deactivation was observed in 3 hours. When slightly thicker layers were applied (5 and 8 LSV sweeps) the deactivation was reduced to 3 and 2 % after 3 hours, respectively.

Another important parameter to take into account when developing overlayers for light absorbers is their optical transparency, especially for APCVD hematite photoanodes which require

front-side illumination for optimal performances.^[6,21] The photoelectrodeposition method used in this work allowed us to obtain ultrathin layers of CoFeO_x and negligible parasitic light absorption was observed when CoFeO_x was deposited with 5 LSV or less (Figure 3.4 a). Consequently, this CoFeO_x material can be considered as optically transparent at its optimal thickness for photoelectrochemical water oxidation. Unless noted otherwise, all further experiments of this work were therefore performed with hematite photoanodes coated with 5 LSV of CoFeO_x . Long-term electrolysis of the CoFeO_x -coated hematite was done at 1.0 and 1.23 V vs RHE under AM 1.5G illumination. A negligible loss of photocurrent was observed at both 1.0 and 1.23 V vs RHE, as shown in Figure 3.4 b. Moreover, the faradaic efficiency for OER of the CoFeO_x -coated hematite anodes was measured at 1.23 V vs RHE and found to be close to 100 % (Figure 3.4 c).

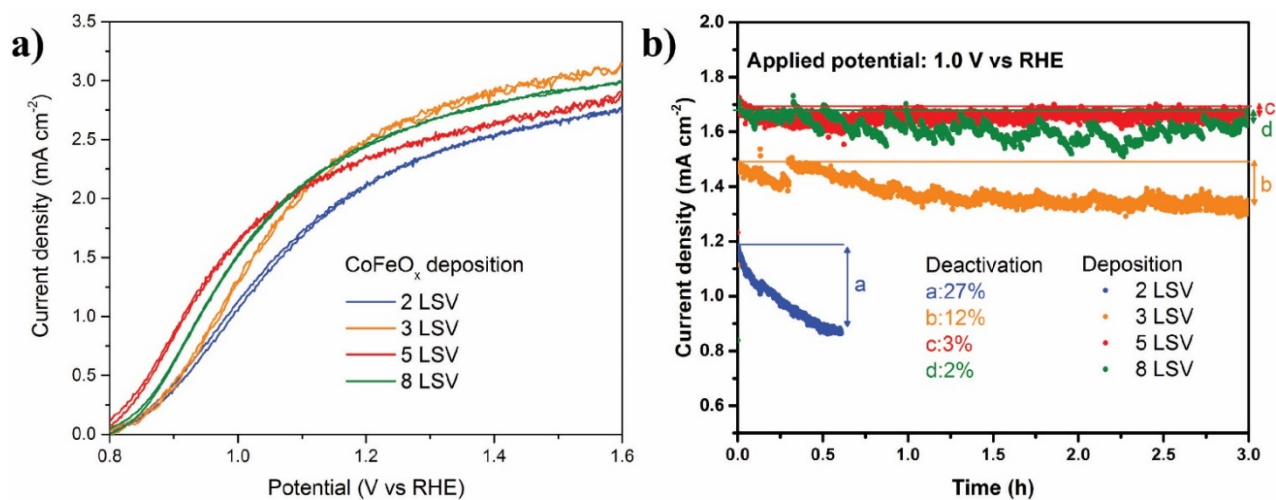


Figure 3.3 a) Polarization curves of hematite photoanodes coated with CoFeO_x with different number of linear sweeps, measured in 1 M KOH under simulated AM 1.5G illumination. Scan rate: 10 mV s^{-1} . b) Constant potential electrolysis at 1.0 V vs RHE under simulated AM 1.5G illumination and in 1 M KOH of hematite anodes coated with CoFeO_x deposited with different number of linear sweeps.

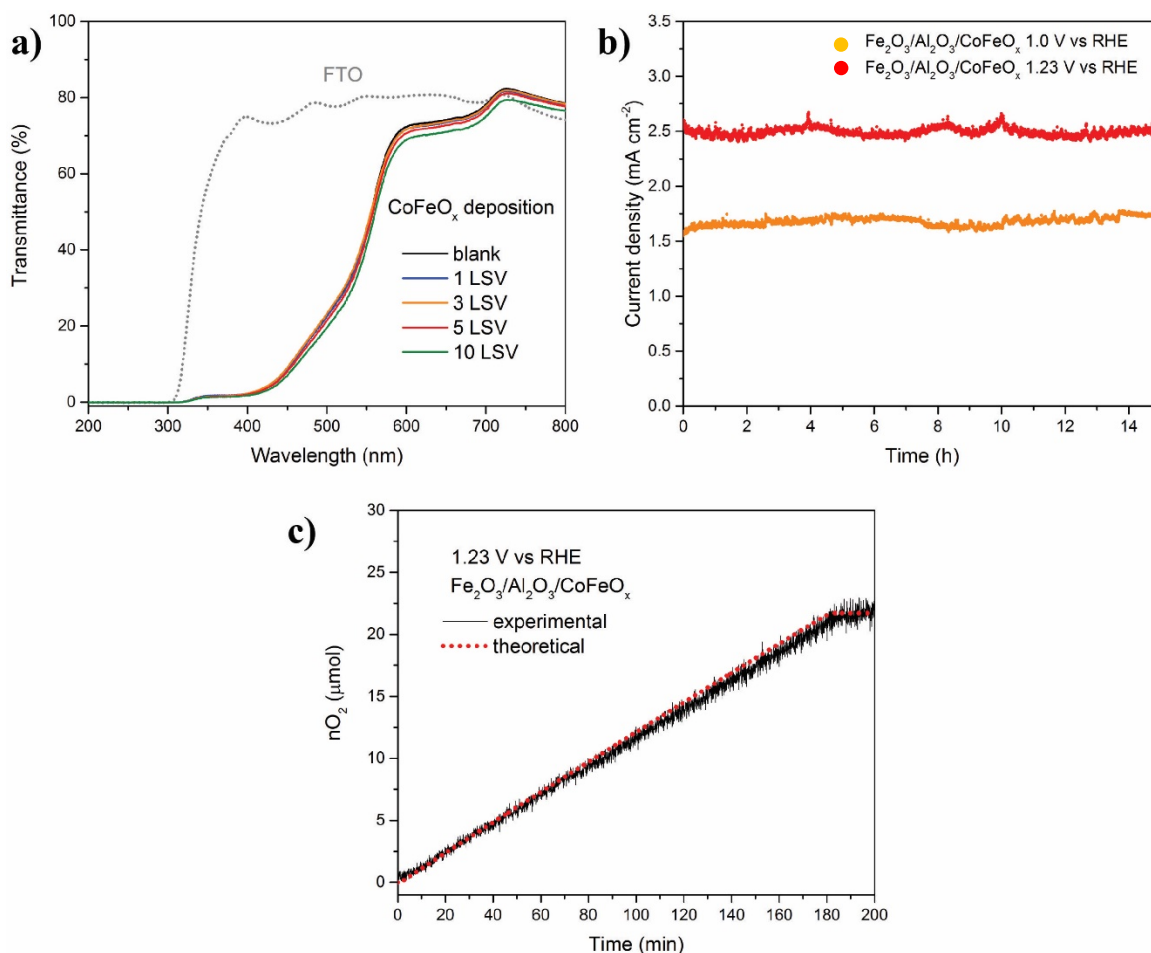


Figure 3.4 a) Transmittance of hematite photoanodes, uncoated and coated with CoFeO_x deposited with different numbers of LSV sweeps. b) Constant potential electrolysis during 15 hours at 1.0 and 1.23 V vs RHE under AM 1.5G illumination in 1 M KOH of CoFeO_x-coated hematite. c) Predicted and measured number of moles of O₂ produced by the CoFeO_x-coated hematite at 1.23 V vs RHE under AM 1.5G illumination.

3.3 Characterization of CoFeO_x overlayer

The chemical composition of the CoFeO_x layer was investigated by X-ray photoelectron spectroscopy (XPS). After deconvolution of the high-resolution spectrum between 775 and 795 eV, the Co 2p_{3/2} signal is located at a binding energy (BE) of 780.4 eV (Figure 3.5 a). This BE is representative of Co in the +2 oxidation state in the form of Co(OH)₂.^[22] This results agrees with our previous study on oxidatively electrodeposited CoFeO_x.^[13] A broad signal peaking at 784.7 eV is associated to the Fe L₃M₄₅M₄₅ Auger line. The high intensity of this Fe LMM Auger line, compared to the Co 2p_{3/2} peak, indicates that the layer of CoFeO_x is thinner than the penetration

depth of X-rays (tens of angstroms) and that the Fe LMM signal arises from the hematite substrate.^[23] This is further confirmed by the $2p_{3/2}$ signal in the Fe 2p high-resolution spectra (Figure 3.5 b). The spectrum of the Fe $2p_{3/2}$ signal is composed of two distinct peaks separated by 1 eV (BE of 709.7 and 710.7 eV) and a prominent satellite band located 8 eV above the $2p_{3/2}$ signal (BE of 718.5 eV). This is characteristic of α -Fe₂O₃. Another peak at 712.5 eV is representative of Fe³⁺ in FeOOH. Moreover, both of these iron oxides can be confirmed by looking at the O 1s spectrum in Figure 3.5 c. Two distinctive peaks can be observed at BE of 531.3 and 529.7 eV and can be assigned to O²⁻ in a hydroxyl environment and in Fe₂O₃, respectively. In the catalyst-free hematite, the Fe LMM Auger peak is also visible in the high resolution spectrum of the Co 2p region (Figure 3.6 a). The FeOOH signal cannot be attributed to the overlayer of CoFeO_x as it is also present in the Fe 2p region of the catalyst-free hematite spectrum (Figure 3.6 b). Additionally,

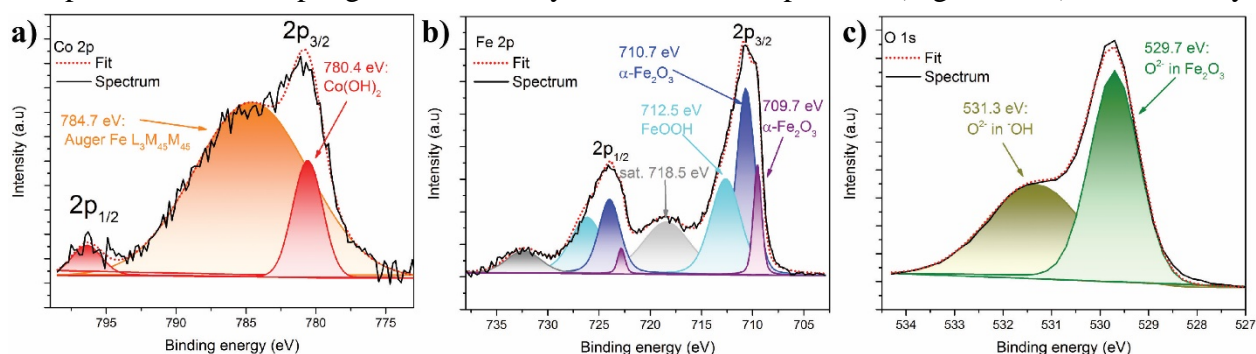


Figure 3.5 XPS spectra (with deconvolution) of the CoFeO_x-coated hematite (5 LSV) with high-resolution spectra of **a)** Co 2p region, **b)** Fe 2p region and **c)** O 1s region.

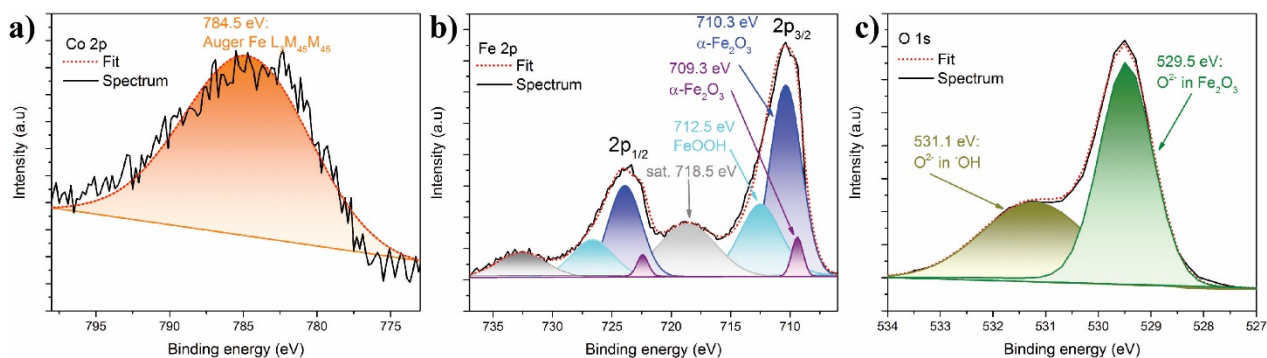


Figure 3.6 XPS spectra (with deconvolution) of the catalyst-free hematite with high-resolution spectra of **a)** Co 2p region, **b)** Fe 2p region and **c)** O 1s region.

the O^{2-} signal in the O 1s region (Figure 3.6 c) at 531.3 eV indicates that FeOOH is also present on the surface of the hematite nanostructure.

The layer of $CoFeO_x$ is thin and is not visible by SEM. No morphological differences were observed between a catalyst-free photoanode and one coated with 5 LSV of $CoFeO_x$ (Figure 3.7 a,b). HR-TEM was employed to determine the thickness of the $CoFeO_x$ overlayer. For this, hematite nanoparticles were ultrasonically detached from the electrode substrate. This analysis further confirms that a $CoFeO_x$ layer is indeed present, but very thin. Without $CoFeO_x$, the edges

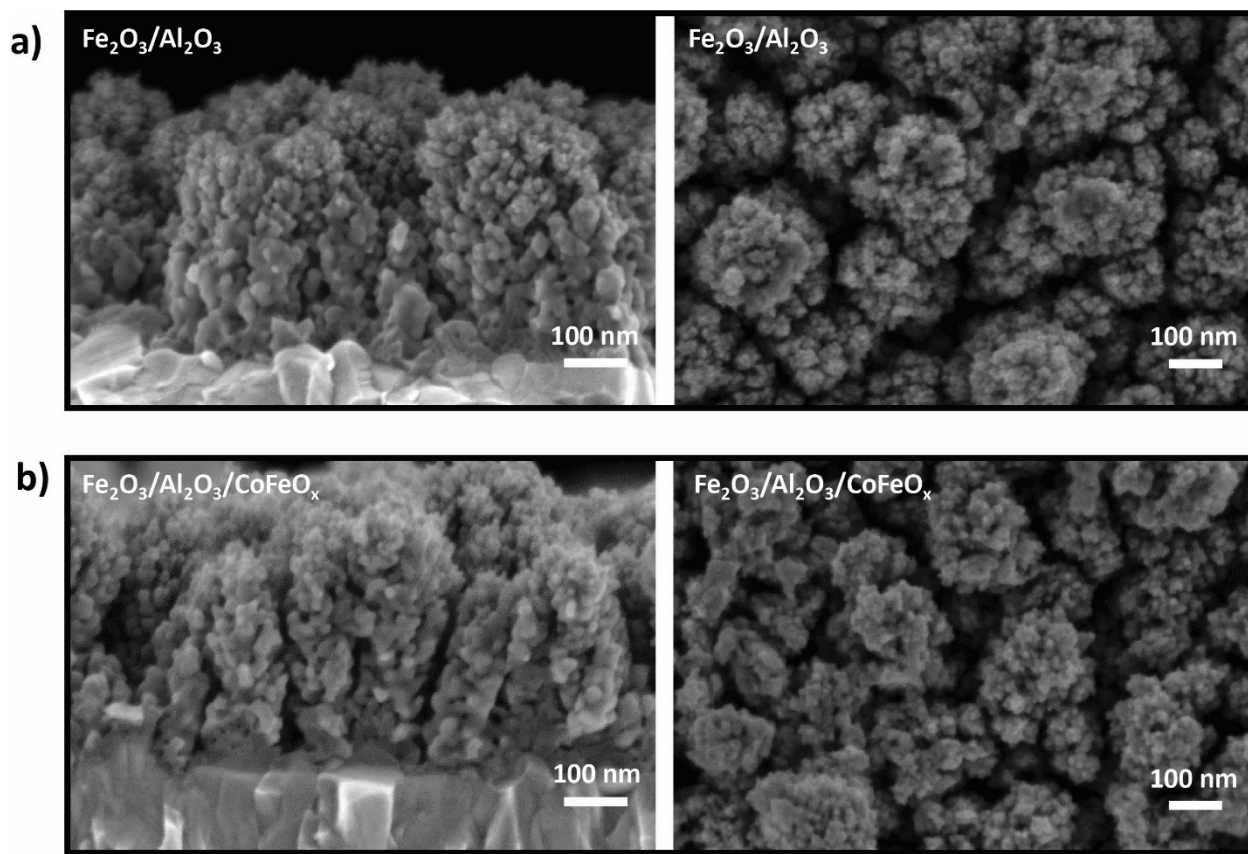


Figure 3.7 SEM images showing cross-section and top-down views of **a)** catalyst-free hematite and **b)** hematite coated with 5 LSV of $CoFeO_x$.

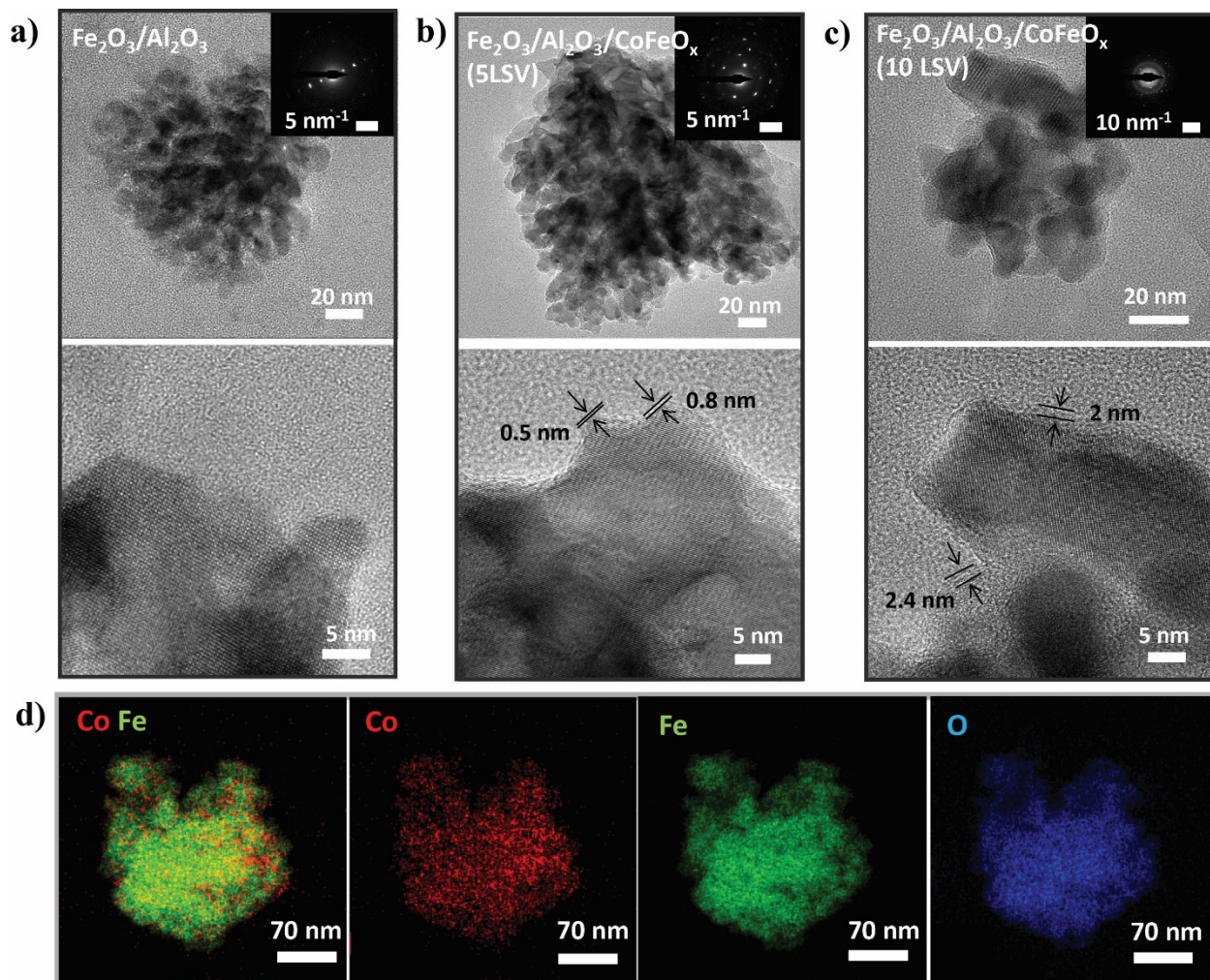


Figure 3. 8 **a)** TEM images of blank hematite (with SAED insert). **b)** TEM images of hematite coated with 5 LSV of CoFeO_x (with SAED insert). **c)** TEM images of hematite coated with 10 LSV of CoFeO_x (with SAED insert). **d)** STEM-EDX mapping of hematite coated with 5 LSV of CoFeO_x .

of the hematite crystals are sharp and clear as seen in Figure 3.8 a. The layer of Al_2O_3 is likely not visibly distinguishable due to the low number of ALD cycles used in this study (6 cycles) and to the fact that ALD of Al_2O_3 is known to result in island-type growth during the initial deposition cycles.^[24] When 5 LSV sweeps are used to photoelectrodeposit CoFeO_x , a thin amorphous layer of 0.5-0.8 nm is visible on the edge of the hematite nanocrystal in the HR-TEM images (Figure 3.8 b). When 10 LSV sweeps are used, a visible amorphous layer of CoFeO_x of ca. 2-2.4 nm can be observed on top of the hematite crystals (Figure 3.8 c). The slight variation of thickness of the CoFeO_x layer is probably due to the photoelectrodeposition method that preferentially deposits CoFeO_x only where holes reach the surface. STEM-EDX was used to map the distribution of Co

atoms on top of the hematite (Figure 3.8 d). The EDX mapping confirms that Co is homogeneously dispersed on hematite. The O and Fe signals are expected to arise primarily from the underlying hematite. Moreover, high magnification STEM-EDX of the CoFeO_x -coated hematite also showed that the concentration of Co was higher on the edge of the particles (as seen in the EDX map and with the intensity of the Fe $\text{K}\beta_1$ and Co $\text{K}\alpha_1$ lines in Figure 3.9 a and b), supporting the fact that the amorphous layer visible on the edge of the hematite crystals is the CoFeO_x layer.

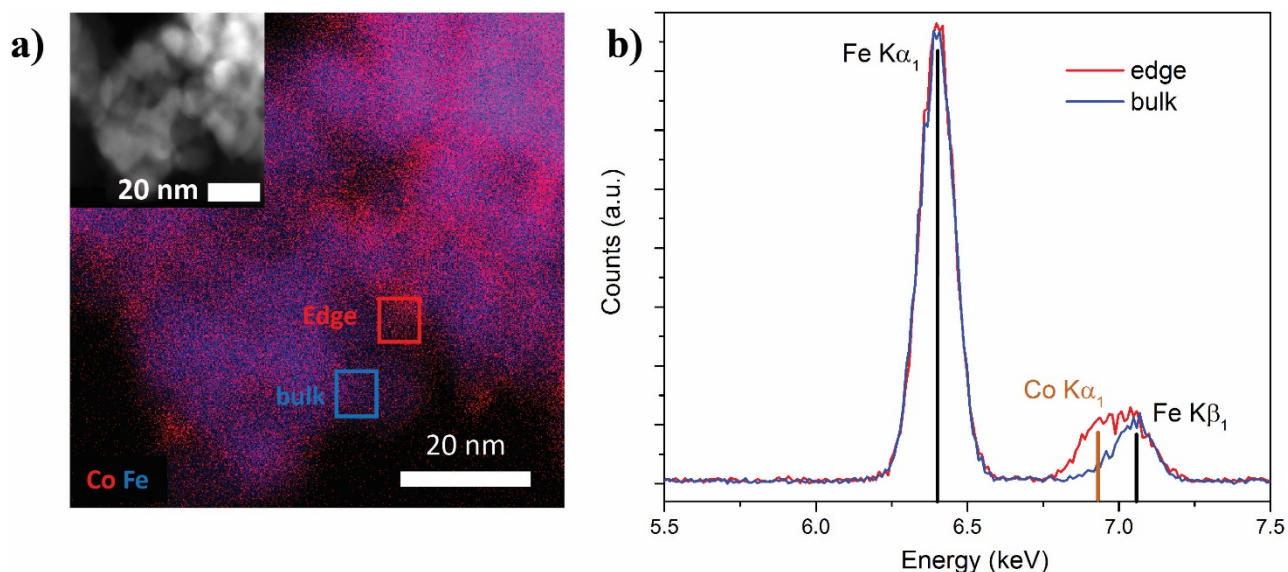


Figure 3.9 a) STEM-EDX image of hematite coated with 10 LSV of CoFeO_x (inset HAADF image). b) EDX spectrum of the edge region (red square in a) and of the bulk region (blue square in a) of the CoFeO_x -coated hematite particle.

3.4 Role of CoFeO_x

Although CoFeO_x is known as a highly active OER catalyst in other systems, we sought to establish whether this material enhances the photoelectrochemical performance of hematite only by accelerating the kinetics of water oxidation, or also by acting on other aspects such as modifying thermodynamics of the system (modification of flat-band potential) or also by suppressing electron-holes recombination on surface trap states.^[14,25,26] To probe the role of the CoFeO_x layer on PEC performance we first measured the charge injection efficiency (η_{inj}) and charge separation efficiency (η_{sep}) using the method developed by Dotan *et al.*, which uses hydrogen peroxide as a hole scavenger.^[27]

The experimentally measured photocurrent J_{photo} can be expressed as the theoretical maximum photocurrent density (J_{max}) that can be obtained from the hematite photoanode multiplied by the charge injection and separation efficiencies (Eq. 3.1). The value of J_{max} was previously determined as 10.9 mA cm^{-2} and corresponds to the integration of the absorption spectrum of a typical APCVD hematite anode with the AM 1.5G solar spectrum (100 mW cm^{-2}).

$$J_{photo} = J_{max} \cdot \eta_{sep} \cdot \eta_{inj} \quad (\text{Eq. 3.1})$$

The experimental photocurrent in 1 M KOH ($J_{photo}(KOH)$) can be expressed with a similar equation (Eq. 3.2).

$$J_{photo}(KOH) = J_{max} \cdot \eta_{sep} \cdot \eta_{inj} \quad (\text{Eq. 3.2})$$

For the obtained photocurrent in KOH electrolyte containing H_2O_2 ($J_{photo}(KOH + \text{H}_2\text{O}_2)$, Eq. 3.3) the charge injection efficiency can be neglected since H_2O_2 is known to be highly efficient at scavenging all photogenerated holes that reach the semiconductor/electrolyte interface ($\eta_{inj} = 1$).^[27]

$$J_{photo}(KOH + \text{H}_2\text{O}_2) = J_{max} \cdot \eta_{sep} \quad \text{Eq. 3.3}$$

From Eq. 3.2 and 3.3, η_{inj} and η_{sep} can be obtained by simple rearrangement and substitution, yielding Eq. 3.4 and 3.5.

$$\eta_{inj} = \frac{J_{photo}(KOH)}{J_{photo}(KOH + \text{H}_2\text{O}_2)} \quad \text{Eq. 3.4}$$

$$\eta_{sep} = \frac{J_{photo}(KOH + \text{H}_2\text{O}_2)}{J_{max}} \quad \text{Eq. 3.5}$$

$J_{photo}(KOH)$ and $J_{photo}(KOH + \text{H}_2\text{O}_2)$ were taken from the steady-state photocurrent densities at potentials between 0.6 and 1.5 V vs RHE (Figure 3.10 a-d). As shown in Figure 3.11 a, the CoFeO_x layer enhances the charge injection efficiency of holes at the semiconductor/electrolyte interface.

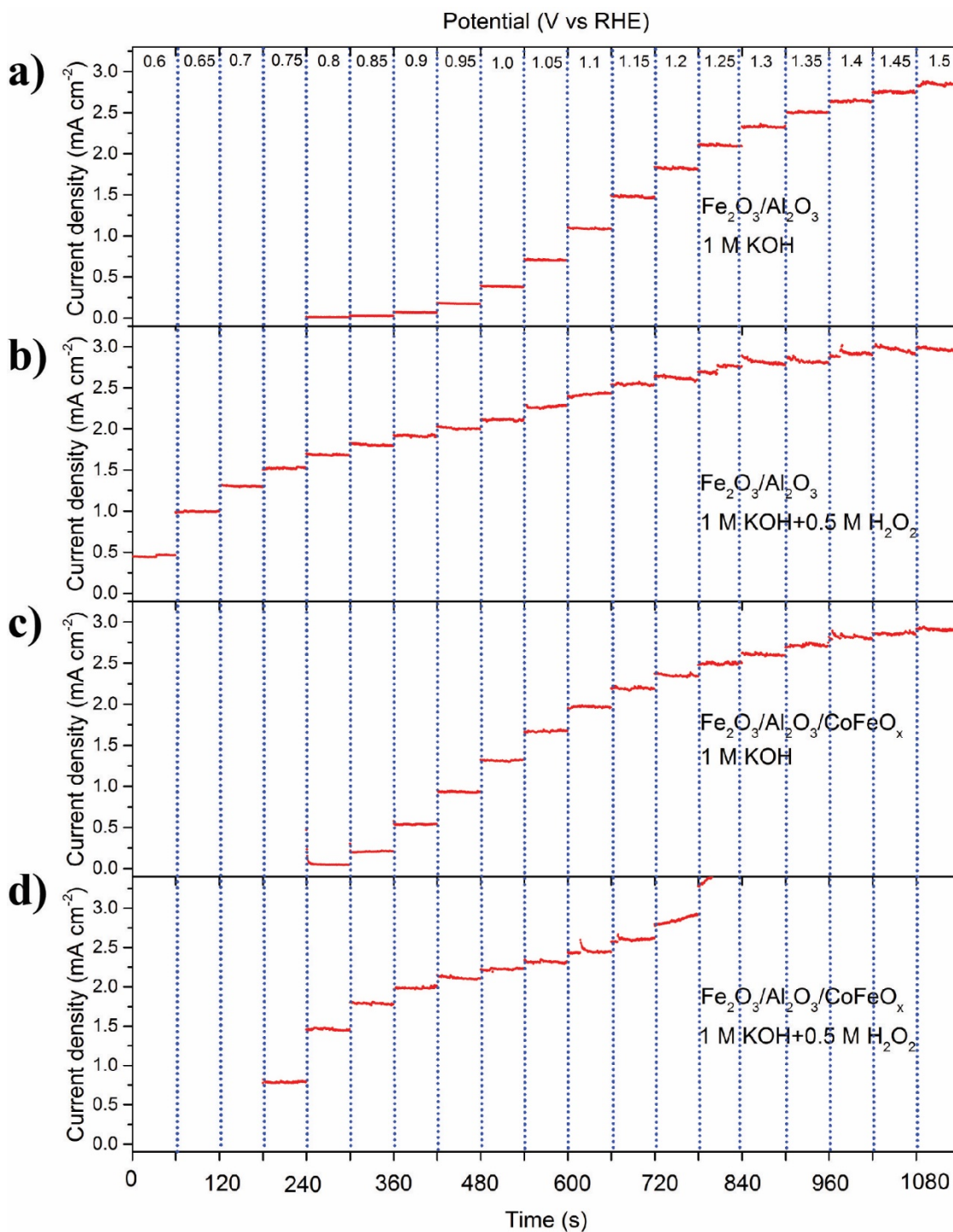


Figure 3.10 Steady-state photocurrents measured by chronoamperometry between 0.6 and 1.5 V vs RHE of **a)** $\text{Fe}_2\text{O}_3/\text{Al}_2\text{O}_3$ in 1 M KOH, **b)** $\text{Fe}_2\text{O}_3/\text{Al}_2\text{O}_3$ in 1 M KOH + 0.5 M H_2O_2 , **c)** $\text{Fe}_2\text{O}_3/\text{Al}_2\text{O}_3/\text{CoFeO}_x$ in 1 M KOH and **d)** $\text{Fe}_2\text{O}_3/\text{Al}_2\text{O}_3/\text{CoFeO}_x$ in 1 M KOH + 0.5 M H_2O_2 .

At 1.0 V vs RHE, the charge injection efficiency is increased from 15 % for the catalyst-free hematite to 57 % for the CoFeO_x-coated hematite. Faster OER kinetics or slower recombination on the surface can explain this significant increase in η_{inj} . Additionally, when CoFeO_x is present, η_{inj} reaches its maximum value and plateaus at approximately 1.15 V vs RHE. This indicates that both photocurrents, in 1 M KOH and in 1 M KOH + 0.5 M H₂O₂ (Figure 3.10 c and d), converge and the applied potential is sufficient enough to suppress recombination at surface trap states. Interestingly, when looking at the charge separation efficiency (η_{sep}) in Figure 3.11 b, two trends can be observed. At potentials above 0.85 V vs RHE, the CoFeO_x layer does not influence the separation efficiency of the hematite. This result is expected as only the surface properties should be modified by the deposition of this oxide layer and bulk charge dynamics of hematite should remain unaffected. However, at potentials lower than 0.85 V vs RHE, the CoFeO_x hematite has a lower charge separation efficiency compared to the catalyst-free hematite. This could arise from increased interfacial recombination between hematite surface and the CoFeO_x overlayer. In contrast to previous reports of cobalt-based catalysts on photoanodes, the charge separation results here suggest that CoFeO_x does not promote charge separation in the bulk by the formation of a p-n junction.^[16,28]

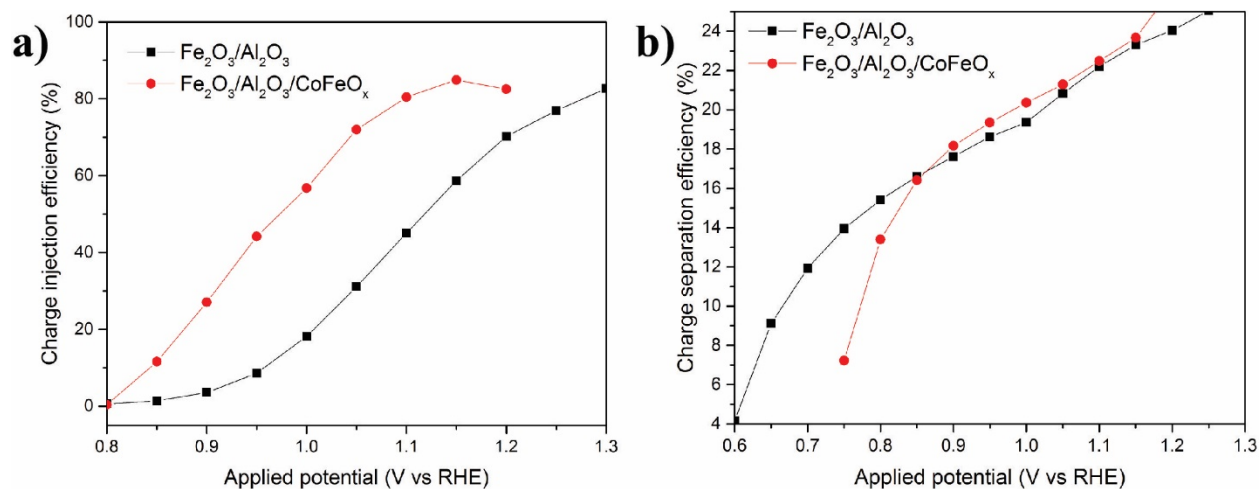


Figure 3.11 a) Charge injection efficiency of Fe₂O₃/Al₂O₃ and Fe₂O₃/Al₂O₃/CoFeO_x. b) Charge separation efficiency of Fe₂O₃/Al₂O₃ and Fe₂O₃/Al₂O₃/CoFeO_x.

We also used photoluminescence (PL) in order to determine whether the CoFeO_x coating could passivate hematite surface states,^[16,29] which also could potentially account for the observed cathodic shift in onset potential. As deposited here, the Al_2O_3 layer is expected to only partially suppress surface trap states of hematite as this layer is not expected to be fully conformal, owing to the low number of ALD cycles used. Therefore, some trap states of hematite could still be present and passivated when CoFeO_x is deposited, Photoluminescence is typically not observed in bulk hematite. After absorption of a photon with energy greater than the bandgap, photo-generated electron-hole pairs recombine in a non-radiative process due to efficient lattice and magnetic relaxation pathways.^[18] However, photoluminescence has been observed in hematite nanocrystals capped with specific surface agent and is largely dependent on surface quality and especially on the density of trap states.^[30] Consequently, if CoFeO_x is able to passivate surface states, photoluminescence emission is expected to increase. Here, no difference of photoluminescence was observed before and after photoelectrodeposition of CoFeO_x on blank hematite or on $\text{Fe}_2\text{O}_3/\text{Al}_2\text{O}_3$ (Figure 3.12 a and b). Therefore, we ruled out that the cathodic shift of onset potential caused by CoFeO_x comes from a significant passivation of surface states. Moreover, when comparing the activity of $\text{Fe}_2\text{O}_3/\text{CoFeO}_x$ and $\text{Fe}_2\text{O}_3/\text{Al}_2\text{O}_3/\text{CoFeO}_x$, the onset potential is the same but a difference in fill factor is observed (Figure 3.13). A higher fill factor is obtained when Al_2O_3 is deposited and the photocurrent density is increased from 1.2 to 1.6 mA cm^{-2} at 1.0 V vs RHE. This result suggests that Al_2O_3 and CoFeO_x play distinctive roles that have a synergetic effect in the enhancement of the hematite photoactivity.

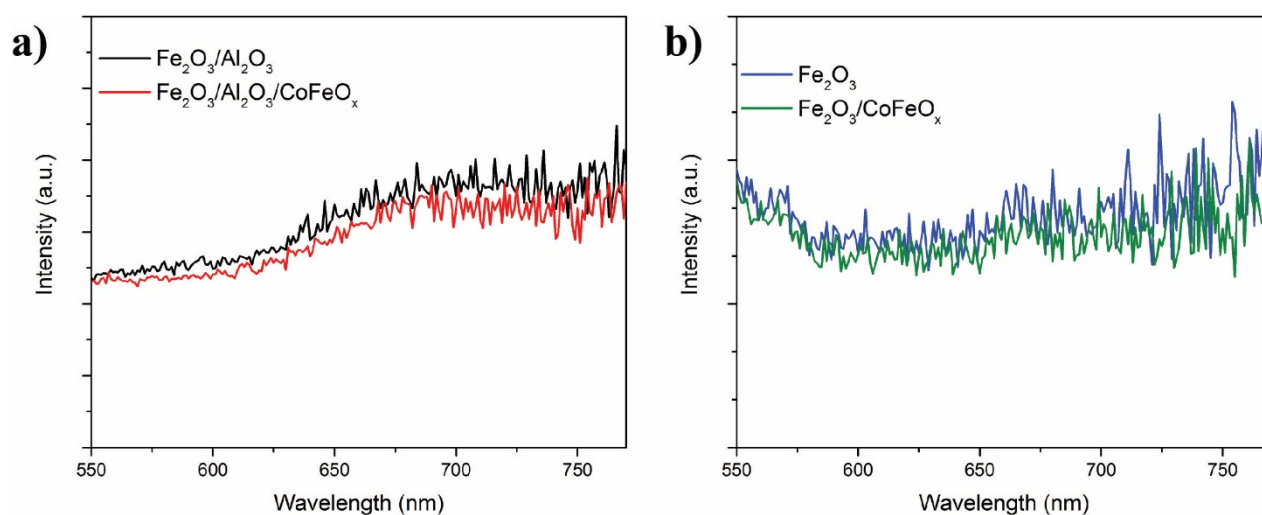


Figure 3.12 a) Photoluminescence emission spectra of catalyst-free and CoFeO_x -coated hematite photoanodes with Al_2O_3 and b) without Al_2O_3 .

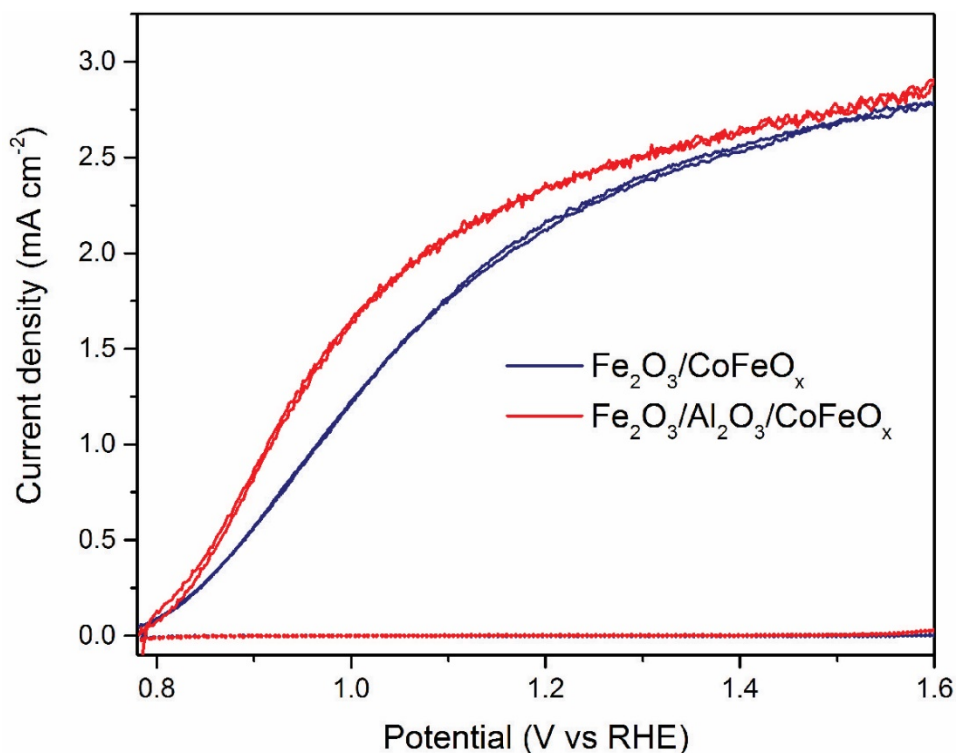


Figure 3. 13 Polarization curves under illumination (lines and in the dark (dotted lines) of CoFeO_x-coated hematite with and without Al₂O₃ in 1 M KOH.

Finally, Du *et al.* recently reported that the observed cathodic shift induced by transition metal oxides layers such as NiFeO_x on hematite was due to an increase in photovoltage, owing to a reduction of the surface Fermi level pinning effect.^[31] In our work, we do not observe the same effect in our system. Both Fe₂O₃/Al₂O₃ and Fe₂O₃/Al₂O₃/CoFeO_x anodes produce similar photovoltages, as seen in Figure 3.14 a and b, of 0.74 and 0.76 V, respectively.

Electrochemical impedance spectroscopy (EIS) under illumination was used to further investigate the PEC behavior of CoFeO_x on hematite. An equivalent circuit developed by Klahr *et al.* and widely used for hematite photoanodes (inset in Figure 3.15 d) was used to fit the impedance data.^[8,17,32-35] This equivalent circuit is composed of a capacitance of the surface states (C_{ss}), a space-charge capacitance (C_{sc}), a resistance to electron-hole recombination via surface states (R_{rec}), a solution resistance (R_s), as well as a charge-transfer resistance (R_{ct}). At different potentials,

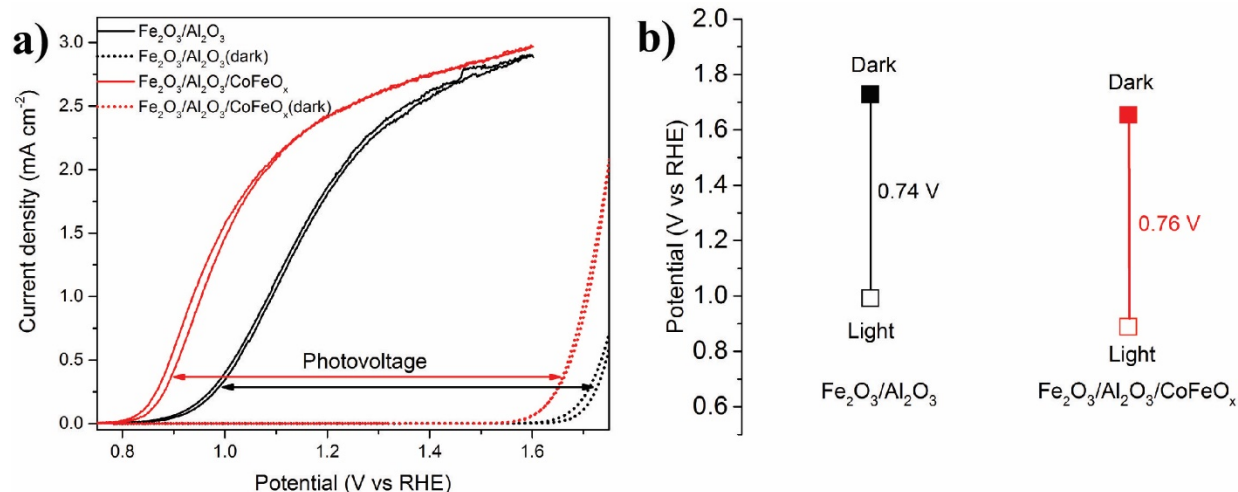


Figure 3. 14 a) Polarization curves in 1 M KOH under illumination and in the dark of catalyst-free and CoFeO_x-coated hematite. **b)** Corresponding extracted photovoltages of catalyst-free and CoFeO_x-coated hematite.

a change in the charge-transfer region of the Bode plot at frequencies between 0.1 and 10 Hz occurs for both Fe₂O₃/Al₂O₃ and Fe₂O₃/Al₂O₃/CoFeO_x (Figure 3.15 a). In the Nyquist plot, shown in Figure 3.16, the semicircle in the low-frequency region, usually associated with the charge-transfer resistance, is clearly smaller for the CoFeO_x-coated hematite anodes compared to the catalyst-free hematite. This translates into a reduction of R_{ct} by approximately one order of magnitude in the onset potential region when CoFeO_x is present (Figure 3.15 b). The recombination resistance (R_{rec}) remains on the same order of magnitude between the catalyst-free and the hematite coated with CoFeO_x (Figure 3.15 b). The charge-transfer rate constant k_{ct} can be obtained by the reciprocal of the time constant, τ , of the $R_{ct}C_{ss}$ unit ($\tau = R_{ct} \times C_{ss}$; $k_{ct} = (R_{ct} \times C_{ss})^{-1}$).^[36] When CoFeO_x is photoelectrodeposited, k_{ct} is increased in the 0.8-1.1 V vs RHE region compared to the catalyst-free hematite. (Figure 3.15 c), indicating that CoFeO_x promotes the oxidation reaction rate on the surface of the hematite photoanode in the onset potential region. The capacitance of the surface states C_{ss} shows a peak for both catalyst-free hematite and CoFeO_x-coated hematite that correlates with the rise of the photocurrent (Figure 3.15 d). By definition, the capacitance is related to the ability of a material to hold charges. In our case, the magnitude of C_{ss} for the coated hematite is greater than for without catalyst. This result suggests that CoFeO_x does not suppress but rather increases the concentration of surface states, possibly by forming oxidized intermediates that can

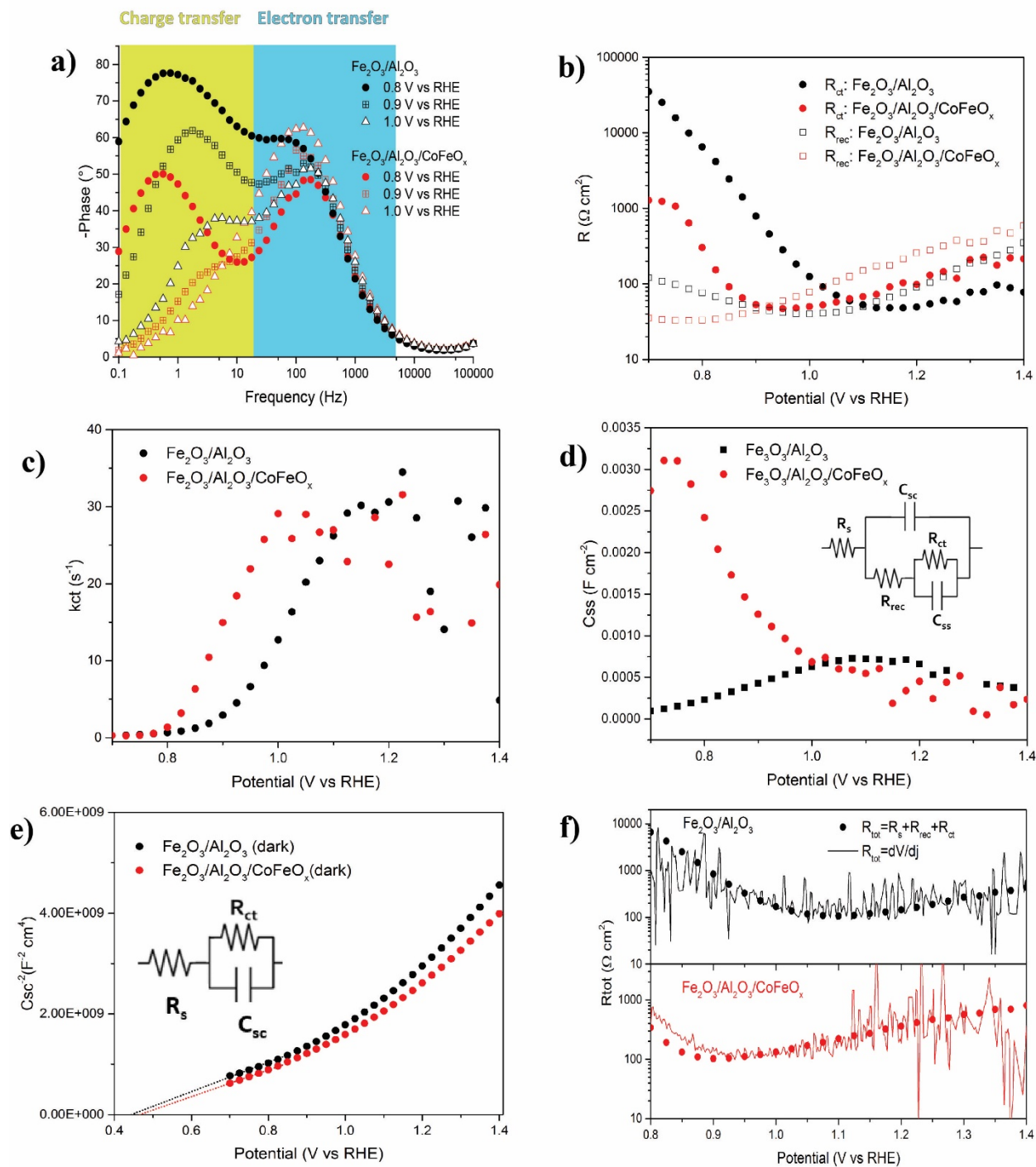


Figure 3.15 a) Bode plot of $\text{Fe}_2\text{O}_3/\text{Al}_2\text{O}_3$ and $\text{Fe}_2\text{O}_3/\text{Al}_2\text{O}_3/\text{CoFeO}_x$ at different potentials under illumination. b) Resistance to charge-transfer (R_{ct}) and resistance to recombination (R_{rec}) of $\text{Fe}_2\text{O}_3/\text{Al}_2\text{O}_3$ and $\text{Fe}_2\text{O}_3/\text{Al}_2\text{O}_3/\text{CoFeO}_x$ at different potentials under illumination. c) Charge-transfer rate constant (k_{ct}) at different potentials for $\text{Fe}_2\text{O}_3/\text{Al}_2\text{O}_3$ and $\text{Fe}_2\text{O}_3/\text{Al}_2\text{O}_3/\text{CoFeO}_x$ under illumination. d) Capacitance of the surface states at different applied potentials of $\text{Fe}_2\text{O}_3/\text{Al}_2\text{O}_3$ and $\text{Fe}_2\text{O}_3/\text{Al}_2\text{O}_3/\text{CoFeO}_x$ under illumination. e) Mott-Schottky plot of $\text{Fe}_2\text{O}_3/\text{Al}_2\text{O}_3$ and $\text{Fe}_2\text{O}_3/\text{Al}_2\text{O}_3/\text{CoFeO}_x$ in the dark. f) Comparison of the total resistance from impedance fits and from the derivative of the photocurrent as a function of the applied potential.

act as more efficient shuttles for transferring holes into the electrolyte. Additionally, the obtained C_{sc} values from impedance measurements in the dark were used in a Mott Schottky plot (Figure 3.15 e) to determine if CoFeO_x could shift the flat-band potential. Nyquist plots taken in the dark (inset in Figure 3.16) exhibit only one semicircle and were fitted by a simple Randles circuit (inset in Figure 3.16 e).^[35] The obtained Mott Schottky plots were super linear. Cesar *et al.* explained this curvature for the APCVD hematite as a decrease of the active surface area, contributing to a change in capacitance, due to depletion of the smallest features of the nanocrystals surface as the applied potential changes.^[6] C_{sc}^{-2} was fitted from 0.7 to 0.85 V vs RHE. This potential range was chosen in our analysis as Mott Schottky assumption of a flat surface is best approximated when the space charge layer is thin, close to the flat-band potential. Moreover, a roughness factor of 20 was taken into account to calculate from the geometrical surface area the total surface that is in contact with the electrolyte.^[6] Both $\text{Fe}_2\text{O}_3/\text{Al}_2\text{O}_3$ and $\text{Fe}_2\text{O}_3/\text{Al}_2\text{O}_3/\text{CoFeO}_x$ yield a flat-band potential close to 0.45 V vs RHE, which is similar to previously reported values for the APCVD hematite.^[6] Therefore, the CoFeO_x shifts the onset potential while leaving the flat-band potential unchanged. Finally, to confirm the validity of the fitting of the EIS measurements, the resistance from the derivative of the polarization curves ($R_{tot} = dV/dJ$) was plotted and compared to the total resistance from impedance ($R_{tot} = R_s + R_{rec} + R_{ct}$). For both catalyst-free and CoFeO_x hematite, R_{tot} matches reasonably well (Figure 3.15 f).

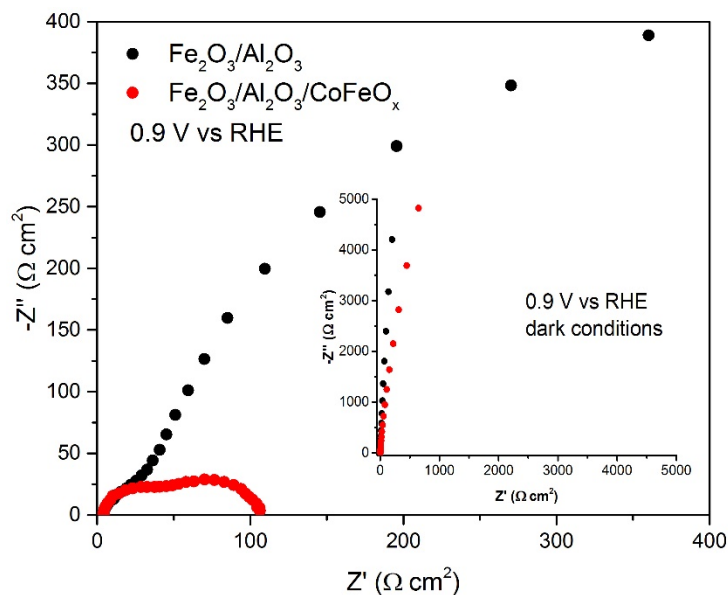


Figure 3.16 $\text{Fe}_2\text{O}_3/\text{Al}_2\text{O}_3$ and $\text{Fe}_2\text{O}_3/\text{Al}_2\text{O}_3/\text{CoFeO}_x$ at 0.9 V vs RHE in 1 M KOH under illumination and in the dark (inset).

3.5 Conclusions

Motivated by the high electrocatalytic activity of the oxidatively electrodeposited CoFeO_x OER catalyst, we developed a photoelectrodeposition method to apply this material on APCVD nanostructured hematite photoanodes. An amorphous, ultrathin (< 1 nm) and optically transparent layer of CoFeO_x was yielded by the optimized photoelectrodeposition. Compared to the catalyst-free hematite, the CoFeO_x -coated hematite provided a substantial 200 mV cathodic shift of the photocurrent onset potential and a stable 8-fold increase in photocurrent density at 1.0 V vs RHE. The CoFeO_x increased the charge injection efficiency at the semiconductor/electrolyte interface by reducing the charge-transfer resistance. Moreover, neither modification of the flat-band potential, photovoltage nor passivation of the surface states were observed upon deposition of CoFeO_x . Together, these results suggest that the enhancement of the PEC activity due to the CoFeO_x overlayer purely arises from a catalytic effect.

3.6 Experimental section

All reagents were purchased from commercial sources and used without additional purification. 18.2 M Ω ·cm Millipore deionized water was used to prepare all the solutions.

Photoelectrochemical experiments

All electrochemical experiments (deposition of catalyst and photoelectrochemical characterization) were performed by using an Autolab PGSTAT302N potentiostat/galvanostat (Metrohm). Electrodes were illuminated from the front side (photoanode/electrolyte interface) with a 450 W Xenon lamp (LAX 1450, Müller Elektronik-Optik) equipped with a KG3 filter (3 mm, Schott) in order to simulate the AM 1.5G spectrum. The light intensity at the electrode surface was adjusted to 100 mW cm⁻² with a calibrated Si solar cell (Newport, calibrated by Newport Corporation PV Lab).

A three-electrode setup was used with the hematite substrate as the working electrode, a platinum wire (for OER measurements) or a titanium wire (for deposition of the CoFeO_x catalyst) as the counter electrode, and an Ag/AgCl (sat. KCl) reference electrode. The hematite substrate was connected to the working electrode contact with a crocodile clip. All measured potentials were converted to the reversible hydrogen electrode scale (RHE) by using the formula $E(\text{RHE}) = E(\text{Ag/AgCl}) + 0.197 + 0.0592 \cdot \text{pH}$. The surface area of the hematite electrodes was delimited with black epoxy glue (Loctite EA9461), with values typically between 0.07 and 0.15 cm².

Photocurrent onset potentials were determined by extrapolating to zero current the linear portion of the J-V curve between 0.5 and 1.5 mA cm⁻².^[12] Photovoltages were determined by subtraction of the potentials to reach 0.3 mA cm⁻² under dark and illumination conditions, respectively.^[37]

APCVD hematite photoanode preparation

An atmospheric pressure chemical vapor deposition process (APCVD) was used to prepare the Si-doped cauliflower hematite samples. The procedure has been described previously by our group.^[10] Briefly, fluorine-doped tin oxide substrates (FTO, TEC 15, Sigma-Aldrich) were put on a hot plate at 545 °C in air for 90s. Argon was bubbled through

tetraethyl orthosilicate (TEOS, >99.0%, Aldrich) and iron pentacarbonyl (FeCO_5 , >99.99%, Aldrich). For the first 90 s, only TEOS vapors were carried from the bubbler and mixed with a flow of air over the hot FTO substrate to form a SiO_2 underlayer, and then TEOS and iron pentacarbonyl vapors were mixed together to grow the nanostructured cauliflower Si-doped hematite for another 90 s. The as-prepared hematite was left on the hot plate for an additional 90 s as an annealing step. The Fe_2O_3 photoanodes were later thermally activated in air on a hot plate for 20 min at 300 °C to increase reproducibility between samples. The top edge of the photoanodes were washed with HCl 6M prior to catalyst deposition to remove all traces of Fe_2O_3 in order to minimize contact resistance with the crocodile clip.

Al_2O_3 overlayer

The deposition of Al_2O_3 was performed in order to improve the performance of the APCVD nanostructured hematite photoanodes. Slightly modified conditions from those previously reported were used.^[18] The Fe_2O_3 photoanodes were loaded in a custom-made hot-wall ALD system (see chapter 2) with the vacuum chamber heated at 130 °C. Six cycles were used to deposit thin Al_2O_3 layers. Each cycle was composed of a 0.05 s pulse of trimethylaluminum (TMA, >98%, Strem Chemicals INC) followed by a 15 s nitrogen purge, and then by a 0.5 s pulse of H_2O_2 (50 wt%, Sigma-Aldrich) followed by a 15 s nitrogen purge. The nitrogen flow was kept a 20 mL s^{-1} during the deposition. The growth per cycle rate of the ALD process was 0.19 nm per cycle. After the ALD deposition, the samples were annealed for 5 min at 350°C in air on a hot plate. Control samples without Al_2O_3 were also annealed with the same procedure.

Catalyst deposition

For the deposition of the CoFeO_x catalyst, an aqueous solution containing 16 mM of cobalt(II) chloride (CoCl_2 , anhydrous, >98%, Fluka) and 5 mM of iron(III) sulfate ($\text{Fe}_2(\text{SO}_4)_3$, hydrate, 97%, Sigma-Aldrich) was prepared in 0.1 M sodium acetate (anhydrous, >99%, Sigma-Aldrich). The hematite substrate was immersed in the as-prepared solution and the deposition of CoFeO_x was performed by linear sweep voltammetry (LSV), scanning the potential from 1.1 to 1.7 V vs RHE at 200 mV s^{-1}

(typically for 1–10 sweeps) under simulated AM 1.5G illumination. The hematite substrate was fully illuminated and the deposition of the CoFeO_x occurred on the whole substrate area (ca. 1.5 cm^2). Only after deposition, the surface was delimited by black epoxy glue (Loctite EA9461) before proceeding with further characterizations.

The CoO_x catalyst for control samples was photoelectrodeposited with the same procedure as the CoFeO_x except that no iron(III) sulfate was added to the deposition solution.

CoFeO_x was electrodeposited by LSV either from 1.7 to 2.0 V vs RHE (scan rate 10 mV s^{-1}), from 1.1-1.7 V vs RHE (scan rate 200 mV s^{-1}) or from 1.8-2.4 V vs RHE (scan rate 200 mV s^{-1}). Those conditions were chosen according to our previous work on electrodeposited metal oxides (for the 1.7-2.0 V vs RHE deposition)^[13] and based on the photoelectrodeposited conditions previously described in this section (1.1-1.7 and 1.8-2.4 V vs RHE) by correcting the potential window with the measured photovoltage (ca. 0.7 V, *vide supra*). The NiFeO_x and Co-Pi catalysts were deposited on APCVD nanostructured hematite with photoelectrodeposition methods described previously by our group.^[9,12]

Characterization

SEM images were obtained with a Zeiss Merlin microscope operated at 2 kV and equipped with an Inlens secondary electron detector. TEM and STEM-EDX images were recorded with a FEI Talos operated at 200 kV. TEM samples were prepared by drop-drying a solution containing the hematite particles onto carbon-coated copper grids. The solution was obtained by sonicating a piece of the hematite sample twice for 30 minutes in MeOH.

XPS analysis was carried out using a PHI VersaProbe II scanning XPS microprobe equipped with a monochromatic Al $K\alpha$ source of 24.8 W with a beam size of $100 \mu\text{m}$. The adventitious carbon 1s peak was calibrated at 284.8 eV and used as an internal standard to compensate for charging effects. Data were fitted by using PHI MultiPak software.

Photoluminescence measurements were obtained with a Horiba Fluorolog 3-22 spectrofluorometer using a 520 nm excitation wavelength (5 nm bandpass at entrance and exit) and front face detection with a standard photomultiplier detector. The emission was scanned from 550 to 780 nm (1 nm increment and 0.1 s integration time).

Electrochemical impedance spectroscopy measurements

The electrochemical impedance spectroscopy (EIS) response of the different hematite photoanodes was measured between 0.7 and 1.4 V vs RHE every 25 mV in 1 M KOH solution under simulated AM 1.5G illumination. The photoanode was let to stabilize for 60 s between each potential step. The EIS response was recorded from 100,000 Hz to 0.1 Hz with 8 points per decade. The data were fitted with Zview software.

Faradaic efficiency measurements

The faradaic yield was evaluated by using an optical fluorescence sensor (Ocean Optics) and an airtight glass H-cell. The cell was purged with N₂ prior to the measurement in order to have an O₂ content lower than 0.5 %. The measurement was done at 1.23 V vs RHE in 1 M KOH.

3.7 Contributions

Laurent Liardet and Jordan E. Katz fabricated the materials and tested the photoelectrochemical activity. Laurent Liardet characterized the structure and the composition of the materials. Xile Hu, Michael Grätzel, Jingshan Luo, Jordan E. Katz and Laurent Liardet analyzed the data and wrote the corresponding paper.

3.8 References

- [1] Hans Wedepohl, K. The composition of the continental crust. *Geochimica et Cosmochimica Acta* **59**, 1217-1232,(1995).
- [2] Sivula, K., Le Formal, F. & Grätzel, M. Solar Water Splitting: Progress Using Hematite (α -Fe₂O₃) Photoelectrodes. *ChemSusChem* **4**, 432-449,(2011).
- [3] Kay, A., Cesar, I. & Grätzel, M. New Benchmark for Water Photooxidation by Nanostructured α -Fe₂O₃ Films. *Journal of the American Chemical Society* **128**, 15714-15721,(2006).
- [4] Wheeler, D. A., Wang, G., Ling, Y., Li, Y. & Zhang, J. Z. Nanostructured hematite: synthesis, characterization, charge carrier dynamics, and photoelectrochemical properties. *Energy & Environmental Science* **5**, 6682-6702,(2012).
- [5] Sivula, K. *Nanostructured α -Fe₂O₃ photoanodes: In Van de Krol R. and Grätzel M. Photoelectrochemical Hydrogen Production.* (Springer, 2012).
- [6] Cesar, I., Sivula, K., Kay, A., Zboril, R. & Grätzel, M. Influence of Feature Size, Film Thickness, and Silicon Doping on the Performance of Nanostructured Hematite Photoanodes for Solar Water Splitting. *The Journal of Physical Chemistry C* **113**, 772-782,(2009).
- [7] Shen, S., Lindley, S. A., Chen, X. & Zhang, J. Z. Hematite heterostructures for photoelectrochemical water splitting: rational materials design and charge carrier dynamics. *Energy & Environmental Science* **9**, 2744-2775,(2016).
- [8] Riha, S. C., Klahr, B. M., Tyo, E. C., Seifert, S., Vajda, S., Pellin, M. J., Hamann, T. W. & Martinson, A. B. F. Atomic Layer Deposition of a Submonolayer Catalyst for the Enhanced Photoelectrochemical Performance of Water Oxidation with Hematite. *ACS Nano* **7**, 2396-2405,(2013).
- [9] Morales-Guio, C. G., Mayer, M. T., Yella, A., Tilley, S. D., Grätzel, M. & Hu, X. An Optically Transparent Iron Nickel Oxide Catalyst for Solar Water Splitting. *Journal of the American Chemical Society* **137**, 9927-9936,(2015).
- [10] Tilley, S. D., Cornuz, M., Sivula, K. & Grätzel, M. Light-Induced Water Splitting with Hematite: Improved Nanostructure and Iridium Oxide Catalysis. *Angewandte Chemie International Edition* **49**, 6405-6408,(2010).
- [11] Zhong, D. K. & Gamelin, D. R. Photoelectrochemical Water Oxidation by Cobalt Catalyst (“Co-Pi”)/ α -Fe₂O₃ Composite Photoanodes: Oxygen Evolution and Resolution of a Kinetic Bottleneck. *Journal of the American Chemical Society* **132**, 4202-4207,(2010).
- [12] Zhong, D. K., Cornuz, M., Sivula, K., Gratzel, M. & Gamelin, D. R. Photo-assisted electrodeposition of cobalt-phosphate (Co-Pi) catalyst on hematite photoanodes for solar water oxidation. *Energy & Environmental Science* **4**, 1759-1764,(2011).
- [13] Morales-Guio, C. G., Liardet, L. & Hu, X. Oxidatively Electrodeposited Thin-Film Transition Metal (Oxy)hydroxides as Oxygen Evolution Catalysts. *Journal of the American Chemical Society* **138**, 8946-8957,(2016).
- [14] Song, F., Bai, L., Moysiadou, A., Lee, S., Hu, C., Liardet, L. & Hu, X. Transition Metal Oxides as Electrocatalysts for the Oxygen Evolution Reaction in Alkaline Solutions: An Application-Inspired Renaissance. *Journal of the American Chemical Society* **140**, 7748-7759,(2018).

- [15] Bhandary, N., Singh, A. P., Ingole, P. P. & Basu, S. Enhancing the Photoelectrochemical Performance of a Hematite Dendrite/Graphitic Carbon Nitride Nanocomposite through Surface Modification with CoFeOx. *ChemPhotoChem* **1**, 70-75,(2017).
- [16] Xu, Y.-F., Wang, X.-D., Chen, H.-Y., Kuang, D.-B. & Su, C.-Y. Toward High Performance Photoelectrochemical Water Oxidation: Combined Effects of Ultrafine Cobalt Iron Oxide Nanoparticle. *Advanced Functional Materials* **26**, 4414-4421,(2016).
- [17] Zhang, J., García-Rodríguez, R., Cameron, P. & Eslava, S. Role of cobalt–iron (oxy)hydroxide (CoFeOx) as oxygen evolution catalyst on hematite photoanodes. *Energy & Environmental Science*,(2018).
- [18] Le Formal, F., Tetreault, N., Cornuz, M., Moehl, T., Gratzel, M. & Sivula, K. Passivating surface states on water splitting hematite photoanodes with alumina overlayers. *Chemical Science* **2**, 737-743,(2011).
- [19] Hisatomi, T., Le Formal, F., Cornuz, M., Brillet, J., Tetreault, N., Sivula, K. & Gratzel, M. Cathodic shift in onset potential of solar oxygen evolution on hematite by 13-group oxide overlayers. *Energy & Environmental Science* **4**, 2512-2515,(2011).
- [20] Le Formal, F., Sivula, K. & Grätzel, M. The Transient Photocurrent and Photovoltage Behavior of a Hematite Photoanode under Working Conditions and the Influence of Surface Treatments. *The Journal of Physical Chemistry C* **116**, 26707-26720,(2012).
- [21] Trotochaud, L., Mills, T. J. & Boettcher, S. W. An Optocatalytic Model for Semiconductor–Catalyst Water-Splitting Photoelectrodes Based on In Situ Optical Measurements on Operational Catalysts. *The Journal of Physical Chemistry Letters* **4**, 931-935,(2013).
- [22] Biesinger, M. C., Lau, L. W. M., Gerson, A. R. & Smart, R. S. C. Resolving surface chemical states in XPS analysis of first row transition metals, oxides and hydroxides: Sc, Ti, V, Cu and Zn. *Applied Surface Science* **257**, 887-898,(2010).
- [23] Moulder, J. F., Stickle, W.F., Sobol, P.E., Bomben, K.D. *Handbook of X-ray Photoelectron Spectroscopy*. (Physical Electronics, Inc, 1995).
- [24] Naumann, V., Otto, M., Wehrspohn, R. B., Werner, M. & Hagendorf, C. Interface and Material Characterization of Thin ALD-Al₂O₃ Layers on Crystalline Silicon. *Energy Procedia* **27**, 312-318,(2012).
- [25] McCrory, C. C. L., Jung, S., Peters, J. C. & Jaramillo, T. F. Benchmarking Heterogeneous Electrocatalysts for the Oxygen Evolution Reaction. *Journal of the American Chemical Society* **135**, 16977-16987,(2013).
- [26] Li, C., Luo, Z., Wang, T. & Gong, J. Surface, Bulk, and Interface: Rational Design of Hematite Architecture toward Efficient Photo-Electrochemical Water Splitting. *Advanced Materials* **30**, 1707502,(2018).
- [27] Dotan, H., Sivula, K., Gratzel, M., Rothschild, A. & Warren, S. C. Probing the photoelectrochemical properties of hematite ([small alpha]-Fe₂O₃) electrodes using hydrogen peroxide as a hole scavenger. *Energy & Environmental Science* **4**, 958-964,(2011).
- [28] Chang, X., Wang, T., Zhang, P., Zhang, J., Li, A. & Gong, J. Enhanced Surface Reaction Kinetics and Charge Separation of p–n Heterojunction Co₃O₄/BiVO₄ Photoanodes. *Journal of the American Chemical Society* **137**, 8356-8359,(2015).
- [29] Cao, D., Luo, W., Feng, J., Zhao, X., Li, Z. & Zou, Z. Cathodic shift of onset potential for water oxidation on a Ti⁴⁺ doped Fe₂O₃ photoanode by suppressing the back reaction. *Energy & Environmental Science* **7**, 752-759,(2014).

-
- [30] Zou, B. S. & Volkov, V. Surface modification on time-resolved fluorescences of Fe₂O₃ nanocrystals. *Journal of Physics and Chemistry of Solids* **61**, 757-764,(2000).
- [31] Du, C., Yang, X., Mayer, M. T., Hoyt, H., Xie, J., McMahon, G., Bischofing, G. & Wang, D. Hematite-Based Water Splitting with Low Turn-On Voltages. *Angewandte Chemie International Edition* **52**, 12692-12695,(2013).
- [32] Klahr, B., Gimenez, S., Fabregat-Santiago, F., Bisquert, J. & Hamann, T. W. Electrochemical and photoelectrochemical investigation of water oxidation with hematite electrodes. *Energy & Environmental Science* **5**, 7626-7636,(2012).
- [33] Klahr, B., Gimenez, S., Fabregat-Santiago, F., Bisquert, J. & Hamann, T. W. Photoelectrochemical and Impedance Spectroscopic Investigation of Water Oxidation with “Co–Pi”-Coated Hematite Electrodes. *Journal of the American Chemical Society* **134**, 16693-16700,(2012).
- [34] Le Formal, F., Pendlebury, S. R., Cornuz, M., Tilley, S. D., Grätzel, M. & Durrant, J. R. Back Electron–Hole Recombination in Hematite Photoanodes for Water Splitting. *Journal of the American Chemical Society* **136**, 2564-2574,(2014).
- [35] Steier, L., Herraiz-Cardona, I., Gimenez, S., Fabregat-Santiago, F., Bisquert, J., Tilley, S. D. & Grätzel, M. Understanding the Role of Underlayers and Overlayers in Thin Film Hematite Photoanodes. *Advanced Functional Materials* **24**, 7681-7688,(2014).
- [36] Peter, L. in *Photoelectrochemical Water Splitting: Materials, Processes and Architectures* Kinetics and Mechanisms of Light-Driven Reactions at Semiconductor Electrodes: Principles and Techniques 19-51 (RSC Publishing, 2013).
- [37] Dotan, H., Mathews, N., Hisatomi, T., Grätzel, M. & Rothschild, A. On the Solar to Hydrogen Conversion Efficiency of Photoelectrodes for Water Splitting. *The Journal of Physical Chemistry Letters* **5**, 3330-3334,(2014).
-

Chapter 4

Amorphous Cobalt Vanadium Oxide as Electrocatalyst for Oxygen Evolution

The results presented in this chapter were published in:

Liardet, L. and Hu, X., Amorphous Cobalt Vanadium Oxide as a Highly Active Electrocatalyst for Oxygen Evolution, *ACS Catalysis*, 2018, 8, 644-650. Reproduced by permission of the American Chemical Society.

4.1 Introduction

Vanadium-based materials have attracted a lot of attention due to their potential application in various domains such as supercapacitors,^[1-3] magnetic materials,^[4,5] photoluminescence,^[6] lithium ion batteries,^[7-9] as well as photo- and electrocatalysis for OER.^[10-12] This chapter focuses on the synthesis and development of a new OER catalyst composed of an amorphous cobalt vanadium oxide.

The development of OER catalysts is often based on empirical strategies. However, significant work has been done to search for theoretical guidelines for catalyst discovery. The "descriptor" approach is attractive as it allows systematic tuning of catalysts using only a single calculable or measurable parameter. Multiple descriptors have been proposed for OER catalysis. For example, successful descriptors are the M-OH bond strength, the e_g occupancy and the free energy difference $\Delta G_{O^*} - \Delta G_{OH^*}$.^[13-15]

Recently, our group measured and reported the intrinsic activity of a range of transition metal oxide thin films as catalysts for water oxidation. A correlation was obtained, in the form of a volcano plot (Figure 4.1), between the mass activity and the M-OH bond strength proposed by Bockris and Otagawa.^[13,16] With the descriptor approach, neither the nature of the active species nor the physical origins of the activity of mixed metal oxides is revealed. The active sites of extensively studied catalysts such as NiFeO_x and CoFeO_x is still under investigations and actively debated.^[17-20] However this descriptor can explain in a much simpler way the superior activity of CoFeO_x and NiFeO_x, compared to their respective unary oxides, by the fact that CoO_x and NiO_x are on a different branch of the volcano plot compared to FeO_x and therefore, their respective mixture may benefit from a balance of M-OH bond strengths to reach an optimal activity. The presence of trace amount of iron, due to accidental incorporation of Fe ions from commercial electrolytes, into transition metal oxide catalysts has been reported to greatly enhance their OER activity.^[20,21]

Given that the presence of Fe is essential in many mixed metal oxides catalytic materials, we became interested in studying and developing iron free oxides in order to enrich the repertoire of OER catalysts. As seen in Figure 4.1, VO_x sits on the same branch as FeO_x in the volcano plot. Therefore, we turned our attention on vanadium-containing oxides. As an early transition metal, vanadium is seldom explored as OER catalytic materials. Only a few recent studies have been

proposed on mixed metal oxides containing vanadium. For example, Sun and coworkers reported the promising OER activity of a NiV layered double hydroxides catalysts and Shi et al. showed that lepidocrocite VOOH was a competent OER catalyst.^[10,22]

According to the volcano plot in Figure 4.1, we hypothesized that CoVO_x might exhibit high OER activity since VO_x and CoO_x are sitting at the two opposite branches. We thus prepared a CoVO_x material in order to verify our hypothesis. This chapter focuses on the development, synthesis and characterization of CoVO_x . Two different approaches were used to produce CoVO_x : Electrodeposition (see section 4.2) and hydrothermal synthesis (see section 4.3).

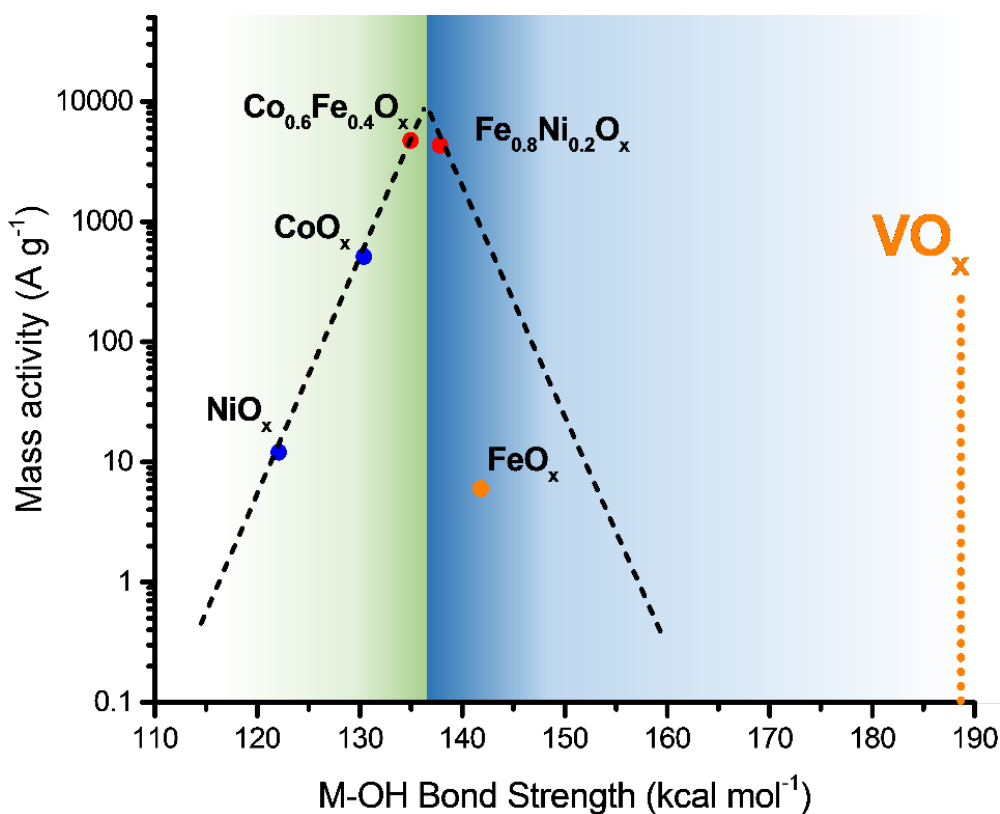


Figure 4.1 Volcano plot of OER activity versus M-OH bond strength, modified from ref. [16] with addition of theoretical M-OH bond strength of vanadium oxide (VO_x) from ref [13].

4.2 Electrodeposited cobalt vanadium oxide catalyst

Initially, we tried to deposit cobalt vanadium oxide with the oxidative electrodeposition method developed by our group.^[16] The electrodeposition was monitored by quartz crystal microbalance (QCM) and is shown in Figure 4.2 a. The CoVO_x layer grows rapidly in the initial linear sweeps (until a loading of approximately $5 \mu\text{g cm}^{-2}$ is reached) and then grows with a more constant trend. After 35 linear sweeps, the mass deposition slows down and the loading starts to plateau at approximately $25 \mu\text{g cm}^{-2}$. The OER activity of this CoVO_x material was evaluated in 1 M KOH (Figure 4.2 b). This catalysts reached 10 mA cm^{-2} at an overpotential of 410 mV. CoFeO_x was also evaluated in the same electrolyte in order to be compared with CoVO_x . CoFeO_x has a higher catalytic activity and reaches 10 mA cm^{-2} at an overpotential of 335 mV.

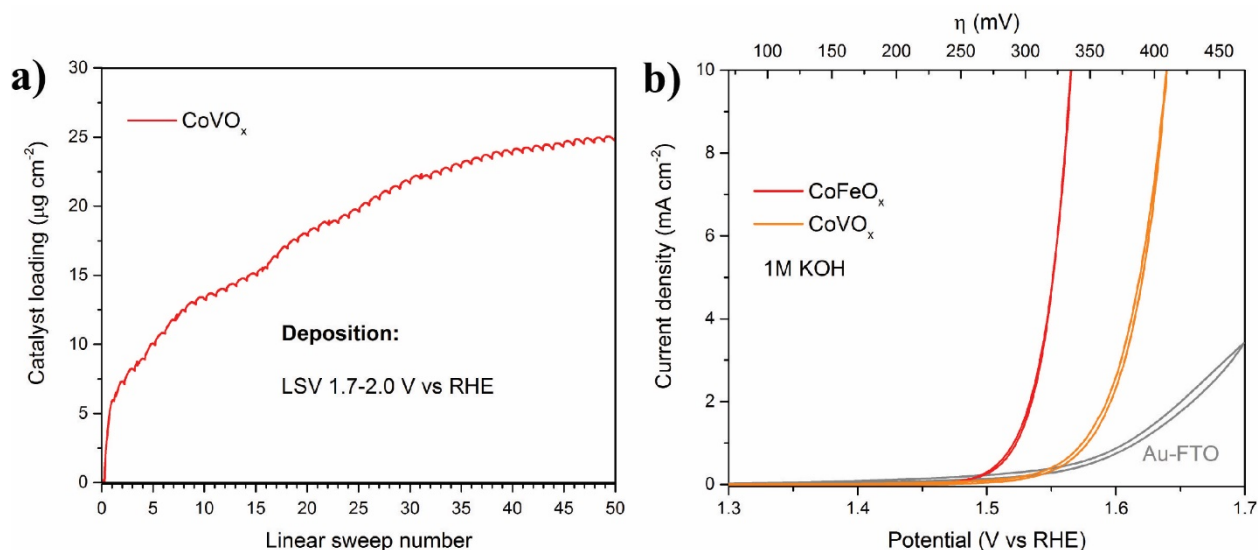


Figure 4.2 a) Evolution of the mass of CoVO_x film during oxidative electrodeposition. **b)** Polarization curves in 1 M KOH of CoVO_x and CoFeO_x electrodeposited on gold-coated FTO (Au-FTO, loading $20 \mu\text{g cm}^{-2}$). Scan rate: 10 mV s^{-1} , iR drop corrected.

The composition of the CoVO_x catalyst was determined by XPS for the as-deposited CoVO_x film (Figure 4.3 a-c). The binding energy (BE) of the Co $2p_{3/2}$ signal is located at 780.7 eV, indicating that Co^{2+} in the form of $\text{Co}(\text{OH})_2$ is present. Additionally, outer-shell excitation satellite peaks are visible at higher BE, indicating high-spin Co^{2+} (Figure 4.3 a).^[23] Vanadium is incorporated in the material in the form of both V^{4+} and V^{5+} , as suggested by the V $2p_{3/2}$ signals located at 516.8 and 517.8 eV, respectively (Figure 4.3 b).^[24,25] The O 1s spectra (Figure 4.3 c)

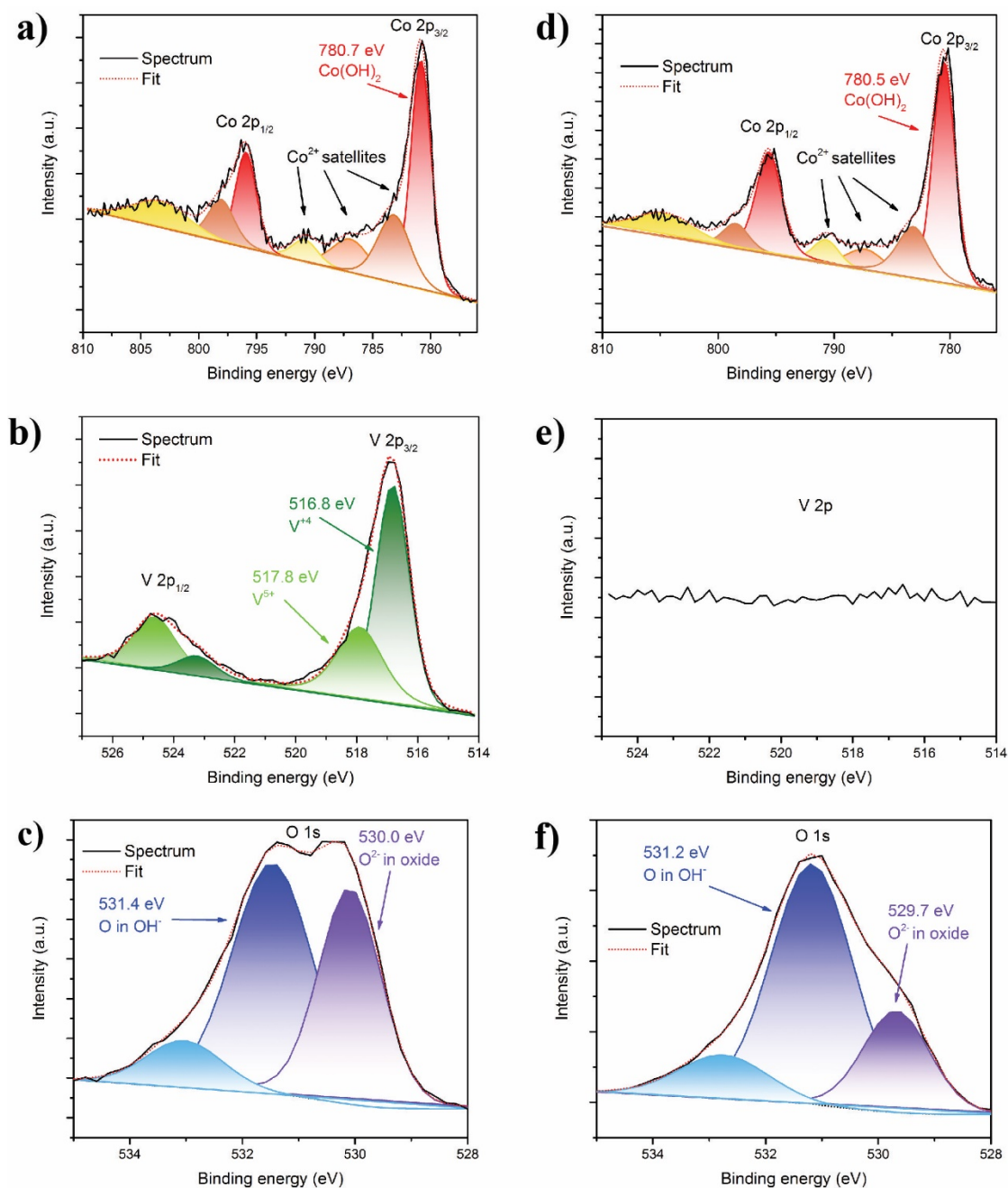


Figure 4.3 XPS spectra of as-deposited CoVO_x with high resolution spectra of **a)** Co 2p region, **b)** V 2p region and **c)** O 1s region. XPS spectra after polarization (30 CV) in 1 M KOH for **d)** Co 2p region, **e)** V 2p region and **f)** O 1s region.

indicates that both oxides (BE of 530.0 eV) and hydroxides (BE of 531.4 eV) are present. XPS was also performed on the same material after polarization by 30 CV in 1 M KOH (Figure 4.3 d-f). The Co 2p spectra (Figure 4.3 d) is similar than the one for the as deposited CoVO_x material

(Figure 4.3 a). The O 1s spectra (Figure 4.3 f) also shows that both hydroxides and oxides species are still present in the material, with a notable change in their ratio compared to the as deposited catalyst (Figure 4.3 c). When looking at the V 2p region of the CoVO_x after polarization (Figure 4.3 e) no vanadium peak is observed, suggesting that vanadium is not stable in the CoVO_x material and dissolves during OER.

Due to the moderate OER catalytic activity of CoVO_x and the depletion of vanadium from the CoVO_x structure, this electrodeposited CoVO_x was not further investigated. Hydrothermal synthesis, as a second synthetic strategy, was used in order to synthesize cobalt vanadium oxide and is explained in section 4.3 of this chapter.

4.3 Hydrothermally deposited cobalt vanadium oxide catalysts

In order to produce a binary metal oxide made of cobalt and vanadium, a similar hydrothermal synthesis procedure (see section 4.5) that the one used by Fan *et al.* to produce NiV LDH was used.^[10] In this chapter, each samples were tested in standard 1 M KOH and in purified Fe free KOH, where trace iron was removed according to a procedure reported by Trotochaud *et al.* in order to probe the OER activity of CoVO_x without parasitic Fe incorporation from the electrolyte.^[20]

4.3.1 Mixed-phase cobalt vanadium oxide

The initial hydrothermal method yielded a mixed phase cobalt vanadium oxide (named *m*-CoVO_x in this work due to its mixed phase composition, *vide infra*). This oxide exhibits high activity for water oxidation and can reach 10 mA cm⁻² at an overpotential of 366 and 358 mV in 1 M KOH and 1 M Fe free KOH electrolytes, respectively. The OER activity is shown in Fig 4.4 a and b. Control samples made with the unary metal oxide constituents of *m*-CoVO_x (CoO_x and VO_x) were also synthesized. Both of them required higher overpotentials for reaching the same current density in both 1 M KOH and 1 M Fe free KOH. Additionally, the overpotentials to reach 10 mA cm⁻² for *m*-CoVO_x do not differ significantly whether trace amount of iron is present or not in the KOH electrolyte. Therefore, iron incorporation does not seem to play an important role in the OER activity of this catalyst, in comparison to NiO_x.^[20,26,27] Tafel slopes (Figure 4.4 c) were extracted

and are 65 (63) mV dec⁻¹ for *m*-CoVO_x, 97 (142) mV dec⁻¹ for VO_x and 57 (59) mV dec⁻¹ for CoO_x in standard 1 M KOH (with Fe free KOH values in parentheses).

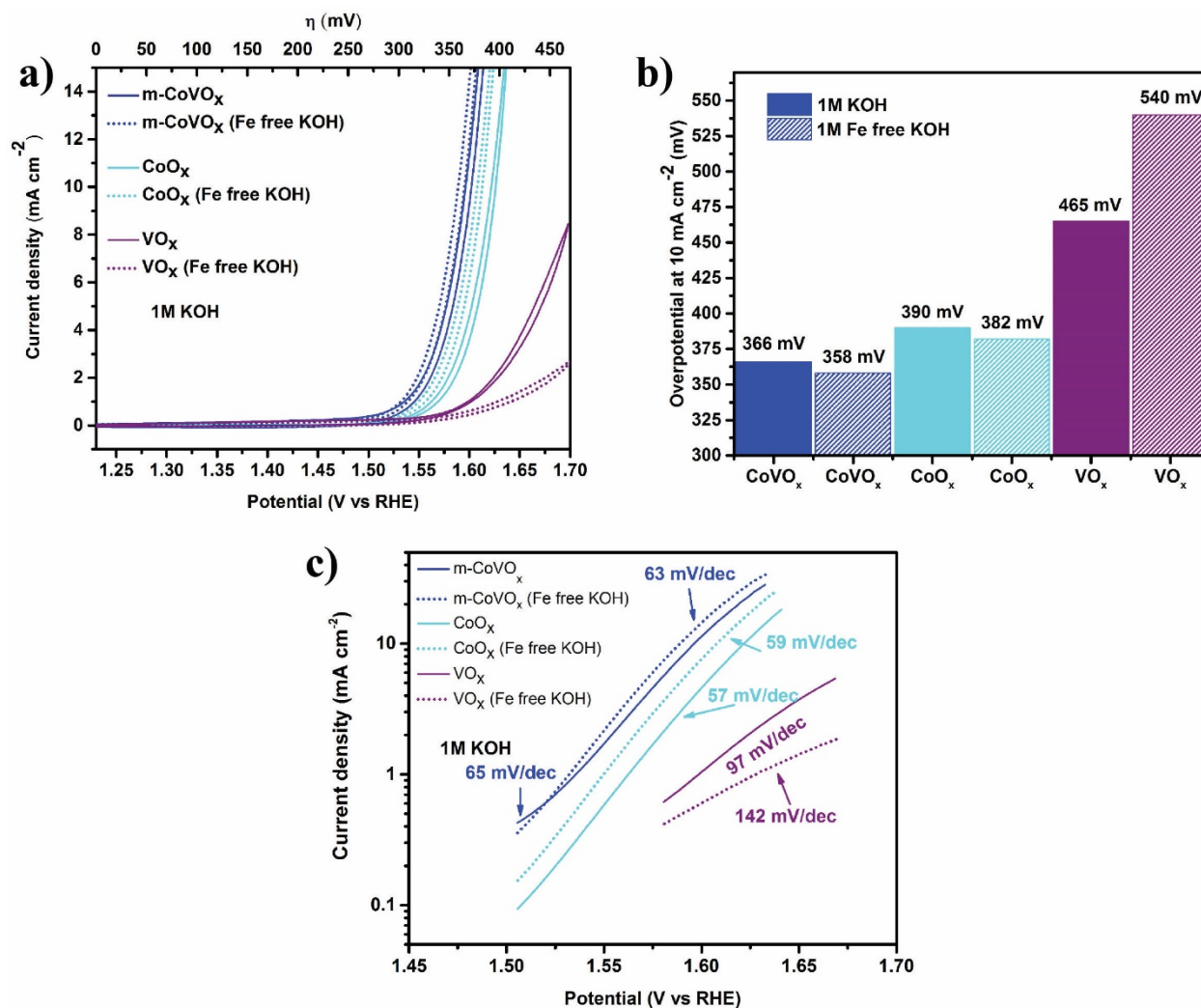


Figure 4.4 a) Polarization curves for *m*-CoVO_x, CoO_x and VO_x on glassy carbon (loadings 140 μg cm⁻²) in 1 M KOH and 1 M Fe Free KOH. Scan rate: 10 mV s⁻¹, iR drop corrected. b) Extracted overpotentials at 10 mA cm⁻². c) Tafel slopes for *m*-CoVO_x, CoO_x and VO_x in 1 M KOH and 1 M Fe Free KOH.

The crystallinity and composition of for *m*-CoVO_x and both control samples (CoO_x and VO_x) were analyzed by X-ray diffraction (XRD). All three samples show evidence of crystallinity (Figure 4.5 a). The *m*-CoVO_x material has similar diffractions peaks than those of the control CoO_x sample (Figure 4.5 b) and no crystalline phase of cobalt vanadium oxide could be identified in the XRD pattern of *m*-CoVO_x. The CoO_x control sample (Figure 4.5 c) exhibits diffraction peaks that correspond to a cobalt chloride carbonate hydroxide hydrate phase (Co(CO₃)_{0.35}Cl_{0.2}(OH)_{1.10} · 1.74

H₂O, JCPDS: 00-038-0547). The crystallinity of the *m*-CoVO_x sample is thus presumed to arise from this cobalt carbonate hydroxide hydrate phase, but not from a crystalline cobalt vanadium oxide. The vanadium oxide control sample (VO_x) was identified as the haggite phase (V₂O₂(OH)₃, JCPDS: 01-072-1228) (Figure 4.5 d).

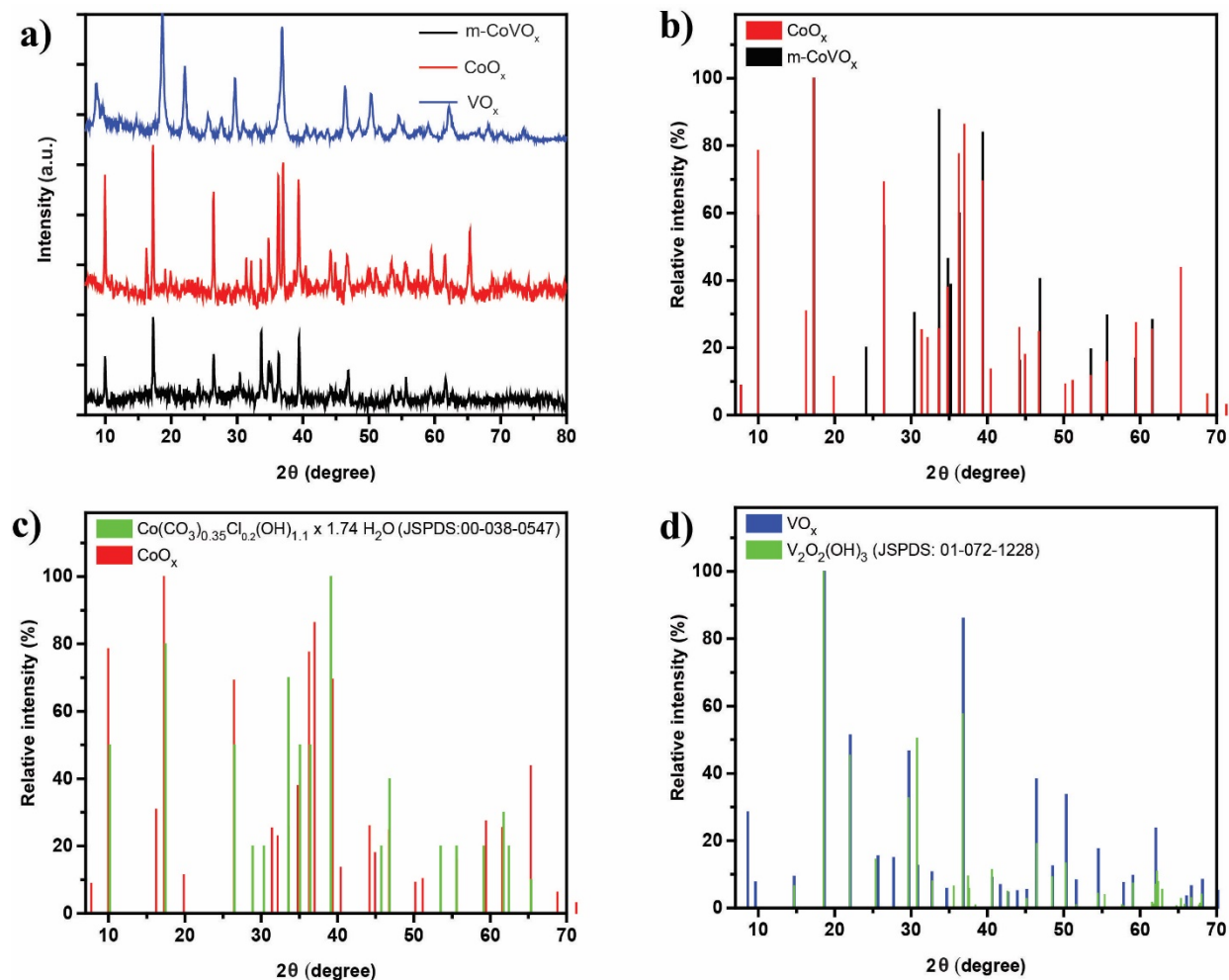


Figure 4.5 a) XRD patterns of *m*-CoVO_x, CoO_x and VO_x. b) Comparison of extracted diffraction peaks of *m*-CoVO_x and CoO_x. c) Comparison of extracted diffraction peaks of CoO_x and Co(CO₃)_{0.35}Cl_{0.2}(OH)_{1.1} · 1.74 H₂O. d) Comparison of extracted diffraction peaks of VO_x and V₂O₂(OH)₃.

The morphology of the different metal oxides was probed by SEM and is shown in Figure 4.6 a. Two different structures were observed in the *m*-CoVO_x material. The first one is composed of nanoneedles and the second one is composed of a more disorganized phase (highlighted red and in blue in the SEM image, respectively). This result gives an additional indication that the *m*-CoVO_x material is not constituted of a single phase but is a mixture of different materials. The

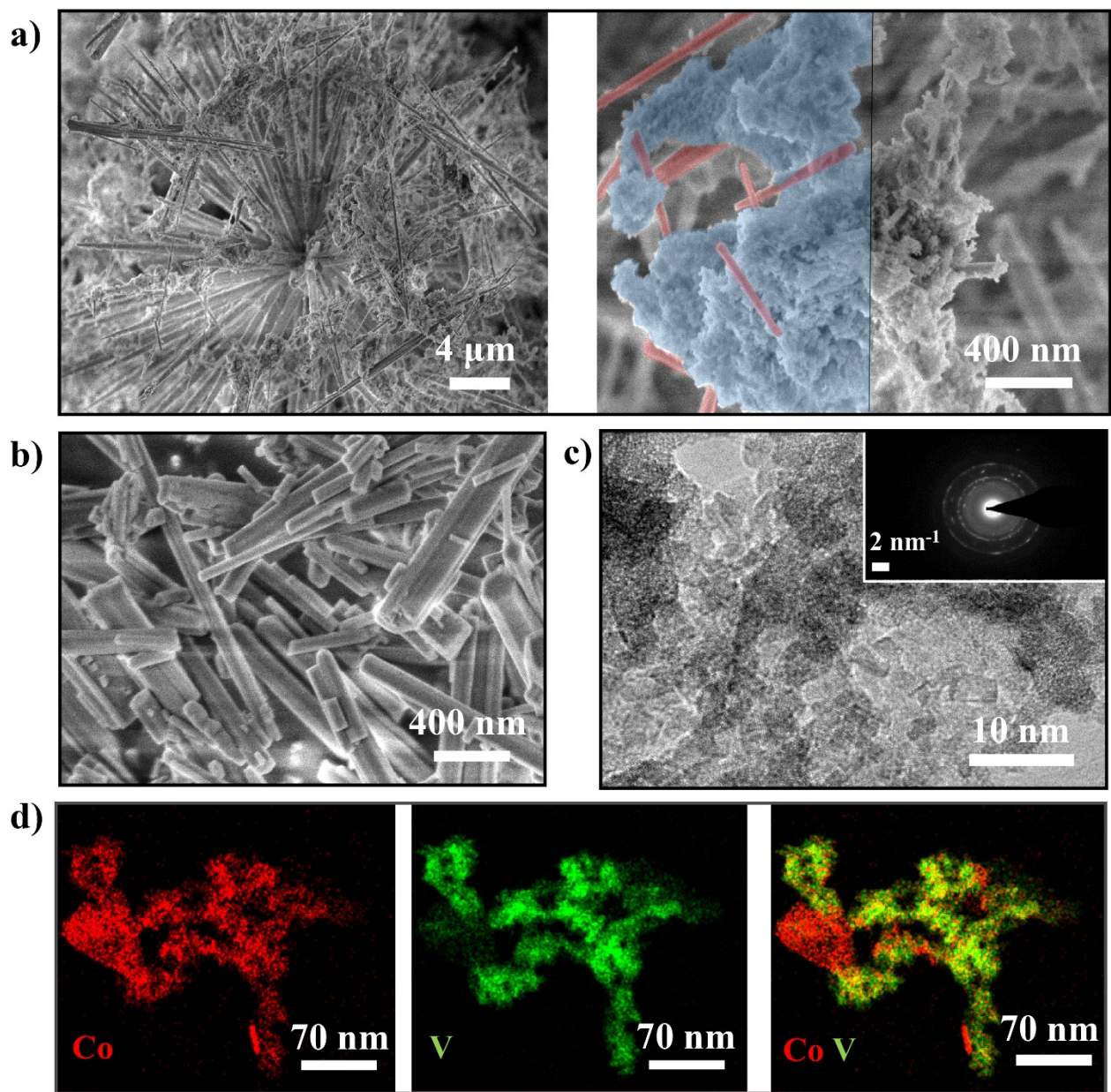


Figure 4.6 a) SEM images of $m\text{-CoVO}_x$. The nanoneedles are highlighted in red and the disorganized phase in blue. b) SEM image of CoO_x . c) TEM image and SAED pattern (inset) of $m\text{-CoVO}_x$. d) STEM-EDX mapping of $m\text{-CoVO}_x$.

nanoneedle phase can be attributed to the cobalt chloride carbonate hydroxide hydrate phase by comparison with the SEM image of the CoO_x control sample shown in Figure 4.6 b. TEM analysis of the disorganized phase (Figure 4.6 c) reveals its polycrystalline nature as lattice fringes can be observed in the HR-TEM image and as seen in the SAED pattern (inset in Figure 4.6 c). STEM-EDX mapping was also performed on the disorganized phase (Figure 4.6 d). Cobalt and vanadium

are continuously observed as a mixture and the cobalt chloride carbonate hydroxide hydrate phase can be seen as red particles on the Co-V map. Therefore, the $m\text{-CoVO}_x$ catalyst is here composed of a heterogeneous mixture with an X-ray amorphous phase containing cobalt and vanadium and a crystalline cobalt chloride carbonate hydroxide hydrate phase.

The hydrothermal method was further used in order to grow the $m\text{-CoVO}_x$ material directly on nickel foam (NF). As seen on SEM images represented in Figure 4.7, the deposited catalyst is also composed of a heterogeneous mixed phase which is composed of microscopic square crystals and intricate nanoleaves. The $m\text{-CoVO}_x$ on nickel foam reaches 10 mA cm^{-2} at overpotentials of 293 and 298 mV in 1 M KOH and 1 M Fe free KOH, respectively (Figure 4.8 a). Tafel slopes for $m\text{-CoVO}_x$ on nickel foam are 49 mV dec^{-1} and 67 mV dec^{-1} in 1 M KOH and 1 M Fe free KOH (inset in

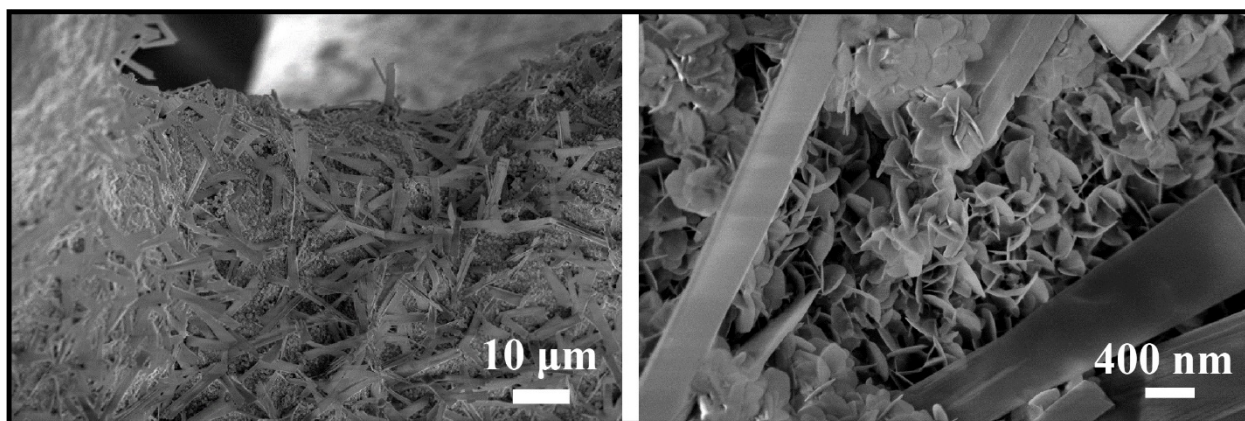


Figure 4.8 SEM images of $m\text{-CoVO}_x$ deposited on nickel foam.

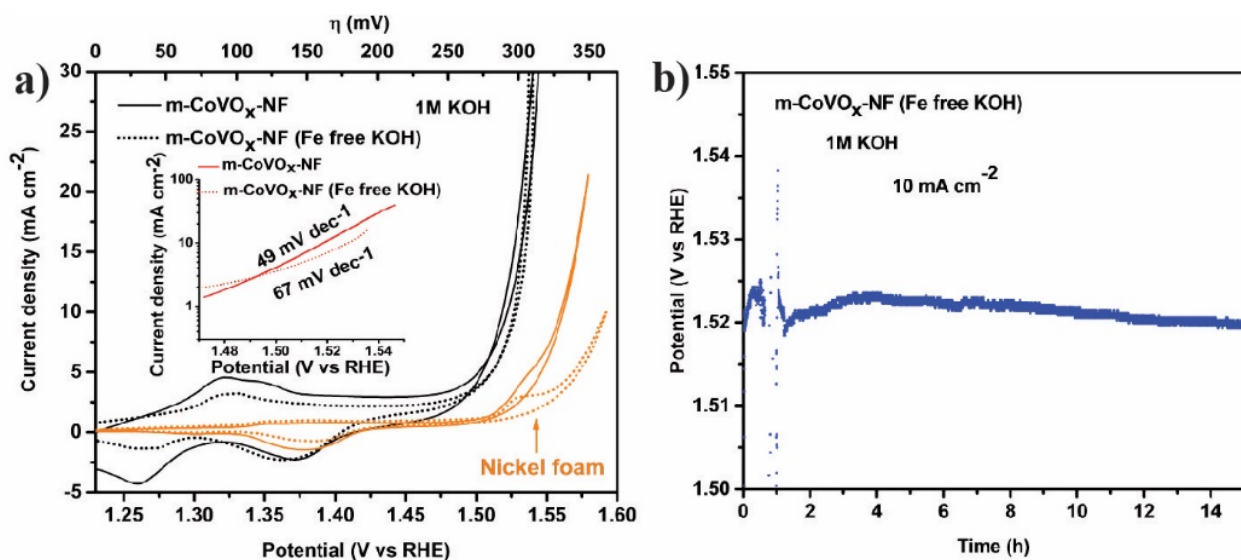


Figure 4.7 a) Polarization curves for $m\text{-CoVO}_x$ on nickel foam and extracted Tafel slopes in 1 M KOH and 1 M Fe free KOH. Scan rate: 1 mV s^{-1} , iR drop corrected. b) Stability of $m\text{-CoVO}_x$ on nickel foam at 10 mA cm^{-2} in 1 M Fe free KOH.

Figure 4.8 a). The stability of this catalyst was evaluated by monitoring the potential at a fixed current density of 10 mA cm^{-2} . No significant changes were observed during 15 h of electrolysis (Figure 4.8 b), indicating good stability.

4.3.2 Pure-phase amorphous cobalt vanadium oxide

The $m\text{-CoVO}_x$ catalyst contains a crystalline cobalt oxide that was less active towards OER than the mixed phase composed of cobalt and vanadium (see section 4.3.1). We considered this cobalt phase as an impurity and focused our efforts in synthesizing a pure single-phase cobalt vanadium oxide material in order to reach a higher activity. This was successful by using the same hydrothermal method but with addition of trisodium citrate as an additive. Different ratios of cobalt and vanadium salts were used in order to optimize the catalytic activity by tuning the composition of the cobalt vanadium oxide. Five different ratios of cobalt to vanadium (Co:V) were tried (Co:V mole ratios in the hydrothermal solution: 5:1, 3:1, 1:1, 1:3 and 1:5). The obtained catalysts were evaluated for water oxidation on a glassy carbon electrode. All catalysts were scanned by cyclic voltammetry in 1 M KOH and 1 M Fe free KOH and the presence of trace iron in the KOH electrolyte did not strongly affect the OER activity as seen in Figure 4.9 a. The Co:V ratio that yielded the highest OER activity was 3:1 (Figure 4.9 b). This material can reach 10 mA cm^{-2} at

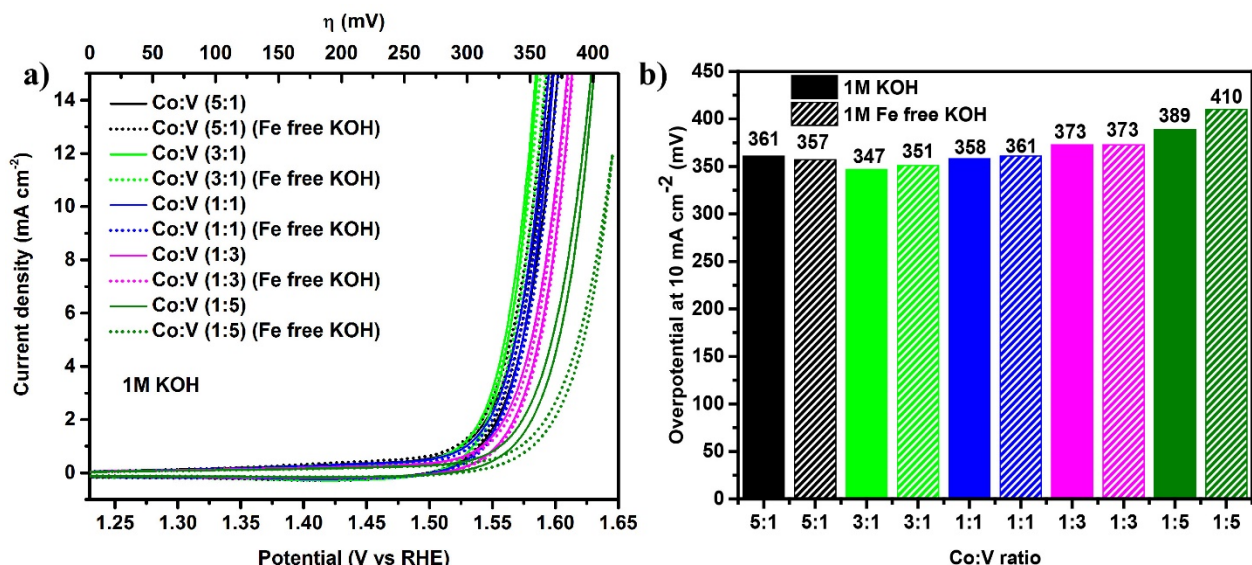


Figure 4.9 a) Polarization curves on glassy carbon (loading $140 \mu\text{g cm}^{-2}$) in 1 M KOH and 1 M Fe free KOH of cobalt vanadium oxides synthesized with different Co:V ratios in the hydrothermal solution. Scan rate: 10 mV s^{-1} , iR drop corrected. **b)** Overpotentials at 10 mA cm^{-2} for the different cobalt vanadium oxides with different Co:V ratios in 1 M KOH and 1 M Fe free KOH.

overpotentials of 347 and 351 mV in 1 M KOH and 1 M Fe free KOH, respectively. All further experiments and characterizations were done on this material with a 3:1 Co:V ratio.

The STEM images and EDX mapping of the cobalt vanadium oxide with a 3:1 Co:V ratio confirmed the formation of cobalt vanadium oxide. Both Co and V are homogeneously dispersed throughout the sample and neither VO_x nor CoO_x particles were observed (Figure 4.10 a). Moreover, the sample has a nanosheet-like morphology (Figure 4.10 b,c). When deposited on nickel foam, this catalytic material homogeneously coats the three-dimensional substrate and has a similar nanosheet-like morphology (Figure 4.10 d). Furthermore, no diffraction peaks are

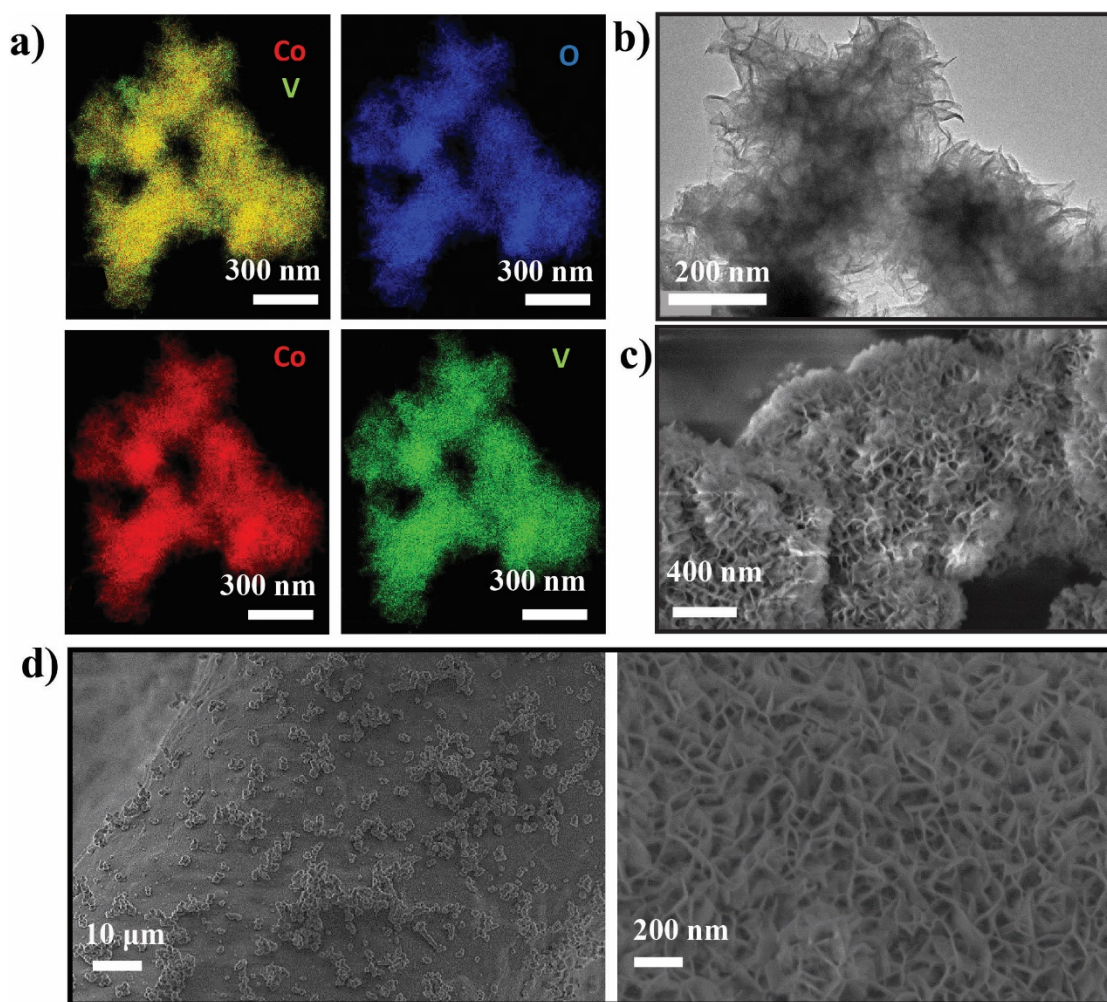


Figure 4.10 a) STEM-EDX mapping of $a\text{-CoVO}_x$. b) TEM image of $a\text{-CoVO}_x$. c) SEM image of $a\text{-CoVO}_x$. d) SEM images of $a\text{-CoVO}_x$ on nickel foam.

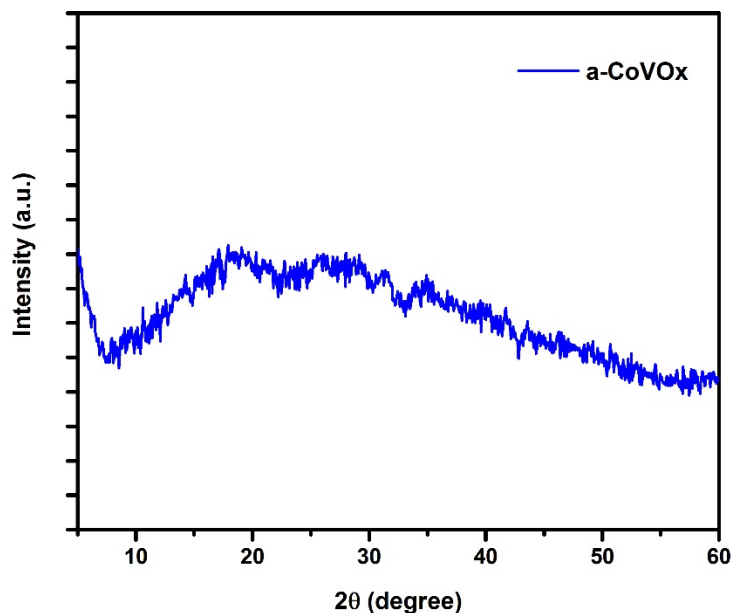


Figure 4.11 XRD pattern of *a*-CoVO_x.

observed in its XRD pattern (Figure 4.11), suggesting it is X-ray amorphous and no CoO_x or VO_x crystalline impurities are present. This confirms the formation of a pure-phase cobalt vanadium oxide, which is labelled as *a*-CoVO_x in this work.

The *a*-CoVO_x catalyst was further characterized by XPS (Figure 4.12). The binding energy (BE) of the Co 2p_{3/2} signal is located at 781.1 eV. Additionally, outer-shell excitation satellite peaks are visible at higher BE, indicating that high-spin Co²⁺ is present (Figure 4.12 a).^[23] As suggested by the V 2p_{3/2} peaks located at a BE of 516.5 eV, vanadium is incorporated into the catalyst in the +4 oxidation state (Figure 4.12 b).^[24,25] The signal in the C 1s region at 288.3 eV is characteristic of carbon atoms in a carbonate group (Figure 4.12 c). In the O 1s region, the signals at a BE of 531.5 and 530.0 eV are representative of oxygen atoms in OH⁻ and O²⁻ in transition-metal (oxy)hydroxides, respectively. The peak at a BE of 532.3 eV, which is characteristic of oxygen atoms in a carbonate group, further suggests the presence of this group in the material (Figure 4.12 d).^[28]

The atomic ratio of cobalt to vanadium (Co:V) determined by XPS is approximately 75%/25% (3:1) and is consistent with the ratio of the two metal salts used for the hydrothermal synthesis in the precursor solution. However, this agreement was somewhat fortuitous as a modest discrepancy was observed for the other synthesized materials between the ratios of the metal salts

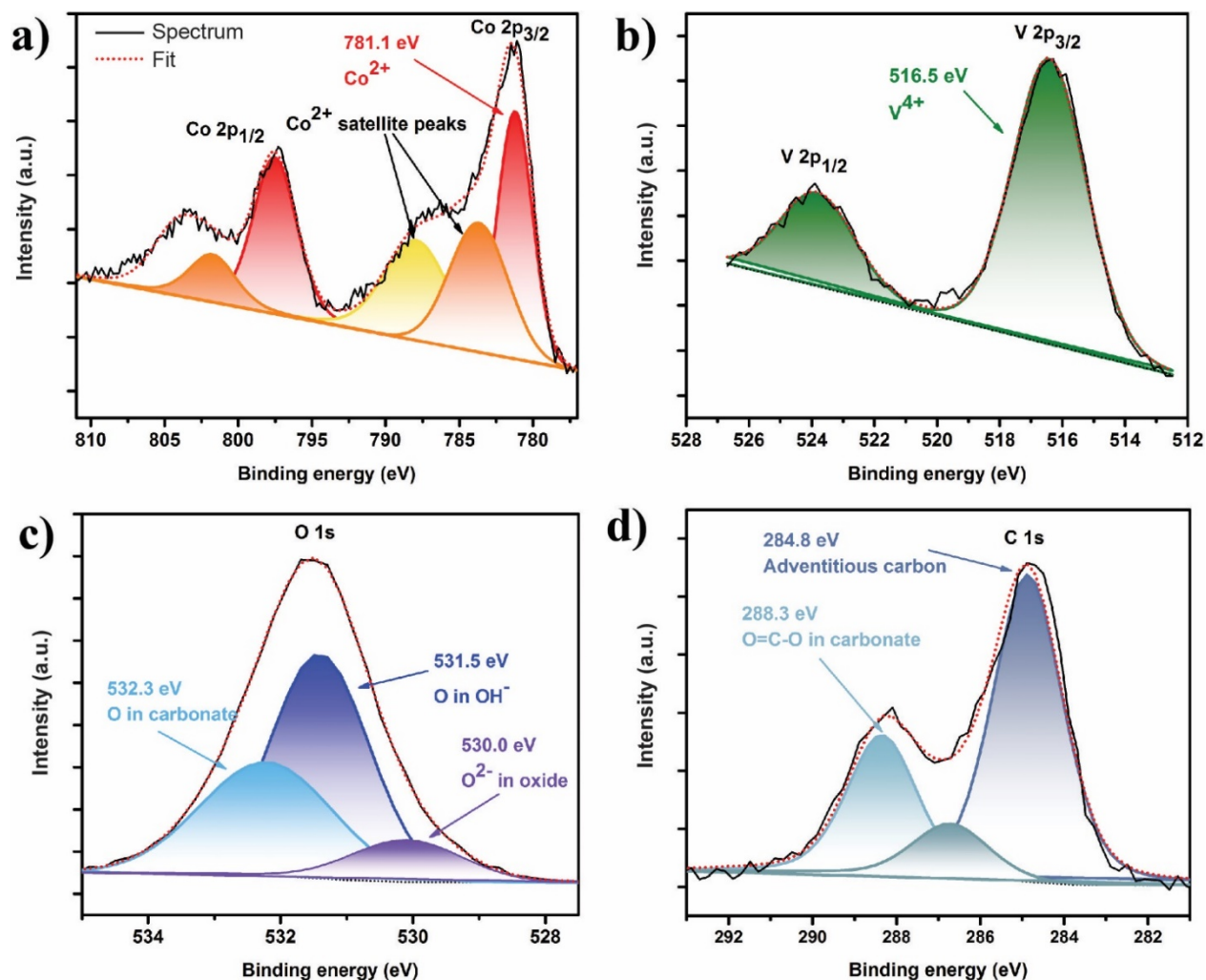


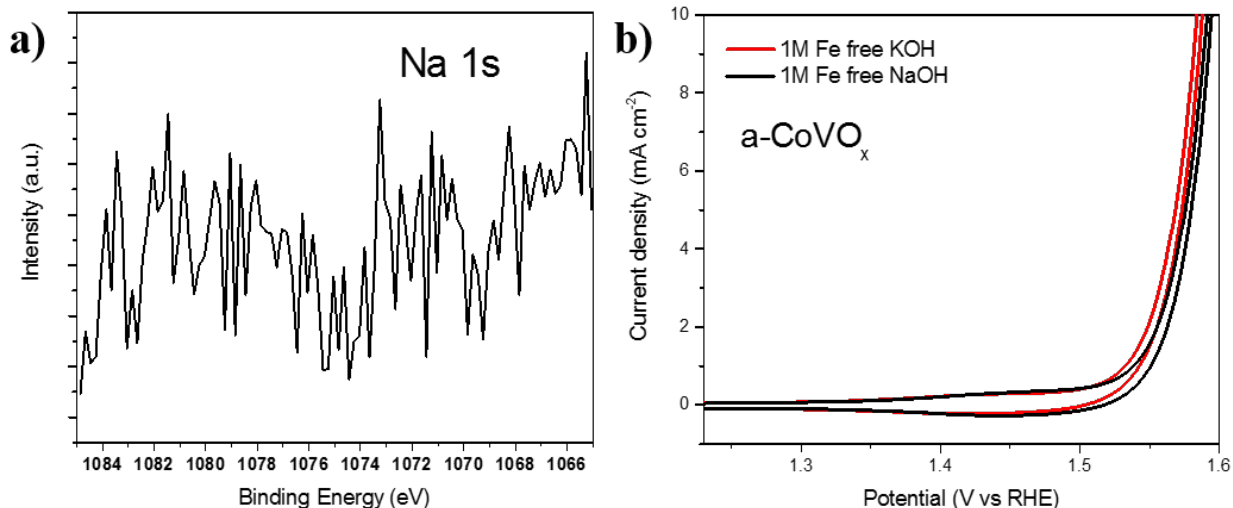
Figure 4.12 XPS spectra of $a\text{-CoVO}_x$ with high resolution spectra of **a)** Co $2p_{3/2}$ region, **b)** V $2p_{3/2}$ region, **c)** O $1s$ region, and **d)** C $1s$ region.

used in the precursor solutions (Co:V of 5:1, 3:1, 1:1 and 1:5) and the ratios of the final catalysts determined by XPS. Those values are summarized in Table 4.1.

A sodium salt (trisodium citrate) was used as an additive to synthesize the pure-phase $a\text{-CoVO}_x$. For this reason, we investigated if sodium incorporation could influence the OER activity of this material. No sodium was found in the structure of $a\text{-CoVO}_x$ after the hydrothermal synthesis (Figure 4.13 a). We performed cyclic voltammetry in Fe free NaOH electrolyte in order to incorporate sodium and probe if the OER activity of $a\text{-CoVO}_x$ was enhanced in this electrolyte compared to Fe free KOH. We determined that the OER activity was not increased while testing $a\text{-CoVO}_x$ in Fe Free NaOH compared to Fe free KOH (Figure 4.13 b).

Table 4.1 Comparison between the Co:V concentration ratios in the deposition solution and the Co:V ratios determined by XPS in the final catalysts.

Catalyst	Deposition bath CoCl ₂ :VCl ₃ ratio	XPS Co:V ratio (atomic %)
C _{0.89} V _{0.11} O _x	5:1	Co: 89%, V 11% (9:1)
C _{0.75} V _{0.25} O _x	3:1	Co: 75%, V 25% (3:1)
C _{0.58} V _{0.42} O _x	1:1	Co: 58%, V 42% (3:2)
C _{0.36} V _{0.64} O _x	1:3	Co: 36%, V 64% (2:3)
C _{0.21} V _{0.79} O _x	1:5	Co: 21%, V 79% (1:4)

**Figure 4.13** a) High resolution XPS spectra of Na 1s region of *a*-CoVO_x. b) Polarization curves on glassy carbon (loading 140 μg cm⁻²) of *a*-CoVO_x in 1 M Fe free KOH and 1 M Fe free NaOH. Scan rate: 10 mV s⁻¹, iR drop corrected.

The catalytic activity of *a*-CoVO_x was measured on glassy carbon and nickel foam (Figure 4.14 a and b). On glassy carbon, the *a*-CoVO_x had an overpotential of 347 and 351 mV at 10 mA cm⁻² in 1 M KOH and 1 M Fe free KOH, with Tafel slopes of 51 and 49 mV dec⁻¹, respectively. When deposited on nickel foam, the *a*-CoVO_x catalyst delivered the same current density at an overpotential of 254 and 262 mV in standard and Fe free KOH, with Tafel slopes of 35 and 34 mV dec⁻¹, respectively.

The overpotential of α -CoVO_x compares well with other cobalt vanadium oxide catalysts reported so far, such as Co₂V₂O₇ nanosheets (340 mV),^[29] Co₃V₂O₈ (359 mV),^[11] and Co₃V₂O₈ nanoroses (391 mV).^[30] Moreover, the α -CoVO_x is highly competitive with other cobalt-containing catalysts on nickel foam. For example Co₃O₄/NF has an overpotential of 497 mV,^[31] NiCo LDH/NF reaches 10 mA cm⁻² at 420 mV,^[32] NiCo DH/N-graphene/NF has an overpotential of 350 mV,^[33] and CoFeO_x/NF and NiCoFeO_x/NF have an overpotential of 260 and 240 mV, respectively.^[16] In addition, the α -CoVO_x immobilized on nickel foam exhibited a considerable catalytic stability and durability. Only a moderate increase of 30 mV in overpotential after 15 h of

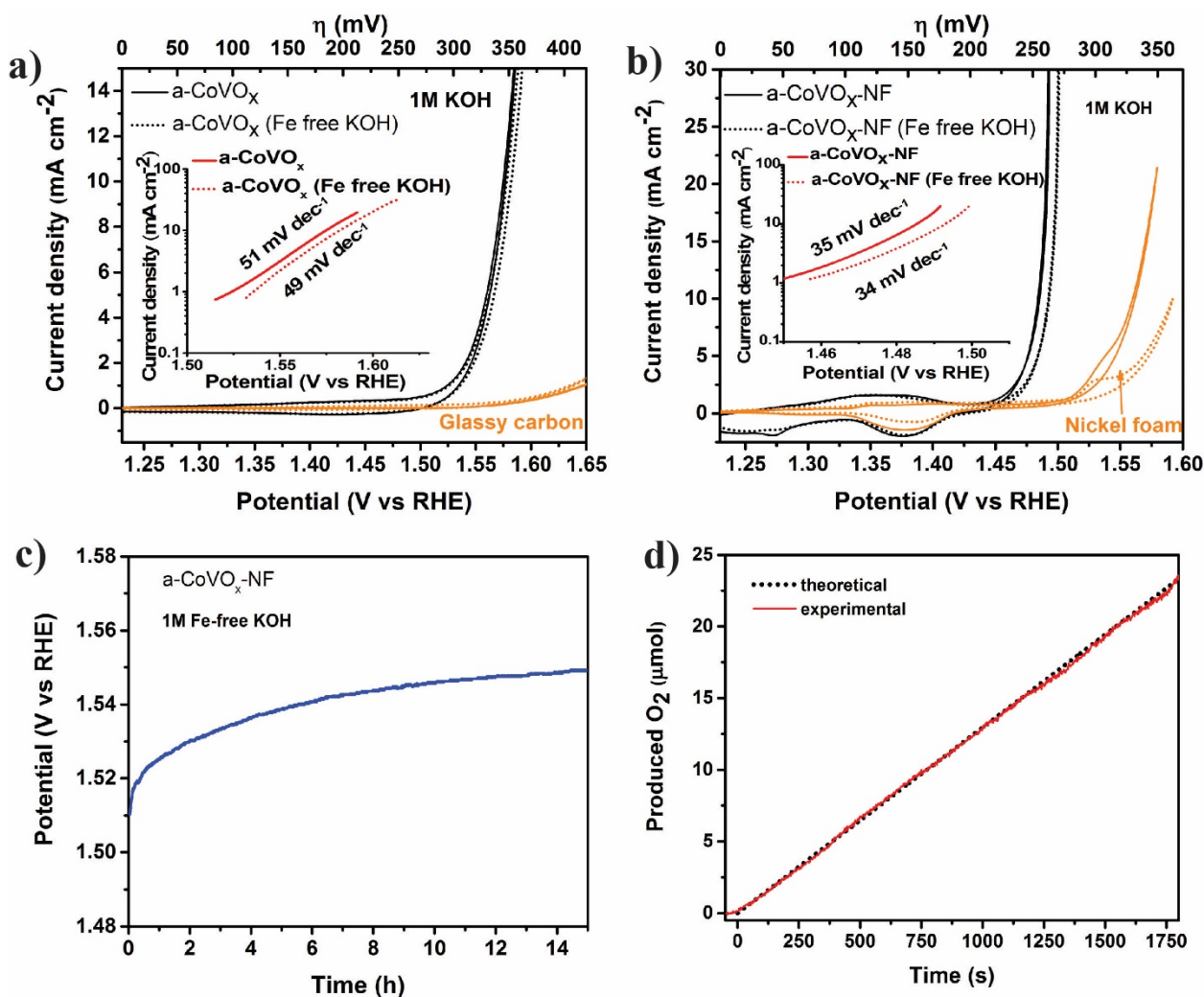


Figure 4.14 **a)** Polarization curves of α -CoVO_x on glassy carbon (loading 140 μg cm⁻²) and Tafel slopes (inset) in 1 M KOH and 1 M Fe free KOH. Scan rate: 10 mV s⁻¹, iR drop corrected. **b)** Polarization curves of α -CoVO_x on nickel foam and Tafel slopes (inset) in 1 M KOH and 1 M Fe free KOH. Scan rate: 1 mV s⁻¹, iR drop corrected. **c)** Stability of the applied potential at 10 mA cm⁻² of α -CoVO_x on nickel foam. **d)** Agreement between measured and predicted moles of O₂ produced by α -CoVO_x on nickel foam, indicating a nearly 100 % faradaic efficiency.

constant anodic polarization at 10 mA cm^{-2} was observed (Figure 4.14 c). Furthermore, the faradaic efficiency for OER was measured to be close to 100 % (Figure 4.14 d).

After the long-term stability test, the elemental composition and morphology of $\alpha\text{-CoVO}_x$ were investigated by STEM-EDX and SEM. After 15 h of anodic electrolysis, a structural degradation can be observed but the $\alpha\text{-CoVO}_x$ catalyst retains its nanosheet-like morphology (Figure 4.15 a-c). The EDX mapping, shown in Figure 4.15 d, indicates that Co and V are still homogeneously dispersed inside the material. In addition to this, no inclusion of nickel from the substrate could be observed after 15 h of electrolysis, as confirmed by the EDX elemental spectrum represented in Figure 4.15 e.

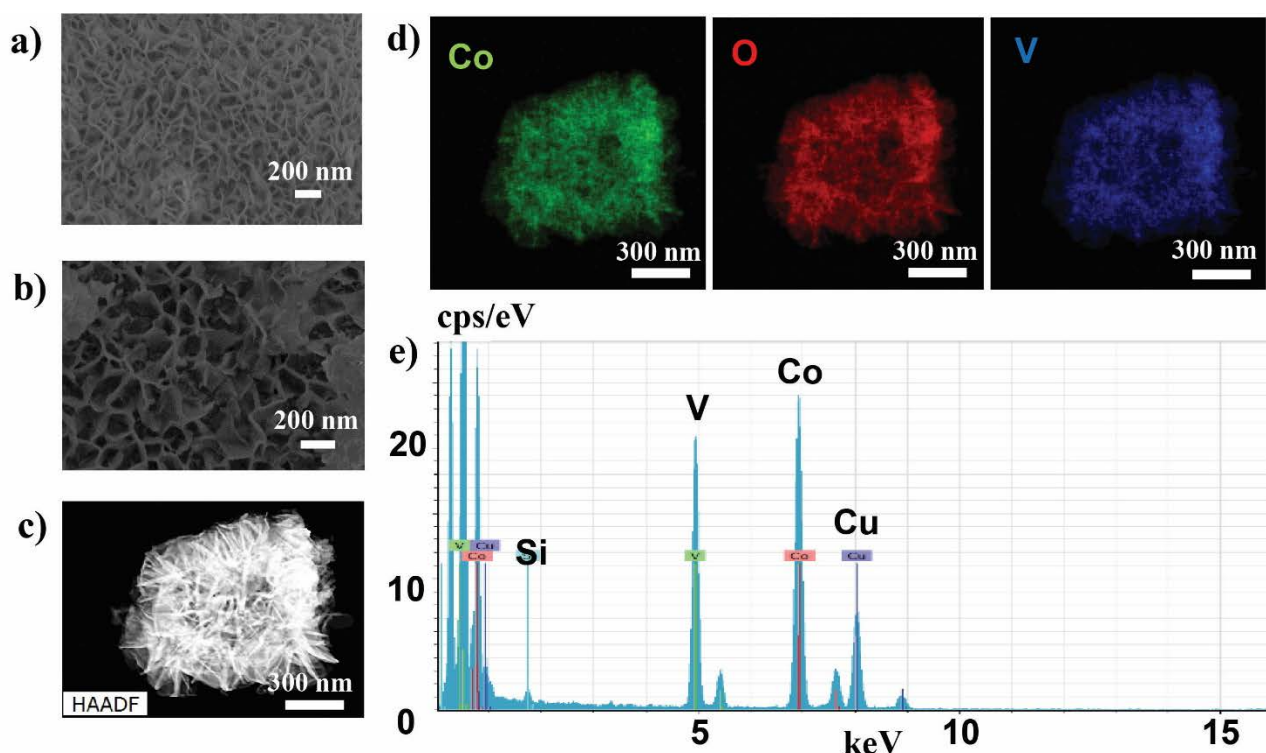


Figure 4.15 **a)** SEM image of $\alpha\text{-CoVO}_x$ on nickel foam before electrolysis. **b)** SEM image of $\alpha\text{-CoVO}_x$ on nickel foam after 15 h of electrolysis in 1 M Fe free KOH at 10 mA cm^{-2} . **c)** STEM image of $\alpha\text{-CoVO}_x$ deposited on nickel foam after 15 h of electrolysis in 1 M Fe free KOH at 10 mA cm^{-2} . **e)** EDX spectrum of $\alpha\text{-CoVO}_x$ initially deposited on nickel foam after 15 h of electrolysis in 1 M Fe free KOH at 10 mA cm^{-2} .

Our group recently reported a volcano plot comparing the mass activity trends of different electrodeposited transition metal (oxy)hydroxides based on their M-OH bond strength.^[16] Bockris and Otagawa proposed that the M-OH bond strength, even though this parameter is not a definitive descriptor of OER activity, should allow the extraction of activity trends for metal oxides.^[13,34]

The bond strength $D(\text{M-OH})$ was defined as the sum of the homolytic $D_{\text{cov}}(\text{M-OH})$ and heterolytic $D_{\text{ion}}(\text{M-OH})$ bond dissociation of a metal hydroxide in the M(III)(OH)_3 form, with $D_{\text{cov}}(\text{M-OH})$ and $D_{\text{ion}}(\text{M-OH})$ calculated from the electronegativity of the metal and OH and enthalpies of formation of OH radical and M(OH)_3 .^[13] For our $\alpha\text{-CoVO}_x$ materials, in order to determine its $D(\text{M-OH})$, we simply considered them as binary mixtures and used a linear combination of the bond strength of the respective unary metal hydroxides (Table 4.2). When taking into consideration the mass activity of $\alpha\text{-CoVO}_x$ with different Co:V atomic ratios (Figure 4.16 a, Table 4.3), we could correlate it with their respective M-OH bond strength and a volcano-shaped plot was obtained (Figure 4.16 b). The agreement between the theoretical lines and the experimental data is surprisingly good given the simplifications made in the construction of this volcano plot. The optimal catalyst found experimentally, $\alpha\text{-Co}_{0.75}\text{V}_{0.25}\text{O}_x$, sits close to the top of the volcano.

Table 4.2 Bond strength of the different $\text{Co}_y\text{V}_{1-y}\text{O}_x$ for physical mixtures calculated using the method proposed by Bockris and Otagawa.^[13]

Mixture of metal hydroxides	M-OH bond strength (kcal mol ⁻¹)
Co-OH	130.4
0.89 Co-OH + 0.11 V-OH	136.8
0.75 Co-OH + 0.25 V-OH	144.9
0.58 Co-OH + 0.42 V-OH	154.8
0.36 Co-OH + 0.64 V-OH	167.6
0.21 Co-OH + 0.79 V-OH	176.3
V-OH	188.5

Table 4.3 Summary of mass activities of the different $\text{Co}_y\text{V}_{1-y}\text{O}_x$ physical mixtures.

Metal oxide	Mass activity (A g ⁻¹ at $\eta = 350$ mV)
CoO_x ($\text{Co}(\text{CO}_3)_{0.35}\text{Cl}_{0.2}(\text{OH})_{1.1} \cdot 1.74 \text{H}_2\text{O}$)	19.2
$\text{Co}_{0.89}\text{V}_{0.11}\text{O}_x$	56.3
$\text{Co}_{0.75}\text{V}_{0.25}\text{O}_x$	69.5
$\text{Co}_{0.58}\text{V}_{0.42}\text{O}_x$	45.6
$\text{Co}_{0.36}\text{V}_{0.64}\text{O}_x$	25.4
$\text{Co}_{0.21}\text{V}_{0.79}\text{O}_x$	6.8
VO_x ($\text{V}_2\text{O}_2(\text{OH})_3$)	2.1

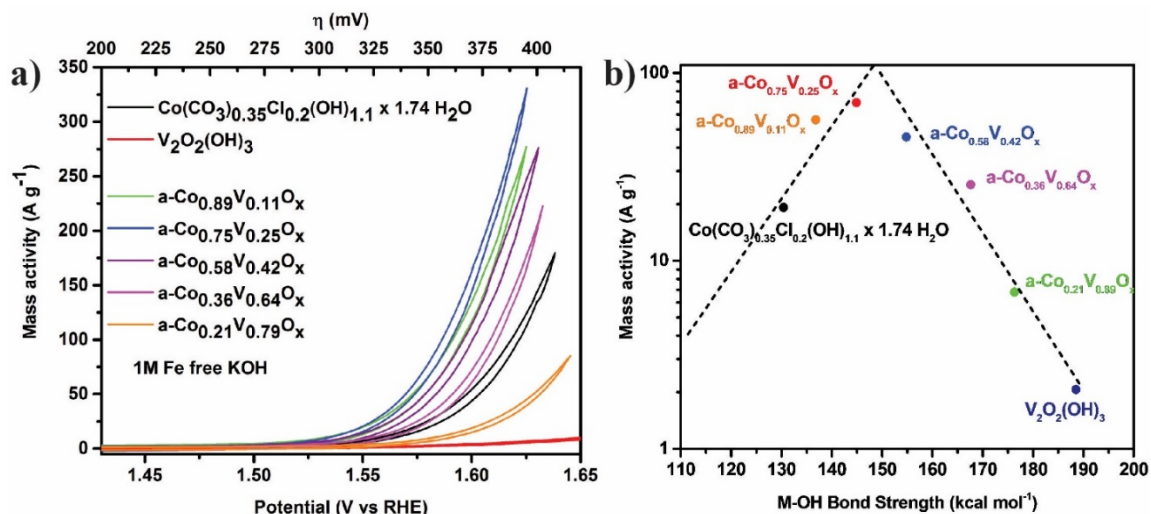


Figure 4.16 a) Mass activity of different $a\text{-Co}_y\text{V}_{1-y}\text{O}_x$ on glassy carbon (loading $140 \mu\text{g cm}^{-2}$). Scan rate 10 mV s^{-1} , iR drop corrected. b) Volcano plot of the mass activity vs M-OH bond strength of various $a\text{-Co}_y\text{V}_{1-y}\text{O}_x$ and control vanadium and cobalt oxides samples.

4.4 Conclusions

On the basis of the volcano plot of OER activity vs M-OH bond strength, cobalt vanadium oxide was predicted to be a highly active OER catalyst. Cobalt vanadium oxide was first produced by oxidative electrodeposition. Due to the moderate OER activity of the deposited CoVO_x and the dissolution of vanadium from its structure during water oxidation, we focused on using another strategy to produce this oxide. For this, we developed a simple hydrothermal route to prepare the targeted compound. A pure-phase, amorphous cobalt vanadium oxide ($a\text{-CoVO}_x$) was obtained and characterized by SEM, STEM-EDX, XPS and XRD. This material exhibited high catalytic activity for oxygen evolution. On a flat glassy carbon electrode, this $a\text{-CoVO}_x$ reached 10 mA cm^{-2} at an overpotential of 347 mV in 1 M KOH electrolyte. The same material, when deposited on nickel foam, had an overpotential of 254 mV at 10 mA cm^{-2} , making it among the most active electrodes in alkaline conditions. Moreover, the activity of various $a\text{-CoVO}_x$ materials with different Co:V ratios correlates with the M-OH bond strength in a volcano-type plot. This work demonstrates the usefulness of a simple descriptor (M-OH bond strength) for experimental developments of OER catalysts. In addition to this, this work advocates for further exploration of vanadium-containing oxides as catalysts for oxygen evolution.

4.5 Experimental section

All reagents were obtained from commercial sources and used without further purification. Millipore deionized water 18.2 M Ω ·cm was used to prepare all the solutions.

Electrodeposition of CoVO_x

The catalysts were electrodeposited by using an Autolab PGSTAT302N potentiostat/galvanostat (Metrohm) in a three-electrode setup. Gold-coated FTO were used and made by sputtering 10 nm of Cr and 100 nm of Au on FTO with a DP650 sputtering equipment (Alliance-Concept). The Au-coated FTO substrates were set as the working electrode, an Ag/AgCl (sat. KCl) electrode was used as reference and a titanium wire was used as the counter electrode. The CoVO_x was anodically electrodeposited with 30 consecutive linear sweeps from 1.7 to 2.0 V vs RHE at 10 mV s⁻¹. The deposition solution was composed of 16 mM of cobalt(II) chloride (CoCl₂, anhydrous, > 98%, Fluka) and 5 mM of vanadium (III) chloride (VCl₃, anhydrous, 97%, Sigma) in a 0.1 M NaOAc supporting electrolyte. Au-coated quartz crystals (10 MHz) were used to determine the CoVO_x deposition rate in an eQCM 10M quartz crystal microbalance (Gamry).

Hydrothermal synthesis

All the catalysts were prepared by hydrothermal synthesis in Teflon-lined stainless steel autoclaves. For *m*-CoVO_x, an aqueous solution containing 30 mM of cobalt(II) chloride (CoCl₂, anhydrous, > 98%, Fluka), 10 mM of vanadium(III) chloride (VCl₃, anhydrous, 97%, Sigma), and 63 mM urea (99%, ACS reagent) was loaded into the autoclave and heated at 150°C for 14 h. The control samples (CoO_x and VO_x), based on only one of the two metals, were prepared by the same procedure except that only the desired metal salt (CoCl₂ or VCl₃) was used with a concentration of 40 mM to keep the total amount of metal cations constant. After the hydrothermal step, the powders were separated by centrifugation at 6000 rpm for 10 min and washed three times with a 50:50 mixture of H₂O and ethanol, with centrifugation between each washing step. The powders were then collected and dried overnight under vacuum at room temperature.

The amorphous pure-phase catalyst (*a*-CoVO_x) was prepared following a procedure similar to the one described above. The only modifications were the addition of 8 mM of trisodium citrate (TSC, anhydrous, 98%, Acros), and purging the solution with N₂. *a*-CoVO_x with different Co:V

atomic ratios ($a\text{-Co}_y\text{V}_{1-y}\text{O}_x$) were synthesized by tuning the ratio of starting materials (CoCl_2 and VCl_3) while keeping the total metal cation concentration at 40 mM.

Electrodes preparation

The prepared catalyst powders (5 mg) were each sonicated twice for 30 min in a mixture of H_2O (1 mL), $i\text{PrOH}$ (0.25 mL) and Nafion solution (10 μL , 5 wt % in EtOH, DuPont) in order to make a homogeneous suspension. Then, 2.5 μL of this suspension was drop cast on a glassy carbon electrode (CH Instruments) with a diameter of 3 mm and previously polished (with 0.05 μm gamma alumina powder on a micro cloth polishing pad, CH Instruments). The drop was allowed to dry in ambient conditions for 30 min. The catalyst loading was 140 $\mu\text{g cm}^{-2}$ in all cases.

The catalysts were also synthesized on nickel foam (thickness 1.6 mm, porosity 95 %, Goodfellow Cambridge Limited) by putting the nickel foam substrate in the same solutions as for the hydrothermal synthesis and heating at 150°C for 14 h. The active area was delimited by applying epoxy glue (SPI Supplies) on the nickel foam and carefully pressing on it with a metal rod to make it fill all the pores in order to prevent electrolyte from reaching the potentiostat clamp by capillary action.

Electrochemical characterization

The OER activity and stability were measured by cyclic voltammetry and chronopotentiometry using an Autolab PGSTAT302N potentiostat/galvanostat (Metrohm). The third CV was taken as representative measurement for all samples on glassy carbon and the tenth CV for the nickel foam substrates. A three-electrode setup was used with either the glassy carbon electrode or nickel foam substrate as working electrode, a platinum wire as counter electrode, and an Ag/AgCl (sat. KCl) reference electrode. Stirring was performed only during the stability measurements. Standard 1 M KOH solution (pH 13.6, Merck) and NaOH solution (pH 13.6, Reactolab) were used as received and/or further purified to remove trace iron using a procedure reported by the Boettcher group.^[20]

The uncompensated resistance for each sample was measured by electrochemical impedance spectroscopy (EIS) in order to correct for the iR drop. The EIS data were collected at 1.20 V vs RHE and by applying 41 frequencies from 100 kHz to 1 Hz (10 mV amplitude). The resistance was determined to be 0.6–0.8 $\Omega \text{ cm}^2$ for the samples on glassy carbon, and 1.0–1.4 $\Omega \text{ cm}^2$ on nickel foam.

Faradaic efficiency measurement

The faradaic efficiency was measured using an airtight glass H-cell with an optical fluorescence sensor (Ocean Optics). Quantification was done for $\alpha\text{-Co}_{0.75}\text{V}_{0.25}\text{O}_x$ deposited on nickel foam. The cell was purged with N_2 to give an initial O_2 content lower than 0.5%. The measurement was done at 10 mA cm^{-2} in 1 M Fe free KOH.

Structural and compositional characterization

The X-ray powder diffraction (XRD) was recorded on a PANalytical Empyrean diffractometer with Bragg–Brentano geometry, equipped with a PIXcel-1D detector. For the measurement, powders were mixed with EtOH and drop-dried on glass slides. Data were analyzed with PANalytical X'Pert HighScore software.

XPS analysis was carried out using a PHI VersaProbe II scanning XPS microprobe with monochromatic Al $K\alpha$ X-ray source of 24.8 W with a beam size of 100 μm . The adventitious carbon 1s peak was calibrated at 284.8 eV and used as an internal standard to compensate for charging effects. Data were fitted by using PHI MultiPak software.

SEM images were taken using a Zeiss Merlin microscope operated at 2 kV and equipped with an Inlens secondary electron detector. TEM images and STEM/EDX maps were recorded using a FEI Talos operated at 200 kV and a FEI Technai Osiris TEM/STEM operated at 200 kV equipped with a high-brightness XFEG gun. TEM samples were prepared by drop-drying either suspension of the powders in EtOH onto carbon coated copper grids or a suspension made by sonicating the nickel foam electrode for 30 min in EtOH to detached catalyst particles from the NF surface

4.6 Contributions

Laurent Liardet fabricated the materials, tested the electrochemical activity and characterized the structure and the composition of the materials. Both Xile Hu and Laurent Liardet analyzed the data and wrote the corresponding paper.

4.7 References

- [1] Yan, Y., Li, B., Guo, W., Pang, H. & Xue, H. Vanadium based materials as electrode materials for high performance supercapacitors. *Journal of Power Sources* **329**, 148-169,(2016).
- [2] Zhang, Y., Liu, Y., Chen, J., Guo, Q., Wang, T. & Pang, H. Cobalt vanadium oxide thin nanoplates: primary electrochemical capacitor application. *Scientific Reports* **4**, 5687,(2014).
- [3] Liu, M.-C., Kong, L.-B., Kang, L., Li, X., Walsh, F. C., Xing, M., Lu, C., Ma, X.-J. & Luo, Y.-C. Synthesis and characterization of M₃V₂O₈ (M = Ni or Co) based nanostructures: a new family of high performance pseudocapacitive materials. *Journal of Materials Chemistry A* **2**, 4919-4926,(2014).
- [4] He, Z., Fu, D., Kyômen, T., Taniyama, T. & Itoh, M. Crystal Growth and Magnetic Properties of BaCo₂V₂O₈. *Chemistry of Materials* **17**, 2924-2926,(2005).
- [5] Zhang, S.-Y., Guo, W.-B., Yang, M., Tang, Y.-Y., Wang, N.-N., Huang, R.-R., Cui, M.-Y. & He, Z.-Z. Synthesis, crystal structure and magnetic property of a new cobalt(II) vanadate. *Journal of Solid State Chemistry* **225**, 78-82,(2015).
- [6] Liu, J. & Li, Y. D. Synthesis and Self-Assembly of Luminescent Ln³⁺-Doped LaVO₄ Uniform Nanocrystals. *Advanced Materials* **19**, 1118-1122,(2007).
- [7] Yang, G., Cui, H., Yang, G. & Wang, C. Self-Assembly of Co₃V₂O₈ Multilayered Nanosheets: Controllable Synthesis, Excellent Li-Storage Properties, and Investigation of Electrochemical Mechanism. *ACS Nano* **8**, 4474-4487,(2014).
- [8] Bai, L., Zhu, J., Zhang, X. & Xie, Y. Reducing hydrated protons co-intercalation to enhance cycling stability of CuV₂O₅ nanobelts: a new anode material for aqueous lithium ion batteries. *Journal of Materials Chemistry* **22**, 16957-16963,(2012).
- [9] Wu, F., Xiong, S., Qian, Y. & Yu, S.-H. Hydrothermal Synthesis of Unique Hollow Hexagonal Prismatic Pencils of Co₃V₂O₈·n H₂O: A New Anode Material for Lithium-Ion Batteries. *Angewandte Chemie International Edition* **54**, 10787-10791,(2015).
- [10] Fan, K., Chen, H., Ji, Y., Huang, H., Claesson, P. M., Daniel, Q., Philippe, B., Rensmo, H., Li, F., Luo, Y. & Sun, L. Nickel–vanadium monolayer double hydroxide for efficient electrochemical water oxidation. *Nature Communications* **7**, 11981,(2016).
- [11] Xing, M., Kong, L.-B., Liu, M.-C., Liu, L.-Y., Kang, L. & Luo, Y.-C. Cobalt vanadate as highly active, stable, noble metal-free oxygen evolution electrocatalyst. *Journal of Materials Chemistry A* **2**, 18435-18443,(2014).
- [12] Guo, W., Chemelewski, W. D., Mabayoje, O., Xiao, P., Zhang, Y. & Mullins, C. B. Synthesis and Characterization of CuV₂O₆ and Cu₂V₂O₇: Two Photoanode Candidates for Photoelectrochemical Water Oxidation. *The Journal of Physical Chemistry C* **119**, 27220-27227,(2015).
- [13] Bockris, J. O. M. & Otagawa, T. The Electrocatalysis of Oxygen Evolution on Perovskites. *Journal of The Electrochemical Society* **131**, 290-302,(1984).
- [14] Suntivich, J., May, K. J., Gasteiger, H. A., Goodenough, J. B. & Shao-Horn, Y. A Perovskite Oxide Optimized for Oxygen Evolution Catalysis from Molecular Orbital Principles. *Science* **334**, 1383-1385,(2011).
- [15] Man, I. C., Su, H.-Y., Calle-Vallejo, F., Hansen, H. A., Martínez, J. I., Inoglu, N. G., Kitchin, J., Jaramillo, T. F., Nørskov, J. K. & Rossmeisl, J. Universality in Oxygen Evolution Electrocatalysis on Oxide Surfaces. *ChemCatChem* **3**, 1159-1165,(2011).

- [16] Morales-Guio, C. G., Liardet, L. & Hu, X. Oxidatively Electrodeposited Thin-Film Transition Metal (Oxy)hydroxides as Oxygen Evolution Catalysts. *Journal of the American Chemical Society* **138**, 8946-8957,(2016).
- [17] Friebel, D., Louie, M. W., Bajdich, M., Sanwald, K. E., Cai, Y., Wise, A. M., Cheng, M.-J., Sokaras, D., Weng, T.-C., Alonso-Mori, R., Davis, R. C., Bargar, J. R., Nørskov, J. K., Nilsson, A. & Bell, A. T. Identification of Highly Active Fe Sites in (Ni,Fe)OOH for Electrocatalytic Water Splitting. *Journal of the American Chemical Society* **137**, 1305-1313,(2015).
- [18] Stevens, M. B., Trang, C. D. M., Enman, L. J., Deng, J. & Boettcher, S. W. Reactive Fe-Sites in Ni/Fe (Oxy)hydroxide Are Responsible for Exceptional Oxygen Electrocatalysis Activity. *Journal of the American Chemical Society* **139**, 11361-11364,(2017).
- [19] Burke, M. S., Kast, M. G., Trotochaud, L., Smith, A. M. & Boettcher, S. W. Cobalt–Iron (Oxy)hydroxide Oxygen Evolution Electrocatalysts: The Role of Structure and Composition on Activity, Stability, and Mechanism. *Journal of the American Chemical Society* **137**, 3638-3648,(2015).
- [20] Trotochaud, L., Young, S. L., Ranney, J. K. & Boettcher, S. W. Nickel–Iron Oxyhydroxide Oxygen-Evolution Electrocatalysts: The Role of Intentional and Incidental Iron Incorporation. *Journal of the American Chemical Society* **136**, 6744-6753,(2014).
- [21] Song, F., Bai, L., Moysiadou, A., Lee, S., Hu, C., Liardet, L. & Hu, X. Transition Metal Oxides as Electrocatalysts for the Oxygen Evolution Reaction in Alkaline Solutions: An Application-Inspired Renaissance. *Journal of the American Chemical Society* **140**, 7748-7759,(2018).
- [22] Shi, H., Liang, H., Ming, F. & Wang, Z. Efficient Overall Water-Splitting Electrocatalysis Using Lepidocrocite VOOH Hollow Nanospheres. *Angewandte Chemie International Edition* **56**, 573-577,(2017).
- [23] Borod'ko, Y. G., Vetchinkin, S. I., Zimont, S. L., Ivleva, I. N. & Shul'ga, Y. M. Nature of satellites in x-ray photoelectron spectra XPS of paramagnetic cobalt (II) compounds. *Chemical Physics Letters* **42**, 264-267,(1976).
- [24] Biesinger, M. C., Lau, L. W. M., Gerson, A. R. & Smart, R. S. C. Resolving surface chemical states in XPS analysis of first row transition metals, oxides and hydroxides: Sc, Ti, V, Cu and Zn. *Applied Surface Science* **257**, 887-898,(2010).
- [25] Silversmit, G., Depla, D., Poelman, H., Marin, G. B. & De Gryse, R. Determination of the V2p XPS binding energies for different vanadium oxidation states (V5+ to V0+). *Journal of Electron Spectroscopy and Related Phenomena* **135**, 167-175,(2004).
- [26] Louie, M. W. & Bell, A. T. An Investigation of Thin-Film Ni–Fe Oxide Catalysts for the Electrochemical Evolution of Oxygen. *Journal of the American Chemical Society* **135**, 12329-12337,(2013).
- [27] Corrigan, D. The Catalysis of the Oxygen Evolution Reaction by Iron Impurities in Thin Film Nickel Oxide Electrodes. *J. of The Electrochemical Society* **134**, 377-384,(1986).
- [28] Moulder, J. F., Stickle, W.F., Sobol, P.E., Bomben, K.D. *Handbook of X-ray Photoelectron Spectroscopy*. (Physical Electronics, Inc, 1995).
- [29] Peng, X., Wang, L., Hu, L., Li, Y., Gao, B., Song, H., Huang, C., Zhang, X., Fu, J., Huo, K. & Chu, P. K. In situ segregation of cobalt nanoparticles on VN nanosheets via nitrating of Co₂V₂O₇ nanosheets as efficient oxygen evolution reaction electrocatalysts. *Nano Energy* **34**, 1-7,(2017).

- [30] Zhang, J., Yuan, B., Cui, S., Zhang, N., Wei, J., Wang, X., Zhang, D., Zhang, R. & Huo, Q. Facile synthesis of 3D porous Co₃V₂O₈ nanoroses and 2D NiCo₂V₂O₈ nanoplates for high performance supercapacitors and their electrocatalytic oxygen evolution reaction properties. *Dalton Transactions* **46**, 3295-3302,(2017).
- [31] Chou, N. H., Ross, P. N., Bell, A. T. & Tilley, T. D. Comparison of Cobalt-based Nanoparticles as Electrocatalysts for Water Oxidation. *ChemSusChem* **4**, 1566-1569,(2011).
- [32] Jiang, J., Zhang, A., Li, L. & Ai, L. Nickel–cobalt layered double hydroxide nanosheets as high-performance electrocatalyst for oxygen evolution reaction. *Journal of Power Sources* **278**, 445-451,(2015).
- [33] Chen, S., Duan, J., Jaroniec, M. & Qiao, S. Z. Three-Dimensional N-Doped Graphene Hydrogel/NiCo Double Hydroxide Electrocatalysts for Highly Efficient Oxygen Evolution. *Angewandte Chemie International Edition* **52**, 13567-13570,(2013).
- [34] Fabbri, E., Haberer, A., Walz, K., Kotz, R. & Schmidt, T. J. Developments and perspectives of oxide-based catalysts for the oxygen evolution reaction. *Catalysis Science & Technology* **4**, 3800-3821,(2014).

Conclusions and Outlook

Atomic layer deposition was used, in Chapter 2, to produce layers of bi- and trimetallic oxides composed of Co, V and Fe such as CoFeO_x , CoVO_x and CoVFeO_x . The catalytic activities of those materials for OER were evaluated. An enhancement of catalytic activity was observed for bi- and trimetallic oxides compared to their single metal oxide components. Moreover, when deposited on nickel foam, those oxides showed high catalytic activity and stability in alkaline conditions, especially CoFeO_x that competes favorably with state-of-the-art OER materials. These results demonstrate the potential of ALD to produce highly active OER catalysts on different substrates.

In Chapter 3, a photoelectrodeposition method was developed to coat APCVD nanostructured hematite photoanodes with an ultrathin layer of CoFeO_x . This layer provided, compared to the catalyst-free hematite, a large increase in photocurrent density and a substantial cathodic shift of the photocurrent onset potential. The origin of the enhancement of the PEC activity provided by the CoFeO_x layer was found to purely arise from an increase of water oxidation kinetics and not from passivation of surface states nor modification of the flat-band or photovoltage. This chapter demonstrated the potential of photoelectrodeposition in OER catalysis for PEC applications.

Chapter 4 focused on the development of a cobalt vanadium oxide OER catalyst. CoVO_x was predicted, on the basis of the volcano plot of OER activity vs M-OH bond strength of transition metal oxides, to be a highly active OER catalyst. In this chapter, both electrodeposition and a hydrothermal method were used to synthesize CoVO_x . Electrodeposition yielded an active CoVO_x . However, the composition of this electrodeposited CoVO_x was not stable during OER and vanadium left the structure of this oxide. We therefore focused on the hydrothermal method that produced a stable, amorphous CoVO_x . When grown on nickel foam, this *a*- CoVO_x provided high OER activity comparable to state-of-the-art OER electrocatalysts.

In summary, various approaches for the synthesis of OER catalysts made of transition metal oxides have been explored. To date, the least explored approach of the ones used in this thesis is atomic layer deposition of OER materials. A large number of mixed metal materials, that are not possible or difficult to produce by other methods, could be fabricated by ALD, thus allowing screening of new materials. Additionally, this technique allows to tune the ratio of different elements inside a material in order to study the compositional influence of this parameter on the

desired properties of the material. Finally, due to the vapor phase characteristics of ALD, a wide variety of nanostructured substrates can be used in ALD processes.

Producing hydrogen gas via water splitting at large scale would preferentially require catalysts produced by widespread methods already in the industrialization state. The synthesis techniques used in this work (ALD; (photo)electrodeposition and hydrothermal growth) are all implemented nowadays at an industrial scale. For example ALD is already widely used in the microelectronic industry.^[1] Electrodeposition is performed at large scales in electroplating processes and hydrothermal methods are widely used in industrial applications such as quartz crystal synthesis.^[2,3] Therefore, utilizing methods that are already used in commercial applications would facilitate the transition between laboratory and large production scales for materials used in water splitting.

In order to avoid the predicted energy and environmental crisis, a shift in today's paradigm on energy production and consumption is necessary. Mature technologies for renewables energy production, such as photovoltaic cells and wind turbines, are already available and widely used. Moreover, their cost is constantly decreasing with the increasing demand for these types of installations. Electricity produced from renewable sources is already highly competitive with the one produced from fossil fuels and a large increase of investments in renewable energies is forecast to happen in the next years.^[4] Early stages of change in political mindsets as well as massive financial investments start to emerge. However, deep changes in our society, such as electrification of transports, housing heating and industrial processes are required in order to fully drop fossil fuels. The Hydrogen Economy is a well suited concept for this as it is based on storage of renewables in the form of hydrogen and is closely related to both the "fuel" and "electricity" paradigms.

We have seen, in this thesis, that production of sustainable hydrogen via water splitting is already possible with well-established technologies such as photovoltaics combined to electrolyzers. On the other hand, PEC water splitting is still on a research phase and no economically viable applications have been developed yet due to technical difficulties. Research is thus still necessary to bring major breakthroughs in PEC water splitting. Additionally, fundamental and applied researches are still required for photovoltaics and electrolyzers as large scale implementation of these systems for producing hydrogen would engender considerations on the abundance of the required elements, as well as the economic sustainability of those systems.

Both the academic and industrial sector should collaborate to a greater extent in order to evaluate the economic potential of new state-of-the-art technological discoveries, develop engineered solutions and accelerate the industrialization of applicable systems.

References

- [1] Parsons, G. N., George, S. M. & Knez, M. Progress and future directions for atomic layer deposition and ALD-based chemistry. *MRS Bulletin* **36**, 865-871,(2011).
- [2] Schlesinger, M. & Paunovic, M. *Modern Electroplating (Fifth Edition)*. (John Wiley & Sons, INC, 2014).
- [3] Buisson, X. & Arnaud, R. Hydrothermal growth of quartz crystals in industry. Present status and evolution. *Journal de Physique IV* **4**, 25-32,(1994).
- [4] IRENA. Global Energy Transformation, a Roadmap to 2050. (2019).

Curriculum Vitae



LAURENT LIARDET

Chemin des Vignes 15, 1009 Pully

+41 79 333 69 54

liardet_laurent@hotmail.com

<https://www.linkedin.com/in/laurent-liardet/>

PROFESSIONAL EXPERIENCE

RESEARCHER

08.2015 - 07.2019

EPFL, Laboratory of Inorganic Synthesis and Catalysis (LSCI)

Development of new coatings, thin films and heterogeneous catalysts for optimizing the efficiency of sustainable hydrogen production via water splitting. Electrochemical systems based on new innovative materials were fabricated and state-of-the-art performances and efficiencies for water splitting were obtained.

Coordination and realization of research projects.

Development and implementation of a "benchtop" atomic layer deposition (ALD) system. New oxide thin films catalysts were fabricated and demonstrated for robust oxygen evolution catalysis in harsh environments.

Laboratory safety coordinator (COSEC). Management and formation of the LSCI team (ca. 20 persons) on safety aspects in laboratory environment.

Clean room working experience.

TEACHING AND LAB ASSISTANT

09.2014 - 12.2018

EPFL

(part time 20 %)

Teaching assistant in organic chemistry and practical chemistry courses

TECHNICAL SKILLS

CHEMICAL AND MATERIAL SYNTHESIS PROCESSES

Atomic layer deposition (ALD), Chemical Vapor Deposition (CVD), Physical Vapor Deposition (PVD, Magnetron sputtering), Electrodeposition, Solvothermal synthesis, Organic synthesis.

PHYSICAL AND STRUCTURAL CHARACTERIZATION TECHNIQUES

Electrochemical characterization (CV, LSV, impedance spectroscopy), X-Ray Photoelectron Spectroscopy (XPS), Scanning Electron Microscopy (SEM), Transmission Electron

Microscopy (TEM and STEM), Powder X-Ray Diffraction (XRD), Energy-Dispersive X-Ray spectroscopy (EDX), Nuclear Magnetic Resonance (NMR), Gas Chromatography and Mass Spectrometry (GC-MS).

EDUCATION

PhD IN CHEMICAL SCIENCES EPFL	07.2019
MASTER OF SCIENCE IN MOLECULAR AND BIOLOGICAL CHEMISTRY EPFL	02.2015
BACHELOR OF SCIENCE IN CHEMISTRY AND CHEMICAL ENGINEERING EPFL	07.2013
ERASMUS EXCHANGE KTH UNIVERSITY, STOCKHOLM, SWEDEN	08.2012-07.2013

AWARDS

EPFL Master Scholarship of Excellency.
Award of the best Master thesis poster.
Bachelor Excellency Award (global average of Bachelor: 5.5/6).

LANGUAGES

English: fluent (C1), editorial fluency
German: intermediate (B1)
French: native language, editorial fluency

INTERESTS

Artisanal beer brewing, Co-founder of a microbrewery (*Les 3 Mousses'quetaires*, 1500-2000L per year)
Mountain hiking, telemark skiing

PERSONAL INFORMATION

Age: 27 (25.08.1991)
Swiss citizenship

PUBLICATIONS

Carlos G. Morales-Guio, Laurent Liardet, Matthew T. Mayer, Stanley D. Tilley, Michael Grätzel and Xile Hu (2015), **Photoelectrochemical Hydrogen Production in Alkaline Solutions Using Cu₂O Coated with Earth-Abundant Hydrogen Evolution Catalysts**. *Angew. Chem. Int. Ed.*, 54: 664–667.

Carlos G. Morales-Guio, Kertin Thorwarth, Bjoern Niesen, Laurent Liardet, Jörg Patscheider, Christophe Ballif and Xile Hu (2015), **Solar Hydrogen Production by Amorphous Silicon photocathodes Coated with a Magnetron Sputter Deposited Mo₂C Catalyst**. *JACS*, 137 (22), 7035-7038.

Carlos G. Morales-Guio, Laurent Liardet and Xile Hu (2016), **Oxidatively Electrodeposited Thin-Film Metal (Oxy)hydroxides as Oxygen Evolution Catalysts**. *JACS*, 138 (28), 8946-8957.

Lucas-Alexandre Stern, Laurent Liardet, Matthew T. Mayer, Carlos Gilberto Morales-Guio, Michael Grätzel and Xile Hu (2017), **Photoelectrochemical deposition of CoP on cuprous oxide photocathodes for solar hydrogen production**. *Electrochimica Acta*, 235, 311-366.

Laurent Liardet and Xile Hu (2018), **Amorphous Cobalt Vanadium Oxide as a Highly Active Electrocatalyst for Oxygen Evolution Reaction**. *ACS Catalysis*, 8, 644-650.

Fang Song, Lichen Bai, Alike Moysiadou, Seunghwa Lee, Chao Hu, Laurent Liardet and Xile Hu (2018), **Transition Metal Oxides as Electrocatalysts for the Oxygen Evolution Reaction in Alkaline Solutions: An Application-Inspired Renaissance**. *JACS*, 140, 7748-7759.

Laurent Liardet, Jordan E. Katz, Jingshan Luo, Michael Grätzel and Xile Hu (2019), **An Ultrathin Cobalt-Iron Oxide Catalyst for Water Oxidation on Nanostructured Hematite Photoanodes**. *Journal of Materials Chemistry A*, 7, 6012-6020.

Lei Zhang, Laurent Liardet, Jingshan Luo, Dan Ren, Michael Grätzel and Xile Hu (2019), **Photoelectrocatalytic Arene C-H Amination**, *Nature Catalysis*, 2, 366-373.

